The Dissertation Committee for Sho Hirose

certifies that this is the approved version of the following dissertation:

Application of Displacement Discontinuity Method To Hydraulic Fracture Propagation in Heterogeneous Rocks

Committee:

Mukul M. Sharma, Supervisor

John T. Foster

David N. Espinoza

Masa Prodanovic

Spyridon A. Kinnas

Application of Displacement Discontinuity Method To Hydraulic Fracture Propagation in Heterogeneous Rocks

by

Sho Hirose

Dissertation

Presented to the Faculty of the Graduate School
of the University of Texas at Austin
in Partial Fulfillment
of the Requirements
for the Degree of

Doctor of Philosophy

The University of Texas at Austin
December 2019

Dedication

To my parents, for their unconditional love, support, and encouragement.

To my brother and sister, for being a constant friend.

Acknowledgements

I would like to first express my sincere gratitude to my supervisor, Dr. Mukul M. Sharma, for his patience, guidance, and encouragement throughout my study at the University of Texas at Austin. He always gave valuable suggestions and guided me to the right track. I would also like to thank my dissertation committee members, Dr. John T. Foster, Dr. David N. Espinoza, Dr. Masa Prodanovic, and Dr. Spyridon A. Kinnas, for their kind advice.

I acknowledge the kind financial support of Japan Petroleum Exploration Co., Ltd. I also express my sincere appreciation to the financial support of Dr. Sharma for the summer semester in 2019. I am extremely grateful to Jin Lee, for her invaluable support throughout the entire period of the program.

I would like to thank all of the members in our group. In particular, I would like to thank Dr. Hisanao Ouchi for introducing me to this wonderful research group. I would also like to specially thank Dr. Johnsoo Hwang, Dr. Ripudaman Manchanda, Dr. Haotian Wang, Dr. Hanyi Wang, and Dr. Kaustubh Shrivastava for valuable discussions and suggestions to my research.

Application of Displacement Discontinuity Method To Hydraulic Fracture Propagation in Heterogeneous Rocks

Sho Hirose, Ph.D.

The University of Texas at Austin, 2019

Supervisor: Mukul M. Sharma

The development of multi-stage hydraulic fracturing technique in horizontal wells enables us to produce oil and gas at economic rate from shale formations, leading to the shale revolution in the United States. Field observations including production history, microseismic mapping, and coring in fractured zones have revealed that the heterogeneity of shale rocks such as natural fractures is likely to have a large impact on oil and gas production from shale reservoirs.

In this dissertation, a new hydraulic fracturing model based on the displacement discontinuity method (DDM) was developed. The major achievements in this research include the extension of DDM to multilayered media, the modeling of the interaction with natural fractures in three dimensions, and the development of a DDM-based hydraulic fracturing simulator.

The formulation of DDM was revisited, and the equivalence of DDM and BEM was mathematically demonstrated. DDM was extended to multilayered media by using the method of images. The new DDM was applied to a three-layered medium

in plain strain containing vertical and horizontal cracks. A sensitivity study suggests that bi-material solutions are sufficient for three-layered media under plain strain conditions.

A DDM-based hydraulic fracturing model was developed. The discretized DDM and flow equations were solved in a segregated or fully coupled manner. A new splitting scheme was proposed to improve the convergence speed of the segregated method. The interaction between hydraulic and natural fractures was modeled for both intersecting and remotely interacting cases in our simulator. Poroelastic effects were partially incorporated into DDM by assuming an undrained condition. It was found that poroelastic effects under the undrained condition were limited to the vicinity of hydraulic fractures.

Hydraulic fracturing simulations were performed in the presence of synthetic natural fracture networks. Synthetic microseismic events were generated, and inversion analyses of the synthetic microseismic data were performed. It was suggested that the density of microseismic events was affected by both the areal density and length distribution of natural fractures.

Table of Contents

List of Tables x

List of Figures xi

Chapter 1: Introduction 1

1.1 Background and Motivation 1

1.2 Research Objectives 3

1.3 Literature Review 3

Chapter 2: Displacement Discontinuity Method 11

2.1 Introduction 11

2.2 Governing Equations 11

2.3 Discretization 19

2.4 Influence Coefficients 21

Chapter 3: Displacement Discontinuity Method for Layered Media 28

3.1 Introduction 28

3.2 The Method of Images 29

3.3 General Image Method 32

3.4 Validation 41

3.5 Application 43

3.6 Conclusion 51

Chapter 4: DDM-Based Hydraulic Fracturing Model 52

4.1 Introduction 52

4.2 Fracture Mechanics 53

4.3 Fluid Mechanics 57

4.4 Solution Strategy 62

4.5 Validation 68

4.6 Results 76
4.7 Conclusion 80
Chapter 5: Interaction Between Hydraulic and Natural Fractures 83
5.1 Introduction 83
5.2 Crossing Criteria 84
5.3 Remote Failure Criteria 105
5.4 Conclusion 112
Chapter 6: Hydraulic Fracturing Simulations in Naturally Fractured Rocks . 114
6.1 Introduction 114
6.2 Generation of Synthetic Natural Fractures 116
6.3 Hydraulic Fracturing Simulations With Natural Fractures 126
6.4 Discussion 137
6.5 Conclusion 137
Chapter 7: Modeling of Microseismic Events 139
7.1 Introduction 139
7.2 Forward Modeling of Synthetic Microseismic Events 141
7.3 Inversion Analysis of Microseismic Data 147
7.4 Application 151
7.5 Conclusion 170
Chapter 8: Conclusion and Future Work 171
8.1 Conclusion 171
8.2 Future Work 175
Appendices 177
Appendix A: Kernel Functions 177
Appendix B: Shape Functions 181
References 183

List of Tables

Table 3.1: The properties used to analyze the pressurized crack in a bi-material. 43

Table 3.2: Properties used for horizontal and vertical pressurized cracks in three-layered media. 45

Table 4.1: Input data used in the comparison of the new and old splitting schemes for a 2D fracture propagation problem. 69

Table 4.2: Simulation parameters used in a 2D fracture propagation problem. 77

Table 5.1: Parameters used to compare crossing criteria with experiments of Zhou et al. (2008). 91

Table 5.2: The rock and fluid properties used in the simulation. 110

Table 6.1: Parameters used to generate natural fracture networks. . . . 126

Table 6.2: Simulation parameters. 131

Table 7.1: The P- and S-wave velocities, rock density, and dynamic elastic moduli. The wave velocities are estimated from Figure B-1 in Stegent and Candler (2018). 152

Table 7.2: The standard deviation of the normal distributions for noise. 156

Table 7.3: The estimated parameters through the inversion analysis of Case 1. 163

Table 7.4: The estimated parameters through the inversion analysis of Case 2. 165

Table 7.5: The standard deviation of the normal distributions for noise. 166

List of Figures

Figure 2.1: A schematic figure of the displacement kernel 14

Figure 2.2: The definition of displacement discontinuity 17

Figure 2.3: A schematic figure of the influence coefficients 20

Figure 3.1: A schematic figure of an isotropic bi-material medium 29

Figure 3.2: A schematic figure of a multilayered isotropic medium 30

Figure 3.3: A schematic figure of the image method in a three-layered medium. A point force is applied at x in the middle layer, and arrows represent reflections and transmissions of the Hansen potentials. The shear modulus and Poisson ratio of the ith layer are G_i and ν_i, respectively. Upper and lower layer interfaces are located at $x_3 = d_{\text{upper}}$ and $x_3 = d_{\text{lower}}$, respectively. . 36

Figure 3.4: A flow chart of the general image method to obtain the potential solution for the middle layer in a three-layered medium. $n_{\max}$ is the maximum number of reflections, $\mathscr{R}_{ij}^{\text{upper}}$ and $\mathscr{R}_{ij}^{\text{upper}}$ are the reflection operator for the upper and lower interfaces, respectively. 38

Figure 3.5: Circular hole near the free surface of a half-plane. 41

Figure 3.6: The tensile stress along the contour of the hole near the free surface under constant hydraulic pressure. θ is the angle from the y-axis in the clockwise direction. The tensile stress is normalized with the pressure. 42

Figure 3.7: A schematic figure of a horizontal crack in a bi-material. The depth of the crack is h, and the length of the crack is $2h$. . . 43

Figure 3.8: The strain energy ratio W/W_0 of a horizontal crack in bi-materials in which a hydraulic pressure $p = 10^{-3}G_1$ is applied. W_0 is the strain energy in the case of $G_1 = G_2 = 1$. 44

Figure 3.9: A schematic of horizontal and vertical cracks in three-layered media. The crack length is h, and the height of the middle layer is h. The shear modulus and Poisson ratio of the ith material are G_i and ν_i. 45

Figure 3.10: The half-width of the horizontal crack in a three-layered medium for different element types in the case of three Gauss points, three images, and $\gamma = 2$. $w_D \coloneqq w/h$ and $x_D \coloneqq x/h$. 47

Figure 3.11: The half-width of the horizontal crack in a three-layered medium for different element types in the case of three Gauss points, three images, and $\gamma = 2$. $w_D \coloneqq w/h$ and $z_D \coloneqq z/h$. 47

Figure 3.12: The half-width of the horizontal crack in a three-layered medium for different number of Gauss points in the case of quadratic elements, eight images, and $\gamma = 2$. $w_D \coloneqq w/h$ and $x_D \coloneqq x/h$. 48

Figure 3.13: The half-width of the horizontal crack in a three-layered medium for different number of Gauss points in the case of quadratic elements, eight images, and $\gamma = 2$. $w_D \coloneqq w/h$ and $z_D \coloneqq z/h$. 48

Figure 3.14: The half-width of the horizontal crack in a three-layered medium for different number of image solutions in the case of quadratic elements, three Gauss points, and $\gamma = 2$. $w_D \coloneqq w/h$ and $x_D \coloneqq x/h$. 49

Figure 3.15: The half-width of the vertical crack in a three-layered medium for different number of image solutions in the case of quadratic elements, three Gauss points, and $\gamma = 2$. $w_D \coloneqq w/h$ and $z_D \coloneqq z/h$. 49

Figure 3.16: The half-width of the horizontal crack in a three-layered medium for different number of image solutions in the case of quadratic elements, three Gauss points, and $\gamma = 5$. $w_D \coloneqq w/h$ and $x_D \coloneqq x/h$. 50

Figure 3.17: The half-width of the vertical crack in a three-layered medium for different number of image solutions in the case of quadratic elements, three Gauss points, and $\gamma = 5$. $w_D \coloneqq w/h$ and $z_D \coloneqq z/h$. 50

Figure 4.1: A flow chart of the fracture propagation algorithm. 64

Figure 4.2: The maximum width of a radial hydraulic fracture in the viscosity-dominated regime without leak-off 71

Figure 4.3: The radius of a radial hydraulic fracture in the viscosity-dominated regime without leak-off 71

Figure 4.4: The width distribution of a radial hydraulic fracture in the viscosity-dominated regime without leak-off at the time step $t = 50$ sec 72

Figure 4.5: The pressure distribution of a radial hydraulic fracture in the viscosity-dominated regime without leak-off at the time step $t = 50$ sec 72

Figure 4.6: The maximum width of a radial hydraulic fracture in the toughness-dominated regime without leak-off 73

Figure 4.7: The radius of a radial hydraulic fracture in the toughness-dominated regime without leak-off 74
Figure 4.8: The width distribution of a radial hydraulic fracture in the toughness-dominated regime without leak-off at the time step $t = 50$ sec 74
Figure 4.9: The pressure distribution of a radial hydraulic fracture in the toughness-dominated regime without leak-off at the time step $t = 50$ sec 75
Figure 4.10: The relaxation factor and the number of iterations for a plain-strain fracture propagation solved with the fixed-width split. 76
Figure 4.11: The relaxation factor for different ω of the fracture compliance split in a 2D planar fracture propagation. 78
Figure 4.12: The number of iterations for different ω of the fracture compliance split in a 2D planar fracture propagation. 78
Figure 4.13: The effect of preconditioning to the coupled matrix of a planar 2D fracture. 79
Figure 4.14: The relaxation factor for the fixed-width split, fracture-compliance split, and fully-coupled methods. 80
Figure 4.15: The number of iterations for the fixed-width split, fracture-compliance split, and fully-coupled methods. 81
Figure 4.16: The ratio of simulation time for the fixed-width split, fracture-compliance split, and fully-coupled methods. The simulation time of the fully coupled method is taken as one. 81

Figure 5.1: A hydraulic fracture intersecting a natural fracture at an angle ϕ. Cylindrical coordinates are shown as r and θ. $\boldsymbol{n}$ and $\boldsymbol{t}$ are the unit normal and tangential vectors of the natural fracture, respectively. 85

Figure 5.2: A flowchart of the fracture propagation algorithm based on the Mohr-Coulomb crossing criterion. 88

Figure 5.3: An example of the initial mesh of hydraulic fracturing simulations with an inclined natural fracture. The notch for the hydraulic fracture is 15 cm in length and 25 cm in height, and the natural fracture is 30 cm in length and 25 cm in height. The unit of the axes is m. 92

Figure 5.4: Fracture meshes after 60 s of fluid injection. The natural fracture is inclined by 30° from the x axis. The SIF-based criterion is used. The stress contrast between the maximum and minimum horizontal stresses are 3, 5, and 7 MPa from the top to bottom, respectively. 93

Figure 5.5: Fracture meshes after 60 s of fluid injection. The natural fracture is inclined by 60° from the x axis. The SIF-based criterion is used. The stress contrast between the maximum and minimum horizontal stresses are 3, 5, and 7 MPa from the top to bottom, respectively. 94

Figure 5.6: Fracture meshes after 60 s of fluid injection. The natural fracture is inclined by 90° from the x axis. The SIF-based criterion is used. The stress contrast between the maximum and minimum horizontal stresses are 3, 5, and 7 MPa from the top to bottom, respectively. 95

Figure 5.7: Fracture meshes after 60 s of fluid injection. The natural fracture is inclined by 30° from the x axis. The ERR-based criterion is used. The stress contrast between the maximum and minimum horizontal stresses are 3, 5, and 7 MPa from the top to bottom, respectively. 97

Figure 5.8: Fracture meshes after 60 s of fluid injection. The natural fracture is inclined by 60° from the x axis. The ERR-based criterion is used. The stress contrast between the maximum and minimum horizontal stresses are 3, 5, and 7 MPa from the top to bottom, respectively. 98

Figure 5.9: Fracture meshes after 60 s of fluid injection. The natural fracture is inclined by 90° from the x axis. The ERR-based criterion is used. The stress contrast between the maximum and minimum horizontal stresses are 3, 5, and 7 MPa from the top to bottom, respectively. 99

Figure 5.10: Fracture meshes after 60 s of fluid injection. The natural fracture is inclined by 60° from the x axis. The ERR-based criterion is used. The stress contrast between the maximum and minimum horizontal stresses is 5 MPa. The fracture width is presented as face colors, and the magnitude of shear slippage and its direction is described as cones with colors. 100

Figure 5.11: Fracture meshes after 60 s of fluid injection. The natural fracture is inclined by 30° from the x axis. The MC-based criterion is used. The stress contrast between the maximum and minimum horizontal stresses are 3, 5, and 7 MPa from the top to bottom, respectively. 101

Figure 5.12: Fracture meshes after 60 s of fluid injection. The natural fracture is inclined by 60° from the x axis. The MC-based criterion is used. The stress contrast between the maximum and minimum horizontal stresses are 3, 5, and 7 MPa from the top to bottom, respectively. 102

Figure 5.13: Fracture meshes after 60 s of fluid injection. The natural fracture is inclined by 90° from the x axis. The MC-based criterion is used. The stress contrast between the maximum and minimum horizontal stresses are 3, 5, and 7 MPa from the top to bottom, respectively. 103

Figure 5.14: The crossing behavior of the hydraulic fracture. The experimental results of Zhou et al. (2008) are presented as well. . . 104

Figure 5.15: The mean stress along the z-axis of a radial crack. $\zeta := z/c$, c is the radius of the crack, and p is the internal pressure applied to the crack surface. Poisson's ratio is 0.25. Tension positive sign convention is used. 109

Figure 5.16: The simulation result of Case 1 (no poroelastic effect). 111

Figure 5.17: The simulation result of Case 2 (poroelastic effects for an oil reservoir). 111

Figure 5.18: The simulation result of Case 3 (poroelastic effects for a gas reservoir). 112

Figure 6.1: A flow chart of geomechanical simulations assisted by microseismic data. 115

Figure 6.2: Fracture length distribution generated by using the power-law distribution. $l_0 = 1\,\mathrm{m}$ and $l_1 = 30\,\mathrm{m}$. The number of samples is 1000. 118

Figure 6.3: Rose diagrams of the von Mises distribution for $\mu' = \pi/2$. The number of samples is 1000. 120

Figure 6.4: An example of bimodal von Mises distribution. The first mode is ${\mu'}_1 = \pi/2$ and ${\kappa'}_1 = 5$, and the second mode is ${\theta'}_2 = 4\pi/3$ and ${\kappa'}_2 = 3$. The mixing parameter is $w = 0.7$. 121

Figure 6.5: Mesh configuration for testing the proposed correction method. Two hydraulic fractures propagate in straight line and eventually intersect. Fracture turning option is disabled. 123

Figure 6.6: Meshes at the end of fracturing simulations without scaling of influence coefficients. Only NaN correction is applied. The simulation using the segregated method did not converge at $t = 7\,\mathrm{s}$. 124

Figure 6.7: Meshes at the end of fracturing simulations with scaling of influence coefficients. NaN correction is also applied. 125

Figure 6.8: Natural fractures generated by using the power-law and von Mises distributions. $\mu = \pi/4$ and $\kappa = 5$. Domain size is $100\,\mathrm{m}$ in the x and y directions. 128

Figure 6.9: The frequency of intersections along the y-axis for different distribution parameters of the power-law distribution. $\mu = \pi/4$ and $\kappa = 5$ are used for the von Mises distribution. The domain size of realizations is $100 \times 100\,\mathrm{m}$ in the x and y directions. Error bars represent the maximum and minimum values found in the realizations. 129

Figure 6.10: Hydraulic fracture propagation in natural fracture networks with remote failure of natural fractures. $\rho_{\mathrm{NF}} = 0.05\,\mathrm{m}^{-2}$, and $S_{\mathrm{hmax}} = 36.44\,\mathrm{MPa}$. Black and red lines represent natural and hydraulic fractures, respectively. 132

Figure 6.11: Hydraulic fracture propagation in natural fracture networks without remote failure of natural fractures. The same natural fracture networks with Fig. 6.10 are used. Blue circles represent differences from Fig. 6.10. 133

Figure 6.12: Hydraulic fracture propagation in natural fracture networks with remote failure of natural fractures. $\rho_{\mathrm{NF}} = 0.05\,\mathrm{m}^{-2}$, and $S_{\mathrm{hmax}} = 39.44\,\mathrm{MPa}$. Black and red lines represent natural and hydraulic fractures, respectively. 134

Figure 6.13: Hydraulic fracture propagation in natural fracture networks with remote failure of natural fractures. $\rho_{\mathrm{NF}} = 0.1\,\mathrm{m}^{-2}$. Black and red lines represent natural and hydraulic fractures, respectively. 135

Figure 6.14: Hydraulic fracture propagation in natural fracture networks with remote failure of natural fractures. Bimodal distribution is used. Mean directions are 45° and 135° from the x axis, and concentration parameter is 5 for both modes. Mixing parameter is 0.5. $\rho_{\mathrm{NF}} = 0.05\,\mathrm{m}^{-2}$. Black and red lines represent natural and hydraulic fractures, respectively. 136

Figure 7.1: A flow chart of geomechanical simulations assisted by microseismic data 140

Figure 7.2: A flowchart of the forward modeling of microseismic events. . 146

Figure 7.3: A schematic figure of the inversion analysis of microseismic data. 148
Figure 7.4: A flowchart of the inversion analysis for the location of microseismic events. 150
Figure 7.5: A flowchart of the inversion analysis for seismic moment. . . 151
Figure 7.6: The moment magnitude and the location of the synthetic microseismic events estimated from the simulation result of Fig. 6.10a. The observation well is shown as a black cross. The color map represents the moment magnitude. 154
Figure 7.7: The moment magnitudes estimated by using the Brune's equation against the moment magnitudes computed by using Eq. 7.1. 155
Figure 7.8: The moment magnitudes estimated by using the Brune's equation with the correct radiation pattern correction factor against the moment magnitudes computed by using Eq. 7.1. 156
Figure 7.9: The moment magnitude and the location of the synthetic microseismic events estimated from the simulation result of Fig. 6.10a. The observation well is shown as a black cross. The color map represents the moment magnitude. 157
Figure 7.10: The moment magnitude and the location of the synthetic microseismic events estimated from the simulation result of Fig. 6.10a. The observation wells are shown as black crosses. The color map represents the moment magnitude. 159
Figure 7.11: The error in the microseismic event locations. 160

Figure 7.12: The location and orientation of a synthetic seismic source and receiver arrays. The arrow represents the slip direction. Lines represents observation wells, and circles represent receivers. Upper figures are a 3D view, and the lower figures are a plan view. 162
Figure 7.13: The measured and estimated low frequency amplitude at each receiver for Case 1. 163
Figure 7.14: The computed and estimated radiation pattern correction factor at each receiver for Case 1. 164
Figure 7.15: The measured and estimated low frequency amplitude at each receiver for Case 2. 165
Figure 7.16: The computed and estimated radiation pattern correction factor at each receiver for Case 2. 166
Figure 7.17: The measured and estimated low frequency amplitude at each receiver for Case 3 with small noise. 167
Figure 7.18: The computed and estimated radiation pattern correction factor at each receiver for Case 3 with small noise. 168
Figure 7.19: The measured and estimated low frequency amplitude at each receiver for Case 3 with large noise. 168
Figure 7.20: The computed and estimated radiation pattern correction factor at each receiver for Case 3 with large noise. 169

Chapter 1: Introduction

1.1 Background and Motivation

When hydraulic fracturing is applied to horizontal wells with many clusters of perforations, multiple, non-planar fractures may grow. The presence of natural fractures and the stress interference between fractures will result in complex fracture patterns that are difficult to model with standard finite element or finite volume methods. If such a domain discretization methods are applied, mesh modification around growing fractures is a non-trivial problem in general.

The displacement discontinuity method (DDM) was first proposed by Crouch (1976) as a subset of the boundary element method (BEM) for crack problems. Crack surfaces are decomposed into straight or flat elements, and the contribution of each element to elastic fields at a given point is computed by using influence functions. DDM possesses several key advantages of BEM :

- Discretization is only over boundaries, making mesh generation easier and reducing the number of unknowns.
- The infinite boundary condition can be handled easily.
- The derivatives of fields can be directly calculated inside the domain or on the boundaries.
- The singular behavior of fields can be readily incorporated.

Because of these merits, the DDM was recently applied to hydraulic fracture simulation, and the impact of stress shadow on multiple hydraulic fracture growth and the effect of natural fractures on hydraulic fracture propagation were investigated (Olson, 2008; Sheibani, 2013; Wu and Olson, 2013; Wu, 2014; Wu and Olson, 2015a,b;

Shrivastava et al., 2017). All these studies assume that the fracture propagates in a homogeneous, elastic medium.

When considering the application of DDM to hydraulic fracture simulations, it is natural to incorporate the effect of layers and natural fractures since the stress field in a layered-medium with natural fractures can be significantly different from that in a homogeneous medium. For layer properties, however, only horizontal stresses and stress intensity factors are taken into account in the conventional DDM due to its theoretical difficulty of incorporating heterogeneity, which comes from the requirement of the fundamental solution for the governing equation. For natural fractures, induced fractures disconnected from hydraulic fractures are often neglected, and only hydraulically-connected fractures are evaluated in hydraulic fracture simulations. Because the shear displacement of isolated fractures is categorized as a contact problem, which is difficult to solve for, the problem is simplified by neglecting such sheared fractures.

It is common to distribute the location, orientation, and extension of natural fractures based on either statistical data obtained from cores and well logs or microseismic data in hydraulic fracture simulations. Microseismic data are thought to represent actual locations of planes of failure in the rock. Hydraulic fracture simulations assisted by microseismic data have been pursued (Weng et al., 2014). However, microseismic data are not always reliable (Warpinski and Wolhart, 2016), and it has been recognized that much of deformation due to hydraulic fracturing occurs aseismically (Maxwell et al., 2008). This prevents a quantitative analysis of fracture networks based on microseismic data.

1.2 Research Objectives

The objective of this research is to evaluate the effect of layers and natural fractures on hydraulic fracture propagation by using displacement discontinuity methods and to more accurately incorporate microseismic data into hydraulic fracture simulations.

1.3 Literature Review

1.3.1 Hydraulic Fracturing Models

The hydraulic fracturing problem is concerned with solving for the change in fracture length, height, and width due to fluid injection. The earliest paper solving such a problem was on the growth of a vertical fracture at constant injection rate with negligible fluid loss into formations (Khristianovic and Zheltov, 1955). Their model assumed the plain strain condition in the vertical direction, constant fluid viscosity, and constant fracture height. Later, Geertsma and de Klerk (1969) incorporated the contribution of the fluid loss into reservoir rocks by using Carter's leak-off model (Howard and Fast, 1957), and the extended model is refered to as the Khristianovitch-Geertsma-de Klerk (KGD) model. Geertsma and de Klerk (1969) also developed a model for a radially growing fracture from a well based on the analytical equation proposed by Sneddon (1946).

Perkins and Kern (1961) proposed another model similar to Khristianovic's model. Their model was also for the growth of a vertical fracture with a fixed height, constant injection rate, and negligible leak-off. The difference from the Khristianovic's model was that Perkins' model assumed a plain strain condition in the lateral direction. Perkins' model was extended by Nordgren (1972) to account for fluid loss, and this model is referred to as the Perkins-Kern-Nordgren (PKN) model.

Pseudo-3D (P3D) models are computational methods developed in 1980's to capture the height growth of a planar fracture. P3D models are primarily divided into cell-based and lumped methods. The cell-based P3D models discretize a planar fracture into cells to reduce a 3D hydraulic fracturing problem to a set of 2D elastic deformation on each cell and 1D lateral fluid flow between the cells. Settari and Cleary (1986) first proposed a cell-based P3D model. Each cell were assumed to be a Griffith-type crack, and its vertical length and width profile were calculated by using analytical equations. On the other hand, lumped models, which were first proposed by Cleary et al. (1983), approximate the growth of a planar fracture with simple equations multiplied by correction or lumped parameters. The deviation of fracture geometry from ideal shapes such as a circular, KGD, and PKN types is lumped into the correction factors. In general, P3D models are computationally quite efficient and fast due to the use of analytical equations or approximations.

In contrast to P3D models, planar 3D models fully discretize a planar fracture into unstructured or cartesian grids, and thus much more accurate results for fracture geometry and fluid distribution can be obtained compared to P3D models. Advani et al. (1990); Lee et al. (1990) proposed the finite element formulation of a hydraulic fracturing model. A planar fracture is discretized into triangular cells, and the elasticity and fluid flow equations are iteratively solved. Naceur et al. (1990) developed a planar 3D model using an indirect BEM. They solved the system of elasticity and fluid flow equations in a fully-coupled manner.

The aforementioned models all assume a planar fracture geometry and solve for the fluid pressure in the fracture and fracture width (not in the surrounding rock matrix). However, the propagation of multiple fractures in parallel from clusters in a stage causes elastic interference between fractures. This is known as the stress shadow effect. Moreover, all shale formations have some geological heterogeneity such as lay-

ers and natural fractures. Hence, fractures initiated from perforations may turn due to the stress shadow effect, propagate along layer interfaces, or create branches when intersecting natural fractures, resulting in complex, non-planar fractures. General methods have been proposed to account for such complex fracture behavior. These methods include the discrete element method (Nagel and Sanchez-nagel, 2011; Yan et al., 2016), the finite element method or the finite volume method with cohesive zone models (Carrier and Granet, 2012; Manchanda et al., 2017), the extended or generalized FEM (Gupta and Duarte, 2014), the boundary element method (Rungamornrat et al., 2005; Rungamornrat, 2006), peridynamics models (Ouchi et al., 2015, 2017), and phase-field models (Mikelić et al., 2015a,b,c).

In recent years, asymptotic solutions of hydraulic fractures based on fracture propagation regimes has been presented. The asymptotic solutions are divided into four solutions: $\mathcal{K}$, $\mathcal{M}$, $\tilde{\mathcal{K}}$, and $\tilde{\mathcal{M}}$-vertex solutions shown in Figure 2 of Bunger et al. (2005). Each vertex represents the dominant mechanism in fracture propagation, i.e. toughness, viscosity, and fluid leak-off.

Savitski and Detournay (2002) developed asymptotic solutions of penny-shaped hydraulic fractures in impermeable rocks. (Garagash and Detournay, 2005) found that the effect of fracture toughness is localized in the vicinity of tips for plain-strain fractures without leak-off. Adachi and Detournay (2002) and Garagash (2006) proposed an analytical solution of a plane-strain fracture driven by a power-law fluid. Detournay (2004) summarized the propagation regimes which appear in hydraulic fracturing in impermeable rocks for both plain-strain and radial fractures. Solutions with leak-off into formations were proposed by Bunger et al. (2005), Hu and Garagash (2010), Garagash et al. (2011), and Dontsov (2016). A review of these asymptotic solutions and their formulations can be found in Detournay (2016).

1.3.2 Displacement Discontinuity Method

The displacement discontinuity method (DDM) is an indirect boundary element method (BEM) for crack problems proposed by Crouch (1976). Fracture surfaces are discretized into small-sized straight or planar elements, and the interaction between these elements is computed by using analytical equations. The coefficients representing the inter-element interaction are called influence coefficients. Each element has one or more collocation points where the discontinuity in displacement fields is computed. Elements with constant displacement discontinuity have only one collocation point per element, while higher-order elements such as linear or quadratic elements have multiple collocation points.

Several analytical equations for the influence coefficients are available for different element types in homogeneous isotropic media. The first paper deriving such an equation was by Rongved and Hill (1957), giving the solution for a rectangular element with constant strength. Salamon (1964) independently obtained the same solution. Crouch (1976) developed the analytical solution for two-dimensional constant elements. Later, solutions for higher-order elements were obtained in both two and three dimensions (Crawford and Curran, 1982; Shou, 1993; Shou and Crouch, 1995; Shou et al., 1997). Analytical solutions for triangular elements were also derived by Kuriyama and Mizuta (1993) and Cheng et al. (2015a), though they diverge when a collocation point lies along the extension of triangle edges.

In addition, some attempts have been made to derive analytical solutions of the influence coefficients in half-space and bi-materials. Crouch (1976) obtained the solution for constant elements in two-dimensional semi-infinite plane. The analytical solution for bi-materials in two dimensions was developed by Crouch and Starfield (1983). These solutions are, however, not often used due to their lengthy and com-

plicated representations. Furthermore, the analytical solutions for three-dimensional elements in half-space or bi-materials have not been found.

Some researchers applied the DDM to layered media. Selcuk and Crouch (1992) combined the bi-material solution of Crouch and Starfield (1983) with domain decomposition to solve boundary value problems in a four layered medium in two dimensions. Shou (1997) and Shou and Napier (1999) claimed that they derived the analytical solution of the influence coefficients for three-layered media using the method of images. However, their solution was actually an approximation because it did not incorporate multiple images (Siebrits and Crouch, 2000). Li et al. (2018) proposed a pseudo 3-D DDM for layered media which only incorporates the vertical variation of far-field stresses.

Other researchers have tried to solve crack problems in layered media from the viewpoint of the BEM. In the BEM, solving crack problems in layered media is understood as finding an appropriate fundamental solution. Wang and Clifton (1990) proposed to multiply a correction factor to the fundamental solution of homogeneous media. The correction factor is estimated by using the fundamental solution for bi-materials. Zhang and Jeffrey (2006) solved hydraulic fracturing problems in three-layered media in two dimensions by deriving the fundamental solution based on the Airy stress functions. The explicit form of the fundamental solution of multilayered media in three dimensions was derived by Yue (1995). The solution was applied to crack problems in a series of papers (Yue and Xiao, 2002; Yue et al., 2003; Xiao and Yue, 2011; Xiao et al., 2012). Xu and Wong (2013) and Wong et al. (2013) claimed that they incorporated layer heterogeneity in their model, though they did not provide any clear explanation about their formulation. Du et al. (1994, 1997) developed a moduli perturbation method to analyze the surface deformation of inhomogeneous media caused by dislocations. Du et al. (2000) used the moduli perturbation method

for downhole tilt meter analysis.

DDM has been widely applied to hydraulic fracturing problems due to its simplicity and high accuracy. In particular, fracture turning can be easily implemented with DDM because it does not require domain discretization. Thus, the effect of stress shadow between multiple growing hydraulic fractures has been analyzed with the aid of DDM (Olson, 2008; Wu and Olson, 2013; Wu, 2014; Wu and Olson, 2015a,b). Furthermore, because the intersection behavior of hydraulic and natural fractures can be simulated based on stress intensity factors (Gu and Weng, 2010) or energy release rates (Dahi Taleghani and Olson, 2013), the DDM is frequently used to simulate fracture propagation in the presence of natural fractures (Olson, 2008; Wu, 2014; Xie et al., 2016; Zhang et al., 2017; Shrivastava et al., 2018; Shrivastava and Sharma, 2018a,b; Chang et al., 2018).

1.3.3 Natural Fractures

The spatial and geometrical distribution of natural fractures has been actively investigated. Davy (1993) analyzed the San Andreas fault system to obtain a function that can fit data over a wide range of fault lengths. Gale et al. (2007) characterized natural fractures observed in cores taken in the Barnett Shale from the viewpoint of orientation, size, and cementation. Hooker et al. (2013) obtained the aperture size, frequency, orientation, and spatial distribution of natural fractures in Cambrian Mesón Group in NW Argentina. Gale et al. (2014) reviewed the common types of natural fractures, their spatial distribution, and mineralization in cores and outcrops from different shale plays. Davy et al. (2018) derived the relationships between elastic properties of rocks and geometrical properties of fracture networks.

It is important to quantify the complexity of synthetically-generated fracture networks in hydraulic fracturing simulations with discrete fracture networks. Feng et al.

(2017) proposed a fracture complexity indicator for quantifying such complexity. On the other hand, Sui et al. (2019) used fractal methods to describe fracture networks. Alghalandis et al. (2015) characterized the connectivity of fracture networks by using a connectivity field.

1.3.4 Microseismic Monitoring

Microseismic monitoring is an effective tool to estimate the lateral length of hydraulic fractures, the effectiveness of hydraulic fracturing in each stage, and the extension of natural fracture networks. The location, orientation, and extension of induced fractures can be obtained from microseismic monitoring. Typical methods for computing the location of microseismic events are hodogram (Warpinski et al., 2005), triangulation (Rutledge and Phillips, 2003), or semblance-based techniques (Rentsch et al., 2007). The orientation and extension of fractures can be simultaneously obtained through moment tensor inversion (MTI) (Vavryčuk, 2007). The moment magnitude and size of microseismic sources, which are called source parameters, are normally calculated based on Brune's equation (Warpinski et al., 2013).

These calculated event locations have some error associated with them due to the low signal-to-noise ratio (S/N), uncertainty in a velocity model (Maxwell et al., 2010; Usher et al., 2013) and geophone-array geometry (Maxwell et al., 2010), anisotropy in elastic moduli (Grechka and Yaskevich, 2014), and observation well bias (Cipolla et al., 2011; Warpinski and Wolhart, 2016). All of these factors can result in a discrepancy between the locations of microseismic events and fractures observed in cores (Warpinski and Wolhart, 2016).

The Gutenberg-Richter relation is a well-known empirical relationship between the number of seismic events and their magnitudes (Ishimoto and Iida, 1939; Gutenberg and Richter, 1944). The slope of the Gutenberg-Richter relation or b-value can be

used to differentiate failures due to hydraulic fracturing and activated natural fractures (Maxwell et al., 2009; Yousefzadeh et al., 2018). Dohmen et al. (2017) showed microseismic events in depleted and non-depleted zones exhibit different b-values. Jiao et al. (2014) pointed out that the magnitudes estimated with Brune's equation were inaccurate for tensile failures, and hence incorrect b-values can be obtained.

Several attempts have been made to integrate microseismic data with hydraulic fracturing simulations. Boroumand and Eaton (2015) used microseismic event locations to calibrate the growth of a 3D planar elliptic fracture model. Maxwell et al. (2015) classified microseismic events into "dry" and "wet" events. The dry events are caused purely by mechanical stress change, and the wet events are triggered by fluid leak-off into natural fractures. Maxwell et al. (2015) observed significantly more wet events than dry events in a hydraulic fracturing simulation in synthetic natural fractures using the discrete element method. Fry et al. (2015) computed magnitudes of microseismic events in fracturing simulations based on the synthetic rock mass method.

Chapter 2: Displacement Discontinuity Method

2.1 Introduction

This chapter describes the formulation of the displacement discontinuity method (DDM), which was introduced by Crouch (1976) as an indirect boundary element method (BEM) for crack problems in homogeneous isotropic elastic media. In the DDM, crack surfaces are discretized into small planar elements, and displacement and stress at an arbitrary point inside the domain are computed as a sum of the contribution from all the elements, or using the principle of superposition.

We start from the governing equation and derive its boundary integral representation, which is known as the Somigliana identity. Then, the numerical discretization of boundary integral equations and the assembly of the system of equations are explained. Finally, we show that DDM and BEM are essentially equivalent in a general manner. Without loss of generality, we restrict our formulation to that for linear isotropic elastic media. Although the media can be homogeneous, which is the case for Crouch (1976), the formulation, in general, is valid for inhomogeneous media.

2.2 Governing Equations

2.2.1 Navier-Cauchy Equation

The equilibrium condition can be expressed as:

$$\sigma_{ji,j} + f_i = 0, \tag{2.1}$$

where σ_{ij} is the stress tensor, and f_i is the body force vector. Index notation and tension positive sign convention are used throughout this dissertation.

The constitutive law of a linear elastic material is the generalized Hook's law:

$$\sigma_{ij} = C_{ijkl}\epsilon_{kl}, \tag{2.2}$$

where C_{ijkl} is the fourth-order stiffness tensor with the symmetry of $C_{ijkl} = C_{jikl}$, $C_{ijkl} = C_{ijlk}$, and $C_{ijkl} = C_{klij}$. ϵ_{ij} is the infinitesimal strain tensor defined by

$$\epsilon_{ij} \coloneqq \frac{1}{2}(u_{j,i} + u_{i,j}), \tag{2.3}$$

where u_i is the displacement vector. For isotropic materials, the stiffness tensor can be expressed in terms of two parameters:

$$C_{ijkl} = \lambda\delta_{ij}\delta_{kl} + G(\delta_{ik}\delta_{jl} + \delta_{il}\delta_{jk}), \tag{2.4}$$

where λ is the first Lamé parameter, G is shear modulus, and δ_{ij} is the Kronecker delta. Substituting Eq. 2.3 and Eq. 2.4 into Eq. 2.2, we obtain

$$\sigma_{ij} = \lambda\delta_{ij}u_{k,k} + G(u_{i,j} + u_{j,i}). \tag{2.5}$$

Assuming a homogeneous medium, the equilibrium condition reduces to the well-known Navier-Cauchy equation:

$$Gu_{i,jj} + (\lambda + G)u_{j,ji} + f_i = 0. \tag{2.6}$$

Using the relationship $\lambda = K - 2G/3$, where K is the bulk modulus, an alternative

expression is obtained.

$$Gu_{i,jj} + \left(K + \frac{1}{3}G\right) u_{j,ji} + f_i = 0. \tag{2.7}$$

2.2.2 Somigliana Identity

For convenience, we define the traction operator $\mathcal{T}$:

$$t_i = \sigma_{ij} n_j = C_{ijkl} n_j u_{k,l} =: \mathcal{T} u_i, \tag{2.8}$$

where t_i is the traction vector, and n_i is the unit normal vector. The traction operator for isotropic materials becomes

$$\mathcal{T} u_i = \lambda n_i u_{k,k} + G n_j (u_{i,j} + u_{j,i}). \tag{2.9}$$

Suppose that u_i is a displacement field due to body forces f_i inside a region Ω bounded by Γ. Let u_i^* is another displacement field due to body forces f_i^*. Then, according to the Betti's reciprocal work theorem, the following equation holds:

$$\int_\Omega (f_i^* u_i - f_i u_i^*) \, \mathrm{d}\Omega = \int_\Gamma (u_i^* t_i - u_i t_i^*) \, \mathrm{d}\Gamma, \tag{2.10}$$

where t_i and t_i^* are traction fields corresponding to u_i and u_i^*, respectively.

We now assume that f_i^* is a concentrated force applied at a source point $x \in \Omega$. Then, the corresponding displacement and traction fields at a field point y take the

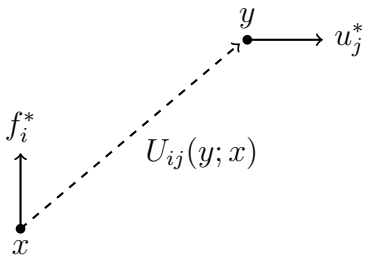

Figure 2.1: A schematic figure of the displacement kernel

following form

$$u_j^*(y) = U_{ij}(y;x) f_i^*(x), \tag{2.11}$$

$$t_j^*(y) = T_{ij}(y;x) f_i^*(x), \tag{2.12}$$

where y is a field point. U_{ij} and T_{ij} are respectively the jth component of displacement and traction at y due to the concentrated body force in the ith direction applied at x. U_{ij} and T_{ij} are called displacement and traction kernels, respectively. A schematic figure of the displacement kernel is shown in Fig. 2.1. The traction and displacement kernels have the following relationship:

$$T_{ij}(y;x) = \mathcal{T}_y U_{ij}(y;x), \tag{2.13}$$

where the subscript y denotes the traction operator is evaluated at y.

The fundamental solutions of the Navier-Cauchy equation are referred to as the Kelvin solutions. They can be found in standard textbooks for BEM, e.g. Gao and Davies (2002), and presented in Appendix A.

Substituting Eq. 2.11 and Eq. 2.12 into Eq. 2.10 and neglecting body forces, we

obtain the Somigliana identity for displacements:

$$u_i(x) = \int_\Gamma U_{ij}(y;x)t_j(y)\,\mathrm{d}\Gamma(y) - \int_\Gamma T_{ij}(y;x)u_j(y)\,\mathrm{d}\Gamma(y), \quad x \in \Omega \setminus \Gamma. \tag{2.14}$$

Applying the traction operator to Eq. 2.14 in terms of the source point x, we obtain the Somigliana identity for tractions:

$$t_i(x) = \int_\Gamma K_{ij}(y;x)t_j(y)\,\mathrm{d}\Gamma(y) - \int_\Gamma H_{ij}(y;x)u_j(y)\,\mathrm{d}\Gamma(y), \quad x \in \Omega \setminus \Gamma. \tag{2.15}$$

K_{ij} and H_{ij} are kernel functions defined by

$$K_{ij}(y;x) \coloneqq \mathcal{T}_x U_{ij}(y;x), \tag{2.16}$$

$$H_{ij}(y;x) \coloneqq \mathcal{T}_x T_{ij}(y;x). \tag{2.17}$$

It should be mentioned that, because the Betti's reciprocal theorem holds for any elastic media, the Somigliana identity is valid not only for homogeneous media but also for inhomogeneous media. That is, the elastic constants, λ and G, can be a function of space.

Before deriving the Somigliana identity for crack problems, the following integral operators are introduced to simplify the formulation hereafter:

$$\left(\mathscr{U}_{ij}v_j\right)_\Gamma(x) \coloneqq \int_\Gamma U_{ij}(y;x)v_j(y)\,\mathrm{d}\Gamma(y), \tag{2.18}$$

$$\left(\mathscr{T}_{ij}v_j\right)_\Gamma(x) \coloneqq \int_\Gamma T_{ij}(y;x)v_j(y)\,\mathrm{d}\Gamma(y), \tag{2.19}$$

$$\left(\mathscr{K}_{ij}v_j\right)_\Gamma(x) \coloneqq \int_\Gamma K_{ij}(y;x)v_j(y)\,\mathrm{d}\Gamma(y), \tag{2.20}$$

$$\left(\mathscr{H}_{ij}v_j\right)_\Gamma(x) \coloneqq \int_\Gamma H_{ij}(y;x)v_j(y)\,\mathrm{d}\Gamma(y). \tag{2.21}$$

Using the above operators, Eq. 2.14 and Eq. 2.15 are simplified into

$$u_i(x) = (\mathscr{U}_{ij} t_j)_\Gamma (x) - (\mathscr{T}_{ij} u_j)_\Gamma (x), \quad x \in \Omega \setminus \Gamma, \tag{2.22}$$

$$t_i(x) = (\mathscr{K}_{ij} t_j)_\Gamma (x) - (\mathscr{H}_{ij} u_j)_\Gamma (x), \quad x \in \Omega \setminus \Gamma. \tag{2.23}$$

To derive the Somigliana identity for crack problems, a crack boundary Γ is split into its positive and negative sides $\Gamma^{\pm}$. Since two sides coincide, the kernels have properties

$$U_{ij}(y^-; x) = U_{ij}(y^+; x), \tag{2.24}$$

$$T_{ij}(y^-; x) = -T_{ij}(y^+; x), \tag{2.25}$$

$$K_{ij}(y^-; x) = K_{ij}(y^+; x), \tag{2.26}$$

$$H_{ij}(y^-; x) = -H_{ij}(y^+; x), \tag{2.27}$$

where the superscript $\pm$ denotes the corresponding boundary surfaces $\Gamma^{\pm}$. Therefore, the Somigliana identity for displacements can be rearranged as (Cruse, 1972, 1978, 1988)

$$\begin{aligned} u_i(x) &= (\mathscr{U}_{ij} t_j)_\Gamma (x) - (\mathscr{T}_{ij} u_j)_\Gamma (x) \\ &= \left[(\mathscr{U}_{ij} t_j)_{\Gamma^-} + (\mathscr{U}_{ij} t_j)_{\Gamma^+}\right](x) - \left[(\mathscr{T}_{ij} u_j)_{\Gamma^-} + (\mathscr{T}_{ij} u_j)_{\Gamma^+}\right](x) \\ &= (\mathscr{U}_{ij} \Sigma t_j)_{\Gamma^+} (x) - (\mathscr{T}_{ij} \Delta u_j)_{\Gamma^+} (x), \end{aligned} \tag{2.28}$$

where $\Sigma t_i(y) \coloneqq t_i(y^+) + t_i(y^-)$, and $\Delta u_i(y) \coloneqq u_i(y^+) - u_i(y^-)$. A schematic figure of Δu_i is shown in Fig. 2.2.

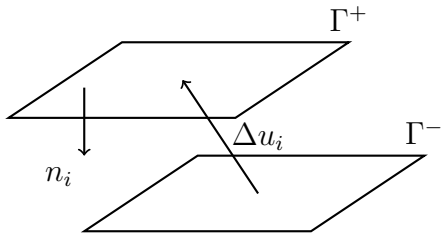

Figure 2.2: The definition of displacement discontinuity

Similarly, the Somigliana identity for tractions reduces to

$$t_i(x) = \left(\mathscr{U}_{ij}\Sigma t_j\right)_{\Gamma^+}(x) - \left(\mathscr{T}_{ij}\Delta u_j\right)_{\Gamma^+}(x). \tag{2.29}$$

Assuming that the traction on the fracture surface is in equilibrium, we have

$$\Sigma t_i(y) = t_i(y^+) + t_i(y^-) = 0. \tag{2.30}$$

Therefore, we obtain the Somigliana identities for crack problems:

$$u_i(x) = -\left(\mathscr{T}_{ij}\Delta u_j\right)_{\Gamma^+}(x), \quad x \in \Omega \setminus \Gamma, \tag{2.31}$$

$$t_i(x) = -\left(\mathscr{H}_{ij}\Delta u_j\right)_{\Gamma^+}(x), \quad x \in \Omega \setminus \Gamma. \tag{2.32}$$

2.2.3 Boundary Integral Equations

The boundary integral equations (BIEs) can be derived from Eq. 2.14 and Eq. 2.15 by letting the source point x approach the boundary Γ. Assuming Γ is sufficiently smooth, the BIEs take the following form (Liu, 2009)

$$\frac{1}{2}u_i(x) = \left(\mathscr{U}_{ij}t_j\right)_{\Gamma}(x) - \left(\mathscr{T}_{ij}u_j\right)_{\Gamma}(x), \quad x \in \Gamma, \tag{2.33}$$

$$\frac{1}{2}t_i(x) = \left(\mathscr{K}_{ij}t_j\right)_{\Gamma}(x) - \left(\mathscr{H}_{ij}u_j\right)_{\Gamma}(x), \quad x \in \Gamma. \tag{2.34}$$

$\mathscr{T}_{ij}$ and $\mathscr{K}_{ij}$ should be interpreted in the Cauchy principal value sense, and $\mathscr{H}_{ij}$ is evaluated by using the Hadamard finite part integral.

To apply the BIEs to fracture problems, the boundary Γ is split into two surfaces $\Gamma^{\pm}$ with some positive distance h. Taking the limit of $h \to 0$, Γ^{+} approaches and finally collapses on Γ^{-}. This limiting process has to be performed carefully because there exist jump terms in the integral operators due to their singularirty. The BIEs for crack problems are given by (Cruse, 1972, 1988; Krishnasamy et al., 1994; Liu, 1998; Liu and Li, 2014)

$$\frac{1}{2}\Sigma u_i(x) = \left(\mathscr{U}_{ij}\Sigma t_j\right)_{\Gamma^+}(x) - \left(\mathscr{T}_{ij}\Delta u_j\right)_{\Gamma^+}(x), \tag{2.35}$$

$$\frac{1}{2}\Delta t_i(x) = \left(\mathscr{K}_{ij}\Sigma t_j\right)_{\Gamma^+}(x) - \left(\mathscr{H}_{ij}\Delta u_j\right)_{\Gamma^+}(x), \tag{2.36}$$

where $\Delta t_i(x) \coloneqq t_i(x^+) - t_i(x^-)$, and $\Sigma u_i(x) \coloneqq u_i(x^+) + u_i(x^-)$. Assuming that the traction on the fracture surface is in equilibrium, we have $\Sigma t_i(x) = 0$ and $\Delta t_i(x) = 2t_i(x^+) = -2t_i(x^-)$. Therefore, Eq. 2.35 and Eq. 2.36 reduce to

$$\frac{1}{2}\Sigma u_i(x) = -\left(\mathscr{T}_{ij}\Delta u_j\right)_{\Gamma^+}(x), \tag{2.37}$$

$$t_i(x^+) = -\left(\mathscr{H}_{ij}\Delta u_j\right)_{\Gamma^+}(x). \tag{2.38}$$

However, Eq. 2.37 is not applicable to fracture problems since neither Σu_i nor Δu_i is known. In contrast, Eq. 2.38 can be used to solve for Δu_i when t_i on Γ^+ is specified, which is the case in hydraulic fracturing simulations. Eq. 2.38 is the BIE for crack problems, and it can be seen as the boundary integral representation of the DDM. It is found that the integral representations of the traction field in Eq. 2.32 and Eq. 2.38 do not change whether x is inside the domain or on the boundary. Therefore, we can always use Eq. 2.32 for $x \in \Omega \cup \Gamma$.

Assuming hydraulic pressure p_f is applied to the crack surface, we have $t_i(x^+) = -p_f n_i(x^+)$ under tension positive sign convention. Thus, we obtain the following BIE for hydraulically pressurized open fractures:

$$p_f n_i(x^+) = (\mathscr{H}_{ij} \Delta u_j)_{\Gamma^+}(x). \tag{2.39}$$

2.3 Discretization

2.3.1 Discretized Boundary Element Formulation

The variation of displacement discontinuities over an element can be expressed in terms of the nodal values of the element by using shape functions:

$$\Delta u_i(\xi) = \sum_{\alpha=1}^{M} N_\alpha(\xi) u_i^\alpha \tag{2.40}$$

where α denotes the αth node, M is the number of nodes in an element, N_α is the shape function for the αth node, and ξ is the intrinsic or local coordinates of the element. Shape functions have the following special properties (Gao and Davies, 2002):

$$N_\alpha(\xi_\beta) = \delta_{\alpha\beta}, \tag{2.41}$$

$$\sum_{\alpha=1}^{M} N_\alpha(\xi) = 1, \tag{2.42}$$

where ξ_β is the βth nodal point in the local coordinates in an element. The Gauss-Chebyshev points are commonly selected as the nodal points of elements (Crawford and Curran, 1982) because of the stress singularity along element edges.

Having discretized the crack surface Γ^+ into N_e elements, we can rewrite the BIEs

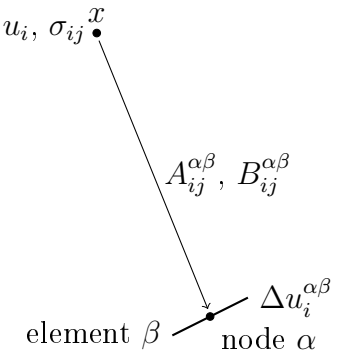

Figure 2.3: A schematic figure of the influence coefficients

Eq. 2.31 and Eq. 2.32 into

$$u_i(x) = \sum_{\beta=1}^{N_e} \sum_{\alpha=1}^{M} A_{ij}^{\alpha\beta}(x) \Delta u_j^{\alpha\beta} \tag{2.43}$$

$$t_i(x) = \sum_{\beta=1}^{N_e} \sum_{\alpha=1}^{M} B_{ij}^{\alpha\beta}(x) \Delta u_j^{\alpha\beta} \tag{2.44}$$

where the superscript β denotes the βth element. $A_{ij}^{\alpha\beta}$ and $B_{ij}^{\alpha\beta}$ are influence coefficients defined by

$$A_{ij}^{\alpha\beta}(x) \coloneqq -\int_{\Gamma_\beta^+} T_{ij}\left[y(\xi); x\right] N_\alpha(\xi) J(\xi)\, \mathrm{d}S(\xi) \tag{2.45}$$

$$B_{ij}^{\alpha\beta}(x) \coloneqq -\int_{\Gamma_\beta^+} H_{ij}\left[y(\xi); x\right] N_\alpha(\xi) J(\xi)\, \mathrm{d}S(\xi) \tag{2.46}$$

where $J(\xi)$ is the Jacobian of coordinate transformation (Gao and Davies, 2002). A schematic figure of the influence coefficients is shown in Fig. 2.3.

2.3.2 Assembly of System of Equations

If the collocation method is used, t_i in Eq. 2.44 is evaluated at nodal points on the boundary x^c, $c = 1, \ldots, P$, to give

$$t_i^c = \sum_{\beta=1}^{N_e} \sum_{\alpha=1}^{M} B_{ij}^{\alpha\beta c} \Delta u_j^{\alpha\beta} \tag{2.47}$$

where $B_{ij}^{\alpha\beta c} = B_{ij}^{\alpha\beta}(x^c)$. In matrix form, the equation is given by

$$\begin{bmatrix} \boldsymbol{t}^1 \\ \boldsymbol{t}^2 \\ \vdots \\ \boldsymbol{t}^P \end{bmatrix} = \begin{bmatrix} \boldsymbol{B}^{111} & \boldsymbol{B}^{211} & \cdots & \boldsymbol{B}^{MN_e 1} \\ \boldsymbol{B}^{112} & \boldsymbol{B}^{212} & \cdots & \boldsymbol{B}^{MN_e 2} \\ \vdots & \vdots & \ddots & \vdots \\ \boldsymbol{B}^{11P} & \boldsymbol{B}^{21P} & \cdots & \boldsymbol{B}^{MN_e P} \end{bmatrix} \begin{bmatrix} \Delta \boldsymbol{u}^{11} \\ \Delta \boldsymbol{u}^{21} \\ \vdots \\ \Delta \boldsymbol{u}^{MN_e} \end{bmatrix} \tag{2.48}$$

This system of equations may be written as

$$\mathbf{A}\mathbf{x} = \mathbf{b} \tag{2.49}$$

The vector $\mathbf{x}$ is composed of all unknown displacement discontinuities. The matrix $\mathbf{A}$ is a coefficient matrix. The vector $\mathbf{b}$ corresponds to the traction applied on the fracture surface. Because the nodal points are uniquely determined in the DDM, we have $P = MN_e$, and hence $\mathbf{A}$ is a square matrix.

2.4 Influence Coefficients

2.4.1 Analytical Expression

Sih and Liebowitz (1968) showed that the solution of the Navier-Cauchy equation for a plane of discontinuity in the x_1x_2 plane can be expressed in terms of a vector

harmonic function $f_i(x)$,

$$u_i(x) = 2(1-\nu)f_{i,3} - (1-2\nu)f_{3,i} + (1-2\nu)\delta_{i3}f_{k,k} - x_3 f_{k,ki} \tag{2.50}$$

where $f_{i,j} = \partial f_i / \partial x_j$. For two dimensional problems, any partial derivatives in the x_2 direction or in terms of x_2 are neglected. The vector harmonic function f_i takes the following form (Shou and Crouch, 1995; Shou et al., 1997):

$$f_i(x) = -\frac{1}{2(1-\nu)} \int \Delta u_i(y) \phi_p(y;x) \, \mathrm{d}S(y) \tag{2.51}$$

ϕ_p is the fundamental solution of the Laplace equation, $\nabla^2 \phi_p(y;x) = -\delta(y-x)$, which is given by

$$\phi_p(y;x) = \begin{cases} \dfrac{1}{4\pi r}, & x, y \in \mathbb{R}^3, \\ -\dfrac{1}{2\pi} \ln r, & x, y \in \mathbb{R}^2, \end{cases} \tag{2.52}$$

where $r \coloneqq \|y - x\|$.

Let us regard the boundary S of Eq. 2.51 as a boundary element Γ_β. Substitution of Eq. 2.40 into Eq. 2.51 gives

$$f_i^\beta(x) = \sum_{\alpha=1}^{M} \Delta \tilde{u}_i^{\alpha\beta} g^{\alpha\beta}(x) \tag{2.53}$$

where

$$g^{\alpha\beta}(x) \coloneqq -\frac{1}{2(1-\nu)} \int_{\Gamma_\beta} N_\alpha(\xi) \phi_p \left[y(\xi); x \right] \, \mathrm{d}S(\xi) \tag{2.54}$$

The tilde denotes that variables are evaluated in the local coordinate system. The analytical integration of the above equation can be found in Crouch (1976), Shou and Crouch (1995), and Shou et al. (1997). We provide the analytical integration for line

and rectangular elements with constant strength in Appendix A for completeness.

Combining Eq. 2.53 with Eq. 2.50, we obtain

$$\tilde{u}_i = \tilde{A}_{ij} \Delta \tilde{u}_j, \tag{2.55}$$

where

$$\left[\tilde{A}_{ij}\right] = \begin{bmatrix} 2(1-\nu)g_{,3} - x_3 g_{,11} & -x_3 g_{,21} & -(1-2\nu)g_{,1} - x_3 g_{,31} \\ -x_3 g_{,12} & 2(1-\nu)g_{,3} - x_3 g_{,22} & -(1-2\nu)g_{,2} - x_3 g_{,32} \\ (1-2\nu)g_{,1} - x_3 g_{,13} & (1-2\nu)g_{,2} - x_3 g_{,23} & 2(1-\nu)g_{,3} - x_3 g_{,33} \end{bmatrix} \tag{2.56}$$

The superscripts $\alpha\beta$ are omitted for brevity. Then, the coordinate transformation from the local coordinate system of the βth element to the global coordinate system is required. Let L_{ij} be the rotation matrix from the local coordinate system of the βth element to the global coordinate system. Noting that the influence coefficients constitute a second-order tensor, the coordinate transformation to the global coordinate system is expressed by

$$A_{ij} = L_{ip} L_{jq} \tilde{A}_{pq} \tag{2.57}$$

where A_{ij} is the influence coefficients in the global coordinate system.

$B_{ij}^{\alpha\beta}$ can be easily obtained by applying the traction operator to the above equation. The final form of the influence coefficients for traction is given by

$$\tilde{B}_{ik}^{\alpha\beta} = \tilde{S}_{ijk}^{\alpha\beta} \tilde{n}_j^{\alpha\beta}, \tag{2.58}$$

where $\tilde{n}_j^{\alpha\beta}$ is the normal vector of the αth node of the βth element in the local coordinate system. $\tilde{S}_{ijk}^{\alpha\beta}$ is the influence function for the ijth component of stress due to the kth component of displacement discontinuity in the local coordinate system,

which is given by

$$\left[\tilde{S}_{ij1}\right] = 2G \begin{bmatrix} 2g_{,13} - x_3 g_{,111} & (1-\nu)g_{,23} - x_3 g_{,112} & \nu g_{,22} + g_{,33} - x_3 g_{,113} \\ & 2\nu g_{,13} - x_3 g_{,122} & -\nu g_{,12} - x_3 g_{,123} \\ & & -x_3 g_{,133} \end{bmatrix}$$

$$\left[\tilde{S}_{ij2}\right] = 2G \begin{bmatrix} 2\nu g_{,23} - x_3 g_{,112} & (1-\nu)g_{,13} - x_3 g_{,122} & -\nu g_{,12} - x_3 g_{,123} \\ & 2g_{,23} - x_3 g_{,222} & \nu g_{,11} + g_{,33} - x_3 g_{,223} \\ & & -x_3 g_{,233} \end{bmatrix}$$

$$\left[\tilde{S}_{ij3}\right] = 2G \begin{bmatrix} g_{,33} + (1-2\nu)g_{,22} - x_3 g_{,113} & -(1-2\nu)g_{,12} - x_3 g_{,123} & -x_3 g_{,133} \\ & g_{,33} + (1-2\nu)g_{,11} - x_3 g_{,223} & -x_3 g_{,233} \\ & & g_{,33} - x_3 g_{,333} \end{bmatrix} \tag{2.59}$$

The lower triangular part is omitted due to its symmetry. The coordinate transformation of $\tilde{B}_{ij}^{\alpha\beta}$ is exactly the same with that of $\tilde{A}_{ij}^{\alpha\beta}$.

The analytical integration of Eq. 2.54 for line, rectangular, and triangular elements with constant strength ($N_\alpha = 1$) are derived by Crouch (1976); Rongved and Hill (1957); Kuriyama and Mizuta (1993), respectively. Those for higher order elements can be found in Crawford and Curran (1982); Shou (1993); Shou and Crouch (1995); Shou et al. (1997); Cheng et al. (2015a).

2.4.2 The Equivalence of BEM and DDM

Although it is often mentioned that Eq. 2.50 is identical to the discretized form of the Somigliana identity for displacements for crack problems, no derivation has been made to the best of author's knowledge. Liu and Li (2014) and Liu (2016) have shown that the Somigliana identity for tractions and Eq. 2.50 reduce to the same

expression in the case of line and rectangular elements with constant strength. We will show that Eq. 2.50 can be derived from the BIEs by using the Papkovich-Neuber potentials.

It is well known that the solution of the Navier-Cauchy equation can be represented in terms of the Papkovich-Neuber potentials Φ_i, ϕ (Fung, 1965; Slaughter, 2002):

$$Gu_i = \Phi_i - \frac{1}{4(1-\nu)} \left(x_j \Phi_j - \phi\right)_{,i}. \tag{2.60}$$

Φ_i and ϕ satisfy

$$\Phi_{i,jj} = -f_i, \tag{2.61}$$

$$\phi_{,ii} = -x_i f_i, \tag{2.62}$$

where f_i is the body force vector. The fundamental solutions to these Poisson equations, where a singular force is applied at y or $f_i = f_i^* \delta(x-y)$, are (Phan-Thien, 1983; Slaughter, 2002)

$$\Phi_i = f_i^* \phi_p(x;y), \tag{2.63}$$

$$\phi = y_i f_i^* \phi_p(x;y). \tag{2.64}$$

Substituting Eq. 2.11, Eq. 2.63, Eq. 2.64 into Eq. 2.60 and exchanging the source and field points, the displacement kernel can be rewritten as

$$U_{ij}(y;x) = \frac{1}{4G(1-\nu)} \left[(3-4\nu)\delta_{ij}\phi_p - r_i \phi_{p,j}\right], \tag{2.65}$$

where $r_i \coloneqq y_i - x_i$, $\phi_p = \phi_p(y;x)$, and $\phi_{p,i} = \partial \phi_p / \partial y_i$. Applying the traction operator

to Eq. 2.65 and noting that $n_i = -\delta_{i3}$, we obtain

$$\begin{aligned} T_{ij}(y;x) &= \mathcal{T}_y U_{ij}(y;x) \\ &= \lambda n_j U_{ik,k} + G n_k (U_{ij,k} + U_{ik,j}) \\ &= -2\nu\delta_{j3}\hat{\phi}_{p,i} - (1-2\nu)(\delta_{i3}\hat{\phi}_{p,j} + \delta_{ij}\hat{\phi}_{p,3}) + r_i\hat{\phi}_{p,j3} \end{aligned} \tag{2.66}$$

where $\hat{\phi}_p \coloneqq \phi_p/\{2(1-\nu)\}$, and $\phi_{p,kk} = 0$ is used in the above derivation.

The partial derivatives of the particular solution are given by

$$\phi_{p,i} = -\frac{r_i}{2(D-1)\pi r^3}, \tag{2.67}$$

$$\phi_{p,ij} = -\frac{\delta_{ij} - D r_{,i} r_{,j}}{2(D-1)\pi r^3} \tag{2.68}$$

where D is dimensions, 2 or 3. Then, the following expression holds

$$r_i\hat{\phi}_{p,j3} = \hat{\phi}_{p,i}\delta_{j3} + r_3\hat{\phi}_{p,ij} - \delta_{ij}\hat{\phi}_{p,3}. \tag{2.69}$$

Substituting into Eq. 2.66, we obtain

$$T_{ij} = 2(1-\nu)\delta_{ij}\hat{\phi}_{p,3} - (1-2\nu)\hat{\phi}_{p,i}\delta_{j3} + (1-2\nu)\delta_{i3}\hat{\phi}_{p,j} - r_3\hat{\phi}_{p,ij} \tag{2.70}$$

Substitution into Eq. 2.31, we have

$$\begin{aligned} u_i = -2(1-\nu)\int \Delta u_i \hat{\phi}_{p,3}\,\mathrm{d}\Gamma + (1-2\nu)\int \Delta u_3 \hat{\phi}_{p,i}\,\mathrm{d}\Gamma \\ - (1-2\nu)\delta_{i3}\int \Delta u_k \hat{\phi}_{p,k}\Gamma - x_3\int \Delta u_k \hat{\phi}_{p,ik}\Gamma \end{aligned} \tag{2.71}$$

Noting that

$$r_{,i} = \frac{\partial r}{\partial y_i} = -\frac{\partial r}{\partial x_i} \tag{2.72}$$

we have

$$\phi_{p,i} = \frac{\partial \phi_p}{\partial y_i} = -\frac{\partial \phi_p}{\partial x_i} \tag{2.73}$$

$$\phi_{p,ij} = \frac{\partial^2 \phi_p}{\partial y_i \partial y_j} = \frac{\partial^2 \phi_p}{\partial x_i \partial x_j} \tag{2.74}$$

In addition, the order of integration and differentiation can be exchanged for $x \in \Omega \backslash \Gamma$. Thus, we obtain

$$\int \Delta u_i \hat{\phi}_{p,j} \, \mathrm{d}\Gamma = -\frac{\partial}{\partial x_j} \left[\int \Delta u_i \hat{\phi}_p \, \mathrm{d}\Gamma \right] = -\frac{\partial f_i}{\partial x_j} = -f_{i,j} \tag{2.75}$$

$$\int \Delta u_k \hat{\phi}_{p,ik} \, \mathrm{d}\Gamma = \frac{\partial^2}{\partial x_i \partial x_k} \left[\int \Delta u_k \hat{\phi}_p \, \mathrm{d}\Gamma \right] = \frac{\partial^2 f_k}{\partial x_i \partial x_k} = f_{k,ik} \tag{2.76}$$

Therefore, Eq. 2.71 reduces to

$$u_i = 2(1-\nu) f_{i,3} - (1-2\nu) f_{3,i} + (1-2\nu) \delta_{i3} f_{k,k} - x_3 f_{k,ik} \tag{2.77}$$

which is identical to Eq. 2.50.

The development of the DDM formalism presented in this Chapter clearly shows the equivalence of the BEM and the DDM approaches. This general formalism will be used in the next chapter to develop solutions for layered, inhomogeneous elastic media.

Chapter 3: Displacement Discontinuity Method for Layered Media

3.1 Introduction

This chapter describes the development and verification of a novel displacement discontinuity method (DDM) for multilayered media. We extends the conventional DDM for homogeneous media to piecewise laterally-homogeneous media, or multilayered media*.

In the previous chapter, we have proved the equivalence of BEM and DDM, in a sense that the analytical integration of the fundamental solutions in BEM yields influence coefficients in DDM. Then, the development of a new DDM for multilayered media is transformed into finding the fundamental solution for multilayered media.

The fundamental solution for multilayered media has been commonly solved by applying integral transforms. These methods include the stiffness matrix, transfer matrix, flexibility matrix, and propagator matrix methods (Singh, 1970; Bufler, 1971; Lin and Keer, 1989). The closed form solution for a multilayered isotropic elastic medium in a half-space and an infinite space by using the two-dimensional Fourier transform and the backward-transfer matrix techniques (Yue, 1995, 1996). Although these methods are successfully applied to layered media, they are numerically expensive due to the need of numerical integration and differentiation, and, hence, are not feasible for large scale problems.

*Parts of this chapter have been reported in Hirose, S. and Sharma, M. M. (2018) Numerical modelling of fractures in multilayered rock formations using a displacement discontinuity method. In *52nd US Rock Mechanics/Geomechanics Symposium*, Seattle, 2018. ARMA-2018-495. The contribution of the author is formulating a new DDM for layered media and performing numerical simulations using the new DDM.

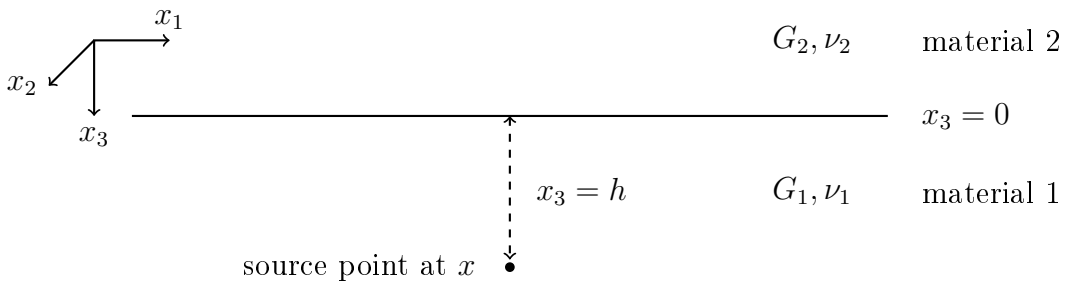

Figure 3.1: A schematic figure of an isotropic bi-material medium

3.2 The Method of Images

The basic idea of the method of images is to create a general solution which will satisfy boundary conditions by superposing another solution. The method of images is widely applied to problems with planar boundaries. An example of the application of the image method to elasticity problems is deriving the fundamental solution for a half-plane and half-space (Melan, 1932; Rongved, 1955). Telles and Brebbia (1981) showed that Melan's solution can be expressed as a sum of the original and image solutions. Another example is developing the fundamental solution for a bonded bi-material shown in Fig. 3.1. The fundamental solution for bi-materials were derived using Papkovich-Neuber potentials (Rongved, 1955; Dundurs and Hetényi, 1965; Huang and Wang, 1991; Chen and Tang, 1997) or nuclei of strains (Vijayakumar and Cormack, 1987; Carvalho and Curran, 1992; Ma and Lin, 2002). It can be also split into the original and complementary solutions.

If a planar boundary is located at $x_3 = 0$, the fundamental solution of displacement in bi-materials takes the following form

$$U_{ij}(y;x) = \begin{cases} U^o_{ij}(y;x) + U^c_{ij}(y;\bar{x}), & y \in \Omega_1, \\ U^c_{ij}(y;x), & y \notin \Omega_1, \end{cases} \tag{3.1}$$

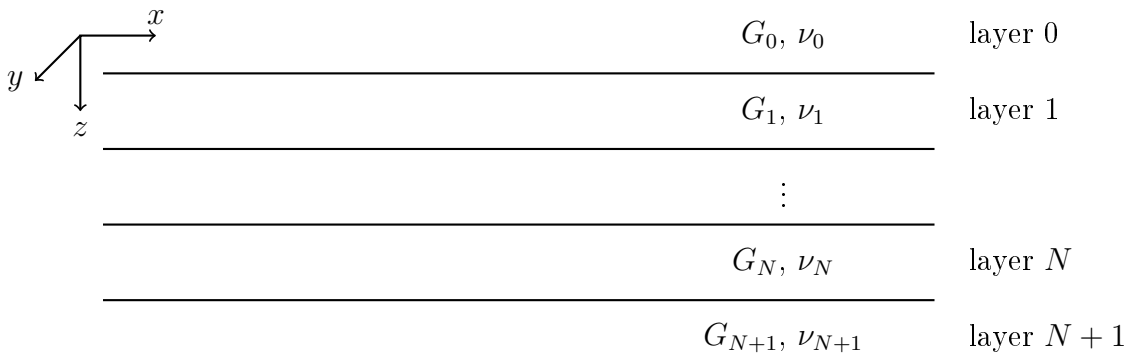

Figure 3.2: A schematic figure of a multilayered isotropic medium

where $\Omega_1 = \{(x_1, x_2, x_3 \mid x_3 > 0)\}$, $x \in \Omega_1$, $\bar{x}$ represents the image of x against the boundary, and the superscripts o and c denotes the original and complementary solutions, respectively. The image of $x = (x_1, x_2, x_3)$ is defined by

$$\bar{x} := \overline{(x_1, x_2, x_3)} = (x_1, x_2, -x_3). \tag{3.2}$$

When the method of images is applied to media having multiple planar boundaries in parallel, the solution of the system is expressed as a sum of the original and an infinite series of image solutions:

$$U_{ij}(y; x) = \begin{cases} U^o_{ij}(y; x) + \displaystyle\sum_{k=1}^{\infty} U^{ck}_{ij}(y; \bar{x}^k), & y \in \Omega_1, \\ \displaystyle\sum_{k=1}^{\infty} U^{ck}_{ij}(y; \bar{x}^k), & y \notin \Omega_1, \end{cases} \tag{3.3}$$

where $x \in \Omega_1$, and the superscript k denotes the kth image point or solution. For instance, the solution of three-layered media can be expressed as an infinite series of Muskhelishvili potentials (Stagni and Lizzio, 1986, 1987) or Hansen potentials (Fares, 1987; Fares and Li, 1988).

Because the traction operator Eq. 2.9 is a linear differential operator, other kernels

T_{ij}, K_{ij}, and H_{ij} for multilayered media have the same form with Eq. 3.3:

$$T_{ij}(y;x) = \begin{cases} T_{ij}^{o}(y;x) + \sum_{k=1}^{\infty} T_{ij}^{ck}(y;\bar{x}^k), & y \in \Omega_1, \\ \sum_{k=1}^{\infty} T_{ij}^{ck}(y;\bar{x}^k), & y \notin \Omega_1, \end{cases} \tag{3.4}$$

$$K_{ij}(y;x) = \begin{cases} K_{ij}^{o}(y;x) + \sum_{k=1}^{\infty} K_{ij}^{ck}(y;\bar{x}^k), & y \in \Omega_1, \\ \sum_{k=1}^{\infty} K_{ij}^{ck}(y;\bar{x}^k), & y \notin \Omega_1, \end{cases} \tag{3.5}$$

$$H_{ij}(y;x) = \begin{cases} H_{ij}^{o}(y;x) + \sum_{k=1}^{\infty} H_{ij}^{ck}(y;\bar{x}^k), & y \in \Omega_1, \\ \sum_{k=1}^{\infty} H_{ij}^{ck}(y;\bar{x}^k), & y \notin \Omega_1, \end{cases} \tag{3.6}$$

where

$$\begin{aligned} T_{ij}^{o} &\coloneqq \mathcal{T}_y U_{ij}^{o}, \quad K_{ij}^{o} \coloneqq \mathcal{T}_x U_{ij}^{o}, \quad H_{ij}^{o} \coloneqq \mathcal{T}_x T_{ij}^{o}, \\ T_{ij}^{ck} &\coloneqq \mathcal{T}_y U_{ij}^{ck}, \quad K_{ij}^{ck} \coloneqq \mathcal{T}_x U_{ij}^{ck}, \quad H_{ij}^{ck} \coloneqq \mathcal{T}_x T_{ij}^{ck}. \end{aligned} \tag{3.7}$$

Substituting into Eq. 2.45 and Eq. 2.46, the influence functions of DDM for multilayered media can be expressed by

$$A_{ij}(x) = A_{ij}^{o}(x) + \sum_{k=1}^{\infty} A_{ij}^{ck}(\bar{x}^k), \tag{3.8}$$

$$B_{ij}(x) = B_{ij}^{o}(x) + \sum_{k=1}^{\infty} B_{ij}^{ck}(\bar{x}^k), \tag{3.9}$$

where A^o_{ij}, B^o_{ij}, A^{ck}_{ij}, and B^{ck}_{ij} are defined by

$$A^o_{ij}(x) \coloneqq -\int_{\Gamma^+_\beta} T^o_{ij}\left[y(\xi);x\right] N_\alpha(\xi) J(\xi)\,\mathrm{d}S(\xi), \tag{3.10}$$

$$B^o_{ij}(x) \coloneqq -\int_{\Gamma^+_\beta} H^o_{ij}\left[y(\xi);x\right] N_\alpha(\xi) J(\xi)\,\mathrm{d}S(\xi), \tag{3.11}$$

$$A^{ck}_{ij}(\bar{x}^k) \coloneqq -\int_{\Gamma^+_\beta} T^{ck}_{ij}\left[y(\xi);\bar{x}^k\right] N_\alpha(\xi) J(\xi)\,\mathrm{d}S(\xi), \tag{3.12}$$

$$B^{ck}_{ij}(\bar{x}^k) \coloneqq -\int_{\Gamma^+_\beta} H^{ck}_{ij}\left[y(\xi);\bar{x}^k\right] N_\alpha(\xi) J(\xi)\,\mathrm{d}S(\xi), \tag{3.13}$$

A^o_{ij} and B^o_{ij} correspond to the influence function for homogeneous media, which are given in Chapter 2. It is found that T^{ck}_{ij} and H^{ck}_{ij} are regular because the image source points $\bar{x}^k$ do not coincide with y, and, consequently, A^{ck}_{ij} and B^{ck}_{ij} can be computed numerically using Gaussian integration.

A major draw back of the method of images is that the derivation of complementary solutions requires both differentiation and integration if the Papkovich-Neuber potential function is used. The general image method developed by Fares and Li (1988) circumvents this difficulty by expressing elastic fields in terms of the Hansen potentials (Hansen, 1935; Ben-menahem and Singh, 1968). The complementary solutions are derived by simply differentiating the Hansen potentials, which enables us to derive image solutions systematically.

3.3 General Image Method

Some linear vector differential equations are separable into three vector functions in some coordinate systems (Morse and Feshbach, 1953). For the Navier-Cauchy equation, three independent sets of vector solutions can be found in the Cartesian or cylindrical coordinates (Ben-menahem and Singh, 1968). Then, the displacement

vector can be always decomposed into three vector functions (Fares, 1987; Fares and Li, 1988):

$$u_i = L_i + F_i + M_i, \tag{3.14}$$

where

$$L_i \coloneqq \phi_{1,i}, \tag{3.15}$$

$$F_i \coloneqq 2\delta_{i3}\phi_{2,3} - 2\delta x_3\phi_{2,i3} - \phi_{2,i}, \tag{3.16}$$

$$M_i \coloneqq \varepsilon_{ij3}\phi_{3,j}, \tag{3.17}$$

$\delta \coloneqq 1/(3-4\nu)$, ε_{ijk} is the permutation symbol, ϕ_i are Handen potentials which are harmonic functions. In vector notation, these vectors are expressed by

$$\mathbf{L} = \nabla\phi_1, \tag{3.18}$$

$$\mathbf{F} = 2\hat{\boldsymbol{e}}_3\frac{\partial\phi_2}{\partial x_3} - 2\delta x_3\nabla\frac{\partial\phi_2}{\partial x_3} - \nabla\phi_2, \tag{3.19}$$

$$\mathbf{M} = \nabla\times\left(\hat{\boldsymbol{e}}_3\phi_3\right), \tag{3.20}$$

where $\hat{\boldsymbol{e}}_3$ is the unit vector in the x_3 direction. It is easy to find that M_i is tangential to x_1x_2 plane and perpendicular to L_i. Moreover, M_i becomes orthogonal to F_i when $\nabla\times\mathbf{M} = \nabla\frac{\partial\phi_3}{\partial x_3}$ holds (Morse and Feshbach, 1953). Hence, M_i is decoupled from the directions spanned by L_i and F_i and represents the antiplane direction.

Let us define the kernel of the Hansen potentials Φ_{ij} by

$$\phi_j^*(y) = \Phi_{ij}(y;x)f_i^*(x), \tag{3.21}$$

where $f_i^*(x)$ is the singular force applied at x, and $\phi_j^*(y)$ is Hansen potential at y due to the singular force. Substituting Eq. 3.21 into Eq. 3.14, the displacement kernel is

given by

$$
\begin{aligned}
U_{i1} &= \Phi_{i1,1} - \Phi_{i2,1} - 2\delta r_3 \Phi_{i2,13} + \Phi_{i3,2} \\
U_{i2} &= \Phi_{i1,2} - \Phi_{i2,2} - 2\delta r_3 \Phi_{i2,23} + \Phi_{i3,1} \\
U_{i3} &= \Phi_{i1,3} + \Phi_{i2,3} - 2\delta r_3 \Phi_{i2,33},
\end{aligned}
\tag{3.22}
$$

where $U_{ij} = U_{ij}(y;x)$, $r_i \coloneqq y_i - x_i$, and the derivatives are taken in terms of y. Other kernel functions can be derived by using Eq. 2.13, Eq. 2.16, and Eq. 2.17.

For 2D problems, the kernel of the Hansen potentials is given by

$$
\begin{aligned}
\Phi_{11} &= K_{2\mathrm{d}} \left\{ r_3\theta - r_1 \log r + (1+\delta) r_1 \right\}, \quad \Phi_{12} = -\Phi_{11}, \\
\Phi_{31} &= K_{2\mathrm{d}} \left\{ -r_1\theta - r_3 \log r + r_3 \right\}, \qquad\quad \Phi_{32} = \Phi_{31},
\end{aligned}
\tag{3.23}
$$

where $K_{2\mathrm{d}} \coloneqq 1/\{4\pi G(1+\delta)\}$, $r \coloneqq |y-x|$, and $\theta \coloneqq \tan^{-1}(r_3/r_1)$. Other components of Φ_{ij} are zero, resulting in $\phi_3 = 0$. In the general image method, the x_2 direction is taken as the antiplane direction. Any components or derivatives related with the x_2 direction are neglected in 2D problems.

For 3D problems, the kernel is given by

$$
\begin{aligned}
\Phi_{11} &= K_{3\mathrm{d}} \frac{r_1 r}{r_{\mathrm{h}}^2}, \qquad & \Phi_{12} &= -\Phi_{11}, \quad \Phi_{13} = 2(1+\delta)\Phi_{21}, \\
\Phi_{21} &= K_{3\mathrm{d}} \frac{r_2 r}{r_{\mathrm{h}}^2}, \qquad & \Phi_{22} &= -\Phi_{21}, \quad \Phi_{23} = -2(1+\delta)\Phi_{11}, \\
\Phi_{31} &= K_{3\mathrm{d}} \ln(r + r_3), \quad & \Phi_{32} &= \Phi_{31}, \qquad \Phi_{33} = 0,
\end{aligned}
\tag{3.24}
$$

where $K_{3\mathrm{d}} \coloneqq 1/\{8\pi G(1+\delta)\}$, and $r_{\mathrm{h}} \coloneqq \sqrt{r_1^2 + r_2^2}$. It should be mentioned that the kernel in 3D problems is given incorrectly in Fares (1987).

Utilizing the Hansen potentials, the complementary solution against a planar interface is derived by simply differentiating the original potential in the x_3 direction in

contrast to the Papkovich-Neuber potentials. For bi-materials with a planar boundary at $x_3 = 0$ shown in Fig. 3.1, the complementary solution of the Hansen potential is given by (Fares and Li, 1988)

$$\Phi_{ij}^c(y;x) = \begin{cases} \mathscr{R}_{jk}\overline{\Phi_{ik}^o(y;x)}, & y \in \Omega_1 \\ \mathscr{T}_{jk}\Phi_{ik}^o(y;x), & y \notin \Omega_1 \end{cases} \tag{3.25}$$

where $x \in \Omega_1$, Φ_{ij}^o is the kernel of the original Hansen potential. $\mathscr{R}_{ij}$ and $\mathscr{T}_{ij}$ are reflection and transmission operators defined by

$$[\mathscr{R}_{ij}] = \begin{bmatrix} 2\delta_1 c_1 h\dfrac{\partial}{\partial y_3} & c_2 - 4\delta_1^2 c_1 h^2 \dfrac{\partial^2}{\partial y_3^2} & 0 \\ c_1 & -2\delta_1 c_1 h\dfrac{\partial}{\partial y_3} & 0 \\ 0 & 0 & c_3 \end{bmatrix} \tag{3.26}$$

$$[\mathscr{T}_{ij}] = \begin{bmatrix} c_4 & -2\left(\delta_1 c_4 - \delta_2 c_5\right) h\dfrac{\partial}{\partial y_3} & 0 \\ 0 & c_5 & 0 \\ 0 & 0 & c_6 \end{bmatrix} \tag{3.27}$$

where $h = x_3$ is the distance from the source point to the boundary, and

$$\begin{gathered} c_1 \coloneqq \frac{\gamma - 1}{\gamma + \delta_1}, \quad c_2 \coloneqq \frac{\gamma\delta_2 - \delta_1}{\gamma\delta_2 + 1}, \quad c_3 \coloneqq \frac{1 - \gamma}{1 + \gamma}, \\ c_4 \coloneqq 1 - c_1, \quad c_5 \coloneqq 1 - c_2, \qquad c_6 \coloneqq 1 + c_3, \\ \gamma \coloneqq G_2/G_1. \end{gathered} \tag{3.28}$$

$\overline{\Phi_j^o(y;x)}$ is given by

$$\overline{\Phi_j^o(y;x)} = \Phi_j^o(\bar{y};\bar{x}), \tag{3.29}$$

where $\bar{y} = \overline{(y_1, y_2, y_3)} = (y_1, y_2, -y_3)$, and $\bar{x} = \overline{(x_1, x_2, x_3)} = (x_1, x_2, -x_3)$. If the

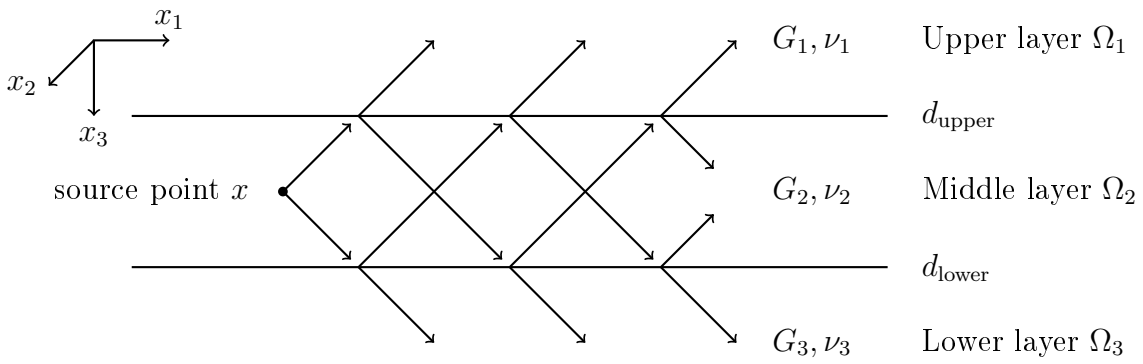

Figure 3.3: A schematic figure of the image method in a three-layered medium. A point force is applied at x in the middle layer, and arrows represent reflections and transmissions of the Hansen potentials. The shear modulus and Poisson ratio of the ith layer are G_i and ν_i, respectively. Upper and lower layer interfaces are located at $x_3 = d_{\text{upper}}$ and $x_3 = d_{\text{lower}}$, respectively.

boundary is located at $x_3 = d$, h and $\bar{x}$ should be evaluated by $h = x_3 - d$ and $\bar{x} = (x_1, x_2, 2d - x_3)$.

Eq. 3.25 is a general relationship between the original and complementary Hansen potentials, which is equivalent to the continuity condition of the displacement and traction along the boundary. For multilayered media, the application of Eq. 3.25 is analogous to the reflection and transmission of elastic waves against layer interfaces as shown in Fig. 3.3. Applying Eq. 3.25 to each boundary and summing up all of the complementary solutions for each layer, we end up with a general solution for the multilayered media in the form of Eq. 3.3.

Since Eq. 3.26 and Eq. 3.27 only contain the differentiation in the x_3 direction, and kernel functions can be obtained from the Hansen potentials through differentiation using Eq. 3.22, Eq. 2.13, Eq. 2.16, and Eq. 2.17, the complementary solutions can be derived by using symbolic or automatic differentiation technique systematically. For example, let us consider a three-layered medium shown in Fig. 3.3. Assuming a point source x is located in the middle layer, the complementary Hansen potentials

for the middle layer can be obtained by following the procedure shown in Fig. 3.4.

3.3.1 Special Treatment for 2D Problems

When the general image method is applied to in-plane 2D problems, a special treatment is required. Since the original Hansen potential Eq. 3.23 contains a linear term in terms of r_1, reflected and transmitted Hansen potentials contain a constant displacement field, which must be subtracted from U_{ij}. This fact was not pointed out in Fares and Li (1988), and, indeed, their application is limited to anti-plane problems.

First, let us consider the case in which a point force is applied to the x direction in two dimensions. The corresponding Hansen potential Φ_{1i} is given by

$$\Phi_{11} = K_{2\mathrm{d}} \left[r_3 \theta - r_1 \log r + (1 + \delta_1) r_1 \right], \tag{3.30}$$

$$\Phi_{12} = -\Phi_{11}, \tag{3.31}$$

Please note Φ_{i3} is zero for 2D problems. Substitution into Eq. 3.25 gives

$$\Phi_{r11}(y; \bar{x}) = -c_2 \bar{\Phi}_{11} + \mathrm{H.O.T.}, \tag{3.32}$$

$$\Phi_{r12}(y; \bar{x}) = c_1 \bar{\Phi}_{11} + \mathrm{H.O.T.}, \tag{3.33}$$

where the subscript r denotes the reflected potential. The terms with higher-order

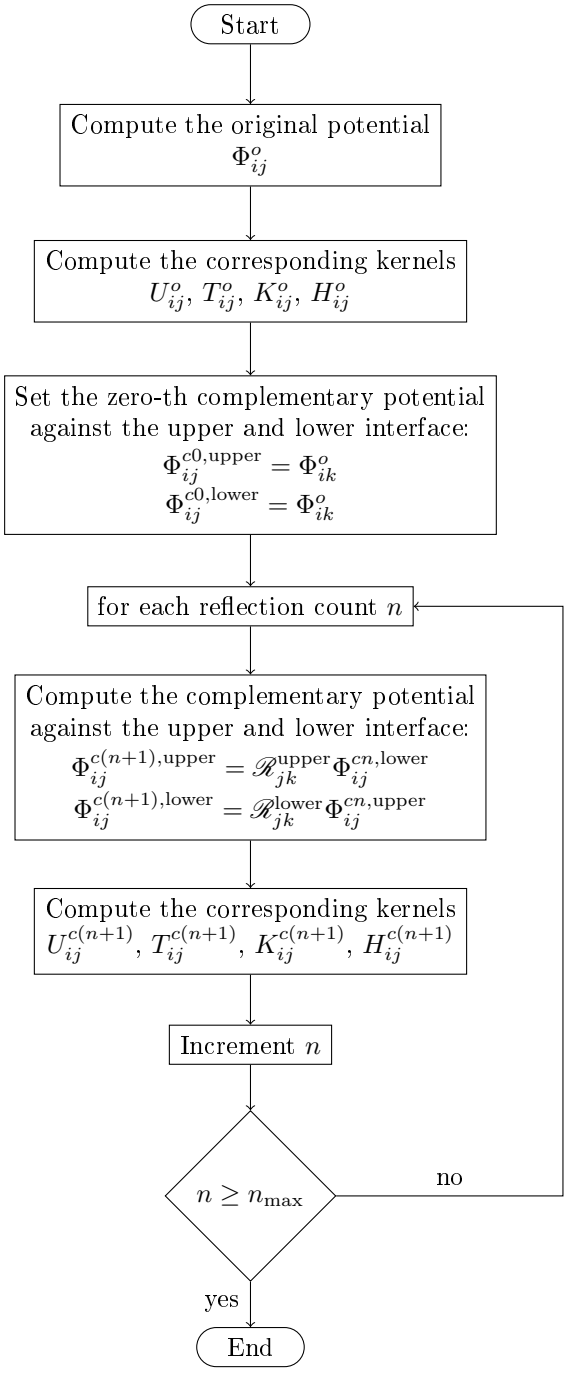

Figure 3.4: A flow chart of the general image method to obtain the potential solution for the middle layer in a three-layered medium. $n_{\max}$ is the maximum number of reflections, $\mathscr{R}^{\mathrm{upper}}_{ij}$ and $\mathscr{R}^{\mathrm{upper}}_{ij}$ are the reflection operator for the upper and lower interfaces, respectively.

derivatives are expressed as H.O.T. Substituting into Eq. 3.22, we obtain

$$\begin{aligned} U_{r11}(y;\bar{x}) &= \Phi_{r11,1} - \Phi_{r12,1} - 2\delta_1(y_3+x_3)\Phi_{r12,13} \\ &= -c_2\bar{\Phi}_{11,1} - c_1\bar{\Phi}_{11,1} - 2\delta_1 c_1(y_3+x_3)\bar{\Phi}_{11,13} + \text{H.O.T.} \\ &= K_{2\text{d}}\left[-(c_1+c_2)\left(-\ln r' + \delta_1\right) - 2\delta_1 c_1\left\{\frac{(y_1-x_1)^2}{r'^2} - 1\right\}\right] + \text{H.O.T.} \\ &= K_{2\text{d}}\delta_1\left(c_1 - c_2\right) + \text{non-linear terms}, \end{aligned} \tag{3.34}$$

where $r'_i = y_i - \bar{x}_i$, and $r' = |y_i - \bar{x}_i|$. It is found that other components do not contain any constant displacement term. The constant displacement in the Hansen potential for one reflection and transmission is, hence, given by

$$[U_{ij}] = \begin{bmatrix} K_{2\text{d}}\delta_1(c_1-c_2) & 0 \\ 0 & 0 \end{bmatrix}. \tag{3.35}$$

For multiple reflections and transmissions, the constant displacement can be derived from the fact that it is only produced from the terms with Φ^o_{11}. Let us decompose the reflection and transmission operators as

$$\mathscr{R}_{ij} = \begin{bmatrix} 0 & c_2 \\ c_1 & 0 \end{bmatrix} + \text{H.O.T.}, \tag{3.36}$$

$$\mathscr{T}_{ij} = \begin{bmatrix} c_4 & 0 \\ 0 & c_5 \end{bmatrix} + \text{H.O.T.}. \tag{3.37}$$

Applying the reflection and transmission operators to the original Hansen potential

multiple times, the Hansen potentials have the following form:

$$\begin{aligned} \Phi_{11} &= A\Phi^o_{11} + \text{H.O.T.}, \quad \Phi_{12} = B\Phi^o_{11} + \text{H.O.T.}, \\ \Phi_{31} &= C\Phi^o_{31} + \text{H.O.T.}, \quad \Phi_{32} = D\Phi^o_{31} + \text{H.O.T.}, \end{aligned} \tag{3.38}$$

where Φ^o_{ij} is given by Eq. 3.23, and A throught D are constants computed as a result of reflections and transmissions. Substituting into Eq. 3.22, we obtain the following constant displacement:

$$[U_{ij}] = K_{2\text{d}} \begin{bmatrix} \delta_1(A-B) + 2\delta_n B & 0 \\ 0 & 0 \end{bmatrix}, \tag{3.39}$$

where δ_1 is evaluated in the material where the original potential was computed, and δ_n is evaluated in the material where the final reflection was computed.

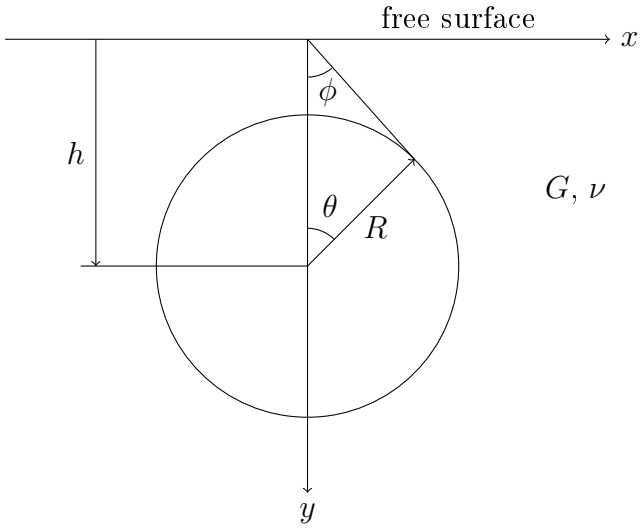

Figure 3.5: Circular hole near the free surface of a half-plane.

3.4 Validation

3.4.1 Circular Hole near a Free Surface of a Half-Plane

The general image method is applied to a circular hole near the free surface of a half-plane shown in Fig. 3.5. A constant hydraulic pressure p is applied to the inside of the hole. The tensile stress along the contour of the hole is given by (Savin, 1961)

$$\sigma_{\theta\theta} = p(1 + \tan^2 \phi), \tag{3.40}$$

where ϕ is defined in Fig. 3.5, and p is the hydraulic pressure applied to the inside of the hole.

The problem is solved by using the conventional BEM in which kernel functions are computed using the general image described in this chapter. Linear elements are used, and the number of elements along the contour of the hole is 48. The Poisson ratio is 0.2, and the pressure is $p = 0.2G$. The depth of the center of the hole is $h = 2$, and the radius of the hole is $R = 1$. The number of gauss points for the numerical

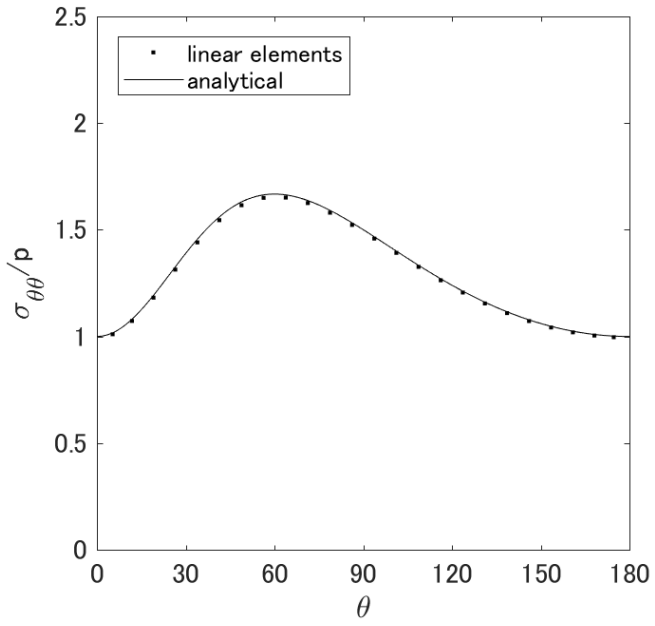

Figure 3.6: The tensile stress along the contour of the hole near the free surface under constant hydraulic pressure. θ is the angle from the y-axis in the clockwise direction. The tensile stress is normalized with the pressure.

integration of the image solution is 3. The tensile stress along the contour of the hole is plotted in Fig. 3.6. The tensile stress is computed by using the indirect method described in Aliabadi (2002). The numerical and analytical solutions of the tensile stress match very well.

3.4.2 A Horizontal Crack in Bi-materials

A horizontal pressurized crack in bi-materials in plain strain is analyzed. A schematic figure of the problem is shown in Fig. 3.7. This problem was first solved by Crouch and Starfield (1983), who analytically derived the influence function of a DDM element for bi-materials. The same parameters with Crouch and Starfield (1983) are used here: the number of elements is 40. The Poisson ratio of both materials is $\nu_1 = \nu_2 = 0.1$. The pressure applied to the horizontal crack is $p = 10^{-3}G_1$.

Table 3.1: The properties used to analyze the pressurized crack in a bi-material.

γ	W/W_0
0.0	1.6930
0.25	1.2411
0.50	1.1070
0.75	1.0406
1.00	1.0000
2.50	0.9045
5.00	0.8598
7.50	0.8418
10.00	0.8320

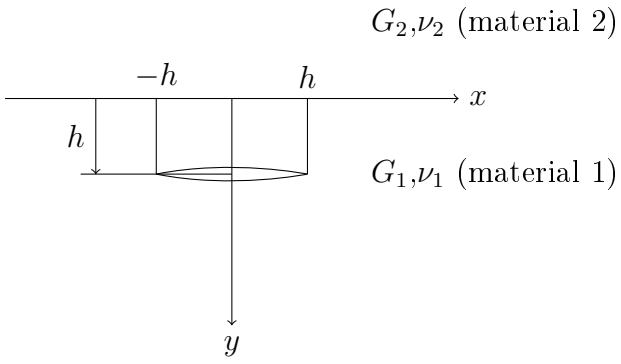

Figure 3.7: A schematic figure of a horizontal crack in a bi-material. The depth of the crack is h, and the length of the crack is $2h$.

The strain energy ratios computed by using the general image method are listed in Table 3.1 and plotted in Fig. 3.8. W is the strain energy when $\gamma = G_2/G_1 = 1$. It is clear that the new method can reproduce the result of Crouch and Starfield (1983).

3.5 Application

3.5.1 Horizontal and Vertical Cracks in Three-Layered Media

The general image method is applied to vertical and horizontal pressurized cracks in three-layered media assuming a plain strain condition. A schematic figure of this problem is shown in Fig. 3.9. The length of the cracks is equal to the height of the

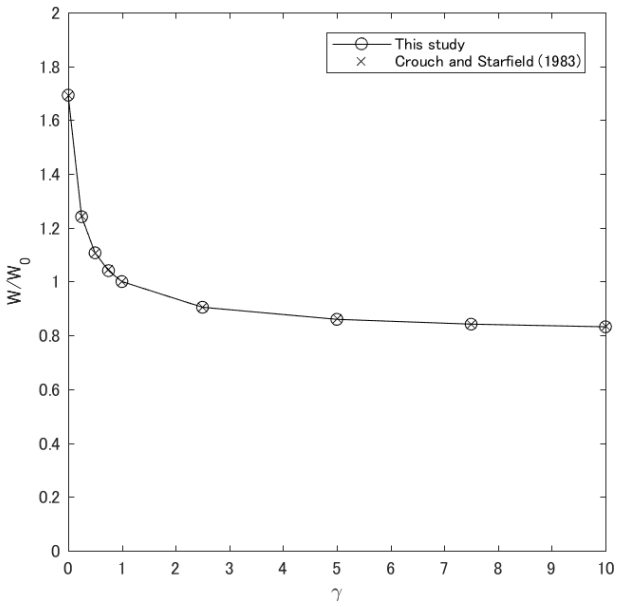

Figure 3.8: The strain energy ratio W/W_0 of a horizontal crack in bi-materials in which a hydraulic pressure $p = 10^{-3}G_1$ is applied. W_0 is the strain energy in the case of $G_1 = G_2 = 1$.

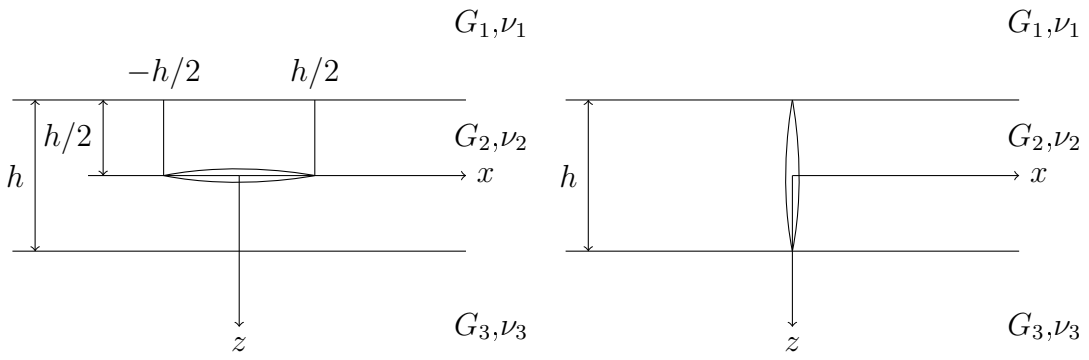

Figure 3.9: A schematic of horizontal and vertical cracks in three-layered media. The crack length is h, and the height of the middle layer is h. The shear modulus and Poisson ratio of the ith material are G_i and ν_i.

Table 3.2: Properties used for horizontal and vertical pressurized cracks in three-layered media.

Element type	constant, linear, quadratic
Number of elements	10
Number of Gauss points	1, 2, 3
Number of images	1, 2, 3
Shear modulus contrast ($\gamma = G_1/G_2 = G_3/G_2$)	2, 5
Poisson ratio ($\nu_1 = \nu_2$)	0.2
Pressure	$p = 10^{-3}G_2$

middle layer, and the center of the cracks is located at the origin. The properties used to solve the problem are listed in Table 3.2. Fig. 3.10 through Fig. 3.17 show the half-width of the pressurized cracks in dimensionless form. The analytical solution for a homogeneous medium with the properties of the middle layer is also plotted (Zehnder, 2012). The dimensionless width and coordinates are defined by $w_D \coloneqq w/h$, $x_D \coloneqq x/h$, and $z_D \coloneqq z/h$, where w is the width of a crack and h is the height of the middle layer. The shear modulus contrast γ is defined against the shear modulus of the middle layer G_2, and the same shear modulus is used for the upper and the lower layers.

Fig. 3.10 and Fig. 3.11 show the effect of element types. Constant elements are less accurate than linear and quadratic elements in the three-layered medium as Crawford and Curran (1982) pointed out for homogeneous media. Fig. 3.12 and Fig. 3.13 show the contribution of the number of Gauss points for the numerical integration of image solutions. Although more Gauss points improve the accuracy of solutions in general, it is observed that the improvement of the accuracy of these cases is very limited. Fig. 3.14 through Fig. 3.17 show the impact of the number of image solutions in the case of $\gamma = 2$ and 5. The number of images required for accuracy depends on both the orientation of the crack and the contrast of shear modulus. While multiple images are required for a horizontal crack, one image is sufficient for a vertical crack. If the contrast of shear modulus is increased, more images are required to obtain an accurate width of the crack as shown in Fig. 3.16. From a practical viewpoint, however, one image produces sufficiently accurate width for both cracks in the case of $\gamma = 2$ and 5. This means that bi-material solutions are sufficient for a three-layered medium up to $\gamma = 5$ under plain strain conditions.

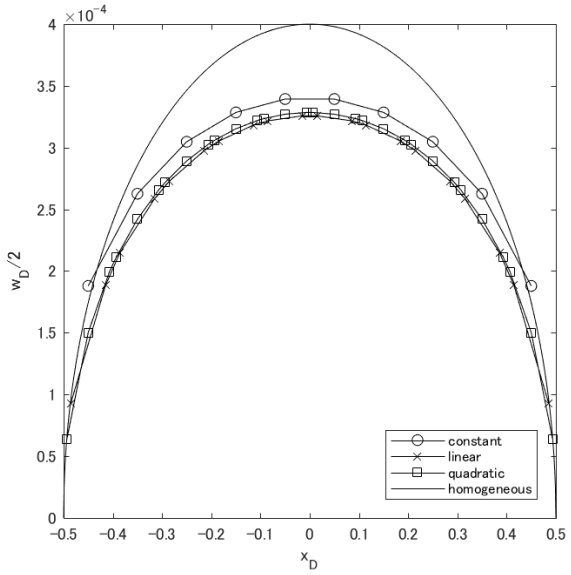

Figure 3.10: The half-width of the horizontal crack in a three-layered medium for different element types in the case of three Gauss points, three images, and $\gamma = 2$. $w_D \coloneqq w/h$ and $x_D \coloneqq x/h$.

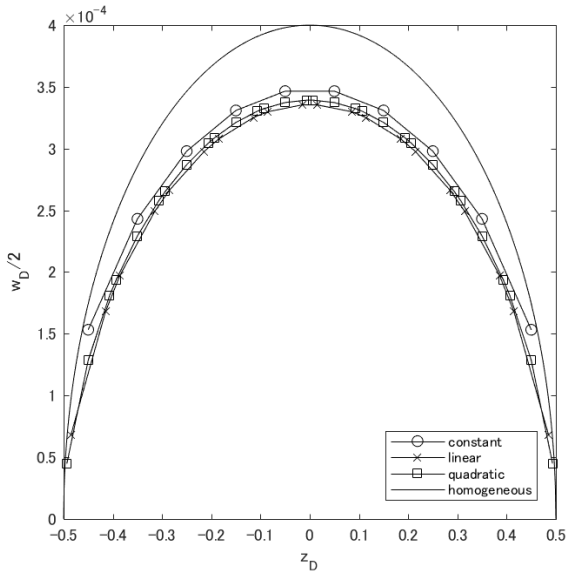

Figure 3.11: The half-width of the horizontal crack in a three-layered medium for different element types in the case of three Gauss points, three images, and $\gamma = 2$. $w_D \coloneqq w/h$ and $z_D \coloneqq z/h$.

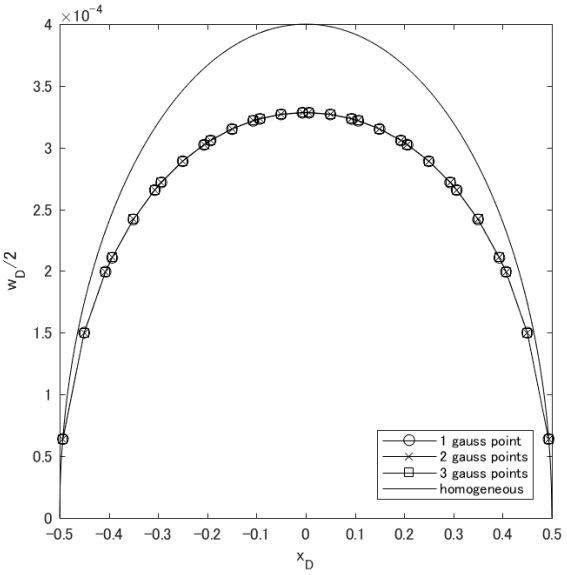

Figure 3.12: The half-width of the horizontal crack in a three-layered medium for different number of Gauss points in the case of quadratic elements, eight images, and $\gamma = 2$. $w_D \coloneqq w/h$ and $x_D \coloneqq x/h$.

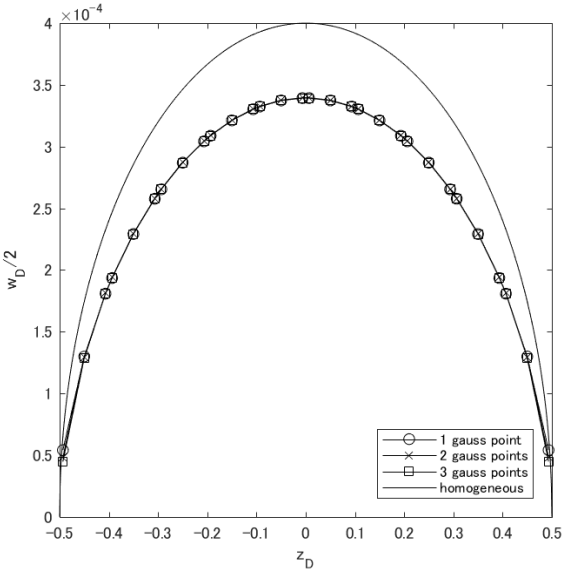

Figure 3.13: The half-width of the horizontal crack in a three-layered medium for different number of Gauss points in the case of quadratic elements, eight images, and $\gamma = 2$. $w_D \coloneqq w/h$ and $z_D \coloneqq z/h$.

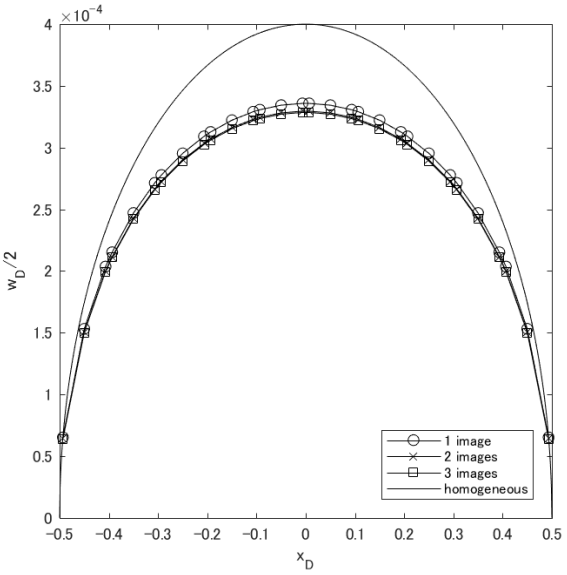

Figure 3.14: The half-width of the horizontal crack in a three-layered medium for different number of image solutions in the case of quadratic elements, three Gauss points, and $\gamma = 2$. $w_D \coloneqq w/h$ and $x_D \coloneqq x/h$.

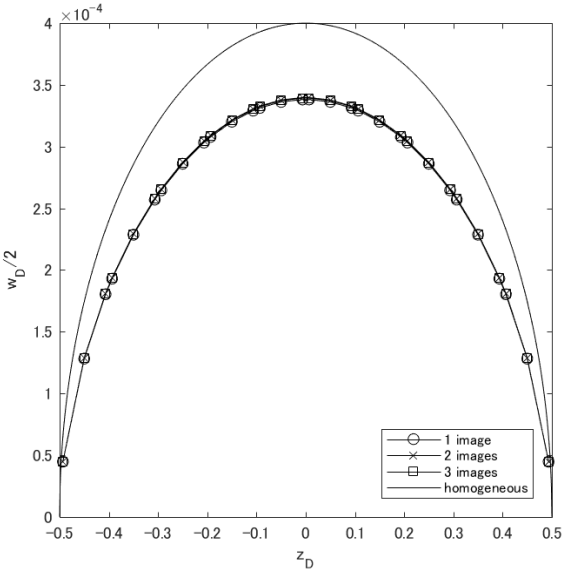

Figure 3.15: The half-width of the vertical crack in a three-layered medium for different number of image solutions in the case of quadratic elements, three Gauss points, and $\gamma = 2$. $w_D \coloneqq w/h$ and $z_D \coloneqq z/h$.

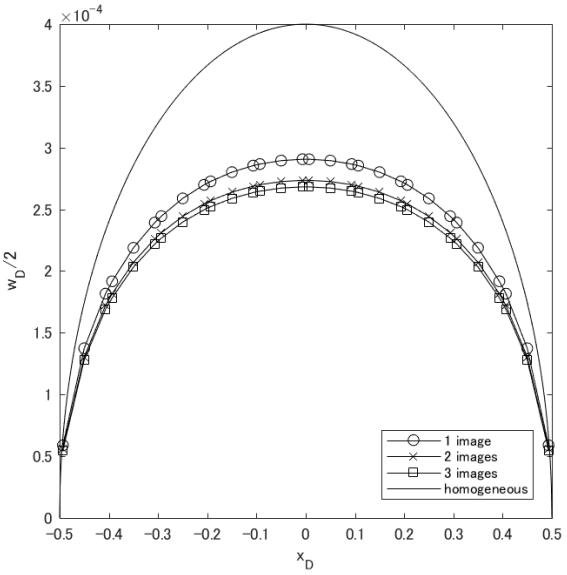

Figure 3.16: The half-width of the horizontal crack in a three-layered medium for different number of image solutions in the case of quadratic elements, three Gauss points, and $\gamma = 5$. $w_D \coloneqq w/h$ and $x_D \coloneqq x/h$.

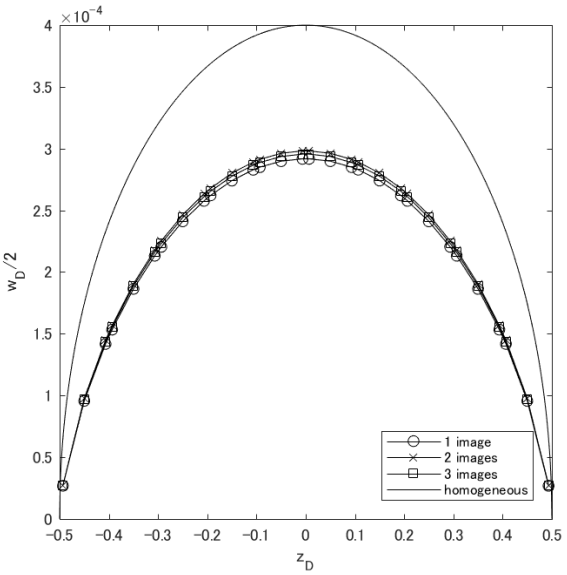

Figure 3.17: The half-width of the vertical crack in a three-layered medium for different number of image solutions in the case of quadratic elements, three Gauss points, and $\gamma = 5$. $w_D \coloneqq w/h$ and $z_D \coloneqq z/h$.

3.6 Conclusion

A new DDM for layered media based on the direct boundary integral formulation with the method of images is presented in this paper. Unlike previous researches using bi-material solutions, the new method can evaluate the contribution of multiple images. It is verified both analytically and numerically by comparison with the Melan solution and the bi-material problem solved by Crouch and Starfield, 1983. Vertical and horizontal cracks in a three-layered medium are investigated by using the new method, and it is found that the critical parameter controlling the computed fracture width is the element type. The number of Gaussian points and images has less impact on crack width. Therefore, the use of bi-material solutions is sufficient for the width calculation of a single crack in the three-layered media with under a plain strain condition.

Chapter 4: DDM-Based Hydraulic Fracturing Model

4.1 Introduction

In Chapter 2, the formulation of DDM was revisited to clarify the equivalence of DDM and BEM. The fact that the DDM formulation is essentially equivalent with BEM means that the numerical techniques used in BEM are also applicable to DDM.

In this chapter, a hydraulic fracturing model in which rock mechanics and fluid dynamics are coupled is developed. DDM is used to simulated the elastic deformation of fractures, while FVM is used to compute the fluid flow inside the fractures with the lubrication theory. Fracture surfaces are discretized into rectangular elements. The elements are allowed to have different sizes.

The fluid is assumed to be slightly compressible with a constant viscosity to simplify the formulation of the fluid flow inside the fracture. The coupling between rock mechanics and fluid dynamics is implemented either in a segregated or fully-coupled manner. Although the fluid and proppant distribution between fractures through the wellbore is important for fracture propagation (Wu and Olson, 2015b; Wu et al., 2016; Yi et al., 2017; Yi and Sharma, 2018), a constant injection rate into each fracture from the wellbore is assumed for simplification. The fluid and proppant distribution, however, can be incorporated into our hydraulic fracturing model in the same way as Shrivastava and Sharma (2018a).

4.2 Fracture Mechanics

4.2.1 Solid Deformation

DDM is used to compute the elastic response of the fracture against the change of fluid pressure. Based on the formulation described in Chapter 2, the displacement discontinuity along the fracture surface and the fluid pressure have the following relationship:

$$-pn_i = -\mathscr{H}_{ij}\Delta u_j + \sigma_{0,ij}n_j, \tag{4.1}$$

where $\sigma_{0,ij}$ is the farfield stress field. Using the constant-strength elements, the above equation can be discretized into

$$\mathbf{A}_{ij}\Delta\mathbf{u}_j + \mathbf{B}_{ij}p_j = \mathbf{f}_i, \tag{4.2}$$

$$\mathbf{B}_{ij} = \delta_{ij}\mathbf{n}_i, \tag{4.3}$$

$$\mathbf{f}_i = -\boldsymbol{\sigma}_0 \cdot \mathbf{n}_i \tag{4.4}$$

where $\mathbf{A}_{ij}$ is the influence coefficient matrix from the collocation point on the ith element to the jth element, δ_{ij} is the Kronecker delta, and $\mathbf{n}_i$ is the normal vector of the ith element.

4.2.2 Fracture Propagation Criteria

We assume small scale yielding (SSY). In other words, we assume that the stress field around a crack tip can be described by linear elastic fracture mechanics (LEFM) because the yielding zone near the crack tip is small enough compared to the crack length (Rice, 1968; Zehnder, 2012). In SSY, the criteria of the initiation and growth of fractures can be described in terms of either stress intensity factors (SIFs) or energy release rate.

4.2.2.1 Maximum-Stress Criteria

In the maximum-stress criteria, the condition of fracture propagation is expressed in terms of SIFs, which represent the magnitude of stress singularity around a crack tip. Since the stress around a crack tip has the singularity of $\sqrt{r}$ in LEFM, SIFs are defined by

$$K_{\mathrm{I}} := \lim_{r \to 0} \sigma_{\theta\theta}|_{\theta=0} \sqrt{2\pi r} \tag{4.5}$$

$$K_{\mathrm{II}} := \lim_{r \to 0} \sigma_{r\theta}|_{\theta=0} \sqrt{2\pi r} \tag{4.6}$$

$$K_{\mathrm{III}} := \lim_{r \to 0} \sigma_{3\theta}|_{\theta=0} \sqrt{2\pi r} \tag{4.7}$$

where r is the distance from the crack tip, and K_{I}, K_{II}, and K_{III} are the mode-I, II, and III SIFs, respectively. The stress components are expressed in the cylindrical coordinate system around the crack tip.

For a crack growing straight ahead, the maximum tensile stress occurs in the direction of $\theta = 0$. Thus, the maximum-stress criterion for pure mode-I fractures is simply given by

$$K_{\mathrm{I}} \geq K_{\mathrm{I}c} \tag{4.8}$$

where $K_{\mathrm{I}c}$ is the mode-I critical SIF. For mixed-mode fractures, the maximum circumferential stress criterion is used (Erdogan and Sih, 1963). It postulates that a crack will propagate in the direction where the maximum circumferential stress occurs when the mode-I SIF in that direction exceeds a critical value:

$$\bar{K}_{\mathrm{I}} \geq K_{\mathrm{I}c} \tag{4.9}$$

where $\bar{K}_{\mathrm{I}}$ is the mode-I SIF in the maximum circumferential stress direction θ_0. $\bar{K}_{\mathrm{I}}$

can be calculated by

$$\bar{K}_{\mathrm{I}} = \frac{1}{2}\cos\frac{\theta_0}{2}\left[K_{\mathrm{I}}(1+\cos\theta_0) - 3K_{\mathrm{II}}\sin\theta_0\right] \tag{4.10}$$

The maximum circumferential stress direction is calculated by (Erdogan and Sih, 1963; Duarte et al., 2001)

$$\tan\frac{\theta_0}{2} = \frac{1}{4}\left[\frac{K_{\mathrm{I}}}{K_{\mathrm{II}}} - \mathrm{sgn}\left(K_{\mathrm{II}}\right)\sqrt{\left(\frac{K_{\mathrm{I}}}{K_{\mathrm{II}}}\right)^2 + 8}\right], \quad -\pi \le \theta \le \pi \tag{4.11}$$

4.2.2.2 Maximum-Energy-Release-Rate Criteria

The energy release rate $\mathscr{G}$ is the energy dissipated to create new crack surfaces defined by

$$\mathscr{G} := -\frac{\partial \Pi}{\partial s} \tag{4.12}$$

where Π is the potential energy, and s is the surface area of the crack. In SSY, SIFs and energy release rate for a crack growing straight ahead are related:

$$\mathscr{G} = \frac{K_{\mathrm{I}}^2}{E'} + \frac{K_{\mathrm{II}}^2}{E'} + \frac{K_{\mathrm{III}}^3}{2G} \tag{4.13}$$

where $E' = E/(1-\nu^2)$ is the plain strain Young's modulus, and G is the shear modulus. If a crack grows in some other direction, the above equation is no longer valid, and numerical computation is required in general. However, under SSY, if we assume

1. The fracture will propagate in the direction of the maximum energy release rate.
2. The fracture grows when the energy release rate reaches a critical value.

Then, the maximum-energy-release-rate criterion for plain-strain fractures can be expressed in the following form (Nuismer, 1975):

$$\mathscr{G} \geq \mathscr{G}_{\mathrm{c}} \tag{4.14}$$

where G_{c} is the critical energy release rate. $\mathscr{G}$ can be calculated by

$$\mathscr{G} = \frac{\bar{K}_{\mathrm{I}}^2}{E'} \tag{4.15}$$

4.2.2.3 Calculation of Stress Intensity Factors

SIFs can be computed from stresses or displacement discontinuities near crack tips. Using special crack tip elements which account for the square-root singularity of displacement discontinuities to crack tips, SIFs can be computed accurately (Crouch and Starfield, 1983; Shou, 1993; Shou and Crouch, 1995; Shou et al., 1997). On the other hand, Schultz (1988) proposed the following simple equations based on the semi-infinite crack solution to estimate SIFs:

$$K_{\mathrm{I}} = \frac{G}{4(1-\nu)} \left(\frac{2\pi}{a}\right)^{\frac{1}{2}} \Delta u_2 \tag{4.16}$$

$$K_{\mathrm{II}} = \frac{G}{4(1-\nu)} \left(\frac{2\pi}{a}\right)^{\frac{1}{2}} \Delta u_1 \tag{4.17}$$

where a is the distance between the center of an element and the crack tip. Displacement discontinuity is evaluated in the local coordinate system in the above equation. The above equations are used in Shou and Crouch (1995), Dong and De Pater (2001), and Yamamoto et al. (2004).

Olson (1991) proposed an empirical equation based on the analytical solution of a finite length crack to compute SIFs from displacement discontinuity

$$K_{\mathrm{I}} = \frac{C_{\mathrm{cor}} E}{4(1-\nu^2)} \left(\frac{\pi}{2a}\right)^{\frac{1}{2}} \Delta u_2 \tag{4.18}$$

$$K_{\mathrm{II}} = \frac{C_{\mathrm{cor}} E}{4(1-\nu^2)} \left(\frac{\pi}{2a}\right)^{\frac{1}{2}} \Delta u_1 \tag{4.19}$$

where $C_{\mathrm{cor}} = 0.806$ is a correction factor, and a is element half-length. Sheibani and Olson (2013) compared the SIFs computed using the Olson's equation with those computed using analytical solutions and showed that Olson's equation has a reasonable accuracy. We use Olson's equation because of its simplicity.

4.3 Fluid Mechanics

4.3.1 Fluid Flow Inside Fractures

Neglecting the gravitational force, the Darcy velocity $\mathbf{v}_d$ per unit fracture depth perpendicular to the flow direction in fractures for a Newtonian fluid is given by (Girault et al., 2016)

$$\mathbf{v}_d = -\frac{k}{\mu_f} \overline{\nabla} p, \tag{4.20}$$

where k denotes the permeability integrated over the width of the fracture, $\overline{\nabla}$ is the surface gradient operator, p is the fluid pressure, and μ_f is the fluid viscosity. Mass conservation in fracture can be written by

$$\frac{\partial(\rho w)}{\partial t} + \overline{\nabla} \cdot (\rho_f \mathbf{v}_d) + \dot{m}_l = \dot{m}_w, \tag{4.21}$$

where $\dot{m}_l$ is a leak-off mass rate per unit area from the fracture domain to the reservoir domain, and $\dot{m}_w$ is a mass rate per unit area from the wellbore to the fracture domain.

We assume the linear dependence of the fluid density on pressure:

$$\rho_f = \rho_{f0}\{1 + c_f(p - p_0)\}, \tag{4.22}$$

where ρ_{f0} is the reference density, c_f is the compressibility, and p_0 is the reference pressure. Because of the small compressibility of liquids ($c_f \ll 1$), the time derivative in Eq. 4.21 can be approximated by

$$\begin{aligned} \frac{\partial(\rho w)}{\partial t} &= w\frac{\partial \rho_f}{\partial p}\frac{\partial p}{\partial t} + \rho_f \frac{\partial w}{\partial t} \\ &= w c_f \rho_{f0}\frac{\partial p}{\partial t} + \rho_f \frac{\partial w}{\partial t} \\ &\approx \rho_{f0}\left(w c_f \frac{\partial p}{\partial t} + \frac{\partial w}{\partial t}\right). \end{aligned} \tag{4.23}$$

Assuming the fluid viscosity is constant and the fracture permeability obeys the cubic law $k = w^3/12$ (Witherspoon et al., 1980; Zimmerman and Yeo, 2000), the divergence term in Eq. 4.21 can be approximated by

$$\begin{aligned} \overline{\nabla} \cdot (\rho_f \mathbf{v}_d) &= \overline{\nabla} \cdot \left(-\frac{\rho_f w^3}{12\mu_f}\overline{\nabla} p\right) \\ &\approx -\frac{\rho_{f0}}{\mu_f'}\overline{\nabla} \cdot (w^3 \overline{\nabla} p), \end{aligned} \tag{4.24}$$

where $\mu_f' = 12\mu_f$.

Carter's leak-off model (Howard and Fast, 1957) is selected to compute the leak-off rate. The leak-off term in Eq. 4.21 can be expressed by

$$m_l = \frac{c_l \rho_f (p - p_r)}{\sqrt{t - \tau}}, \tag{4.25}$$

where c_l is the leak-off coefficient, p_r is the pore pressure in the reservoir domain, t is the current time, and τ is the exposure time at which the fracture surface is created.

The leak-off coefficient is given by

$$\sqrt{\frac{k_r \phi c_f}{\pi \mu_f}}, \tag{4.26}$$

where k_r is the rock permeability, and ϕ is the rock porosity.

Substituting Eq. 4.23, Eq. 4.24, and Eq. 4.25 into Eq. 4.21 and dividing by ρ_{f0}, we obtain

$$c_f w \frac{\partial p}{\partial t} + \frac{\partial w}{\partial t} - \frac{1}{\mu'_f} \overline{\nabla} \cdot (w^3 \overline{\nabla} p) + \frac{c_l (p - p_r)}{\sqrt{t - \tau}} = q_w, \tag{4.27}$$

where $q_w = \dot{m}_w / \rho_{f0}$ is the volumetric rate per unit area at the reference pressure from the wellbore to the fracture domain.

The discretization of Eq. 4.27 using the finite volume method will be described hereafter. Our discretization is similar to that of Settgast et al. (2017). The integral form of Eq. 4.27 over the ith element is given by

$$\int_{S_{fi}} c_f w \frac{\partial p}{\partial t} \, \mathrm{d}S + \int_{S_{fi}} \frac{\partial w}{\partial t} \, \mathrm{d}S - \frac{1}{\mu'_f} \int_{S_{fi}} \overline{\nabla} \cdot (w^3 \overline{\nabla} p) \, \mathrm{d}S + \int_{S_{fi}} \frac{c_l (p - p_r)}{\sqrt{t' - \tau}} \, \mathrm{d}S = \int_{S_{fi}} q_w \, \mathrm{d}S \tag{4.28}$$

The temporal derivatives are evaluated using the backward Euler method:

$$\frac{\partial \psi}{\partial t} = \frac{\psi^{n+1} - \psi^n}{\Delta t}, \tag{4.29}$$

where ψ is any scalar or vector field, $\psi^{n+1} = \psi(t + \Delta t)$, $\psi^n = \psi(t)$, Δt is the time step length, and n is the time step count. This is first-order accurate in time.

The volume integrals are calculated using the mid-point rule

$$\int_{S_{fi}} \psi \, \mathrm{d}S = \psi_i S_{fi} \tag{4.30}$$

where $\psi_i = \psi(\boldsymbol{x}_i)$, and $\boldsymbol{x}_i$ is the center of the surface S_{fi}. Applying the divergence theorem to the third integral term in Eq. 4.28, we have

$$\int_{S_{fi}} \overline{\nabla} \cdot (w^3 \overline{\nabla} p) \, \mathrm{d}S = \oint_{\partial S_{fi}} w^3 \frac{\partial p}{\partial n} \, \mathrm{d}l, \tag{4.31}$$

The line integral in the above equation can be split into the sum of integrals over the cell edges. Using the mid-point rule, each line integral can be evaluated by

$$\oint_{\partial S_{fi}} w^3 \frac{\partial p}{\partial n} \, \mathrm{d}l = \sum_e w_e^3 l_e \left(\frac{\partial p}{\partial n} \right)_e, \tag{4.32}$$

where l is the edge length. The directional gradient of pressure at the mid-point of edges is evaluated implicitly

$$\left(\frac{\partial p}{\partial n} \right)_e = \frac{p_j - p_i}{d_e}, \tag{4.33}$$

where j is the neighbor point of i, and d_e is the distance between $\boldsymbol{x}_i$ and $\boldsymbol{x}_j$ along the surface.

For simplification, we neglect pressure drop through perforations and inside wellbores. In addition, each wellbore is assumed to be connected to only one fracture element. Then, the mass balance in the ith wellbore can be expressed by

$$c_f \int_{V_{wi}} \frac{\partial p_i}{\partial t} \, \mathrm{d}V + \int_{S_{fi}} q_w \, \mathrm{d}S = q_{wi} \tag{4.34}$$

where V_{wi} is the ith wellbore volume, and q_{wi} is the volumetric injection rate into the ith wellbore. Assuming uniform pressure inside the wellbore, we have

$$c_f V_{wi} \frac{p_i^{n+1} - p_i^n}{t} + \int_{S_{fi}} q_w \, \mathrm{d}S = q_{wi} \tag{4.35}$$

Applying these discretization, we obtain the following equation:

$$c_f \left(S_{fi} w_i^{n+1} + V_{wi}\right) \frac{p_i^{n+1} - p_i^n}{\Delta t} + S_{fi} \frac{w_i^{n+1} - w_i^n}{\Delta t} + S_{fi} \Lambda_i (p_i^{n+1} - p_r) - \sum_e K_e^{n+1} (p_j^{n+1} - p_i^{n+1}) = q_{wi} \quad (4.36)$$

where $\Lambda_i = c_l / \sqrt{t - \tau_i}$, and $K_e = l_e w_e^3 / \mu_f' d_e$. The first and fourth non-linear terms in the above equation can be linearized by evaluating width explicitly. Therefore, noting that $w_i = -\mathbf{n}_i \cdot \Delta \mathbf{u}_i$, we have

$$\mathbf{C}_{ij} \Delta \mathbf{u}_j^{n+1,k+1} + D_{ij} p_j^{n+1,k+1} = g_i, \quad (4.37)$$

where

$$\mathbf{C}_{ij} = \begin{cases} -\dfrac{S_{fi}}{\Delta t} \mathbf{n}_i^\top, & \text{for } i = j, \\ 0 & \text{for } i \neq j, \end{cases} \quad (4.38)$$

$$D_{ij} = \begin{cases} \left(S_{fi} w_i^{n+1,k} + V_{wi}\right) \dfrac{c_f}{\Delta t} + S_{fi} \Lambda_i + \displaystyle\sum_e K_e^{n+1,k}, & \text{for } i = j, \\ -K_e^{n+1,k}, & \text{for } i \neq j, \end{cases} \quad (4.39)$$

$$g_i = q_{wi} + \left(S_{fi} w_i^{n+1,k} + V_{wi}\right) \frac{c_f p_i^n}{\Delta t} + \frac{S_{fi} w_i^n}{\Delta t} + S_{fi} \Lambda_i p_r. \quad (4.40)$$

The superscripts $k+1$ and k denote the iteration count.

4.4 Solution Strategy

The DDM and flow equations are combined to form a coupled system of equations:

$$\begin{bmatrix} \mathbf{A} & \mathbf{B} \\ \mathbf{C} & \mathbf{D} \end{bmatrix} \begin{bmatrix} \Delta\mathbf{u} \\ \mathbf{p} \end{bmatrix}^{k+1} = \begin{bmatrix} \mathbf{f} \\ \mathbf{g} \end{bmatrix} \tag{4.41}$$

or

$$\mathcal{A}\mathbf{x}^{k+1} = \mathbf{b}, \tag{4.42}$$

$$\mathcal{A} = \begin{bmatrix} \mathbf{A} & \mathbf{B} \\ \mathbf{C} & \mathbf{D} \end{bmatrix}, \quad \mathbf{x} = \begin{bmatrix} \Delta\mathbf{u} \\ \mathbf{p} \end{bmatrix}, \quad \mathbf{b} = \begin{bmatrix} \mathbf{f} \\ \mathbf{g} \end{bmatrix}$$

where time step $n+1$ is omitted for brevity. There are two common approaches to solve this coupled system of equations: the segregated method and the fully coupled method. The segregated method iteratively solves the DDM and flow equations based on matrix splitting techniques, while the fully coupled method directly solves the coupled system.

Solving the coupled system of equations is continued until convergence. The convergence criterion of the solution is given by

$$\frac{\max_i |p_i^{k+1} - p_i^k|}{\max_i |p_i^k|} < \epsilon_p \tag{4.43}$$

$$\frac{\max_{i,j} |\Delta u_{j,i}^{k+1} - \Delta u_{j,i}^k|}{\max_{i,j} |\Delta u_{j,i}^k|} < \epsilon_u \tag{4.44}$$

where $\Delta u_{j,i}$ is the jth component of the displacement discontinuity of ith element, and ϵ_p and ϵ_u are tolerances for pressure and displacement discontinuity, respectively. $\epsilon_p = \epsilon_u = 1.0 \times 10^{-6}$ is used in this dissertation.

When the iterations have converged, the fracture propagation criterion is checked

along the edges of the fracture. New elements are added in front of the tip edges which satisfy the propagation criterion. The size of new elements is the same with that of the owner element of the crack tip edges unless otherwise stated. The propagation direction is determined using the maximum circumferential stress criterion. A flow chart of the fracture propagation algorithm is shown in Fig. 4.1.

4.4.1 Segregated Method

4.4.1.1 Fixed-Width Split

A common matrix splitting technique used in the DDM-flow coupling is the fixed-width split. That is, solving the flow equation while freezing the fracture width, and then solving the DDM equation to obtain the displacement discontinuity, or vice versa. The fixed-width split can be expressed by

$$\begin{bmatrix} \mathbf{A} & \mathbf{B} \\ \mathbf{C} & \mathbf{D} \end{bmatrix} \begin{bmatrix} \Delta\mathbf{u} \\ \mathbf{p} \end{bmatrix}^{k+1} = \begin{bmatrix} \mathbf{A} & \mathbf{B} \\ O & \mathbf{D} \end{bmatrix} \begin{bmatrix} \Delta\mathbf{u} \\ \mathbf{p} \end{bmatrix}^{k+1} + \begin{bmatrix} O & O \\ \mathbf{C} & O \end{bmatrix} \begin{bmatrix} \Delta\mathbf{u} \\ \mathbf{p} \end{bmatrix}^{k} \tag{4.45}$$

This is analogous to the drained or fixed-strain split in geomechanics-flow coupling problems (Kim et al., 2011a). Substituting into the original equation, we obtain the expression for the fixed-width split:

$$\begin{bmatrix} \mathbf{A} & \mathbf{B} \\ O & \mathbf{D} \end{bmatrix} \begin{bmatrix} \Delta\mathbf{u} \\ \mathbf{p} \end{bmatrix}^{k+1} = \begin{bmatrix} O & O \\ -\mathbf{C} & O \end{bmatrix} \begin{bmatrix} \Delta\mathbf{u} \\ \mathbf{p} \end{bmatrix}^{k} + \begin{bmatrix} \mathbf{f} \\ \mathbf{g} \end{bmatrix} \tag{4.46}$$

This equation can be solved iteratively in the following manner:

1. Solve the flow equation using $\mathbf{p}^{k+1} = \mathbf{D}^{-1}(\mathbf{g} - \mathbf{C}\Delta\mathbf{u}^{k})$.
2. Solve the DDM equation using $\Delta\mathbf{u}^{k+1} = \mathbf{A}^{-1}(\mathbf{f} - \mathbf{B}\mathbf{p}^{k+1})$.

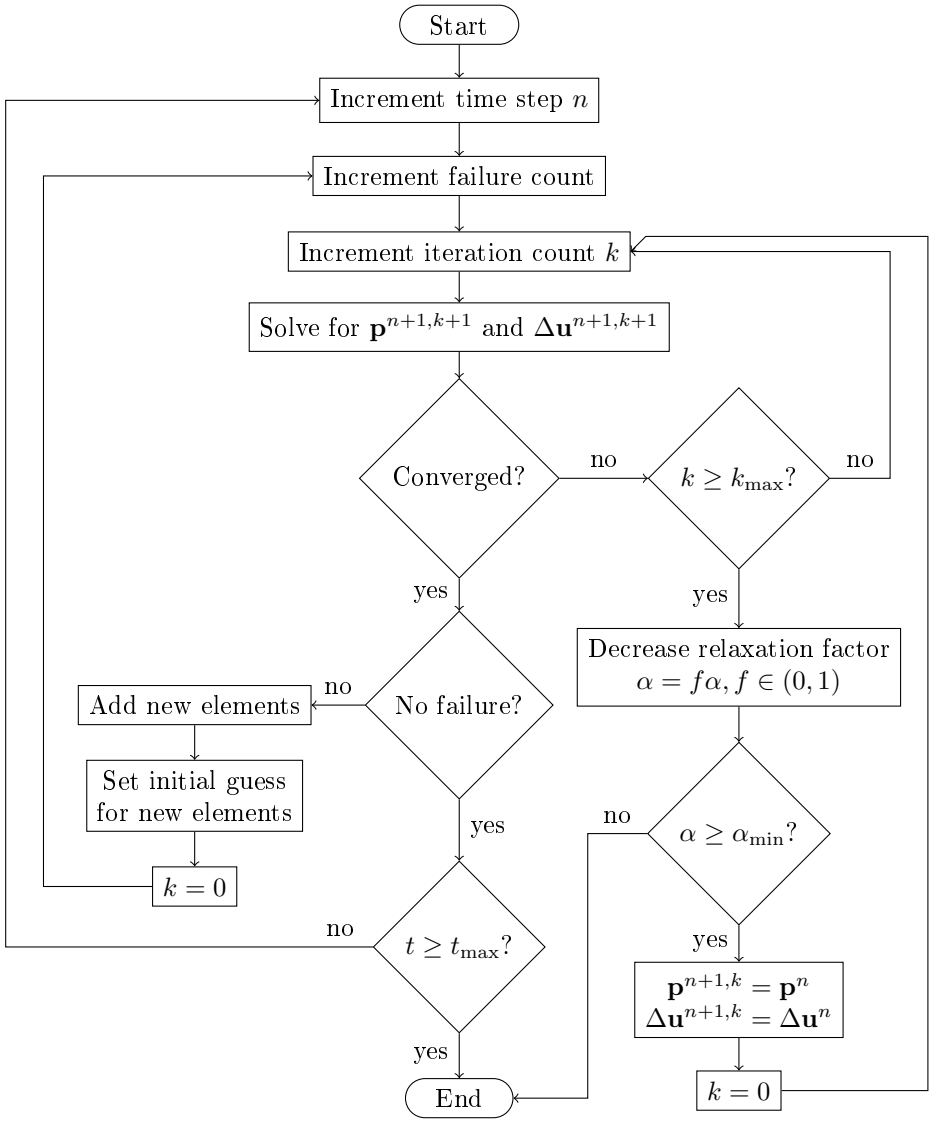

Figure 4.1: A flow chart of the fracture propagation algorithm.

This is a preconditioned Richardson iteration with a block triangular preconditioner (Castelletto et al., 2015). New predicted values are relaxed at each step using a relaxation factor $\alpha \in (0, 1]$:

$$\psi^{k+1} \leftarrow \alpha\psi^{k+1} + (1-\alpha)\psi^{k} \tag{4.47}$$

The same relaxation factors are used in this dissertation for pressure and displacement discontinuity, though different values can be applied.

The segregated method has the advantages of easy implementation and less memory requirement due to its smaller matrix size compared to the fully coupled method. Thus, it has been used by many researchers, e.g. Yamamoto et al. (2004), Wu and Olson (2013), Wu (2014), Wu and Olson (2015a), and Shrivastava et al. (2017). However, it is observed that the fixed-width split requires a small relaxation factor, typically around 0.1, resulting in slow convergence. Moreover, iterations sometimes do not converge at all even if a very small relaxation factor is used. The slow convergence and instability problems have been also reported in the case of the fixed-strain and drained split in geomechanics-flow coupling problems (Kim et al., 2011a,b,c).

4.4.1.2 Fracture Compliance Split

A new splitting scheme, which is called fracture compliance split in this dissertation, is proposed to obtain higher convergence speed and better numerical stability. The key idea is to incorporate the pressure dependence of fracture width into the flow equation. We assume that the pressure dependence of fracture width in the flow equation can be approximated by

$$w_i^{k+1} - w_i^{k} = c_i(p_i^{k+1} - p_i^{k}), \tag{4.48}$$

where c_i is the fracture compliance. The fracture compliance is estimated from the self-influence coefficients of DDM:

$$c_i = \begin{cases} \dfrac{\pi(1-\nu)a_i}{G}, & \text{for 2D line elements,} \\ \dfrac{\pi(1-\nu)}{G} \cdot \dfrac{a_i b_i}{\sqrt{a_i^2 + b_i^2}}, & \text{for 3D rectangular elements,} \end{cases} \tag{4.49}$$

where G is shear modulus, ν is Poisson ratio, a_i and b_i are the half-lengths of DDM elements in the local x and y directions, respectively. Substituting into the flow equation, we obtain the following matrix splitting:

$$\begin{bmatrix} \mathbf{A} & \mathbf{B} \\ \mathbf{C} & \mathbf{D} \end{bmatrix} \begin{bmatrix} \Delta\mathbf{u} \\ \mathbf{p} \end{bmatrix}^{k+1} = \begin{bmatrix} \mathbf{A} & \mathbf{B} \\ O & \mathbf{D} + \omega\mathbf{C}' \end{bmatrix} \begin{bmatrix} \Delta\mathbf{u} \\ \mathbf{p} \end{bmatrix}^{k+1} + \begin{bmatrix} O & O \\ \mathbf{C} & -\omega\mathbf{C}' \end{bmatrix} \begin{bmatrix} \Delta\mathbf{u} \\ \mathbf{p} \end{bmatrix}^{k}, \tag{4.50}$$

where $\omega \in [0, 1]$ is a relaxation factor. $\omega = 0$ corresponds to the fixed-width splitting scheme. $\mathbf{C}'$ is a diagonal matrix defined by

$$\mathbf{C}' := \frac{1}{\Delta t} \mathrm{diag}\left\{ S_{f1} c_1, \cdots, S_{fN} c_N \right\}, \tag{4.51}$$

where N is the number of cells. Eq. 4.50 can be solved iteratively in the following manner:

1. Solve the flow equation using $\mathbf{p}^{k+1} = (\mathbf{D} + \omega\mathbf{C}')^{-1}(\mathbf{g} - \mathbf{C}\Delta\mathbf{u}^k + \omega\mathbf{C}'\mathbf{p}^k)$.
2. Solve the DDM equation using $\Delta\mathbf{u}^{k+1} = \mathbf{A}^{-1}(\mathbf{f} - \mathbf{B}\mathbf{p}^{k+1})$.

This splitting scheme takes the fracture compliance term $\mathbf{C}'$ as a source correction term in the flow equation. The contribution of the correction term tends to disappear as the solution converges. The new splitting scheme is analogous to the fixed-stress split in Kim et al. (2011a).

4.4.2 Fully Coupled Method

The fully coupled method solves Eq. 4.41 directly and determines $\Delta\mathbf{u}$ and $\mathbf{p}$ simultaneously. That is, the solution vector at the new iteration count is computed by

$$\begin{bmatrix} \Delta\mathbf{u} \\ \mathbf{p} \end{bmatrix}^{k+1} = \begin{bmatrix} \mathbf{A} & \mathbf{B} \\ \mathbf{C} & \mathbf{D} \end{bmatrix}^{-1} \begin{bmatrix} \mathbf{f} \\ \mathbf{g} \end{bmatrix}. \tag{4.52}$$

Iterations are continued until convergence. Assuming that the number of cells is N and the dimensions is D, the fully coupled approach requires to solve $(D+1)N$ equations with the same number of unknowns, i.e. displacement discontinuity and fracture pressure.

Since the coupled system of equations involves two quantities with different units, the coefficients in the equation have significantly different scales. Thus, they must be scaled to have the same order of magnitude. For example, Settgast et al. (2017) scaled the coupled system of equations using the maximum force and mass of each cell. The scaling process in this dissertation is combined with the preconditioning process to give

$$\mathcal{M}_1^{-1}\mathcal{A}'\mathbf{y} = \mathcal{M}_1^{-1}\mathbf{b} \tag{4.53}$$

$$\mathcal{A}' \coloneqq \mathcal{A}\mathcal{M}_2, \tag{4.54}$$

$$\mathbf{y} \coloneqq \mathcal{M}_2^{-1}\mathbf{x}, \tag{4.55}$$

where $\mathcal{M}_1$ and $\mathcal{M}_2$ are block-diagonal left and right preconditioning matrices, respec-

tively. The preconditioning matrices are defined by

$$\mathcal{M}_1 := \begin{bmatrix} \mathbf{M}_u & O \\ O & \mathbf{M}_p \end{bmatrix}, \tag{4.56}$$

$$\mathcal{M}_2 := \begin{bmatrix} s_u\mathbf{I} & O \\ O & s_p\mathbf{I} \end{bmatrix}, \tag{4.57}$$

$$\mathbf{M}_u := s_u \mathrm{diag}\left\{\mathbf{A}_{11}, \ldots, \mathbf{A}_{NN}\right\}, \tag{4.58}$$

$$\mathbf{M}_p := s_p \mathrm{diag}\left\{D_{11}, \ldots, D_{NN}\right\}, \tag{4.59}$$

$$s_u := \max_{i,j}\left\{|\Delta u_{j,i}|\right\}, \tag{4.60}$$

$$s_p := \max_{i}\left\{|p_i|\right\}. \tag{4.61}$$

s_u and s_p are scaling factors for displacement discontinuity and pressure, respectively.

Using the fully-coupled method, faster convergence and better numerical stability can be obtained in general. Therefore, the method is used for highly non-linear systems such as hydraulic fracturing using non-Newtonian fluids, e.g. Olson and Wu (2012) and Wu (2014).

4.5 Validation

4.5.1 A Radial Fracture

Our hydraulic fracturing model is compared with the analytical solutions of radial fractures developed by Dontsov (2016). The input data for each model are presented in Table 4.1.

The radius, maximum width, and net-pressure of $\mathcal{M}$-vertex or viscosity-dominated

Table 4.1: Input data used in the comparison of the new and old splitting schemes for a 2D fracture propagation problem.

Parameters	Unit	$\mathcal{M}$-vertex	$\mathcal{K}$-vertex
Initial fracture size	m	0.3×0.3	
Element size	m	0.1	
Time step length	sec	1.0	
S_{hmin}	MPa	8.0	
Shear modulus	GPa	24.0	
Poisson ratio		0.25	
K_{Ic}	$\text{MPa}\,\text{m}^{1/2}$	1.0	5.0
Reference density	kg/m^3	1000	
Reference pressure	MPa	3.2	
Viscosity	cP	1.0	
Compressibility	$1\,/\,\text{MPa}$	4.4×10^{-4}	
Leak-off coefficient	$\text{m}\,\text{s}^{-1/2}\,\text{Pa}^{-1}$	0	
Injection rate	m^3/s	0.01	
Wellbore volume	m^3	0.005	
Initial well pressure	MPa	10.0	
Initial fracture width	mm	4.0×10^{-3}	1.0×10^{-2}

solution are given by

$$R = 0.6944 \left(\frac{Q_w^3 E' t^4}{\mu'_f} \right)^{\frac{1}{9}} \tag{4.62}$$

$$w_{\max} = 1.1901 \left(\frac{\mu'^2_f Q_w^3 t}{E'^2} \right)^{\frac{1}{9}} \tag{4.63}$$

$$p_{\text{net}} = 2.4019 \left(\frac{\mu'_f E'^2}{t} \right)^{\frac{1}{3}} \mathcal{F}(0, 0.397, \frac{5}{8}) \tag{4.64}$$

where R is the radius of the fracture, Q_w is injection rate, t is elapsed time, and $\mu'_f = 12\mu_f$. $\mathcal{F}$ is an integral function defined in Dontsov (2016). The radius, maximum

width, and net-pressure of $\mathcal{K}$-vertex or toughness-dominated solution are given by

$$R = 0.8546 \left(\frac{Q_w E' t}{K'} \right)^{\frac{2}{5}} \tag{4.65}$$

$$w_{\max} = 0.6537 \left(\frac{K'^4 Q_w t}{E'^4} \right)^{\frac{1}{5}} \tag{4.66}$$

$$p_{\text{net}} = 0.3004 \left(\frac{K'^6}{E' Q_w t} \right)^{\frac{1}{5}} \tag{4.67}$$

where

$$K' = 4 \left(\frac{2}{\pi} \right)^{\frac{1}{2}} K_{\text{Ic}} \tag{4.68}$$

The simulation and analytical results of the maximum width and the radius of the radial hydraulic fracture of $\mathcal{M}$-vertex solution are plotted in Fig. 4.2 and Fig. 4.3. The width and pressure distribution of the fracture in the end of the simulation are shown in Fig. 4.4 and Fig. 4.5. The fracture radius in the simulation results is calculated by

$$R = \sqrt{\frac{A_f}{\pi}} \tag{4.69}$$

where A_f is total fracture area.

It is found that the numerical results at early time do not agree with the analytical solution as shown in Fig. 4.2 and Fig. 4.3. This is because the initial size of mesh elements is too large compared to the size of the fracture. As the fracture grows, the size of mesh elements becomes small compared to the fracture size, and thus the numerical solution approaches the analytical solution. Moreover, The simulated fracture radius is larger than the analytical one though the growing speed of the fracture of the numerical and analytical results agrees. This can be explained by the discretization using square elements. Because of the use of square elements, the geometry of the radial fracture is not well approximated in the simulation.

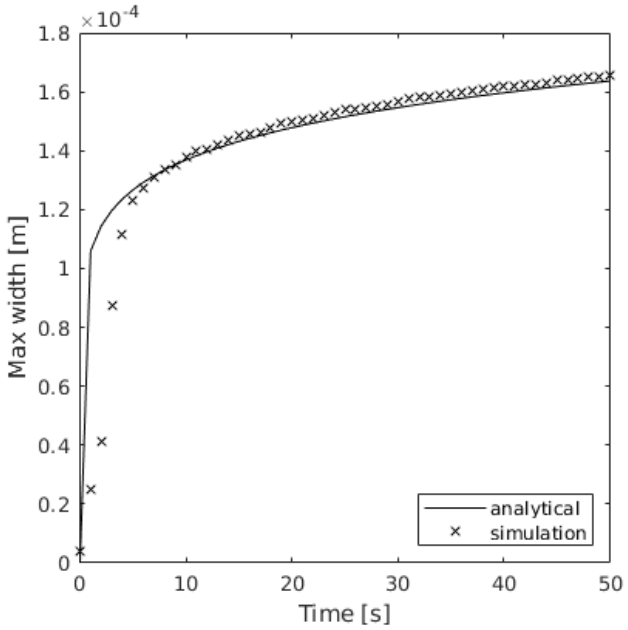

Figure 4.2: The maximum width of a radial hydraulic fracture in the viscosity-dominated regime without leak-off

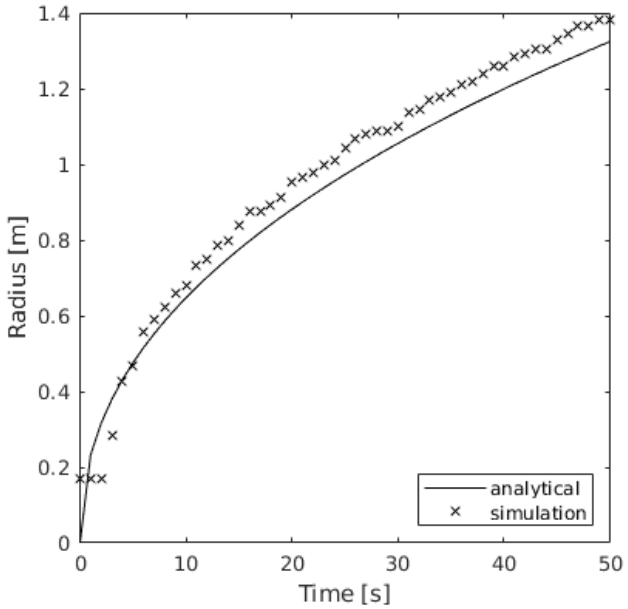

Figure 4.3: The radius of a radial hydraulic fracture in the viscosity-dominated regime without leak-off

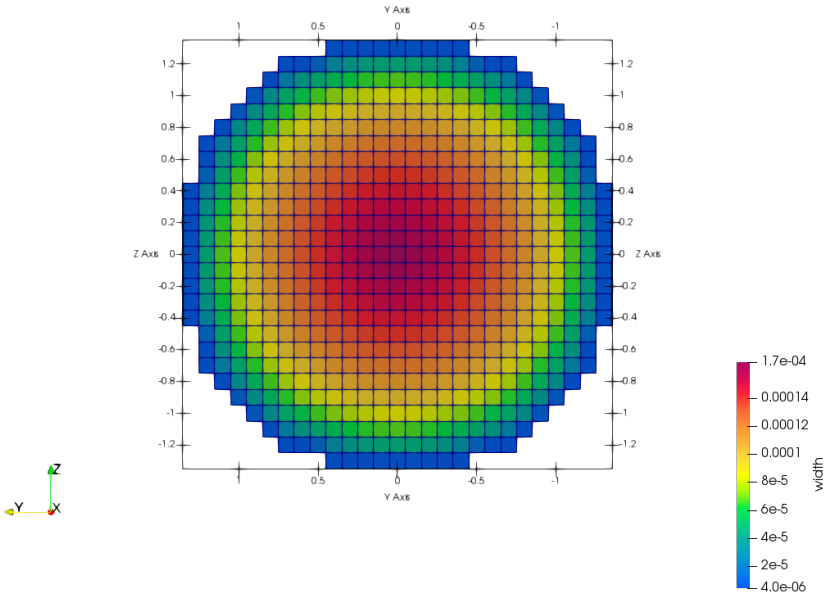

Figure 4.4: The width distribution of a radial hydraulic fracture in the viscosity-dominated regime without leak-off at the time step $t = 50$ sec

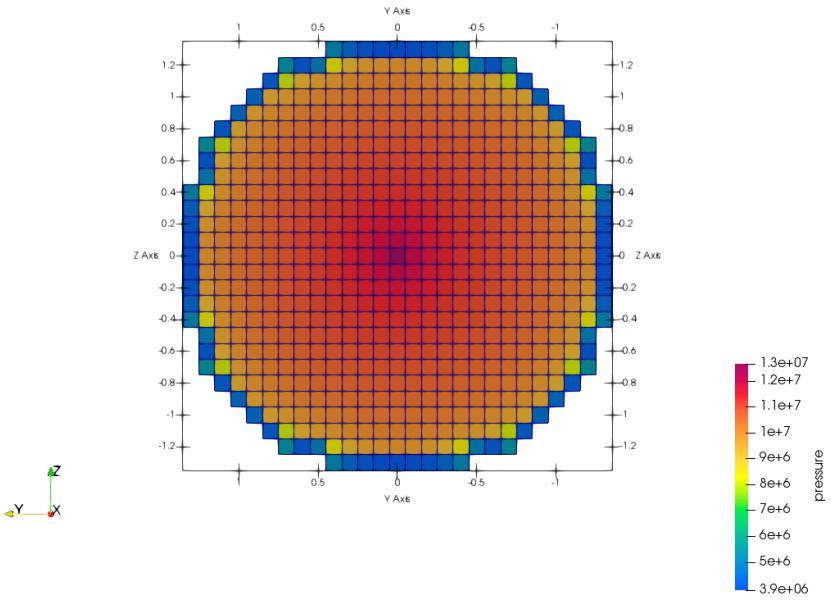

Figure 4.5: The pressure distribution of a radial hydraulic fracture in the viscosity-dominated regime without leak-off at the time step $t = 50$ sec

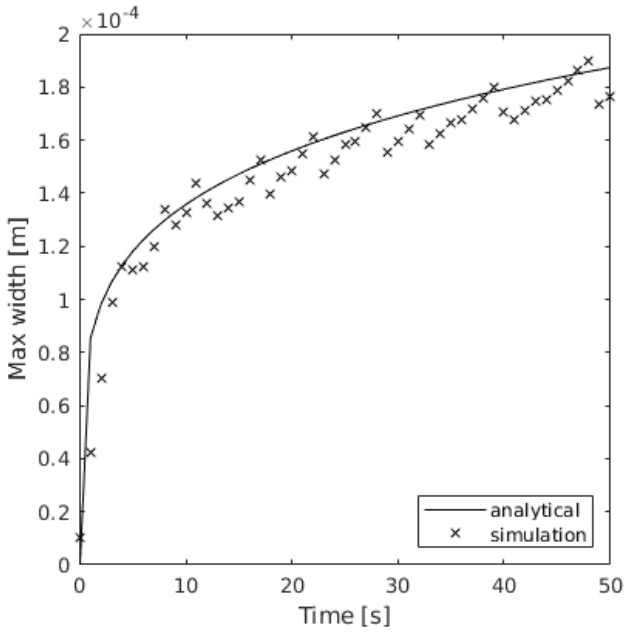

Figure 4.6: The maximum width of a radial hydraulic fracture in the toughness-dominated regime without leak-off

The maximum width and the radius of the radial fracture of the $\mathcal{K}$-vertex solution are shown in Fig. 4.6 and Fig. 4.7. The width and pressure distribution of the fracture in the end of the simulation are also shown in Fig. 4.8 and Fig. 4.9.

Similar to the $\mathcal{M}$-vertex solution, the early-time numerical results deviate from the analytical solution due to the large element size compared to the fracture size. The non-smoothness of the simulation results originates from how new elements are created in the mesh. Since new elements are added in a predetermined size, the increase of the fracture area is not smooth when the fracture grows. Thus, every time the fracture expands, the fracture pressure drops abruptly to satisfy the material balance in the fracture domain. This can be avoided if an adaptive mesh is used though it complicates the simulation algorithm.

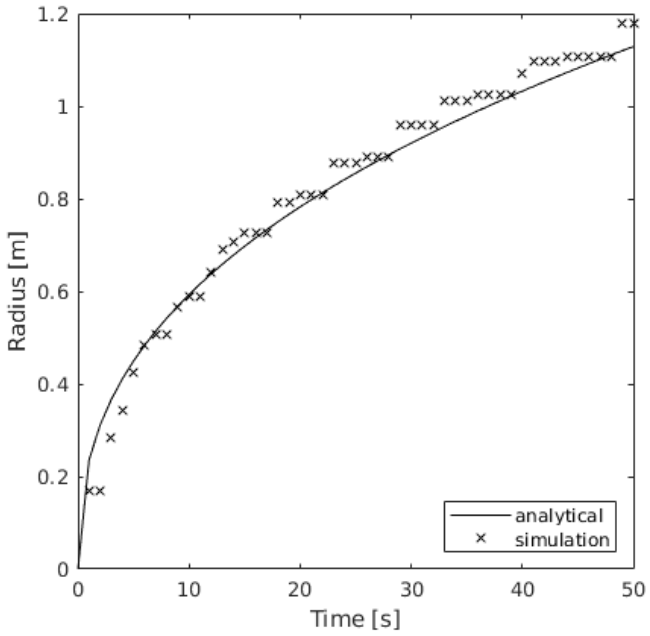

Figure 4.7: The radius of a radial hydraulic fracture in the toughness-dominated regime without leak-off

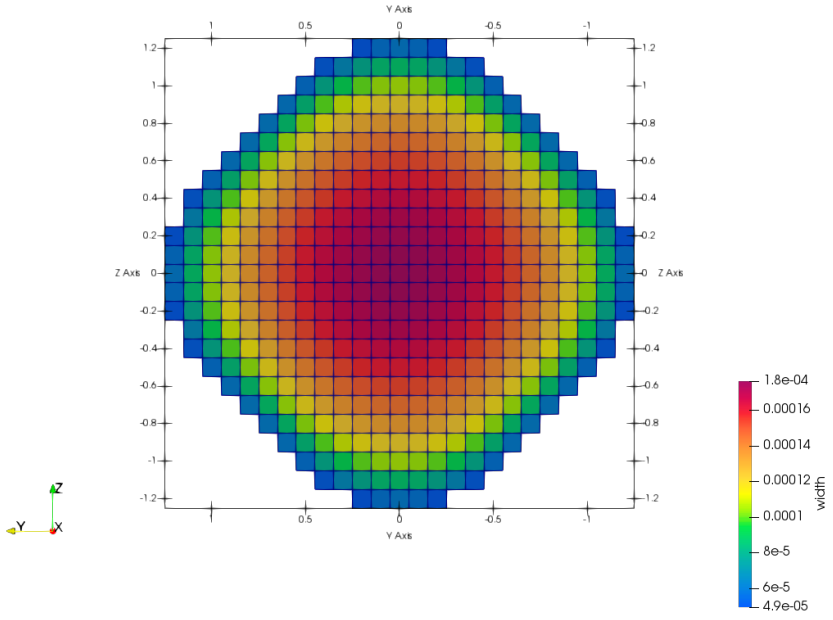

Figure 4.8: The width distribution of a radial hydraulic fracture in the toughness-dominated regime without leak-off at the time step $t = 50$ sec

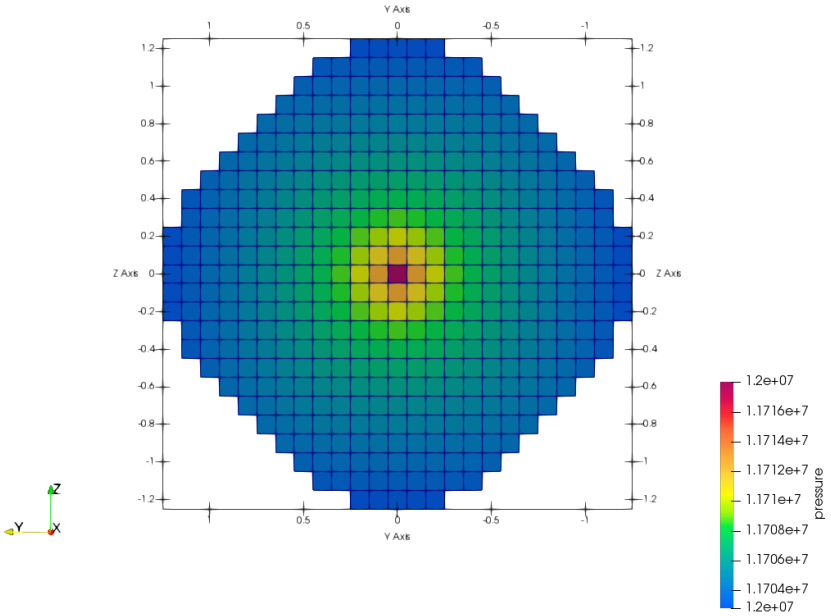

Figure 4.9: The pressure distribution of a radial hydraulic fracture in the toughness-dominated regime without leak-off at the time step $t = 50$ sec

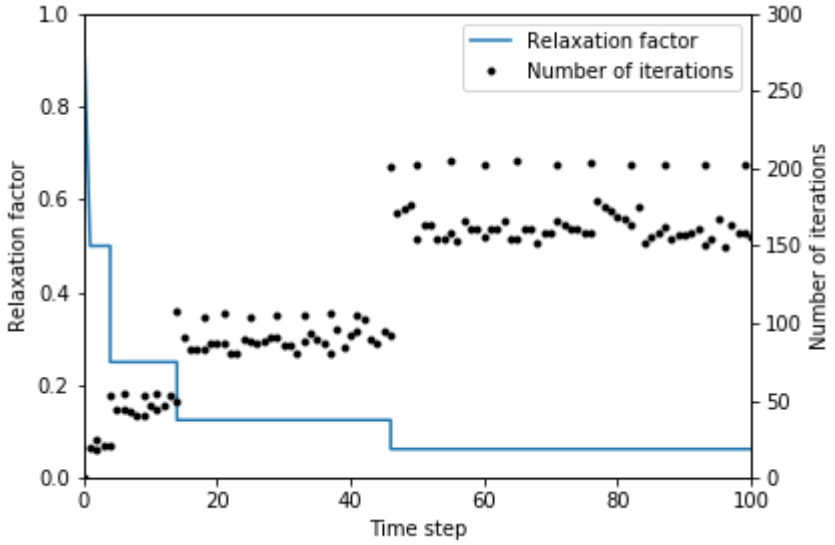

Figure 4.10: The relaxation factor and the number of iterations for a plain-strain fracture propagation solved with the fixed-width split.

4.6 Results

4.6.1 Comparison of Matrix Splitting Techniques

A 2D fracture propagation problem is solved by using the fixed-width split with parameters listed in Table 4.2. The flow equation is solved using the BiCGSTAB method with the incomplete LU factorization preconditioner, while the DDM equation is solved using the BiCGSTAB method with the block-diagonal preconditioner.

The relaxation factor and the number of iterations for the problem is shown in Fig. 4.10. The relaxation factor decreases from 1 to 0.0625 as the fracture grows, while the number of iterations increases from around 20 to 150-200. Because of the fully-populated nature of the DDM influence matrix, the cost of solving the DDM equation is significantly more expensive than that of solving the flow equation. Thus, this large number of iterations negates the aforementioned advantages of the fixed-width split, especially in large scale problems, resulting in slow convergence.

Table 4.2: Simulation parameters used in a 2D fracture propagation problem.

Parameters	
Initial fracture length [m]	3.0
Element length [m]	1.0
Fracture height [m]	1.0
Time step length [sec]	1.0
S_{hmin} [MPa]	0.50
Shear modulus [GPa]	10.0
Poisson ratio	0.25
Reference density [kg/m^3]	1000
Reference pressure [MPa]	1.0
Viscosity [cP]	1.0
Compressibility [1/MPa]	4.5×10^{-4}
Leak-off coefficient [m/$\sqrt{\text{sec}}\cdot$ Pa]	0
Injection rate [m^3/s]	5.0×10^{-4}
Wellbore volume [m^3]	0.50
Initial well pressure [MPa]	1.0
Initial fracture width [mm]	0.10

The fixed-width and fracture-compliance splitting schemes are compared by using the same problem. The relaxation factor and the number of iterations are plotted in Fig. 4.11 and Fig. 4.12 for various ω. $\omega = 0$ corresponds to the fixed-width split. It is clearly shown that the correction term in the fracture compliance split improves the convergence rate of the coupled system since the relaxation factor increases from 0.0625 to 0.25 as ω increases from zero to one. As a result, the number of iterations reduces from 150-200 to 60.

4.6.2 Comparison of Segregated and Fully Coupled Methods

Before comparing the segregated and fully coupled methods, the effect of pre-conditioning in the fully-coupled method is tested by using the problem used in the previous section. The coupled matrix $\mathcal{A}$ of a 2D planar fracture at the initial state is calculated using the parameters listed in Table 4.2. Scaling factors s_u and s_p are

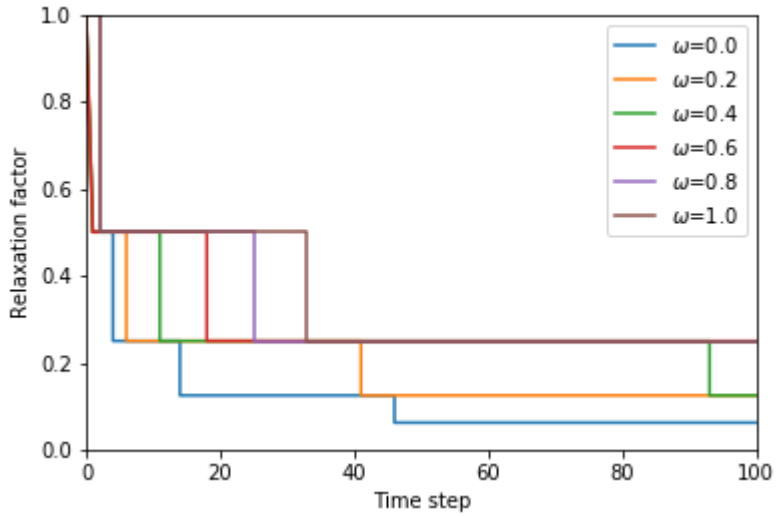

Figure 4.11: The relaxation factor for different ω of the fracture compliance split in a 2D planar fracture propagation.

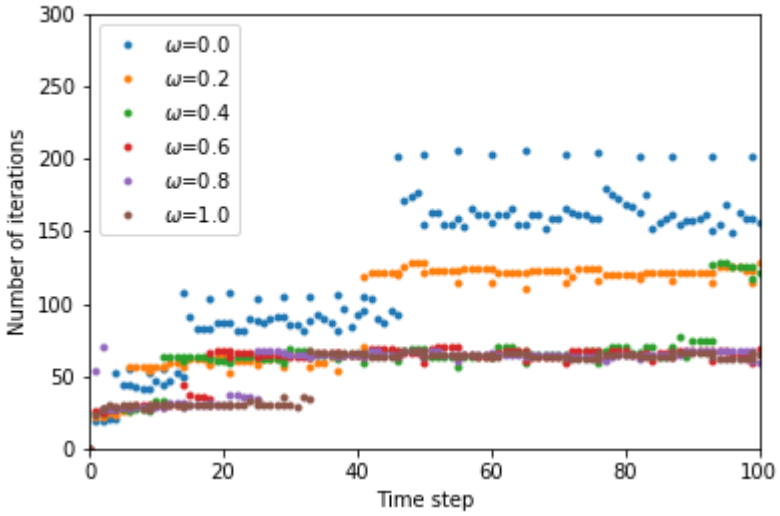

Figure 4.12: The number of iterations for different ω of the fracture compliance split in a 2D planar fracture propagation.

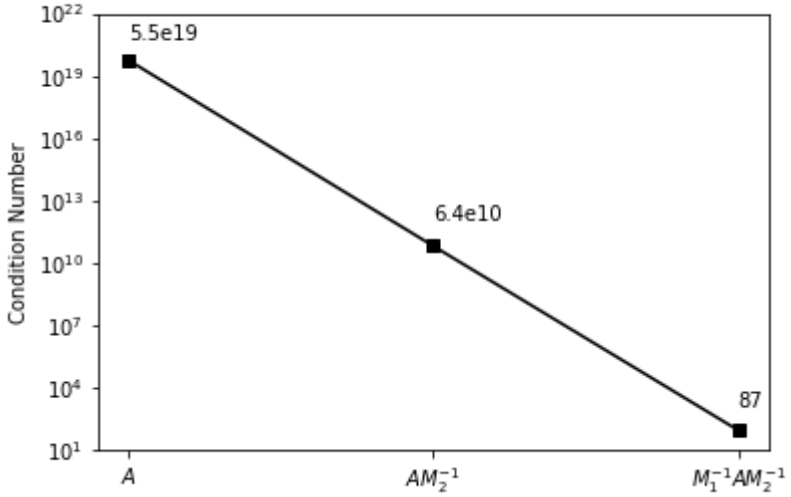

Figure 4.13: The effect of preconditioning to the coupled matrix of a planar 2D fracture.

selected as 10^3 and 10^6, respectively.

The condition numbers of $\mathcal{A}$, $\mathcal{A}\mathcal{M}_2^{-1}$, and $\mathcal{M}_1^{-1}\mathcal{A}\mathcal{M}_2^{-1}$ are plotted in Fig. 4.13. The original coupled matrix $\mathcal{A}$ has a significantly large condition number, meaning that iterative solvers will take a large number of iterations to converge or may fail to solve the equations. Applying the left and right preconditioning matrices to the coupled matrix, the condition number decreased drastically from 5.5×10^{19} to 87. This shows the importance of preconditioning in the fully coupled method.

Next, the segregated and fully coupled methods are compared in the same problem. BiCGSTAB is used to solve the coupled system of equations in the fully coupled method. The relaxation factor and the number of iterations are plotted in Fig. 4.14 and Fig. 4.15, respectively. It is found that the fully coupled method enables us to solve the equations without relaxation ($\alpha = 1$). The number of iterations of the fully coupled method, which is around 5 in this case, is significantly smaller than that of the segregated methods. This faster and stable convergence of the fully coupled

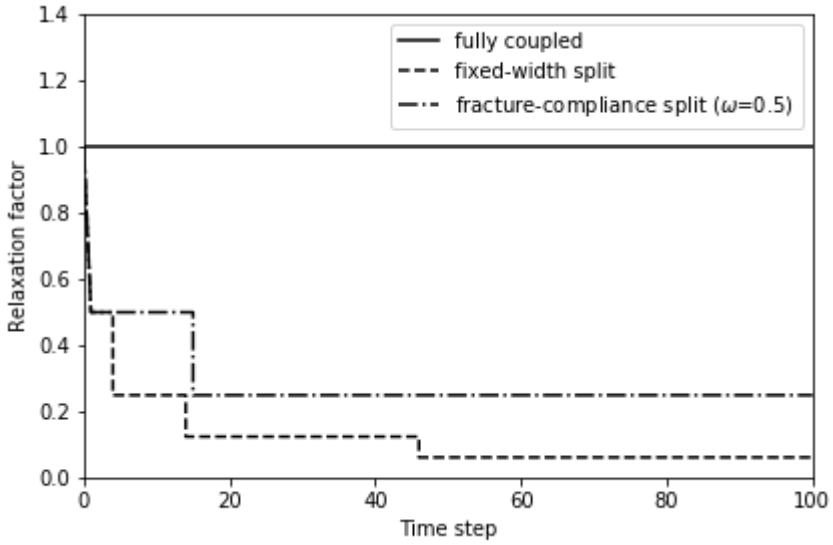

Figure 4.14: The relaxation factor for the fixed-width split, fracture-compliance split, and fully-coupled methods.

method result in the shortest simulation time among the three methods as shown in Fig. 4.16. The fixed-width split is nearly six times slower than the fully coupled method. Although the fracture-compliance split is more than two times faster than the fixed-width split, it is still nearly 2.5 times slower than the fully-coupled method. Therefore, the fully coupled method should be selected if possible in the cases where DDM and flow equations are coupled to solve hydraulic fracturing problems. The fully coupled method can become computationally more expensive for large problems (with a large number of elements) as the size of the matrix grows.

4.7 Conclusion

A hydraulic fracturing model is formulated as a coupled problem of fracture mechanics and fluid dynamics in the fracture in this chapter. The solid deformation is described by using DDM, while the fluid flow inside the fracture is solved using a FVM. The fracturing fluid is assumed to be slightly compressible and to have

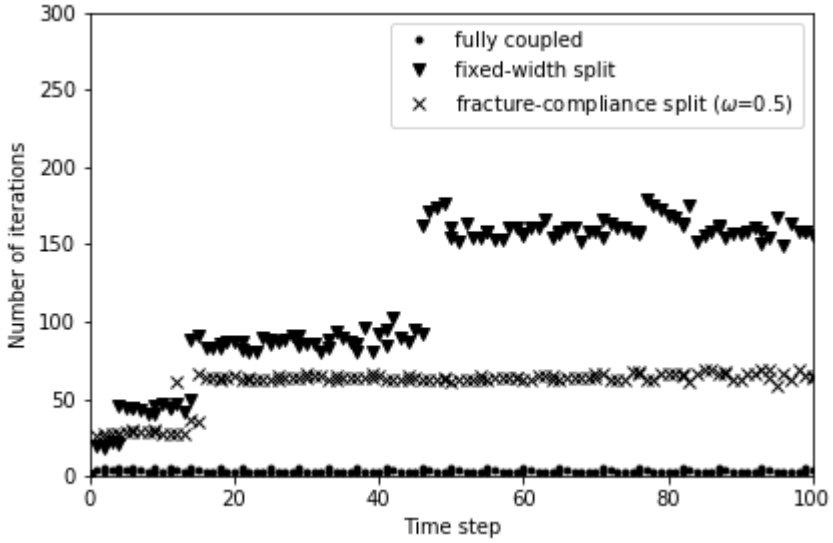

Figure 4.15: The number of iterations for the fixed-width split, fracture-compliance split, and fully-coupled methods.

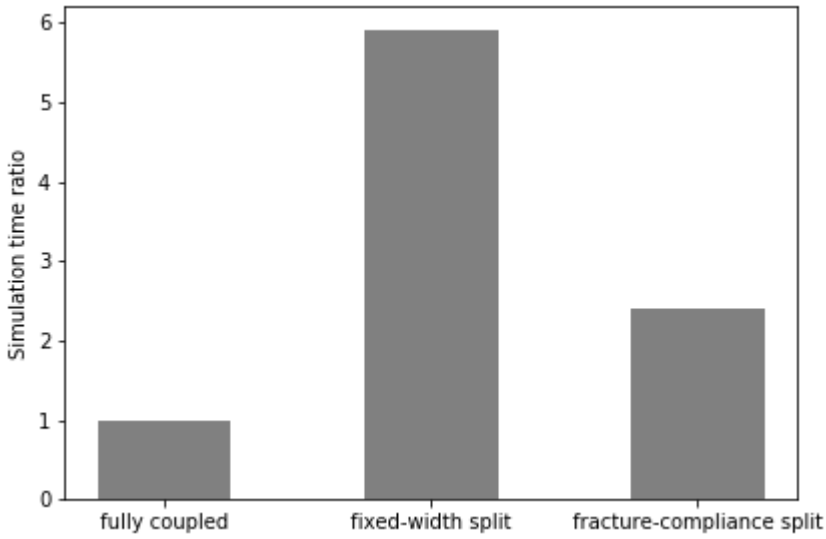

Figure 4.16: The ratio of simulation time for the fixed-width split, fracture-compliance split, and fully-coupled methods. The simulation time of the fully coupled method is taken as one.

constant viscosity. Fracture conductivity is approximated by using the classical lubrication theory. The fracturing model is verified through the comparison with the analytical solutions of a radial fracture growth. In addition, three solution strategies to solve the coupled system of equations are developed and tested. Those includes fixed-width split, fracture-compliance split, and fully coupled method. The fixed-width and fracture-compliance splitting schemes are categorized as segregated methods since they iteratively solve the coupled system of equations. It is shown that the fully coupled method is the best in terms of convergence speed, numerical stability, and simulation time.

Chapter 5: Interaction Between Hydraulic and Natural Fractures

5.1 Introduction

The previous chapter focuses on modeling the hydraulic fracture propagation without intersection with other fractures. However, since natural fractures are major factors in oil and gas production from shale formations, modeling the interaction between hydraulic and natural fractures is essential for hydraulic fracturing simulations in shale reservoirs. This chapter describes the crossing criteria of hydraulic fractures against natural fractures and the remote failure of natural fractures caused by hydraulic fracture propagation.

A large number of experimental studies on the interaction between hydraulic and natural fractures have been reported (Blanton, 1982; Zhou et al., 2008; Gu et al., 2012; Cheng et al., 2015b; Guo et al., 2014; Lee et al., 2014; Fatahi et al., 2017), and several criteria for hydraulic and natural fracture intersection have been proposed to assess whether a hydraulic fracture cross a natural fracture (Blanton, 1982, 1986; Warpinski and Teufel, 1987; Renshaw and Pollard, 1995; Gu and Siebrits, 2008; Dahi-Taleghani and Olson, 2011). These criteria are formulated based on

- The Mohr-Coulomb failure criterion evaluated on natural fractures.
- Energy release rates at the intersection point of hydraulic and natural fractures.

The criteria are explained and compared with experimental results in this chapter.

Natural fractures not connected to hydraulic fractures can fail in shear mode due to an increase in stress and pore pressure induced by hydraulic fractures. While the

induced stress can be computed easily by using DDM, the evaluation of pore pressure using DDM requires the fundamental solution of the poroelastic equation (Carvalho and Curran, 1998; Zhou and Ghassemi, 2009), which is significantly more complicated than the Navier-Cauchy equation. We will show that the pore pressure increase can be easily evaluated in DDM by assuming an undrained condition.

5.2 Crossing Criteria

5.2.1 Crossing Criteria Based on the Mohr-Coulomb Failure Criterion

When a hydraulic fracture intersects a natural fracture, the hydraulic fracture will either cross or be deflected. This conditions under which the hydraulic fracture crosses the natural fracture can be expressed by the Mohr-Coulomb failure criterion. Namely, the hydraulic fracture is deflected into the natural fracture if the normal or tangential stresses acting on the natural fracture exceeds its critical value

$$\sigma_{\mathrm{n}} \geq T_0, \tag{5.1}$$

$$|\sigma_{\mathrm{t}}| \geq \sigma_{\mathrm{tc}} \coloneqq S_0 - C(\sigma_{\mathrm{n}} + p), \tag{5.2}$$

where T_0 is tensile strength, S_0 is shear strength, C is the frictional coefficient, p is pore pressure, and σ_{t} and σ_{n} are shear and normal stresses on the natural fracture, respectively. Tension-positive sign convention is used here. If either of the above equations does not hold, the hydraulic fracture turns into the direction of the natural fracture.

Consider a hydraulic fracture intersecting a natural fracture as shown in Fig. 5.1. The normal and tangential stresses on the natural fracture can be calculated by

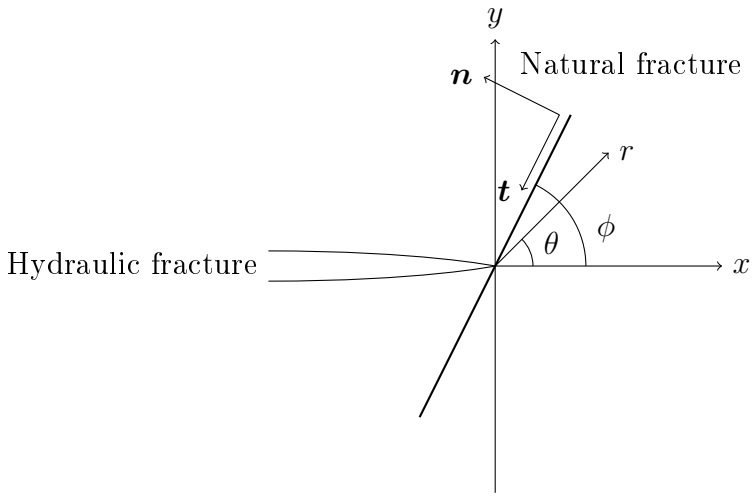

Figure 5.1: A hydraulic fracture intersecting a natural fracture at an angle ϕ. Cylindrical coordinates are shown as r and θ. $\boldsymbol{n}$ and $\boldsymbol{t}$ are the unit normal and tangential vectors of the natural fracture, respectively.

(Jaeger et al., 2007)

$$\sigma_{\mathrm{n}} = \frac{1}{2}(\sigma_{xx} + \sigma_{yy}) - \frac{1}{2}(\sigma_{xx} - \sigma_{yy})\cos 2\phi - \sigma_{xy}\sin 2\phi, \tag{5.3}$$

$$\sigma_{\mathrm{t}} = \frac{1}{2}(\sigma_{xx} - \sigma_{yy})\sin 2\phi - \sigma_{xy}\cos 2\phi, \tag{5.4}$$

where σ_{ij} is the stress tensor on the natural fracture. The normal and tangential directions are defined in Fig. 5.1.

Blanton (1982, 1986) and Warpinski and Teufel (1987) evaluated the normal and shear stresses from farfield stress

$$\sigma_{ij}(r, \theta) = \sigma_{0ij}, \tag{5.5}$$

where σ_{0ij} is the farfield stress tensor. On the other hand, Renshaw and Pollard (1995) incorporated the stress induced by the hydraulic fracture in the case of orthogonal intersections. Gu and Weng (2010) extended Renshaw and Pollard's model

to non-orthogonal cases, and the validity of their criterion is checked with laboratory experiments in Gu et al. (2012). In the model, the stress tensor on the natural fracture is evaluated from the asymptotic stress solution around the tip of a semi-infinite crack (Zehnder, 2012)

$$\sigma_{ij}(r,\theta) = \sigma_{0ij} + \frac{K_{\mathrm{I}}}{\sqrt{2\pi r}} f_{ij}(\theta) + \frac{K_{\mathrm{II}}}{\sqrt{2\pi r}} g_{ij}(\theta), \tag{5.6}$$

where K_{I} and K_{II} are mode I and II stress intensity factors (SIFs), respectively. r and θ are the cylindrical coordinates around the crack tip shown in Fig. 5.1. f_{ij} and g_{ij} are given by

$$\begin{bmatrix} f_{xx} \\ f_{yy} \\ f_{xy} \end{bmatrix} = \begin{bmatrix} \cos\frac{\theta}{2}\left(1 - \sin\frac{\theta}{2}\sin\frac{3\theta}{2}\right) \\ \cos\frac{\theta}{2}\left(1 + \sin\frac{\theta}{2}\sin\frac{3\theta}{2}\right) \\ \sin\frac{\theta}{2}\cos\frac{\theta}{2}\cos\frac{3\theta}{2} \end{bmatrix}, \tag{5.7}$$

$$\begin{bmatrix} g_{xx} \\ g_{yy} \\ g_{xy} \end{bmatrix} = \begin{bmatrix} \sin\frac{\theta}{2}\left(-2 - \cos\frac{\theta}{2}\cos\frac{3\theta}{2}\right) \\ \sin\frac{\theta}{2}\cos\frac{\theta}{2}\cos\frac{3\theta}{2} \\ \cos\frac{\theta}{2}\left(1 - \sin\frac{\theta}{2}\sin\frac{3\theta}{2}\right) \end{bmatrix}. \tag{5.8}$$

The stress tensor is evaluated at $(r,\theta) = (r_{\mathrm{c}},\phi)$, where r_{c} is a critical radius, and ϕ is the orientation of the natural fracture. r_{c} represents the fracture process zone around the crack tip.

Renshaw and Pollard (1995) assume discontinuous propagation across natural fractures. That is, a hydraulic fracture crosses a natural fracture through reinitiation of a small fracture in the opposite side of the natural fracture. Then, the critical

radius is estimated from

$$\sigma_{yy}\left(r_{\mathrm{c}}, \phi\right) = T_{0,\mathrm{rock}}, \tag{5.9}$$

where the subscript rock denotes the parameter of the rock. Gu and Weng (2010) computed the radius from

$$\sigma_1(r_{\mathrm{c}}, \phi) = T_{0,\mathrm{rock}}, \tag{5.10}$$

where σ_1 is the maximum principle stress. Rearranging the above equation, a quadratic function of r_{c} is obtained.

In this dissertation, we assume continuous propagation across natural fractures, and the critical radius is treated as an input parameter specific to each material to avoid the complicated computation of the critical radius in Eq. 5.10. If failure on natural fracture faces is detected, we let the hydraulic fracture turn along the natural fracture. Fig. 5.2 shows a flowchart of the fracture propagation algorithm using the MC crossing criterion combined with the maximum-stress criterion.

5.2.2 Crossing Criteria Based on Energy Release Rates

Dahi Taleghani (2009) and Dahi-Taleghani and Olson (2011) proposed a crossing criterion based on energy release rates to incorporate the effect of mechanical properties of cemented natural fractures. The criterion states that the hydraulic fracture propagates in the direction where the ratio of the energy release rate $\mathscr{G}$ to its critical value $\mathscr{G}_{\mathrm{c}}$ is at the maximum. Because of the presence of the natural fracture, not only $\mathscr{G}$ but also $\mathscr{G}_{\mathrm{c}}$ is a function of the direction θ.

Let us assume that the inclusion of the natural fracture does not affect the stress field around the hydraulic fracture because of the small width of the natural fracture. Under the assumption of small scale yielding, the energy release rate of the hydraulic

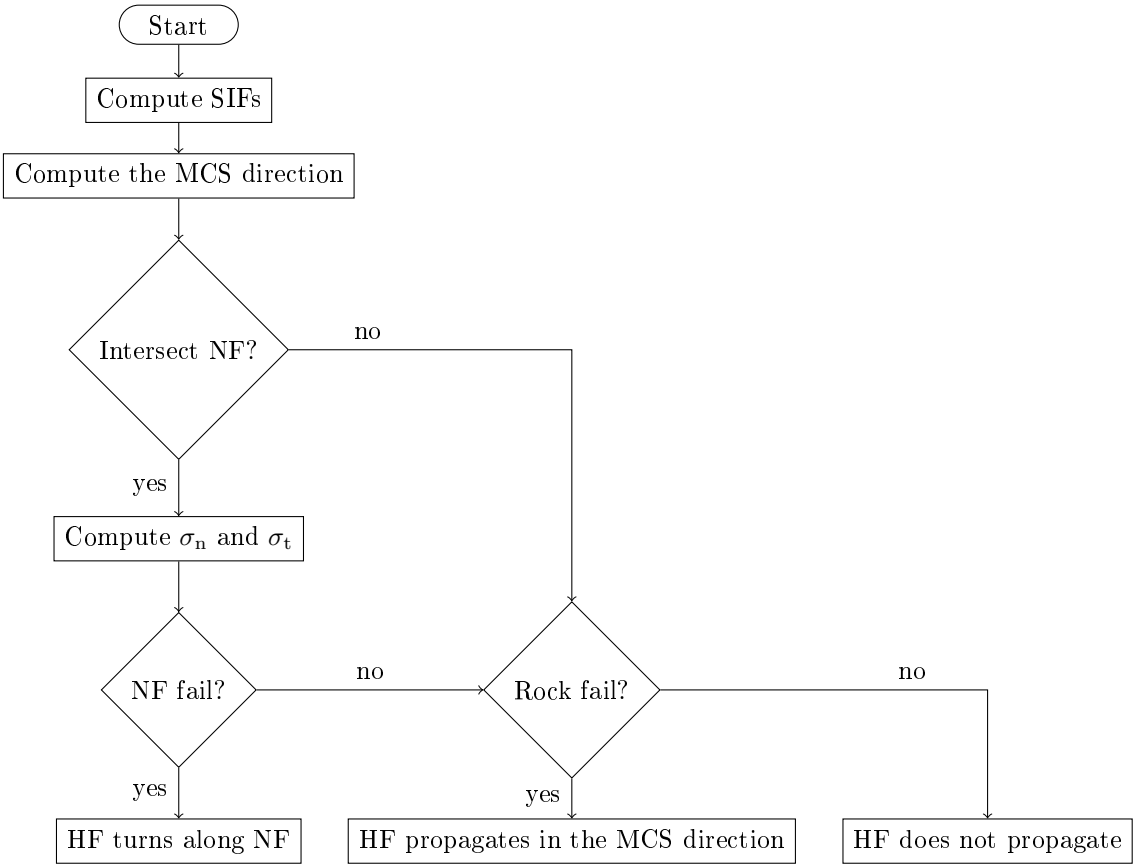

Figure 5.2: A flowchart of the fracture propagation algorithm based on the Mohr-Coulomb crossing criterion.

fracture shown in Fig. 5.1 can be expressed as

$$\mathscr{G}(\theta) = \frac{\bar{K}_{\mathrm{I}}(\theta)}{E'(\theta)} + \frac{\bar{K}_{\mathrm{II}}(\theta)}{E'(\theta)}, \tag{5.11}$$

where E' is the plain strain Young's modulus, and $\bar{K}_{\mathrm{I}}$ and $\bar{K}_{\mathrm{II}}$ are mode I and II stress intensity factors in the direction of θ. E' is given by

$$E'(\theta) = \begin{cases} E'_{\mathrm{rock}}, & \theta \neq \phi, \\ E'_{\mathrm{NF}}, & \theta = \phi. \end{cases} \tag{5.12}$$

$\bar{K}_{\mathrm{I}}$ and $\bar{K}_{\mathrm{II}}$ can be expressed as (Nuismer, 1975)

$$\bar{K}_{\mathrm{I}}(\theta) = \frac{1}{2}\cos\frac{\theta}{2}\left[K_{\mathrm{I}}(1+\cos\theta) - 3K_{\mathrm{II}}\sin\theta\right], \tag{5.13}$$

$$\bar{K}_{\mathrm{II}}(\theta) = \frac{1}{2}\cos\frac{\theta}{2}\left[K_{\mathrm{I}}\sin\theta + K_{\mathrm{II}}(3\cos\theta - 1)\right]. \tag{5.14}$$

The critical energy release rate can be calculated by

$$\mathscr{G}_{\mathrm{c}}(\theta) = \frac{K_{\mathrm{Ic}}(\theta)}{E'(\theta)} + \frac{K_{\mathrm{IIc}}(\theta)}{E'(\theta)}, \tag{5.15}$$

where

$$K_{ic}(\theta) = \begin{cases} K_{ic,\mathrm{rock}}, & \theta \neq \phi, \\ K_{ic,\mathrm{NF}}, & \theta = \phi, \end{cases} \tag{5.16}$$

where $i = \mathrm{I}$ or II, and K_{ic} is the mode-i critical SIF.

If there is no natural fracture, we assume that the hydraulic fracture will propagate in the maximum circumferential stress direction θ_0, which can be computed from

Eq. 4.11. Consequently, the hydraulic fracture will cross the natural fracture when $\mathscr{G}(\theta_0)/\mathscr{G}_{\mathrm{c,rock}} > \mathscr{G}(\phi)/\mathscr{G}_{\mathrm{c,NF}}$ and will be deflected otherwise.

5.2.3 Crossing Criteria Based on Stress Intensity Factors

Similar to the criteria based on energy release rates, the crossing criteria based on SIFs can be developed. The hydraulic fracture propagates in the direction where the ratio of $\bar{K}_{\mathrm{I}}$ to K_{Ic} is at the maximum. $\bar{K}_{\mathrm{I}}$ and K_{Ic} are the function of θ as shown in the previous section. The hydraulic fracture will cross the natural fracture when $\bar{K}_{\mathrm{I}}(\theta_0)/K_{\mathrm{Ic,rock}} > \bar{K}_{\mathrm{I}}(\phi)/K_{\mathrm{Ic,NF}}$ and will be deflected otherwise.

5.2.4 Comparison of Crossing Criteria

The crossing criteria based on the Mohr-Coulomb, energy release rates, and SIFs are compared with experimental data presented in Zhou et al. (2008). We denote the crossing criteria based on the Mohr-Coulomb, energy release rates, and SIFs as MC, ERR, and SIF crossing criteria, respectively. 3D DDM is used for fracture mechanics. We assume fracture surface is always parallel to the z direction due to a large vertical stress. Table 5.1 shows the parameters used for the comparison.

Fig. 5.3 shows an example of the initial mesh. The hydraulic fracture is expressed as a notch whose length and height are respectively 15 cm and 25 cm, and the natural fracture is expressed as a plane of weakness whose length and height are respectively 30 cm and 25 cm. The hydraulic fracture is assumed to be confined in the height direction and grow only in the horizontal direction. The natural fracture is oriented from the maximum horizontal stress direction by 30°, 60°, or 90°. A fluid with the viscosity of 135 cP is injected into the hydraulic fracture from the origin at 1 cm^3/s. The hydraulic fracture will either cross or turn along the natural fracture according to the crossing criteria when it intersects the natural fracture, and it keeps propagating

Table 5.1: Parameters used to compare crossing criteria with experiments of Zhou et al. (2008).

Parameters		Unit	Value
Element size		cm	5
Orientation			30°, 60°, 90°
Max. horizontal stress		MPa	6, 8, 10, 13
Min. horizontal stress		MPa	3
Vertical stress		MPa	20
Rock	Shear modulus	GPa	3.415
	Poisson's ratio		0.23
	K_{Ic}	$\mathrm{MPa\,m^{1/2}}$	2.0
	Cohesion	MPa	0.5
	Pore pressure	MPa	0.0
	Leakoff coefficient		0.0
Natural Fracture	Shear modulus	GPa	3.415
	Poisson's ratio		0.23
	Friction coefficient		0.38
	K_{Ic}	$\mathrm{MPa\,m^{1/2}}$	0.5
	Tensile strength	MPa	0.5
	Cohesion	MPa	3.2
	Critical radius	cm	1.0
Fluid	Compressibility	MPa$^-$1	4.545×10^{-4}
	Viscosity	cP	135
	Reference pressure	MPa	10
	Reference density	$\mathrm{kg\,/\,m^3}$	1000
Injection rate		$\mathrm{cm^3\,/\,s}$	1.0
Injection time		s	50
Wellbore volume		$\mathrm{cm^3}$	10

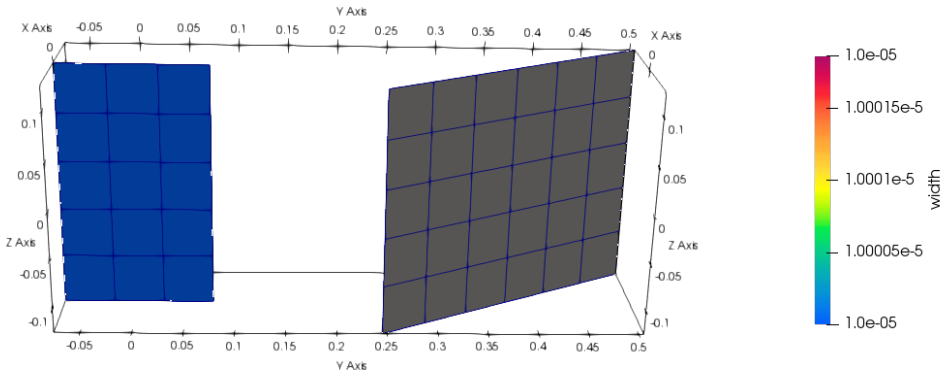

Figure 5.3: An example of the initial mesh of hydraulic fracturing simulations with an inclined natural fracture. The notch for the hydraulic fracture is 15 cm in length and 25 cm in height, and the natural fracture is 30 cm in length and 25 cm in height. The unit of the axes is m.

in the maximum horizontal stress direction after reaching the edge of the natural fracture.

Fig. 5.4 through Fig. 5.6 show the crossing behavior in the case of the SIF crossing criterion for different natural fracture orientations and horizontal stress contrasts. Since the SIF crossing criterion does not include the farfield stress in its formulation, the crossing behavior is not affected by the horizontal stress contrasts. After the hydraulic fracture is deflected along the natural fracture, it feels the maximum horizontal stress, resulting in the smaller width and length of the hydraulic fracture as the stress contrast increases.

Fig. 5.7 through Fig. 5.9 show the crossing behavior of the ERR crossing criterion for different natural fracture orientations and horizontal stress contrasts. Because the ERR crossing criterion does not take the farfield stress into account as well as the SIF crossing criterion, the stress contrast has no effect on the crossing behavior. The natural fracture is found to break more easily compared to the SIF crossing criterion

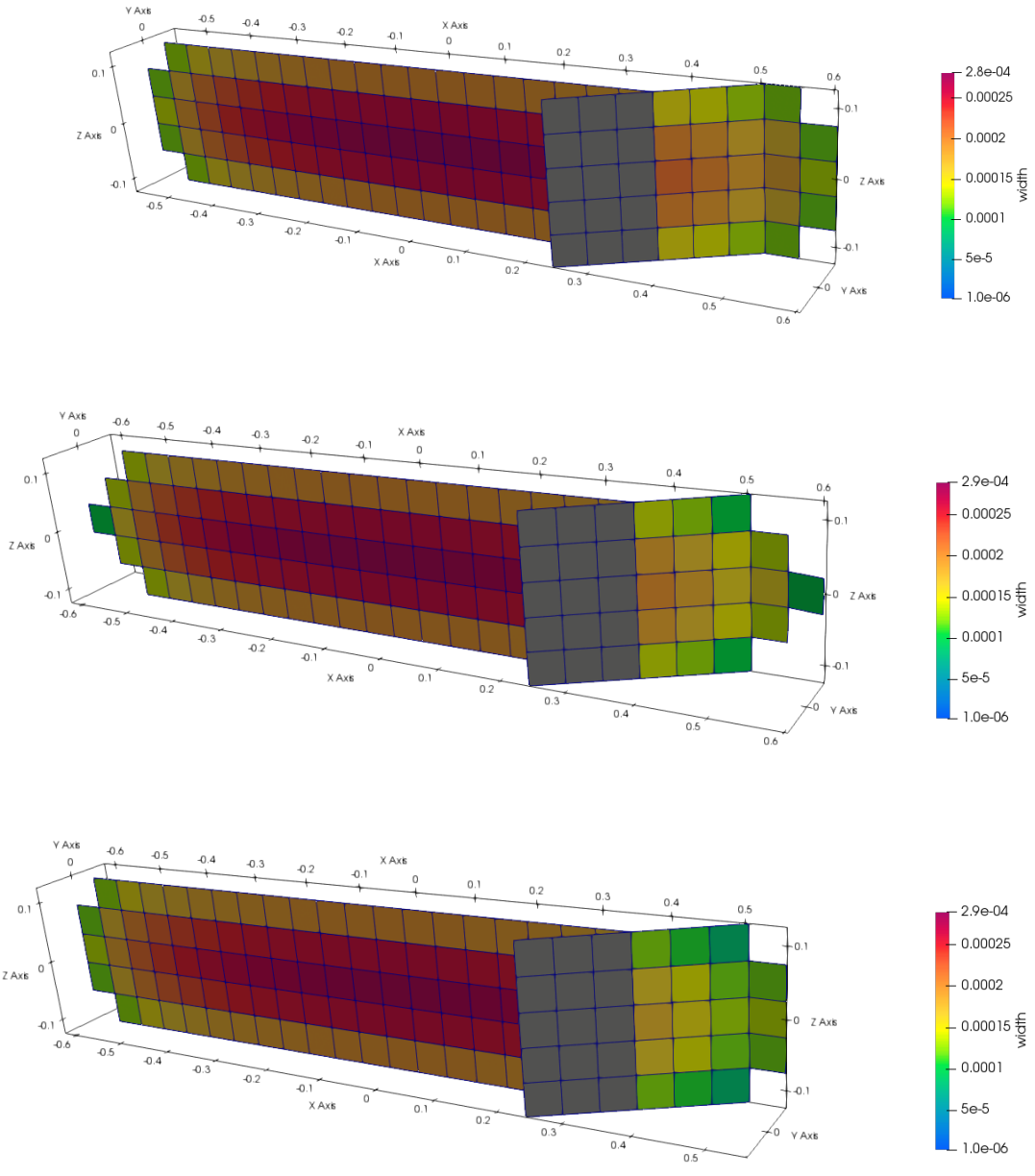

Figure 5.4: Fracture meshes after 60 s of fluid injection. The natural fracture is inclined by 30° from the x axis. The SIF-based criterion is used. The stress contrast between the maximum and minimum horizontal stresses are 3, 5, and 7 MPa from the top to bottom, respectively.

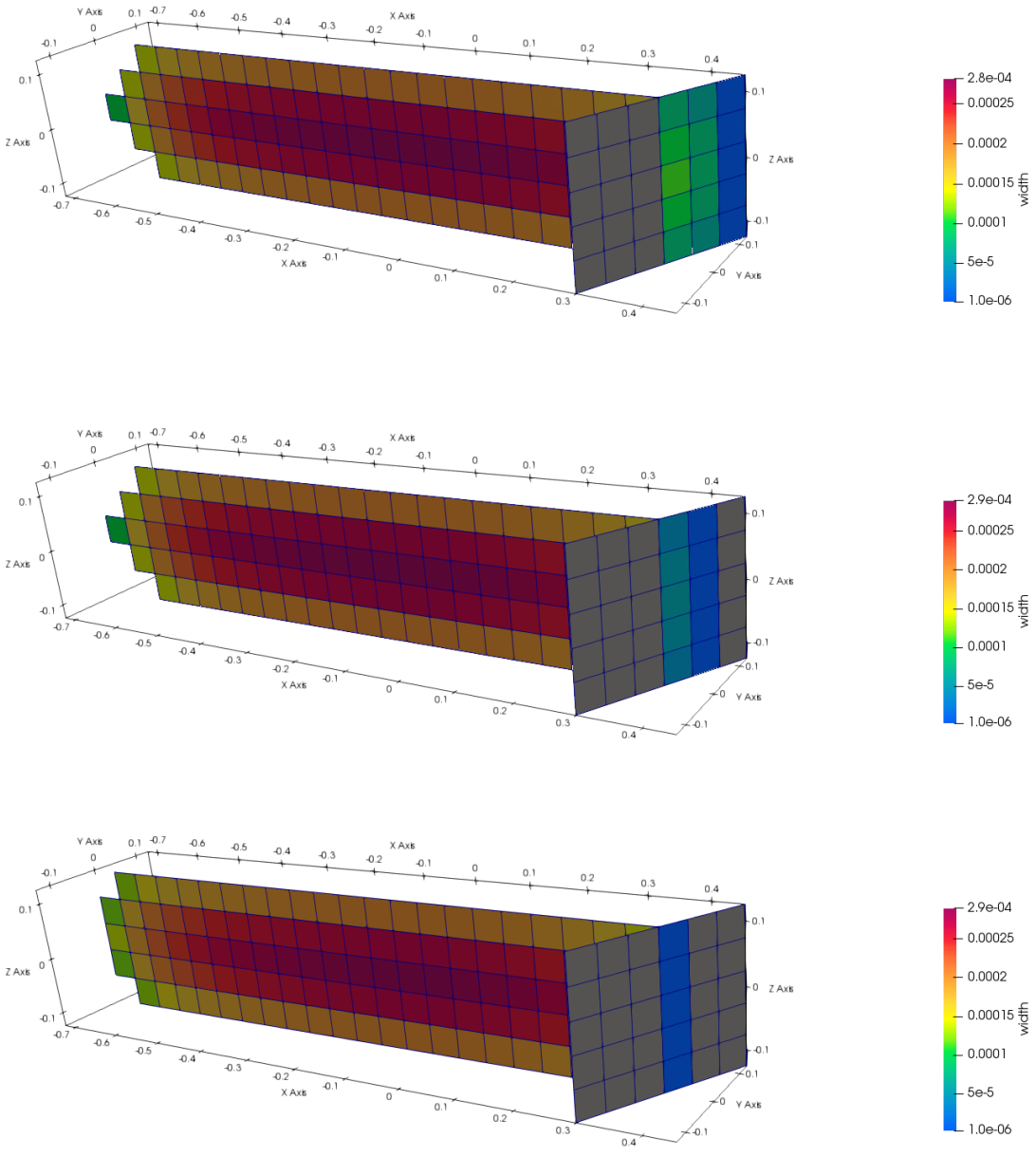

Figure 5.5: Fracture meshes after 60 s of fluid injection. The natural fracture is inclined by 60° from the x axis. The SIF-based criterion is used. The stress contrast between the maximum and minimum horizontal stresses are 3, 5, and 7 MPa from the top to bottom, respectively.

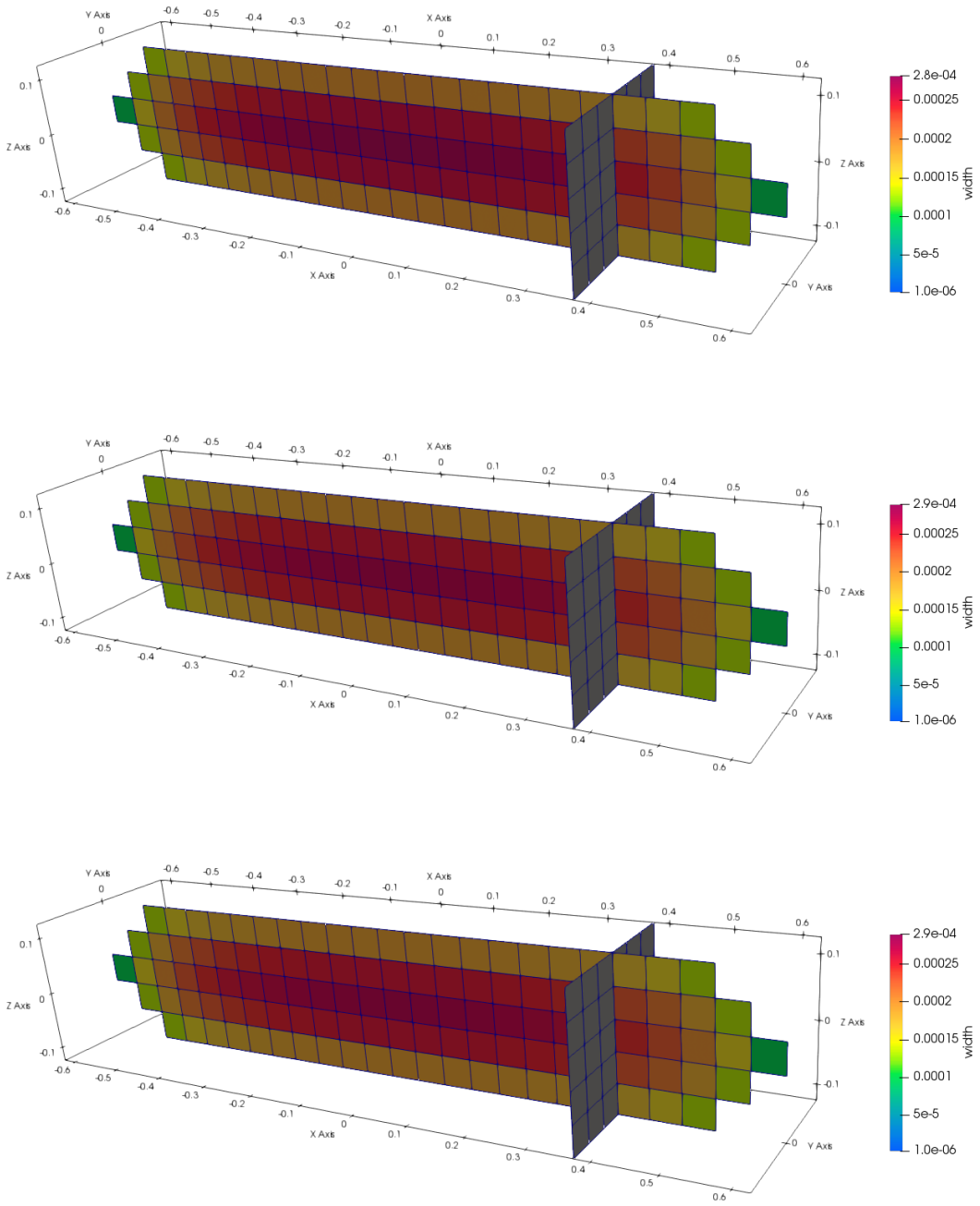

Figure 5.6: Fracture meshes after 60 s of fluid injection. The natural fracture is inclined by 90° from the x axis. The SIF-based criterion is used. The stress contrast between the maximum and minimum horizontal stresses are 3, 5, and 7 MPa from the top to bottom, respectively.

due to the contribution of the mode-II SIF, which comes from the large shear slip on the natural fracture faces as shown in Fig. 5.10.

Fig. 5.11 through Fig. 5.13 show the crossing behavior of the MC crossing criterion for different natural fracture orientations and horizontal stress contrasts. Tensile strength is 5 MPa, cohesion is 3.2 MPa, friction coefficient is 0.38, and critical radius is 5mm. Since the farfield stress is taken into account in the MC crossing criterion, the crossing behavior depends on the horizontal stress contrast. The cases with low horizontal stress contrasts show the deflected fracture propagation, while those with high stress contrasts show the hydraulic fracture crosses the natural fracture. These results agree with the experimental results of Zhou et al. (2008). It is found that the fracture propagation along the natural fracture after deflection is slower compared to the SIF and ERR crossing criteria.

The crossing behavior of the hydraulic fracture is summarized in Fig. 5.14 in terms of the orientation of the natural fracture and the stress difference between the maximum and minimum horizontal stresses. Among these three criteria, only the Mohr-Coulomb-based criterion exhibits the dependency on the farfield stress, which is consistent with experimental results.

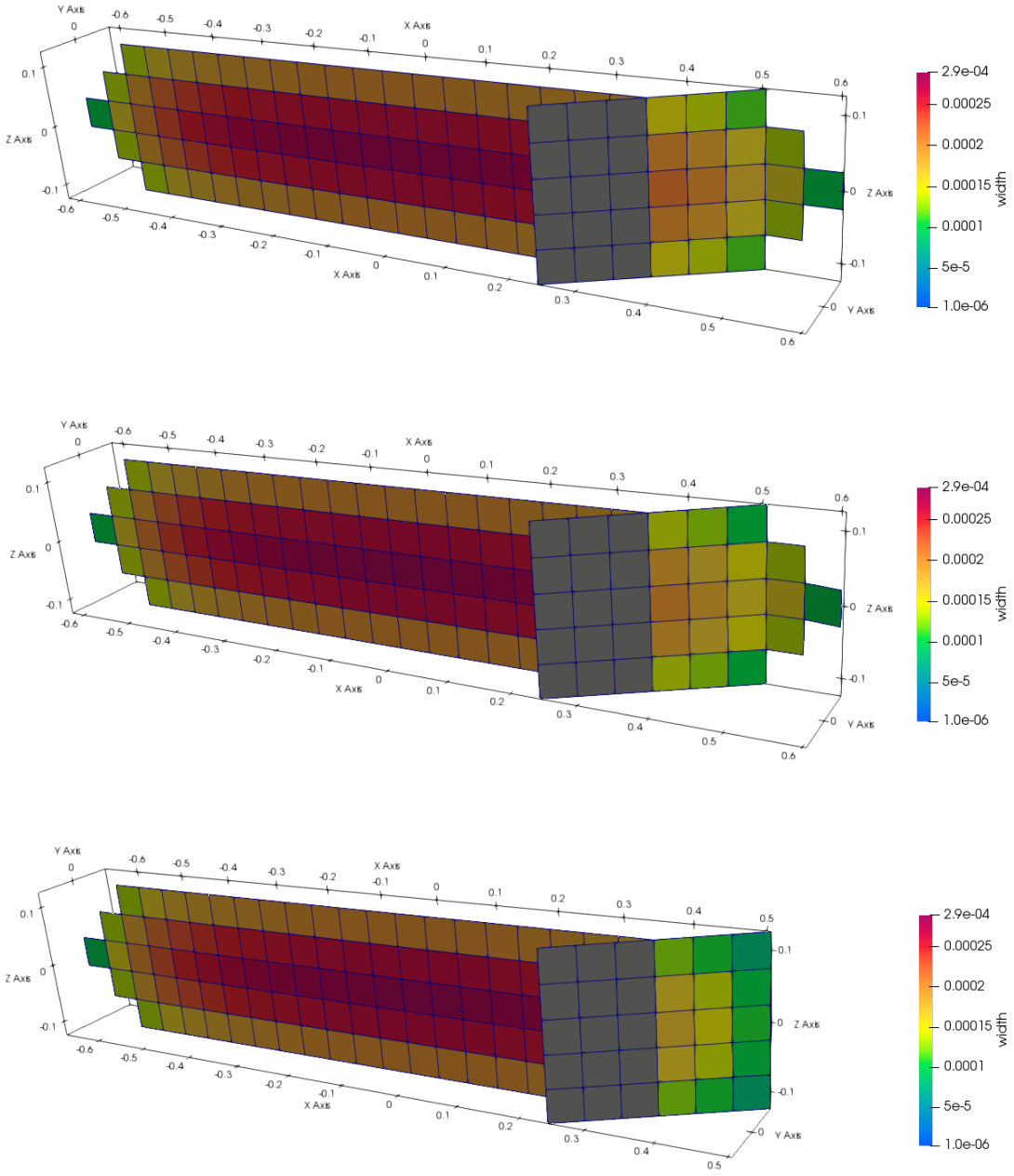

Figure 5.7: Fracture meshes after 60 s of fluid injection. The natural fracture is inclined by 30° from the x axis. The ERR-based criterion is used. The stress contrast between the maximum and minimum horizontal stresses are 3, 5, and 7 MPa from the top to bottom, respectively.

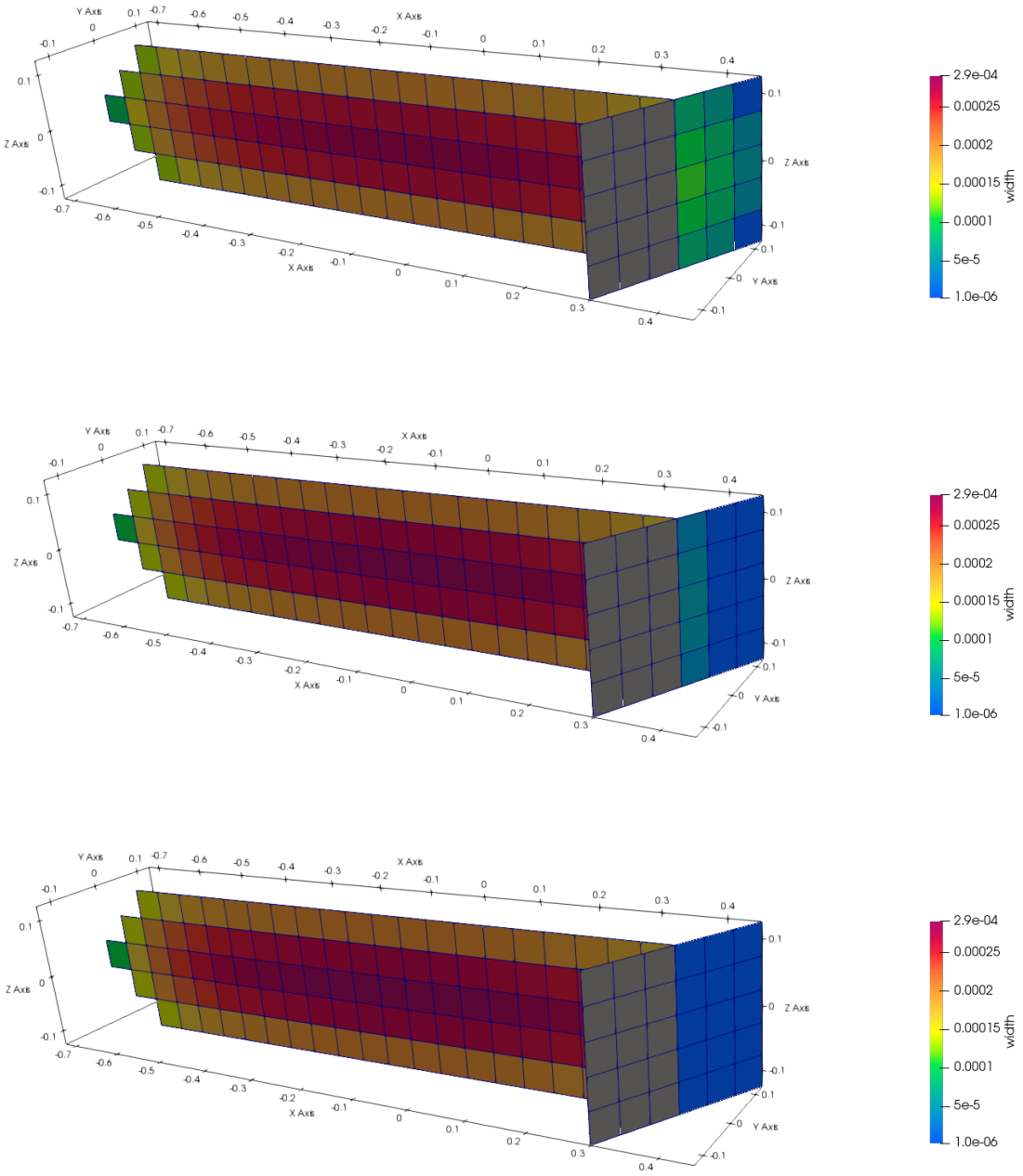

Figure 5.8: Fracture meshes after 60 s of fluid injection. The natural fracture is inclined by 60° from the x axis. The ERR-based criterion is used. The stress contrast between the maximum and minimum horizontal stresses are 3, 5, and 7 MPa from the top to bottom, respectively.

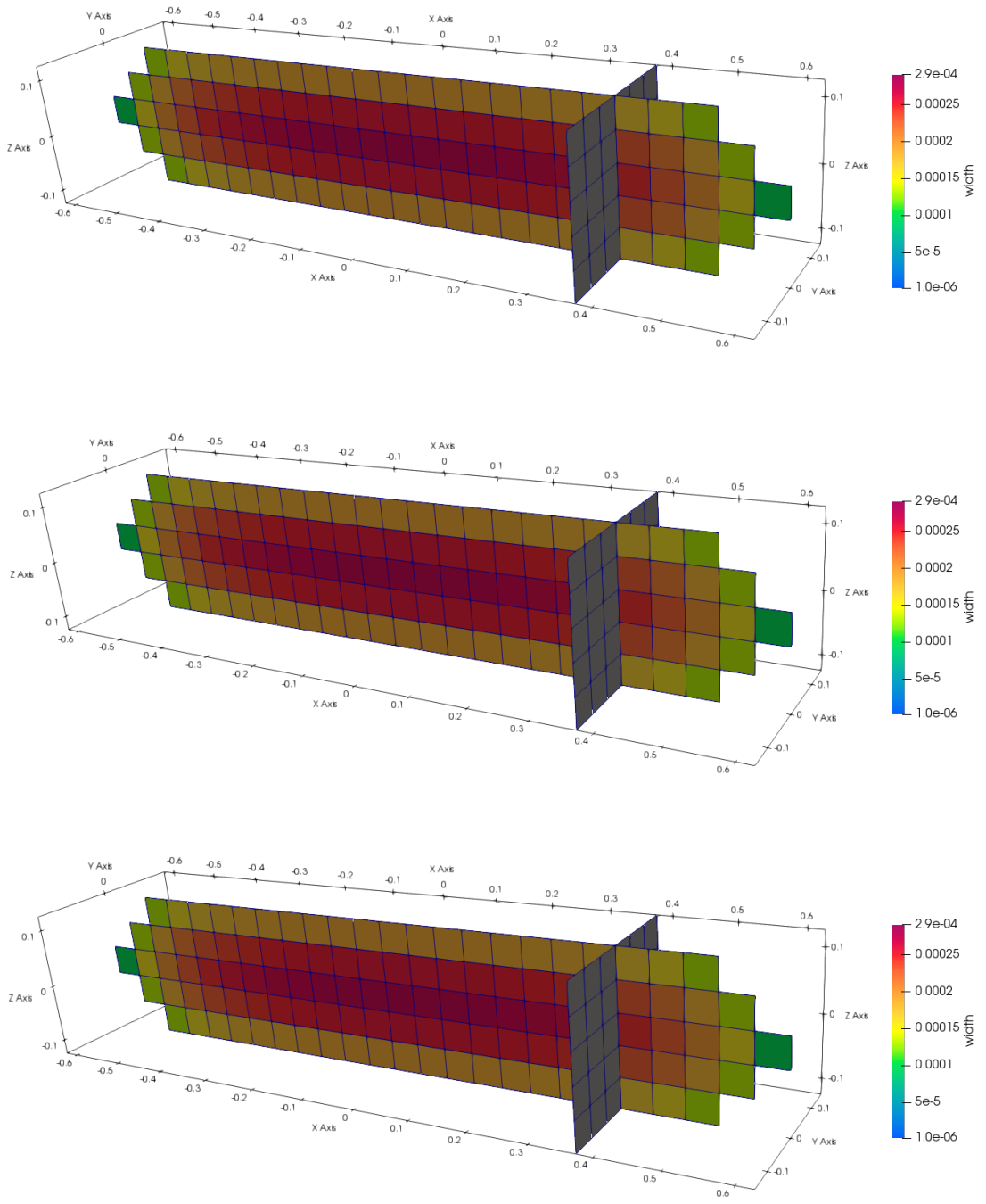

Figure 5.9: Fracture meshes after 60 s of fluid injection. The natural fracture is inclined by 90° from the x axis. The ERR-based criterion is used. The stress contrast between the maximum and minimum horizontal stresses are 3, 5, and 7 MPa from the top to bottom, respectively.

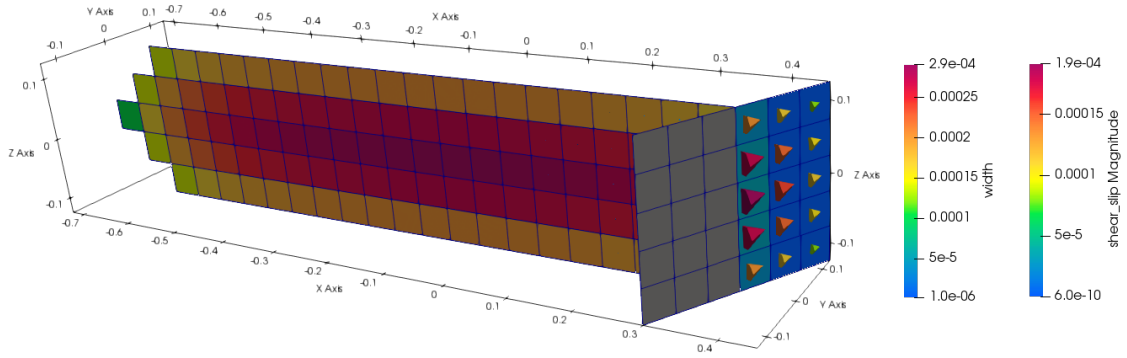

Figure 5.10: Fracture meshes after 60 s of fluid injection. The natural fracture is inclined by 60° from the x axis. The ERR-based criterion is used. The stress contrast between the maximum and minimum horizontal stresses is 5 MPa. The fracture width is presented as face colors, and the magnitude of shear slippage and its direction is described as cones with colors.

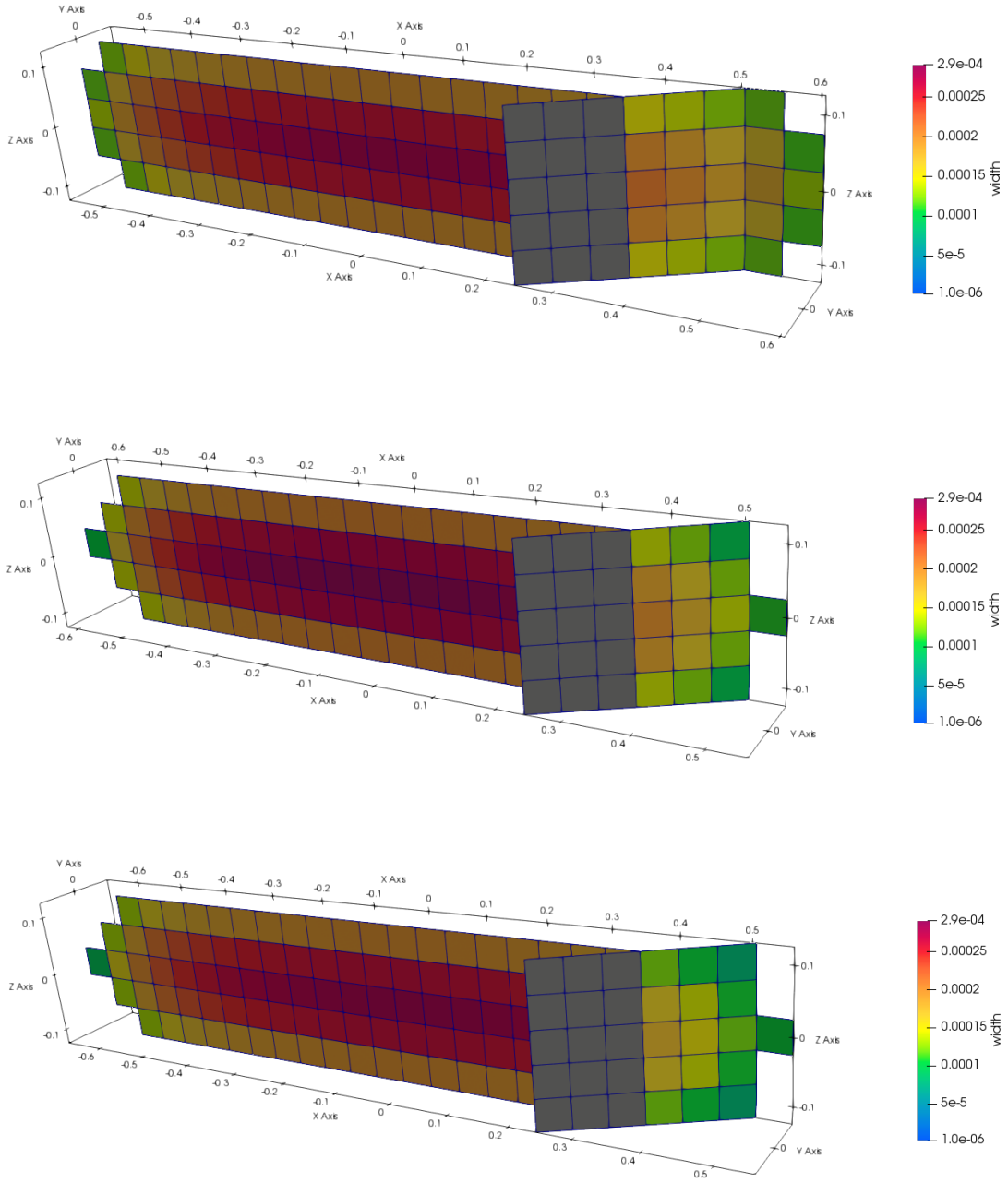

Figure 5.11: Fracture meshes after 60 s of fluid injection. The natural fracture is inclined by 30° from the x axis. The MC-based criterion is used. The stress contrast between the maximum and minimum horizontal stresses are 3, 5, and 7 MPa from the top to bottom, respectively.

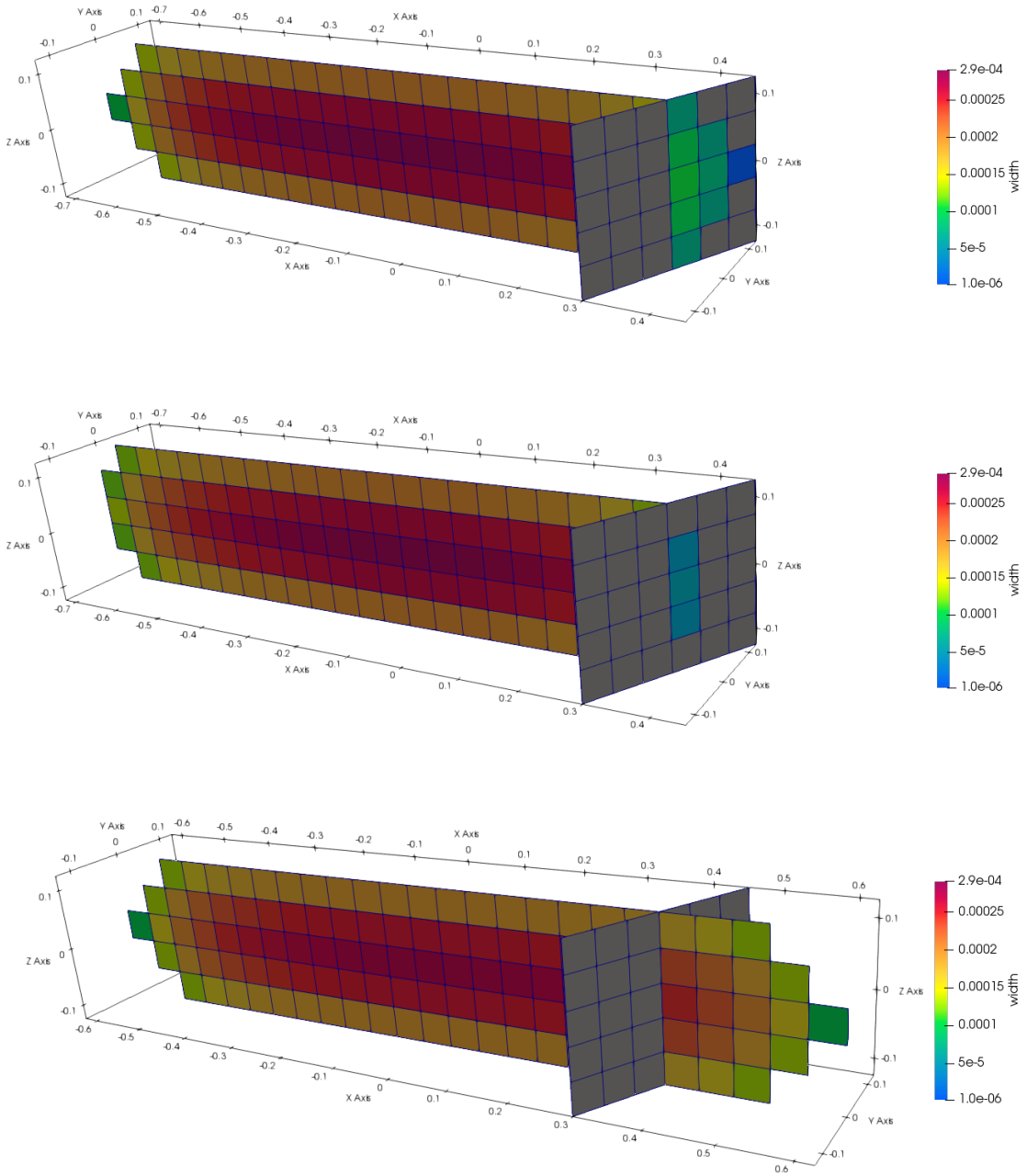

Figure 5.12: Fracture meshes after 60 s of fluid injection. The natural fracture is inclined by 60° from the x axis. The MC-based criterion is used. The stress contrast between the maximum and minimum horizontal stresses are 3, 5, and 7 MPa from the top to bottom, respectively.

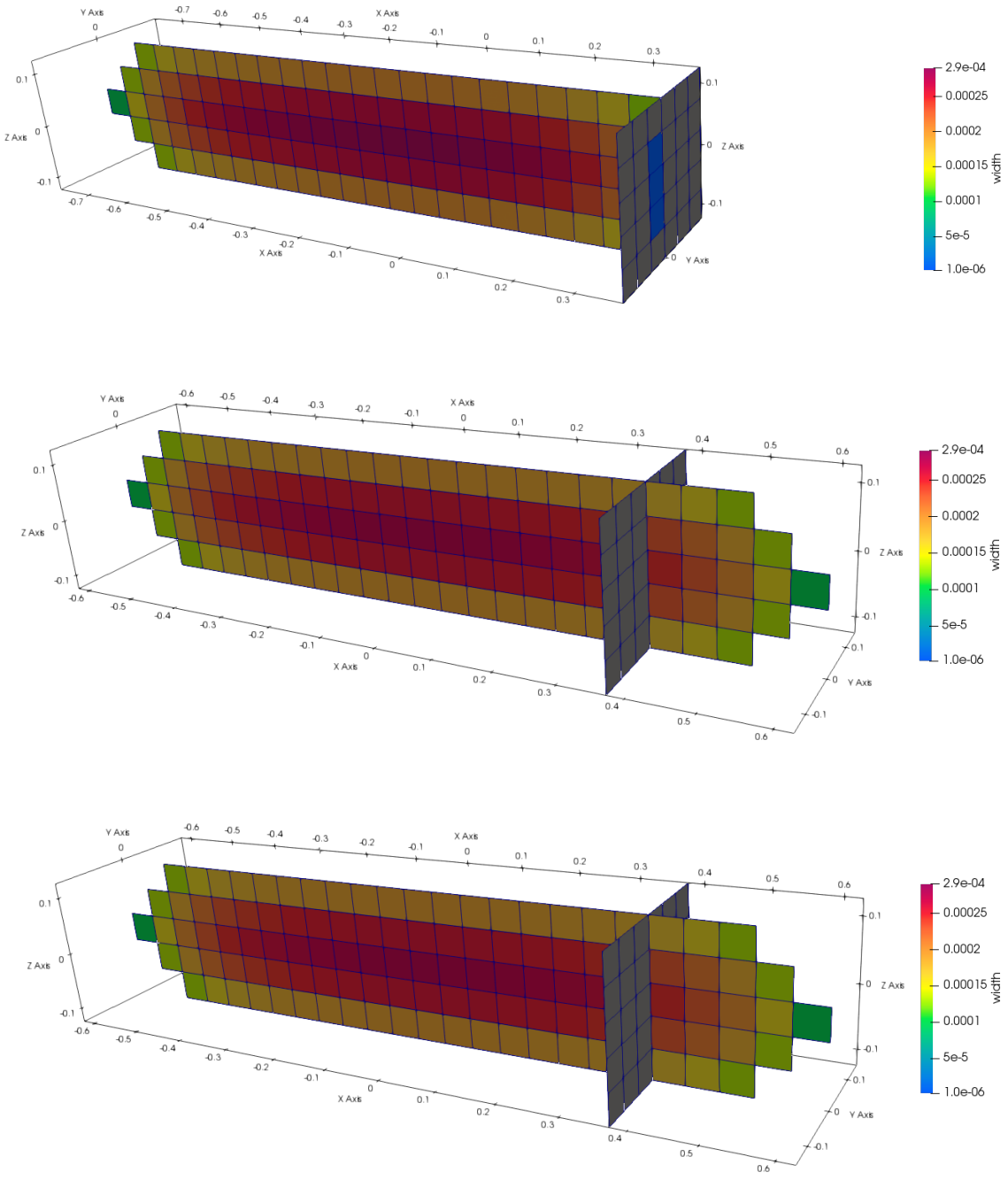

Figure 5.13: Fracture meshes after 60 s of fluid injection. The natural fracture is inclined by 90° from the x axis. The MC-based criterion is used. The stress contrast between the maximum and minimum horizontal stresses are 3, 5, and 7 MPa from the top to bottom, respectively.

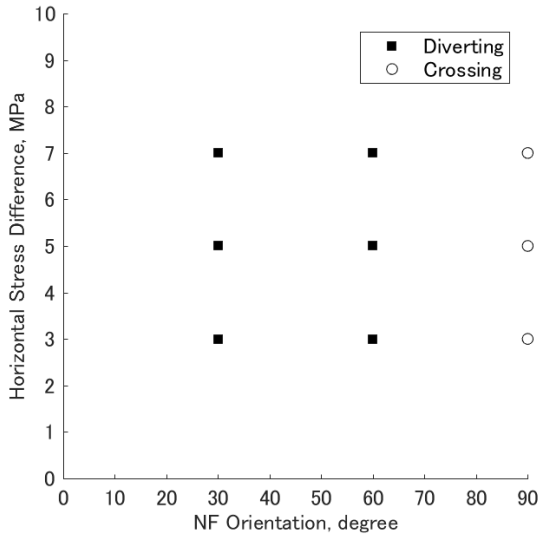

(a) SIF-based criterion

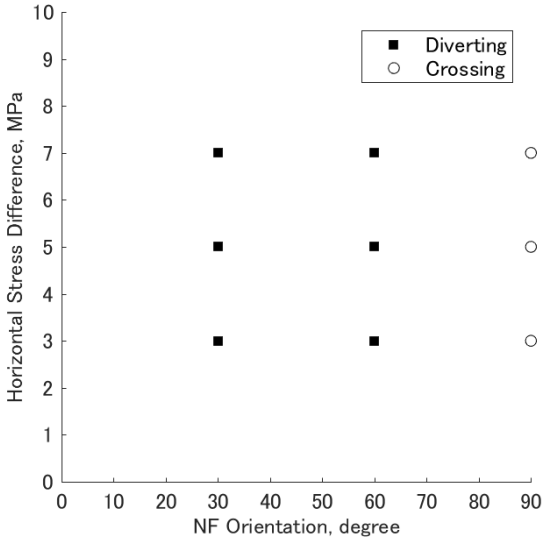

(b) ERR-based criterion

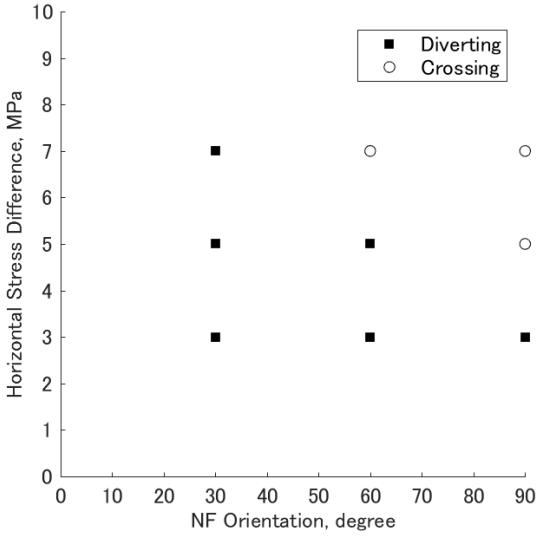

(c) MC-based criterion

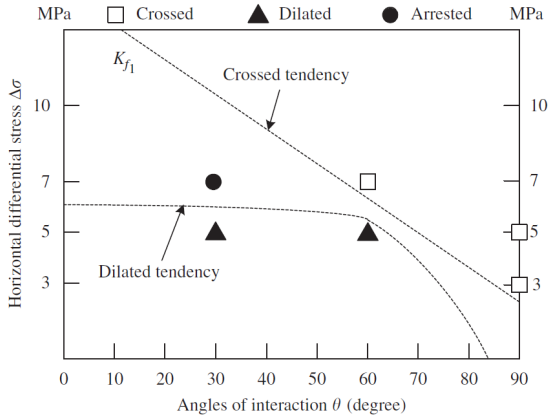

(d) Zhou et al. (2008)

Figure 5.14: The crossing behavior of the hydraulic fracture. The experimental results of Zhou et al. (2008) are presented as well.

5.3 Remote Failure Criteria

5.3.1 Incorporating Poroelastic Effects into DDM

Natural fractures not connected with hydraulic fractures will not fail in opening mode because shale formations are under compression due to the overburden stress. Instead, they can fail in shear mode due to induced stresses and pore pressure increase caused by hydraulic fractures. The Mohr-Coulomb criterion is used in this dissertation to check whether shear failure occurs on remote natural fractures. While the shear and normal stresses acting on natural fractures can be computed by using DDM, the change of pore pressure in natural fractures due to the fluid leak-off from hydraulic fractures cannot be calculated unless the fundamental solutions for poroelasticity is used (Ghassemi and Roegiers, 1996; Zhou and Ghassemi, 2009, 2011). However, we will show that the poroelasticity can be partially incorporated into the DDM by assuming an undrained condition.

Since shale has very low permeability, we can assume an undrained condition during hydraulic fracturing operations. In the undrained condition, the stress and pore pressure in rocks can be expressed by (Wang, 2000)

$$\sigma_{ij} - \sigma_{0ij} = 2G\epsilon_{ij} + \left(K_{\mathrm{u}} - \frac{2}{3}G\right)\epsilon_{kk}\delta_{ij}, \tag{5.17}$$

$$p - p_0 = -B(\sigma_{\mathrm{m}} - \sigma_{\mathrm{m0}}), \tag{5.18}$$

where G is the shear modulus, K_{u} is the undrained bulk modulus, ϵ_{ij} is the strain tensor, B is the Skempton's coefficient, σ_{m} is mean stress, σ_{m0} is the mean farfield stress, and p_0 is the initial pore pressure. The undrained bulk modulus can be expressed by

$$K_{\mathrm{u}} = K + \frac{\alpha^2 K_s K_f}{\phi K_s + (\alpha - \phi)K_f}, \tag{5.19}$$

where ϕ is porosity, α is the Biot coefficient, and K_s and K_f are the bulk modulus of solid and fluid, respectively. The Biot coefficient relates the bulk modulus of solid and rock:

$$\alpha = 1 - \frac{K}{K_s}, \tag{5.20}$$

where K is the bulk modulus of rock. Then, the Skempton's coefficient reads

$$B = \frac{K_{\mathrm{u}} - K}{\alpha K_{\mathrm{u}}}. \tag{5.21}$$

On the other hand, the stress in linear elasticity can be expressed as,

$$\sigma_{ij} - \sigma_{0ij} = 2G\epsilon_{ij} + \left(K - \frac{2}{3}G\right)\epsilon_{kk}\delta_{ij}. \tag{5.22}$$

Comparing Eq. 5.17 and Eq. 5.22, it is found that the constitutive equation does not alter its expression under the undrained condition except that the undrained elastic constants are used. It means that pore pressure change can be partially incorporated into DDM by using the undrained elastic constants.

Hereafter, we derive the influence coefficients for the mean stress. Using DDM, the stress at an internal point can be expressed as,

$$\sigma_{ij}(x) = \sigma_{0ij} + \sum_{\beta=1}^{N_c}\sum_{\alpha=1}^{M} S_{ijk}^{\alpha\beta}(x)\Delta u_k^{\alpha\beta}, \tag{5.23}$$

where S_{ijk} is the influence coefficients for stress in the global coordinate system, M is the number of nodes per element, and N_c is the number of elements. The mean stress σ_{m} is thus given by

$$\sigma_{\mathrm{m}}(x) = \sigma_{\mathrm{m}0} + \sum_{\beta=1}^{N_c}\sum_{\alpha=1}^{M} S_{\mathrm{m}k}^{\alpha\beta}(x)\Delta u_k^{\alpha\beta}, \tag{5.24}$$

where $S_{\mathrm{m}k}$ is the influence coefficients for mean stress given by

$$S_{\mathrm{m}k} = \begin{cases} \dfrac{S_{11k} + S_{33k}}{2}, & \text{for 2D,} \\ \dfrac{S_{11k} + S_{22k} + S_{33k}}{3}, & \text{for 3D.} \end{cases} \tag{5.25}$$

In the local coordinate system, the influence coefficients can be expressed by

$$\tilde{S}_{\mathrm{m}k} = \begin{cases} \dfrac{\tilde{S}_{11k} + \tilde{S}_{33k}}{2}, & \text{for 2D,} \\ \dfrac{\tilde{S}_{11k} + \tilde{S}_{22k} + \tilde{S}_{33k}}{3}, & \text{for 3D,} \end{cases} \tag{5.26}$$

where the tilde denotes the local coordinate system, and $\tilde{S}_{ijk}$ is given by Eq. 2.59. Noting $g_{,kk} = 0$ in Eq. 2.59, the influence coefficients for mean stress in two dimensions become

$$\left[\tilde{S}_{\mathrm{m}k}\right] = 2G \begin{bmatrix} g_{,13} & g_{,33} \end{bmatrix}, \tag{5.27}$$

and, in three dimensions,

$$\left[\tilde{S}_{\mathrm{m}k}\right] = \frac{4G(1+\nu)}{3} \begin{bmatrix} g_{,13} & g_{,23} & g_{,33} \end{bmatrix}. \tag{5.28}$$

Noting that the influence coefficients for the mean stress constitutes a vector, the coordinate transformation to the global coordinates is given by

$$S_{\mathrm{m}i} = L_{ij} \tilde{S}_{\mathrm{m}j}, \tag{5.29}$$

where L_{ij} is the rotation matrix from the local to global coordinate system.

5.3.2 Validation

The mean stress field around a radial crack for non-poroelastic materials ($B = 0$) can be computed from the analytical solution developed by Sneddon (1946). The stress along the axis of symmetry, $r = 0$, in the cylindrical coordinates is given by (Sneddon, 1946; Manchanda, 2015)

$$\sigma_r = \sigma_\theta = \frac{p}{\pi}\left[(1+2\nu)\left(\frac{\zeta}{1+\zeta^2} - \tan^{-1}\frac{1}{\zeta}\right) + \frac{2\zeta}{(1+\zeta^2)^2}\right], \tag{5.30}$$

$$\sigma_z = \frac{2p}{\pi}\left[\frac{\zeta(\zeta^2-1)}{(1+\zeta^2)^2} - \tan^{-1}\frac{1}{\zeta}\right], \tag{5.31}$$

$$\sigma_{r\theta} = 0, \tag{5.32}$$

where $\zeta \coloneqq z/c$, c is the radius of the crack, and p is the internal pressure applied to the crack surface.

Fig. 5.15 shows the mean stress along the axis of symmetry, $r = 0$, of a radial crack. Tension positive sign convention is used. Analytical solution of Sneddon (1946) and numerical results of 3D DDM are plotted against ζ. Poisson's ratio is 0.25. It clearly shows the validity of the mean stress calculated by using 3D DDM.

5.3.3 Poroelastic Effects on Remote Failure of Natural Fractures

Hydraulic fracturing simulations are performed to analyze poroelastic effects on the remote failure of natural fractures under an undrained condition. A planar hydraulic fracture grows from the origin, and it is constrained in a formation of 22 m in height. The element size is 2 m. The rock and fluid properties used in the simulations are listed in Table 5.2.

Natural fractures are randomly distributed in a region of 50 m in x-axis and 100 m in y-axis at a fixed angle of 45° from the maximum horizontal stress direction (y-axis)

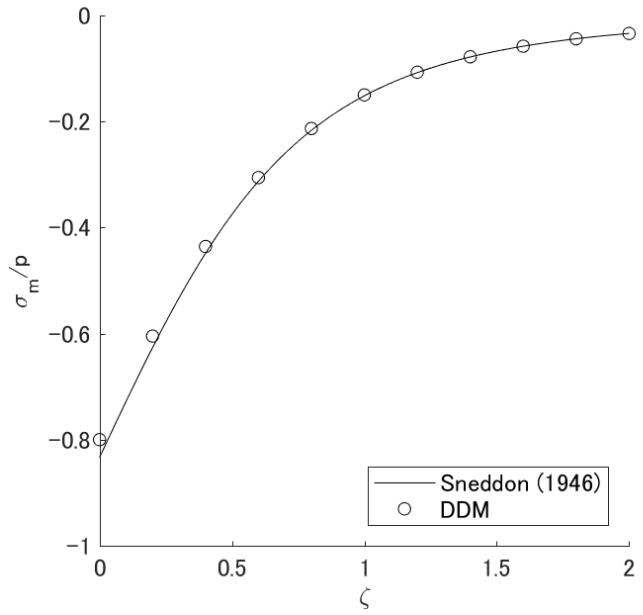

Figure 5.15: The mean stress along the z-axis of a radial crack. $\zeta := z/c$, c is the radius of the crack, and p is the internal pressure applied to the crack surface. Poisson's ratio is 0.25. Tension positive sign convention is used.

on the xy plane. The distance between hydraulic and natural fractures is 25 m at a maximum. The natural fractures are placed only on the $z = 0$ plane because the region of induced stresses created by the hydraulic fracture becomes the largest on that plane. In addition, the mechanical properties of natural fractures are set such that the natural fractures are close to a critical state (Zoback, 2007).

Fig. 5.16 through 5.18 show the distribution of failed natural fractures around the hydraulic fracture. Intact natural fractures are shown as wire frames. Fig. 5.16 does not include poroelastic effects, while Fig. 5.17 and 5.18 include poroelastic effects. Fig. 5.17 and 5.18 assume the reservoir fluids are oil and gas, respectively. The undrained bulk modulus and the Skempton's coefficient are calculated from the Biot coefficient, shear modulus, and the bulk modulus.

It is observed that the distance between failed natural fractures and the hydraulic

Table 5.2: The rock and fluid properties used in the simulation.

Parameters	Case 1	Case 2	Case 3
Poroelasticity	Off	On	On
Shear modulus		6.62 GPa	
Bulk modulus		11.03 GPa	
Biot coefficient	–	0.8	0.8
Reservoir fluid type	–	Oil	Gas
Fluid bulk modulus	–	2.2 GPa	30.0 MPa
Undrained bulk modulus	–	19.03 GPa	11.16 GPa
Undrained Poisson's ratio	–	0.3441	0.2524
Skempton's coefficient	0	0.5255	0.01456
Initial pore pressure		30.20 MPa	
Fracturing fluid viscosity		1 cp	
Fracturing fluid compressibility		4.545×10^{-4} 1/MPa	
Reservoir permeability		0 mD	
Reservoir porosity		0.15	
Maximum horizontal stress		39.44 MPa	
Minimum horizontal stress		35.85 MPa	
Vertical stress		45.00 MPa	
K_{Ic}		1.5 MPa $\mathrm{m}^{0.5}$	
Friction coefficient for NFs		0.25	
Cohesion of NFs		0 MPa	
Orientation of NFs from y-axis		45°	
Injection rate		0.01 m^3/s	
Wellbore volume		5 m^3	
Injection time		25 s	

fracture is not large for all of the three cases. These results indicate that the induced stresses created by the hydraulic fracture affect only a small distance from the hydraulic fracture, and poroelastic effects in the undrained condition are small. It is also found that reservoir fluids affect the magnitude of induced stresses caused by poroelastic effects. More natural fractures fail in the oil reservoir than in the gas reservoir as shown in Fig. 5.17 and Fig. 5.18. This can be explained by the larger Skempton's coefficient in the oil reservoir, which is the result of the larger bulk modulus of oil than that of gas.

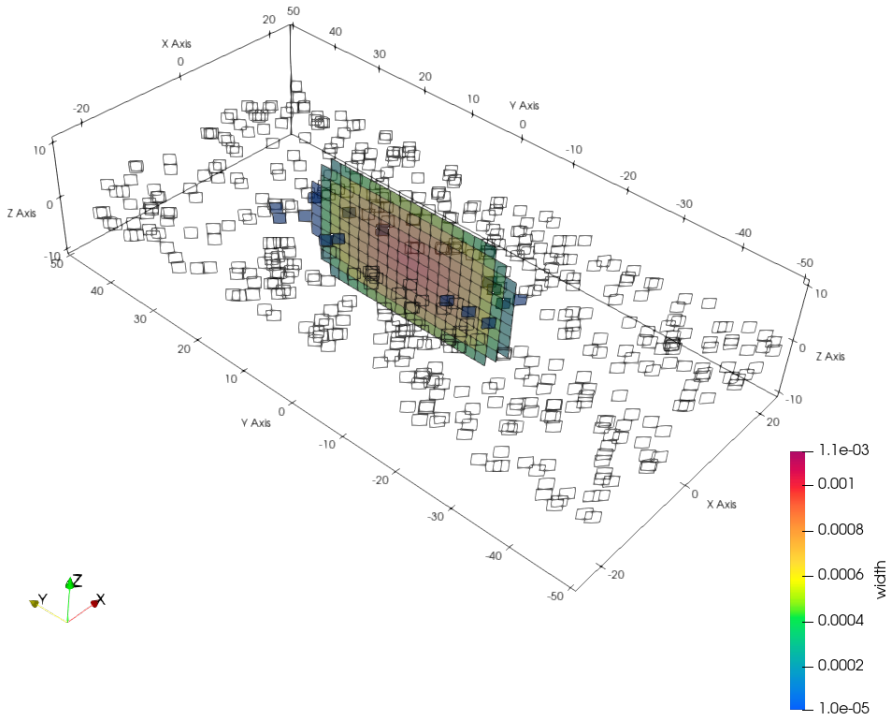

Figure 5.16: The simulation result of Case 1 (no poroelastic effect).

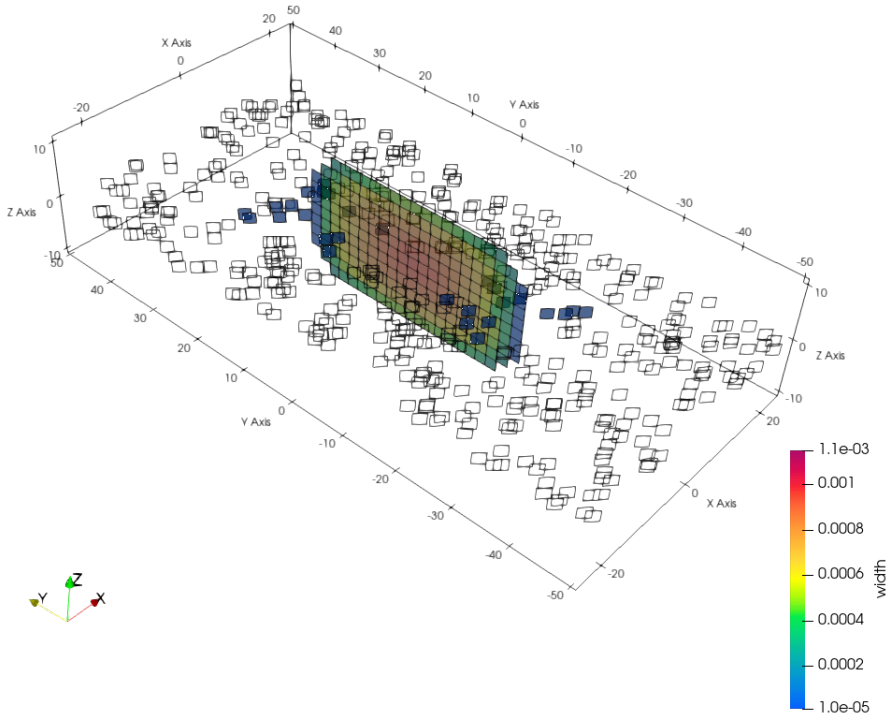

Figure 5.17: The simulation result of Case 2 (poroelastic effects for an oil reservoir).

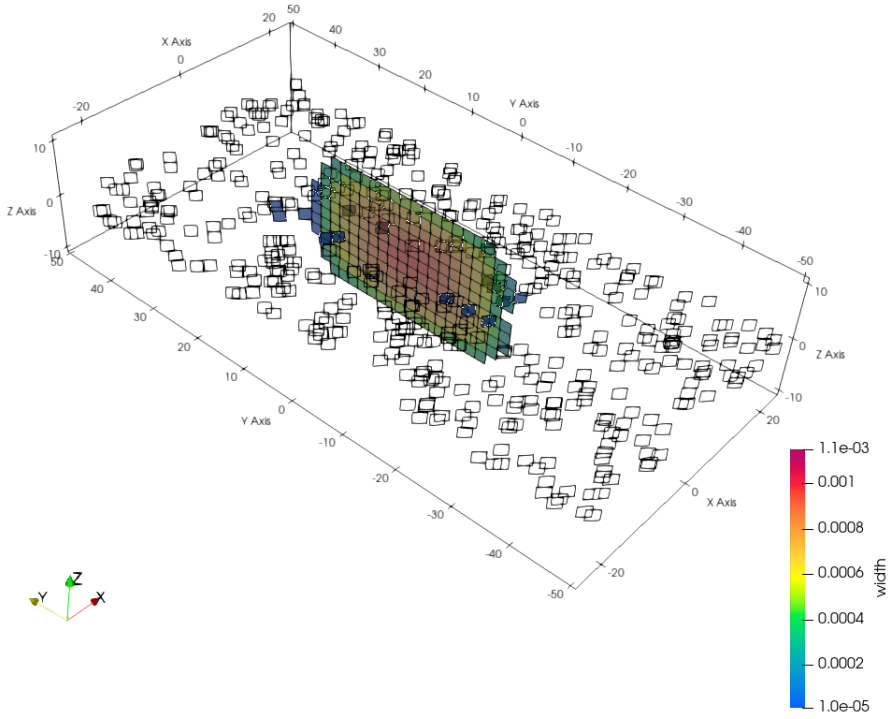

Figure 5.18: The simulation result of Case 3 (poroelastic effects for a gas reservoir).

5.4 Conclusion

The interaction of hydraulic and natural fractures is modeled. When a hydraulic fracture intersects a natural fracture, the crossing condition of the hydraulic fracture is described by using either stress intensity factors, energy release rates or the Mohr-Coulomb failure criterion. These intersection criteria are compared with the experimental results of Zhou et al. (2008), and it is shown that the crossing criterion based on the Mohr-Coulomb failure criterion can incorporate the effect of farfield stress and agrees with the experimental results.

The remote failure of natural fractures is modeled by using the Mohr-Coulomb failure criterion, and poroelasticity is incorporated into DDM by assuming an undrained condition to simulate the increase of pore pressure due to the propagation of hydraulic fractures. The pore pressure is related to the mean stress through the Skempton's

coefficient. The influence coefficients for mean stresses in DDM are derived and validated by comparing with the analytical solution of Sneddon (1946). It is found that poroelastic effects under the undrained condition on the remote failure of natural fractures are small. In addition, oil reservoirs exhibit larger poroelastic effects than the gas reservoirs in our simulations. The remote failure of natural fractures is limited to the vicinity of a growing hydraulic fracture even when poroelastic effects are partially incorporated.

Chapter 6: Hydraulic Fracturing Simulations in Naturally Fractured Rocks

6.1 Introduction

In Chapter 5, crossing criteria for intersections between hydraulic and natural fractures are described, and simulation results are compared with the experimental results of Zhou et al. (2008). In addition, poroelasticity is incorporated into DDM by assuming an undrained condition to evaluate remote failure of natural fractures.

Since natural fractures are one of the primary factors that control the fluid production rate from shale formations, it is essential to incorporate natural fractures as discrete fracture networks (DFNs) into hydraulic fracturing simulations. Although natural fractures are statistically distributed in many cases, they can sometimes be better described by using microseismic data. Our ultimate goal is to perform hydraulic fracturing simulations assisted by microseismic data as shown in Fig. 6.1.

This chapter describes hydraulic fracturing simulations with rocks that contain natural fracture networks. Natural fractures are distributed by using the power-law distribution for fracture length and the von Mises distribution for fracture orientation. Not only single mode distributions but also bimodal distributions are evaluated for fracture orientation. Fracture intersections in natural fracture networks are handled by simply correcting influence coefficients in the DDM matrix. Hydraulic fracturing simulations are performed, and the contribution of different properties of the natural fracture network are statistically evaluated.

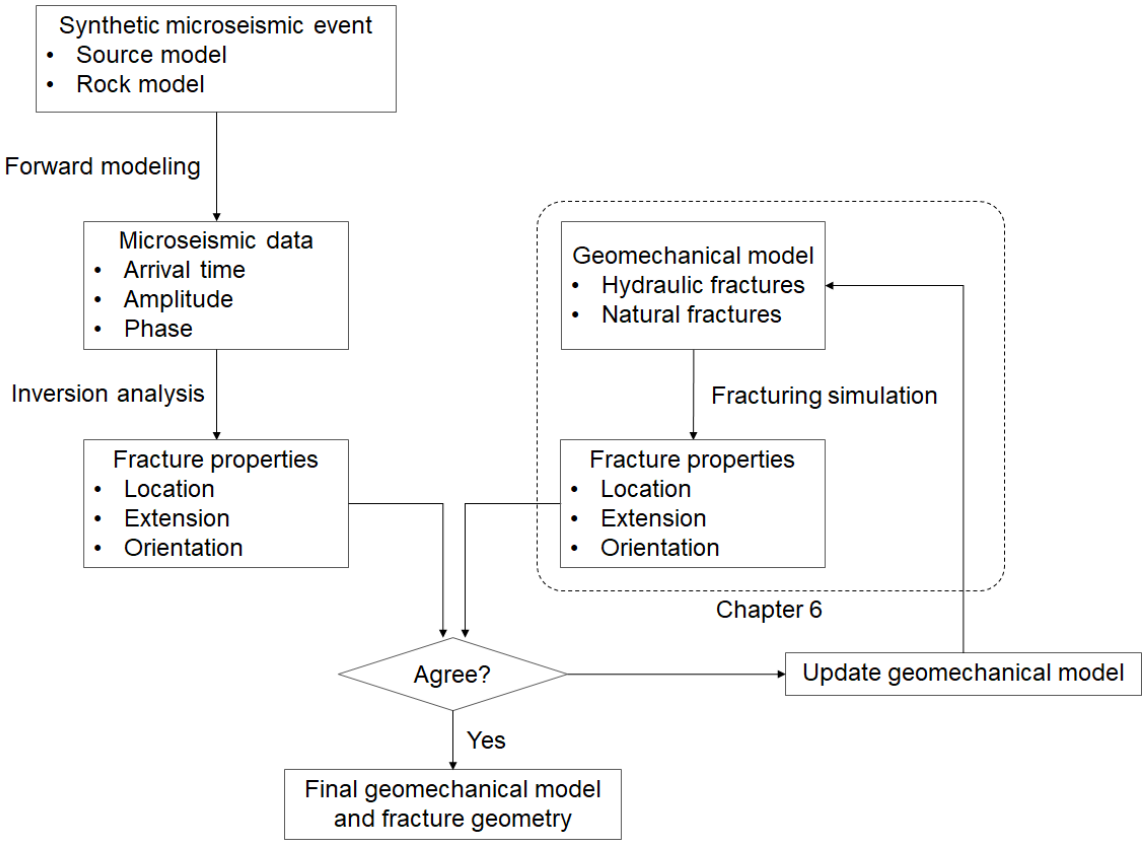

Figure 6.1: A flow chart of geomechanical simulations assisted by microseismic data.

6.2 Generation of Synthetic Natural Fractures

6.2.1 Natural Fracture Length Distribution

The statistical distribution of the length of natural fractures can be described by the power-law distribution (Davy, 1993)

$$f(l) = Al^{-a}, \quad a > 1, \tag{6.1}$$

where l is the length of the natural fractures, and A and a are constants. The cumulative distribution is given by

$$\begin{aligned} F(l) &= \int_{l_0}^{l} f(l')\,\mathrm{d}l' \\ &= \frac{A(l_0^{-b} - l^{-b})}{b}, \end{aligned} \tag{6.2}$$

where l_0 is the lower limit of the distribution, and $b \coloneqq a - 1$. Given the upper limit of the distribution l_1, from the condition of $F(l_1) = 1$, we have

$$A = \frac{b}{l_0^{-b} - l_1^{-b}}. \tag{6.3}$$

Thus, we obtain the following density and cumulative distribution functions for the power-law distribution

$$f(l) = \frac{bl^{-a}}{l_0^{-b} - l_1^{-b}}, \tag{6.4}$$

$$F(l) = \frac{l_0^{-b} - l^{-b}}{l_0^{-b} - l_1^{-b}}. \tag{6.5}$$

If the upper limit is taken to be infinity $l_1 \to \infty$, we have

$$f(l) = \frac{bl^{-a}}{l_0^{-b}}, \tag{6.6}$$

$$F(l) = \frac{l_0^{-b} - l^{-b}}{l_0^{-b}}. \tag{6.7}$$

Using the cumulative function, the power-law distribution of the fracture length can be generated.

Davy (1993) estimated the parameter a from the length distribution of the San Andreas fault, resulting in $a = 2.1$ for the density function and $a = 2.8$ for the cumulative function. Wu (2014) uses $a = 1$ to 3 for hydraulic fracturing simulations using a simplified DDM approach. Shrivastava et al. (2017) selected $a = 3$ to analyze the hydraulic fractures in the Hydraulic-Fracturing Test Site (HFTS) (Courtier et al., 2017; Ciezobka et al., 2018; Kumar et al., 2018; Maity and Ciezobka, 2019). Fig. 6.2 shows an example of fracture lengths obeying the power-law distribution with $l_0 = 1\,\mathrm{m}$ and $l_1 = 30\,\mathrm{m}$. The number of fractures is 100. In the case of $a = 3$, most of the fracture lengths are biased near the lower limit, l_0.

6.2.2 Orientation distribution

Since fracture orientation is represented as a function of azimuth (θ), a distribution function suitable for a azimuthally varying quantity must be used. The von Mises distribution, which corresponds to the normal distribution for such data, has the following density function (Fisher, 1993)

$$f(\theta \mid \mu, \kappa) = \frac{1}{2\pi I_0(\kappa)} \exp\left[\kappa \cos(\theta - \mu)\right], \quad 0 \le \theta < 2\pi, \quad 0 \le \kappa < \infty, \tag{6.8}$$

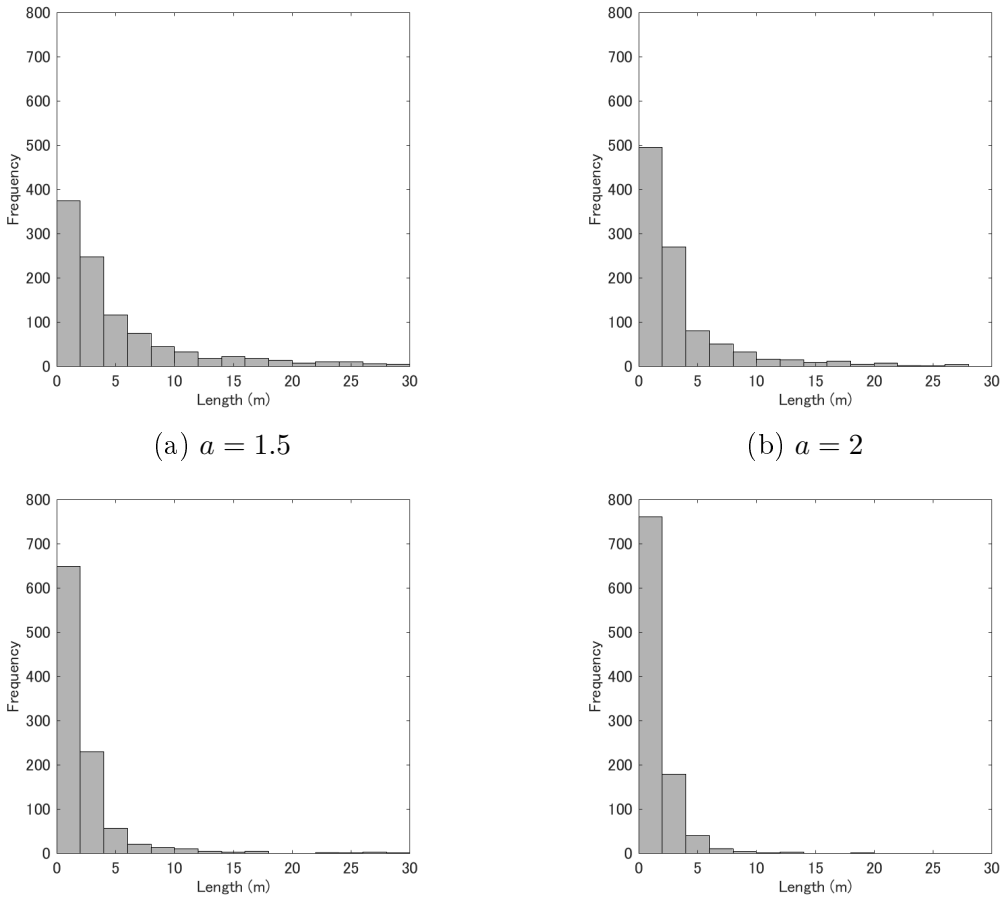

(a) $a = 1.5$ (b) $a = 2$

(c) $a = 2.5$ (d) $a = 3$

Figure 6.2: Fracture length distribution generated by using the power-law distribution. $l_0 = 1\,\mathrm{m}$ and $l_1 = 30\,\mathrm{m}$. The number of samples is 1000.

where θ is the orientation, μ is the mean direction, and κ is the concentration parameter. I_0 is the modified Bessel function of the first kind of zero-th order defined by

$$I_0(\kappa) \coloneqq \frac{1}{2\pi} \int_0^{2\pi} \exp\left[\kappa \cos(\theta - \mu)\right]. \tag{6.9}$$

The von Mises distribution is produced by using the algorithm due to Best and Fisher (1979), which can be also found in Fisher (1993).

Given fracture orientation data, the angle doubling procedure is required to estimate μ and κ since fracture orientation has diametrically bimodal circular distributions. The angle doubling procedure is

1. Let $\theta' = 2\theta$.
2. If $\theta' \geq 2\pi$, let $\theta' = \theta' - 2\pi$.

The mean direction and the concentration parameter of θ' is then estimated as μ' and κ'. Conversely, the von Mises distribution can be generated from the above μ' and κ' in the following manner:

1. Generate θ' from μ' and κ'.
2. Use $\theta = \theta'/2$ to generate natural fractures. Add $\theta = \theta'/2$ and $\theta = \theta'/2 + \pi$ to create a rose diagram.

Fig. 6.3 show the examples of the von Mises distribution for different concentration parameters. $\mu' = \pi/2$ is used. The actual mean directions are 45° and 225°.

Natural fractures often have two distinct principal directions (Li, 2014; Shrivastava et al., 2018). The density function of bimodal distributions can be expressed by

$$f(\theta) = wf(\theta \mid \mu_1, \kappa_1) + (1 - w)f(\theta \mid \mu_2, \kappa_2), \tag{6.10}$$

where w is a mixing factor of the two modes ($0 \leq w \leq 1$), and the subscript denotes

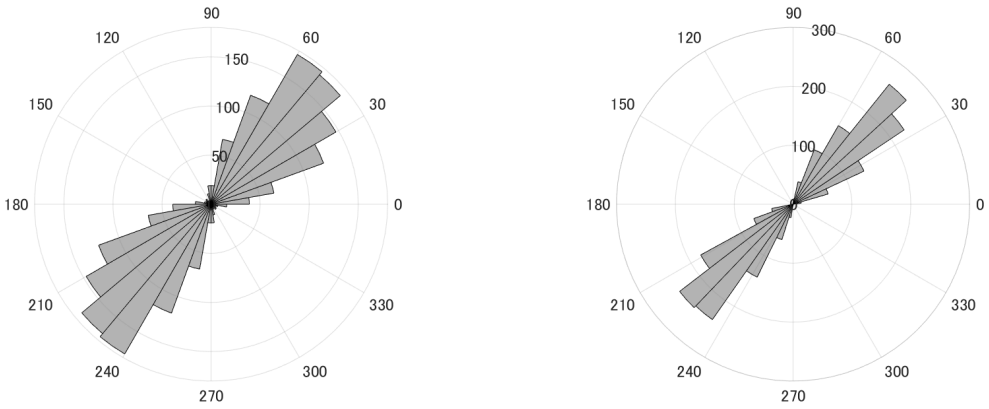

(a) $\kappa' = 2$ (b) $\kappa' = 5$

Figure 6.3: Rose diagrams of the von Mises distribution for $\mu' = \pi/2$. The number of samples is 1000.

the first and second mode distributions. Then, the following procedures create a bimodal distribution:

1. Generate a random value x obeying a uniform distribution between 0 and 1.
2. If $x < w$, generate θ' using the first mode distribution, and generate θ' using the second mode distribution otherwise.

Fig. 6.4 shows an example of the bimodal von Mises distribution. The first mode is ${\mu'}_1 = \pi/2$ and ${\kappa'}_1 = 5$, and the second mode is ${\theta'}_2 = 4\pi/3$ and ${\kappa'}_2 = 3$. The mixing parameter is $w = 0.7$. The actual mean directions are 45° and 225° for the first mode and 120° and 300° for the second mode.

6.2.3 Fracture Intersection in Mesh

Fracture networks are generated by using the length and orientation distribution functions. The generated fracture lengths are rounded because of the discretization which uses fixed-size elements. Although the end-to-end connection of elements is required to avoid singularities in DDM (Farmahini-Farahani and Ghassemi, 2016), the implementation of generating such a mesh is difficult. Instead, we generate a frac-

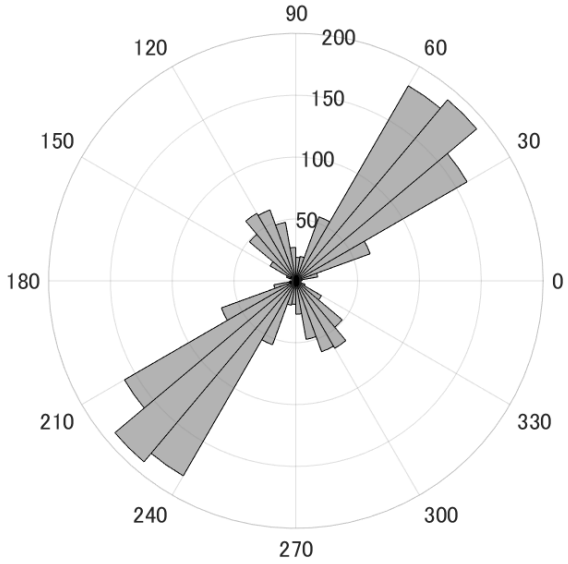

Figure 6.4: An example of bimodal von Mises distribution. The first mode is $\mu'_1 = \pi/2$ and $\kappa'_1 = 5$, and the second mode is $\theta'_2 = 4\pi/3$ and $\kappa'_2 = 3$. The mixing parameter is $w = 0.7$.

ture mesh without the end-to-end connection for simplification, and the singularity problem is circumvented by correcting the influence coefficients of DDM.

The correction procedure for the influence coefficients has two steps. First, any influence coefficients computed as NaN due to the singularity of the Green's function of DDM are recalculated by averaging the influence coefficients at two neighboring points. Second, any influence coefficients larger than the self influence coefficients are scaled using the following procedure. For each block column i,

1. Calculate the maximum self-influence coefficients, $\max|\mathbf{A}_{ii}|$.
2. If $\max|\mathbf{A}_{ij}| > \alpha \max|\mathbf{A}_{ii}|$, where $\alpha \geq 1$ is a scaling factor, scale the block matrix $\mathbf{A}_{ij}$ by

$$\mathbf{A}_{ij} = \alpha \mathbf{A}_{ij} \cdot \frac{\max|\mathbf{A}_{ii}|}{\max|\mathbf{A}_{ij}|}. \tag{6.11}$$

The scaling procedures are tested by using a simple problem shown in Fig. 6.5. Two hydraulic fractures grow straight and eventually intersect at 45°. At the intersection

point, one of the edges of an element lies on the center of another element, causing the singularity problem. The element size is 1 m. The problems is solved by using the segregated or fully coupled method.

Fig. 6.6 shows the results of simulations without scaling. Only NaN correction is applied to the DDM influence matrix. The simulation using the segregated method did not converge when two fractures intersected, while that using the fully coupled method converged. The fracture width of one of the intersected elements in the case of the fully coupled method becomes significantly larger than that of the other elements, indicating the computation is inaccurate due to the large influence coefficients of the intersected elements.

Fig. 6.7 represents the simulation result with scaling. $\alpha = 1$ is used, and NaN correction is also applied. In this case, the segregated method converged when two fractures intersected, and both segregated and fully coupled methods produce the same width profile at the end of the simulations.

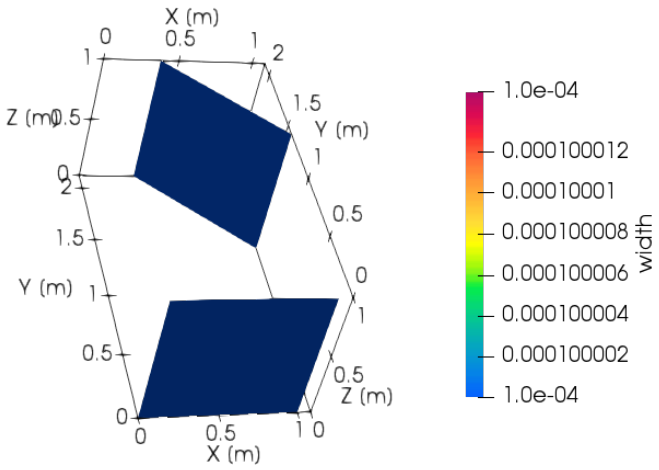

(a) Initial mesh. One fracture grows from the origin, and the other fracture grows from $(x, y) = (0.7322, 1.7678)$.

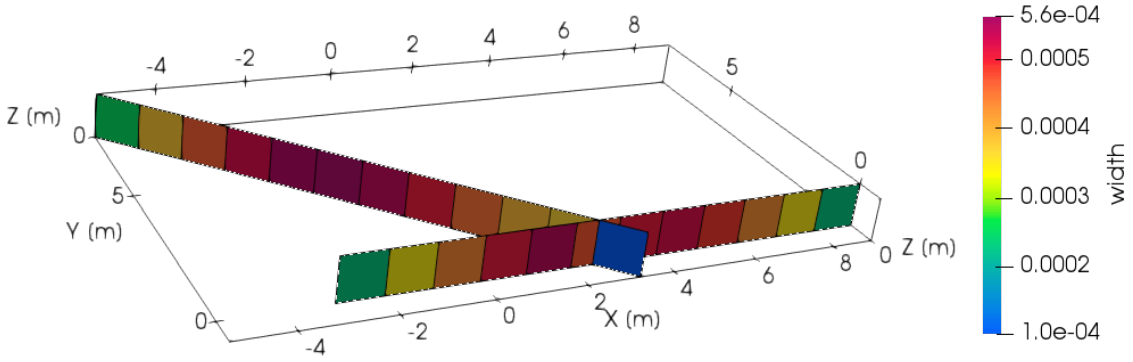

(b) Mesh when two hydraulic fractures intersect at $(x, y) = (2.5, 0.0)$.

Figure 6.5: Mesh configuration for testing the proposed correction method. Two hydraulic fractures propagate in straight line and eventually intersect. Fracture turning option is disabled.

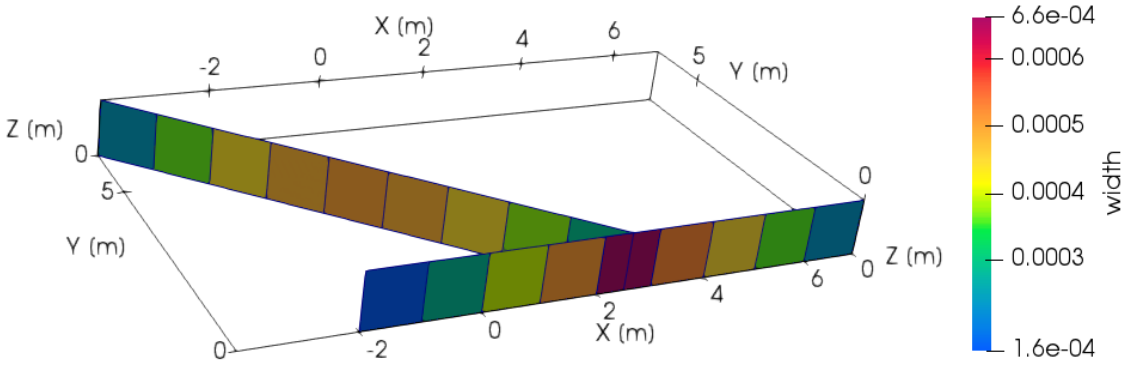

(a) Mesh at $t = 7\,\mathrm{s}$ using the segregated method.

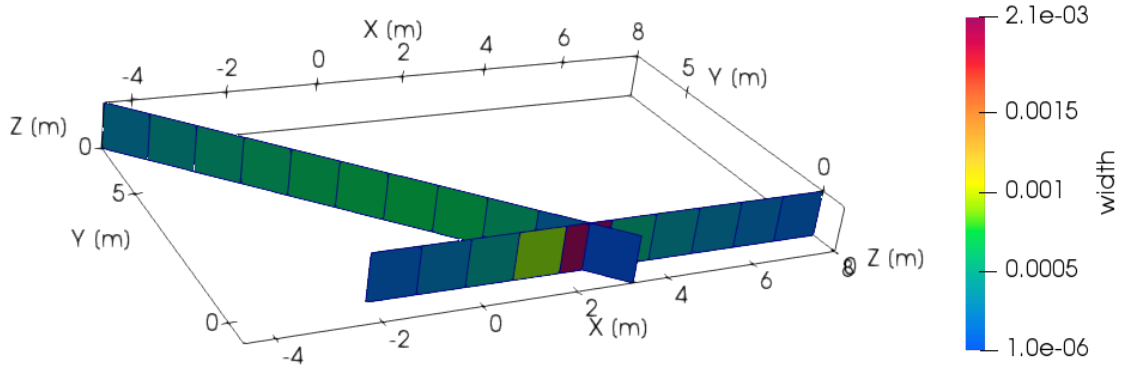

(b) Mesh at $t = 10\,\mathrm{s}$ using the fully coupled method.

Figure 6.6: Meshes at the end of fracturing simulations without scaling of influence coefficients. Only NaN correction is applied. The simulation using the segregated method did not converge at $t = 7\,\mathrm{s}$.

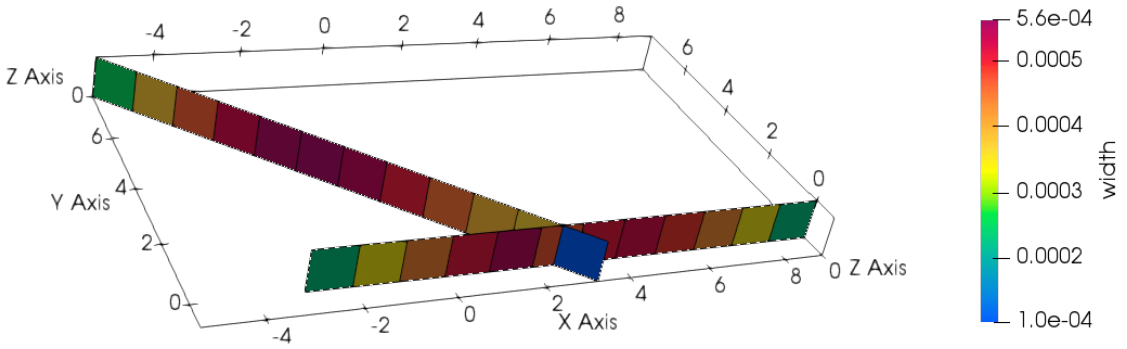

(a) Mesh at $t = 10\,\mathrm{s}$ using the segregated method.

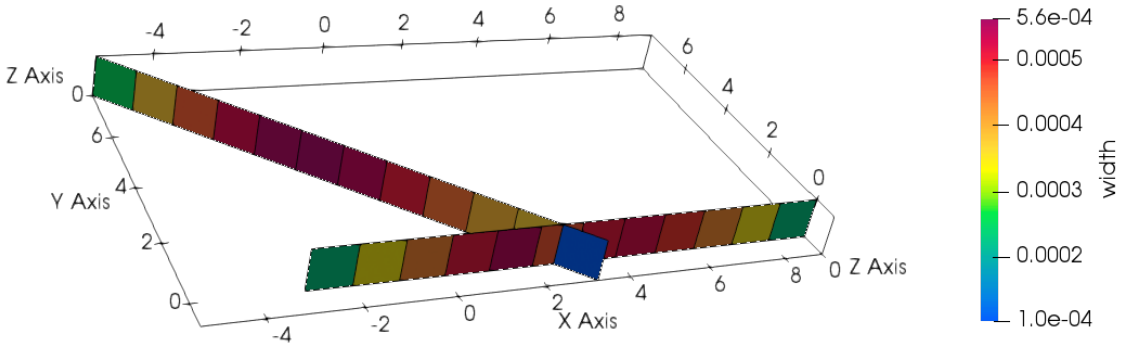

(b) Mesh at $t = 10\,\mathrm{s}$ using the fully coupled method.

Figure 6.7: Meshes at the end of fracturing simulations with scaling of influence coefficients. NaN correction is also applied.

Table 6.1: Parameters used to generate natural fracture networks.

μ	45°
κ	5
l_0	1 m
l_1	30 m
a	2, 3
Fracture areal density, ρ_{NF}	0.05, 0.1 m^{-2}
Element size	1 m

6.3 Hydraulic Fracturing Simulations With Natural Fractures

Natural fracture networks are generated by using the power-law distribution for fracture lengths and the von Mises distribution for fracture orientation. We assume vertical natural fractures with the same height. We simulate hydraulic fracture propagation from three perforation clusters in a stage. We assume a constant injection rate for each cluster and neglect fluid distribution caused by flow resistance inside hydraulic fractures for simplification (Wu, 2014; Manchanda, 2015). Elements are square, and their edge length is 1 m. Parameters used to generate natural fractures are listed in Table 6.1. The number of natural fractures to generate N_{NF} is determined as

$$N_{\mathrm{NF}} = \rho_{\mathrm{NF}} A, \tag{6.12}$$

where ρ_{NF} is an areal density of natural fractures, and A is the area of simulations.

Fig. 6.8 shows natural fractures generated by using the power-law and von Mises distributions. Domain size is 100 m×100 m. Smaller a leads to longer natural fractures, and natural fractures tend to intersect more frequently. To quantitatively analyze the frequency of intersections, we generated 10 realizations for each set of $a = 2, 3$ and $\rho_{NF} = 0.05$, 0.1 m^{-2} and calculated the frequency of intersections along the y-axis per length. The result is shown in Fig. 6.9. It clearly shows that larger

ρ_{NF} and smaller a increase the possibility of intersections. It was found that the effect of ρ_{NF} to the intersection frequency became smaller for larger a when $\mu = \pi/4$ and $\kappa = 5$ were used for the von Mises distribution. For $a = 2$, the frequency of intersections is almost a linear function of the areal density of natural fractures.

Hydraulic fracturing simulations are performed using parameters listed in Table 6.2. The parameters are chosen from Shrivastava et al. (2018). Natural fractures are distributed in a 100 m×200 m region by using parameters listed in Table 6.1. 3D DDM is used for fracture mechanics. We use the fully coupled method to avoid non-convergence issues frequently observed in hydraulic fracturing simulations with natural fractures. Because of simulation time and implementation difficulty, fractures have only one element height at the same depth.

Fig. 6.10 shows hydraulic fracture propagation in natural fracture networks with $a = 2$, 3 for the power-law distribution. Black and red lines represent natural and hydraulic fractures, respectively. Perforations are located at $x = -10$, 0, 10 m along the x axis. Natural fractures not connected to hydraulic fractures are allowed to fail according to the Mohr-Coulomb failure criterion. The maximum horizontal stress is 36.44 MPa in the y direction. Hydraulic fractures tend to intersect natural fractures more frequently and create more branches to extend in the x direction in the case of $a = 2$ than $a = 3$.

Fig. 6.11 shows hydraulic fracture propagation in the same natural fracture networks with Fig. 6.10 but natural fractures not connected to hydraulic fractures are not allowed to fail. Blue circles represent differences with Fig. 6.10. It is found that the number of branches decreases by neglecting remote failure of natural fractures in the case of $a = 2$.

Fig. 6.12 shows hydraulic fracture propagation in the same natural fracture network with Fig. 6.10 but uses a larger horizontal stress contrast, $S_{\mathrm{hmax}} = 39.44$ MPa.

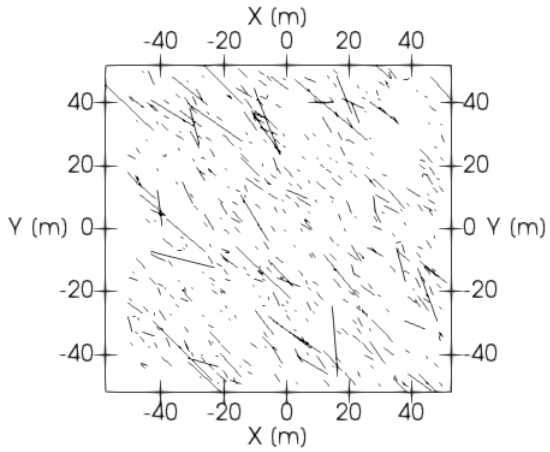

(a) $a = 2$, $\rho_{\mathrm{NF}} = 0.05\,\mathrm{m}^{-2}$

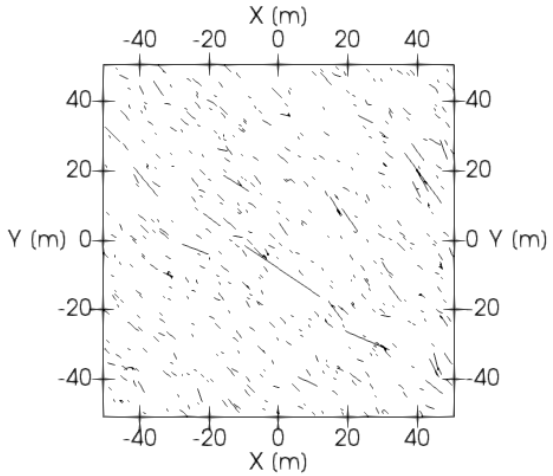

(b) $a = 3$, $\rho_{\mathrm{NF}} = 0.05\,\mathrm{m}^{-2}$

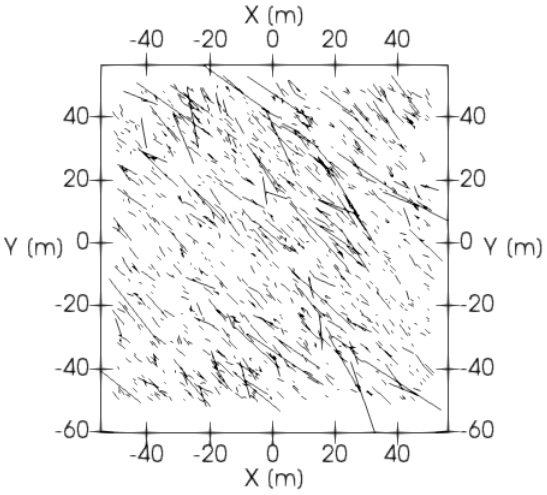

(c) $a = 2$, $\rho_{\mathrm{NF}} = 0.1\,\mathrm{m}^{-2}$

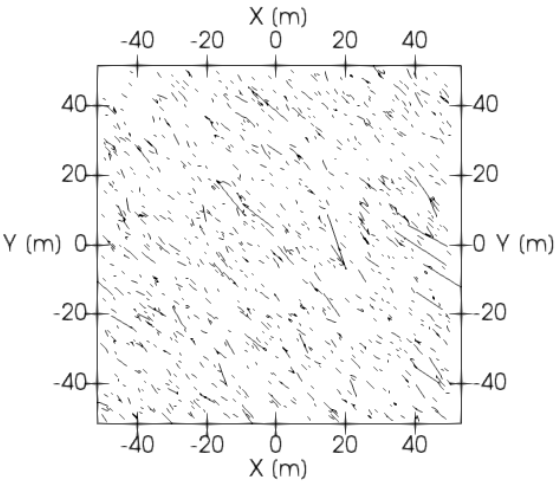

(d) $a = 3$, $\rho_{\mathrm{NF}} = 0.1\,\mathrm{m}^{-2}$

Figure 6.8: Natural fractures generated by using the power-law and von Mises distributions. $\mu = \pi/4$ and $\kappa = 5$. Domain size is 100 m in the x and y directions.

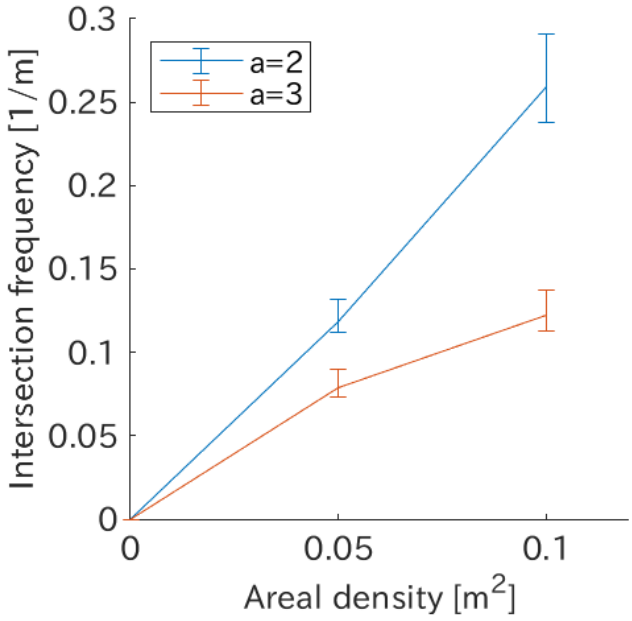

Figure 6.9: The frequency of intersections along the y-axis for different distribution parameters of the power-law distribution. $\mu = \pi/4$ and $\kappa = 5$ are used for the von Mises distribution. The domain size of realizations is $100 \times 100\,\mathrm{m}$ in the x and y directions. Error bars represent the maximum and minimum values found in the realizations.

Although hydraulic fractures are deflected when they intersect natural fractures, they immediately turn in the maximum horizontal stress direction after they reach an edge of natural fractures. In the case of $a = 3$, hydraulic fractures propagate almost straight from the perforations since there is smaller number of intersections with natural fractures compared to $a = 2$.

Fig. 6.13 shows hydraulic fracture propagation in dense natural fracture networks. $\rho_{\mathrm{NF}} = 0.1\,\mathrm{m}^{-2}$ is used. Hydraulic fractures intersect natural fractures more frequently and preferentially propagate in the mean direction of the natural fracture distribution.

Fig. 6.14 shows hydraulic fracture propagation in a bimodal natural fracture distribution. Mean directions are selected as 45° and 135° from the x axis, and concentration parameters are 5 for both modes. Mixing parameter of two modes is 0.5. Comparing Fig. 6.10 and Fig. 6.12, more branches and intersections are observed in the case of $S_{\mathrm{hmax}} = 36.44\,\mathrm{MPa}$. Since natural fractures are oriented in two distinct principal directions, hydraulic fractures do not have one preferred propagation direction as observed in Fig. 6.10 through Fig. 6.12 and Wu (2014).

Table 6.2: Simulation parameters.

Time step length	1 s
Simulation time	70 s
S_{hmax}	36.44 MPa
S_{hmin}	35.85 MPa
S_{v}	45.00 MPa
Shear modulus	6.62 GPa
Poisson's ratio	0.25
Leak-off coefficient	0.0
Pore pressure	27.01 MPa
K_{Ic}	$3\,\mathrm{MPa\,m^{0.5}}$
Characteristic length	0.005 m
NF cohesion	0 MPa
NF friction coefficient	0.25
Skempton's coefficient	1
NF K_{Ic}	$0.5\,\mathrm{MPa\,m^{0.5}}$
Fluid viscosity	1 cP
Fluid compressibility	$4.4 \times 10^{-4}\,\mathrm{MPa^{-1}}$
Reference density	$1000\,\mathrm{kg\,m^{-3}}$
Wellbore volume	$5.0\,\mathrm{m^3}$
Injection rate	$2.0 \times 10^{-3}\,\mathrm{m^3\,s^{-1}}$

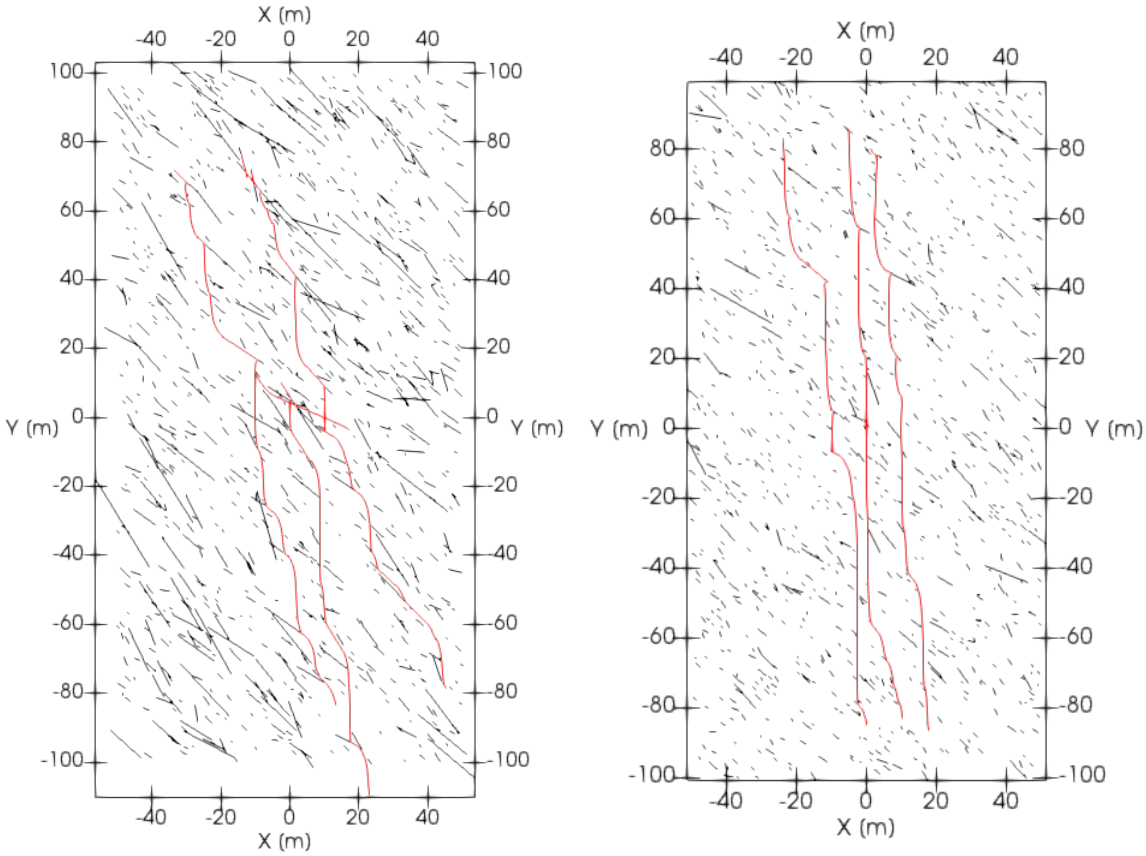

(a) $a = 2$ (b) $a = 3$

Figure 6.10: Hydraulic fracture propagation in natural fracture networks with remote failure of natural fractures. $\rho_{\mathrm{NF}} = 0.05\,\mathrm{m}^{-2}$, and $S_{\mathrm{hmax}} = 36.44\,\mathrm{MPa}$. Black and red lines represent natural and hydraulic fractures, respectively.

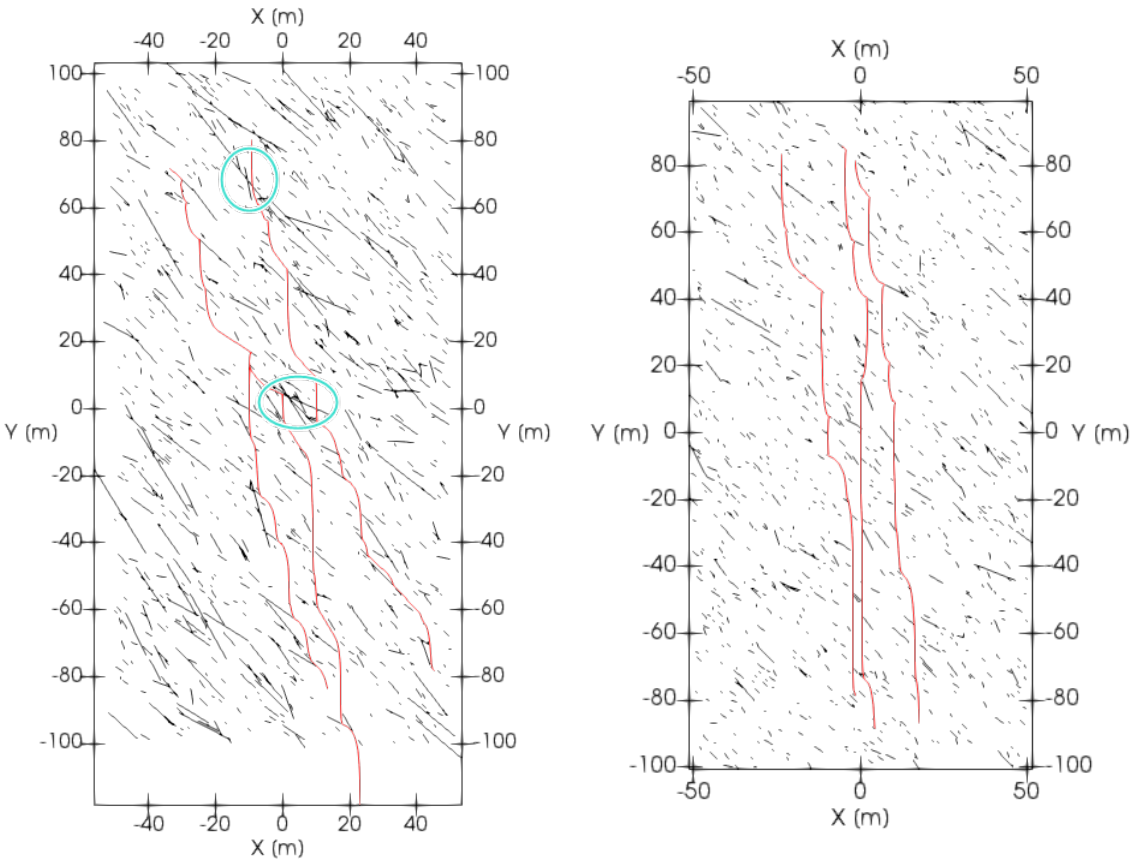

(a) $a = 2$ (b) $a = 3$

Figure 6.11: Hydraulic fracture propagation in natural fracture networks without remote failure of natural fractures. The same natural fracture networks with Fig. 6.10 are used. Blue circles represent differences from Fig. 6.10.

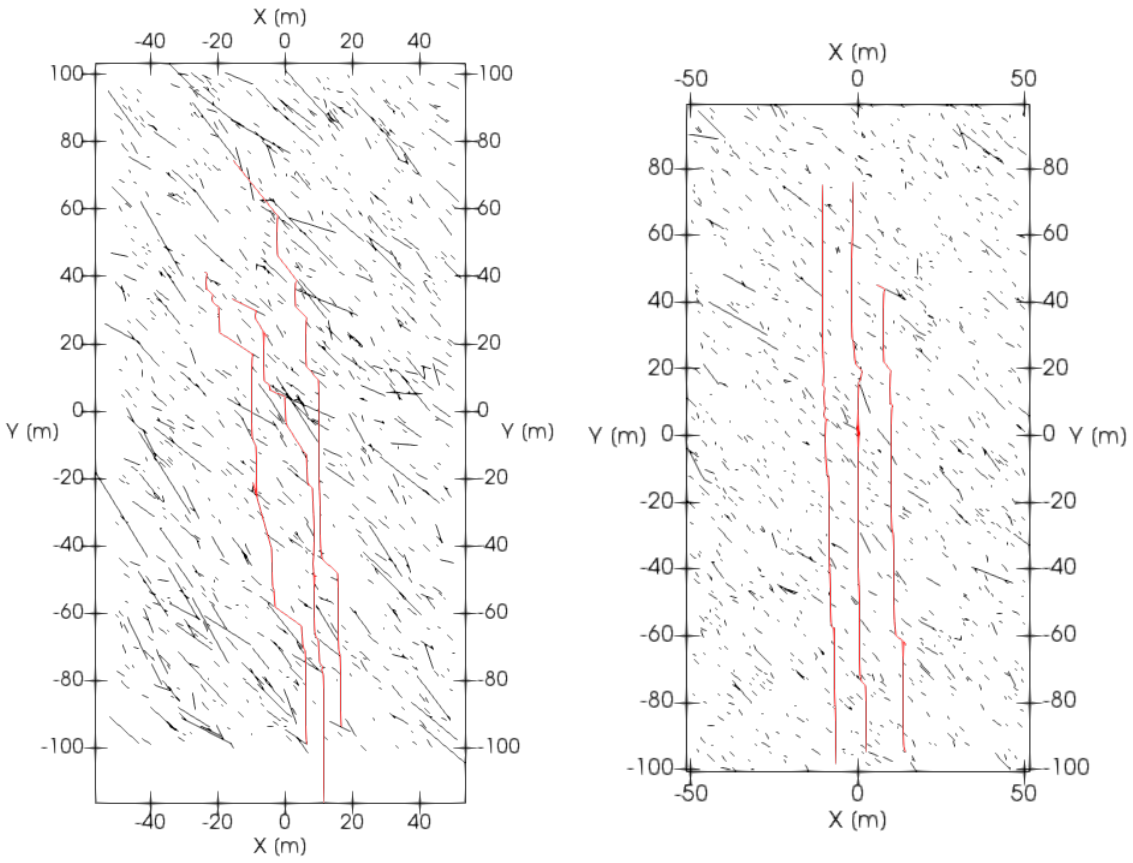

(a) $a = 2$ (b) $a = 3$

Figure 6.12: Hydraulic fracture propagation in natural fracture networks with remote failure of natural fractures. $\rho_{\mathrm{NF}} = 0.05\,\mathrm{m}^{-2}$, and $S_{\mathrm{hmax}} = 39.44\,\mathrm{MPa}$. Black and red lines represent natural and hydraulic fractures, respectively.

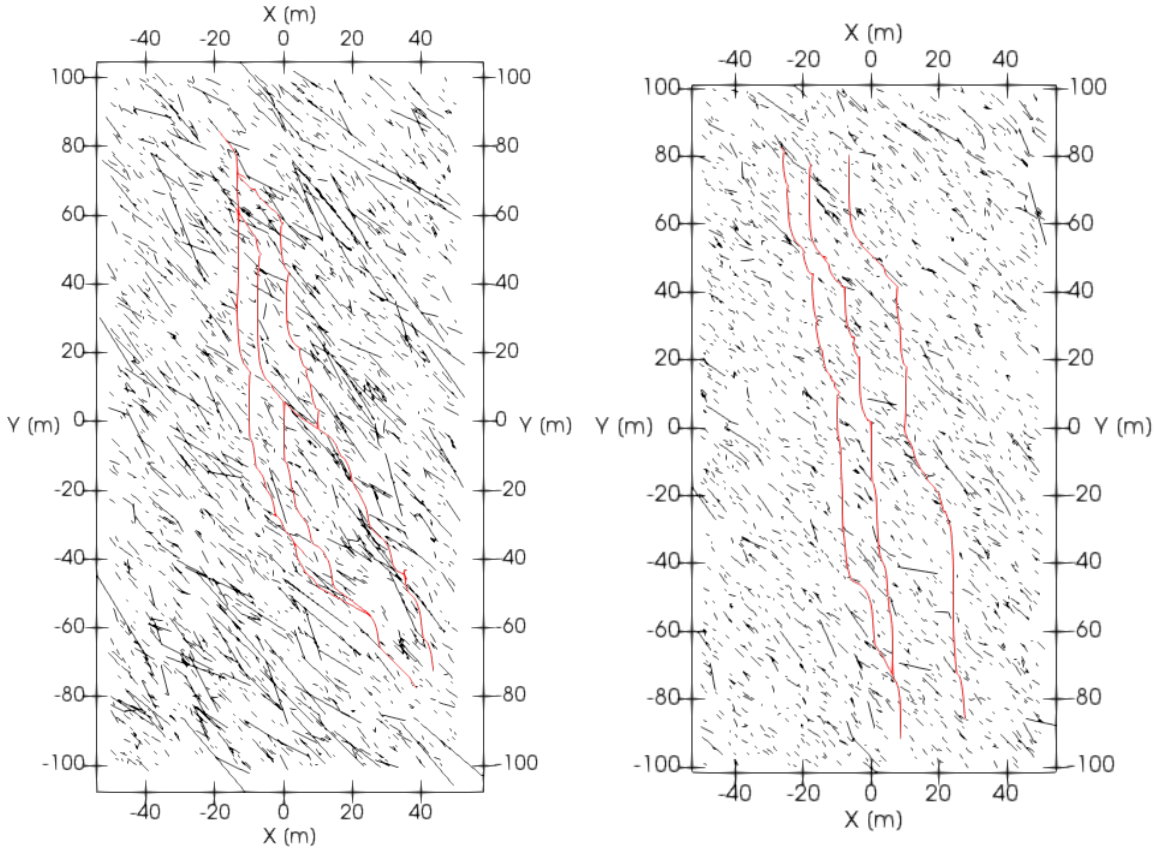

(a) $a = 2$ (b) $a = 3$

Figure 6.13: Hydraulic fracture propagation in natural fracture networks with remote failure of natural fractures. $\rho_{\mathrm{NF}} = 0.1\,\mathrm{m}^{-2}$. Black and red lines represent natural and hydraulic fractures, respectively.

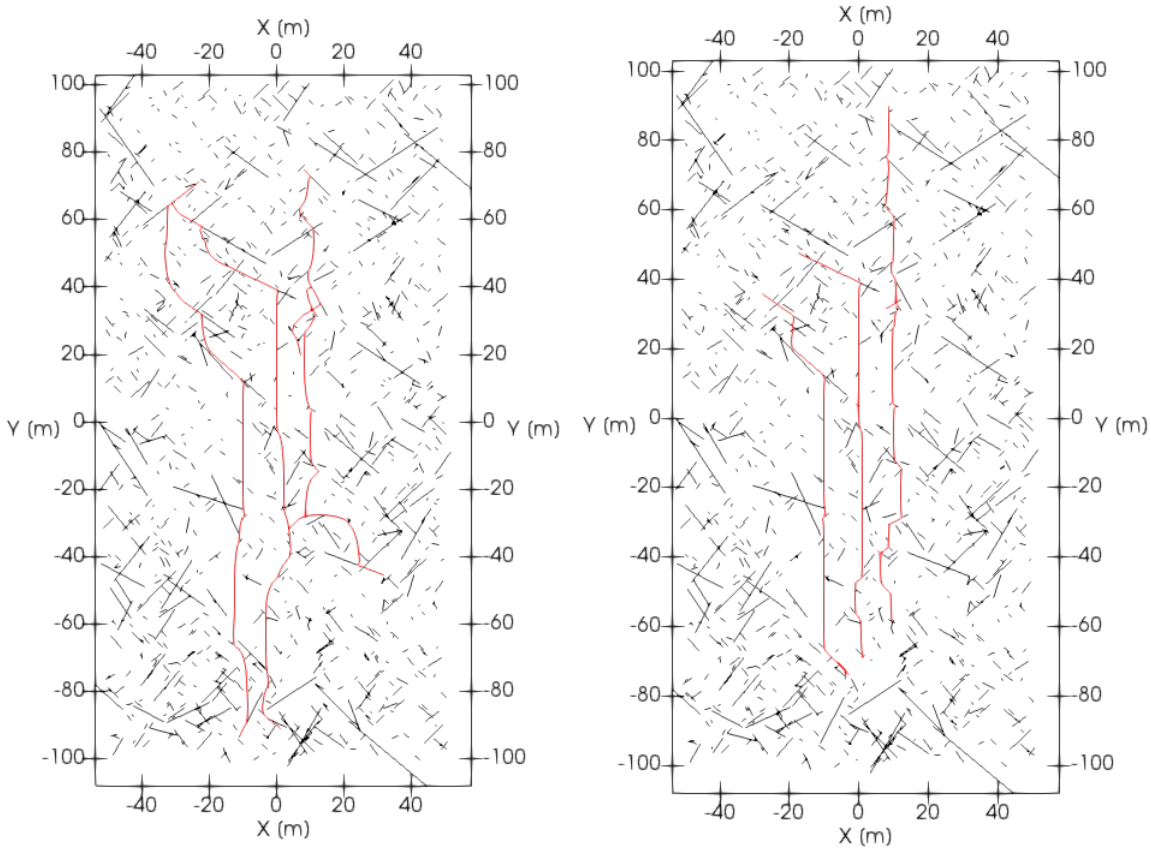

(a) $S_{\mathrm{hmax}} = 36.44\,\mathrm{MPa}$ (b) $S_{\mathrm{hmax}} = 39.44\,\mathrm{MPa}$

Figure 6.14: Hydraulic fracture propagation in natural fracture networks with remote failure of natural fractures. Bimodal distribution is used. Mean directions are 45° and 135° from the x axis, and concentration parameter is 5 for both modes. Mixing parameter is 0.5. $\rho_{\mathrm{NF}} = 0.05\,\mathrm{m}^{-2}$. Black and red lines represent natural and hydraulic fractures, respectively.

6.4 Discussion

Hydraulic fracturing simulations are performed in the previous section using various parameters. Comparing Fig. 6.10 and Fig. 6.11, we observe that more branches are created by incorporating remote failure of natural fractures. Since stress change and pore pressure increase are limited in the vicinity of hydraulic fractures as discussed in Chapter 5, the remote failure condition is likely to be satisfied at intersection points to create branches. This means that the remote failure can be an important factor to generate complex fracture networks, especially when natural fractures have a low friction coefficient.

While a large horizontal stress contrast forces hydraulic fractures to propagate in the maximum horizontal stress direction, the distribution of natural fractures also affects the propagation direction of hydraulic fractures as shown in Fig. 6.12. If a natural fracture distribution is denser, hydraulic fractures intersect natural fractures more frequently and propagate in the mean direction of the natural fractures (Fig. 6.13). We find that bimodal distribution of natural fractures creates more complex hydraulic fractures since natural fractures have more intersections than single mode distribution. Field observations of natural fracture distribution suggest natural fractures have more than one principal direction (Li, 2014; Shrivastava et al., 2018), incorporating multiple modes for natural fracture orientations is essential to simulation complex hydraulic fracture propagation.

6.5 Conclusion

Hydraulic fracturing simulations with natural fracture networks are performed. Natural fractures are distributed by using the power-law distribution for fracture length and the von Mises distribution for fracture orientation. End-to-end connection

of elements when natural fractures are distributed is neglected for simplification. The singularity problem caused by neglecting the end-to-end connection is circumvented by correcting influence coefficients of DDM.

Sensitivity analysis of hydraulic fracture propagation in natural fracture networks revealed the following results:

- When $a = 2$ is used in the power-law distribution with the von Mises distribution of $\mu = \pi/4$ and $\kappa = 5$, the frequency of intersections of hydraulic and natural fractures is almost a linear function of the areal density of natural fractures.
- More branches are created by considering remote failure of natural fractures.
- A larger horizontal stress contrast forces hydraulic fractures to propagate in the maximum horizontal stress direction.
- Denser natural fractures create more intersections between hydraulic and natural fractures.
- Bimodal distribution for natural fracture orientations leads to more complex hydraulic fracture networks.

Chapter 7: Modeling of Microseismic Events

7.1 Introduction

The distribution of natural fractures (NFs) in hydraulic fracturing simulations is commonly determined based on statistical parameters observed in cores and well logs. The synthetic NF networks, however, can be different from the actual ones because of the error associated with the statistical parameters and mechanical properties of NFs. Thus, the geometry of hydraulic fractures given from the simulations can also differs from reality. To improve the accuracy of hydraulic fracturing simulations with NFs, it is natural to incorporate microseismic data into the simulations as shown in Fig. 7.1. The location, extension, and orientation of fractures can be obtained through the inversion analysis of microseismic data. They can be compared with those produced from hydraulic fracturing simulations, and the input data of the simulations can be updated based on the difference between the observed and simulated data.

In the previous chapter, we performed hydraulic fracturing simulations in the presence of synthetic natural fractures. This chapter describes modeling of microseismicity triggered by hydraulic fracturing. First, we briefly describe the forward modeling of synthetic microseismic events, which is the modeling of microseismic sources and wave propagation from a source to receivers. To analyze microseismic sources, seismic moment and moment magnitude are explained. The moment magnitudes of synthetic microseismic events are computed from the simulation results presented in Chapter 6, and the areal distribution of the events are discussed. Second, simple inversion analyses of synthetic microseismic data are performed. We use the low frequency amplitude and the radiation pattern correction factor as matching

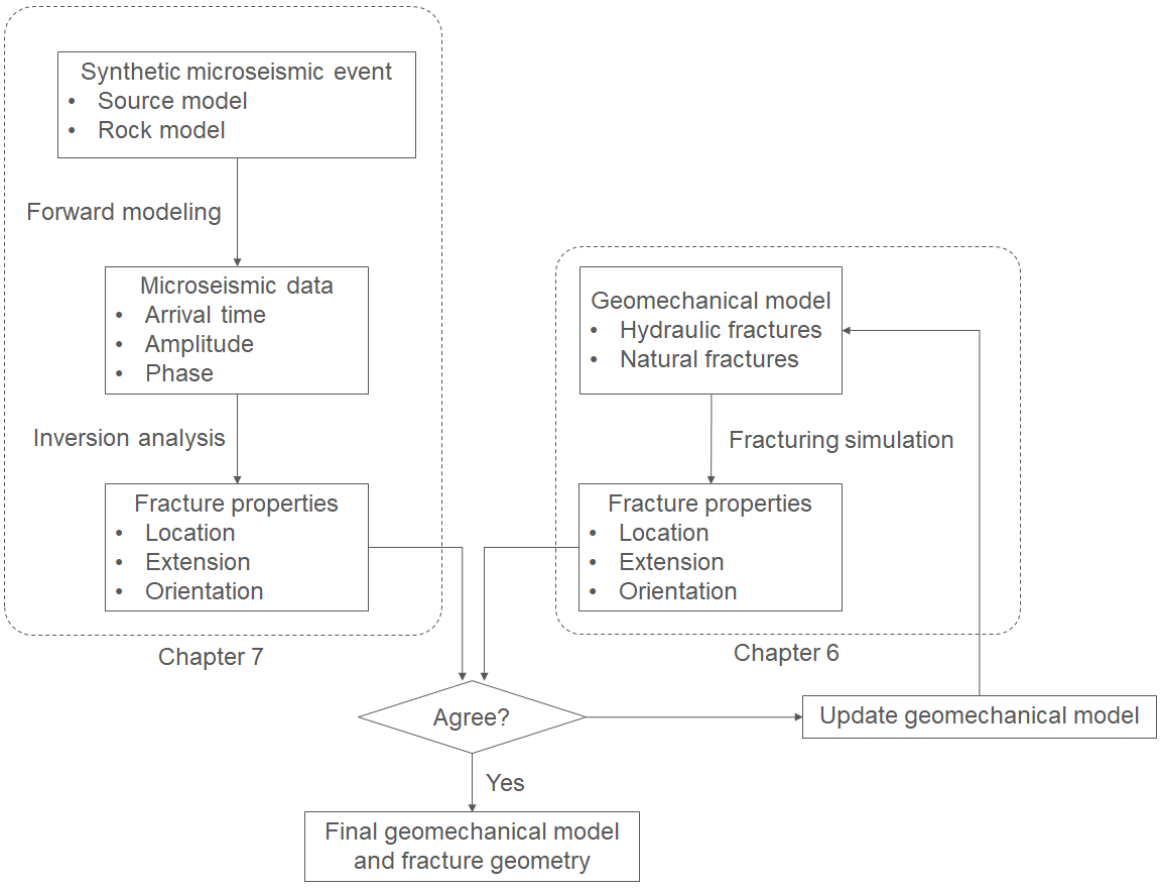

Figure 7.1: A flow chart of geomechanical simulations assisted by microseismic data

parameters for inversion the analysis to simplify the problem.

7.2 Forward Modeling of Synthetic Microseismic Events

This section describes the forward modeling of synthetic microseismic events. In other words, if a fracture slips, what is the observed wave form at receivers? The forward modeling of microseismic events in geophysics normally requires a source model which describes the slip of a fracture surface as a function of time, typically in milliseconds, and a velocity model of the reservoir. However, normal hydraulic fracturing simulations including our model are not capable of computing fracture failure in such a small time scale due to the assumption of quasi-static conditions. Moreover, the computation of full waveform at receivers using a detailed geophysical model is beyond the scope of this dissertation. We circumvent the full waveform analysis by assuming the low frequency limit of displacements.

7.2.1 Seismic Moment, Moment Magnitude, and Seismic Moment Tensor

The magnitude of microseismic events is expressed by the seismic moment by assuming shear failure along a fault surface. The seismic moment M_0 is defined as (Aki and Richard, 2002)

$$M_0 \coloneqq GAd, \tag{7.1}$$

where G is shear modulus, A is the area of the fracture, and d is the average distance of slip over the fault. If the elastic properties, area, and slip distance of a seismic source are known, we can directly compute the seismic moment by using Eq. 7.1. It should be mentioned that the seismic moment is a scale to measure the magnitude of seismic sources and independent of observation points.

Because of the broad range of seismic moment, it is common to use moment

magnitude M_w instead of seismic moment. Moment magnitude is a logarithmic scale of the seismic moment defined as (Kanamori, 1977)

$$M_w \coloneqq \frac{2}{3} \log_{10} M_0 - 6.0, \tag{7.2}$$

where M_0 is in N m. The moment magnitude of microseismic events observed during hydraulic fracturing operations is typically much lower than zero. For instance, Warpinski et al. (2012) reported moment magnitude of microseismicity measured in the Barnett, Marcellus, Eagle Ford, and Woodford shales ranging between -4 and -1.

While the magnitude of microseismic events is expressed with seismic moment or moment magnitude, which assumes shear failure of the events, hydraulic fractures contain non-zero tensile component in their slip vector in general. For earthquakes with tensile components, the seismic moment tensor M_{ij} is defined (Aki and Richard, 2002):

$$M_{ij} \coloneqq \iint_{\Sigma} C_{ijkl} \Delta u_k n_l \, \mathrm{d}\Sigma, \tag{7.3}$$

where C_{ijkl} is a fourth-order elastic tensor, Δu_i is the slip vector, n_i is the normal of the fault, and Σ is the fault surface. The moment tensor (MT) can be computed from seismic waveforms generated by seismic events. This is referred to as MT inversion.

MT is conventionally decomposed into the isotropic (ISO), double couple (DC), and compensated linear vector dipole (CLVD) components in MT inversion analysis (Knopoff and Randall, 1970; Vavryčuk, 2001).

$$M_{ij} = M_{ij}^{\mathrm{ISO}} + M_{ij}^{\mathrm{DC}} + M_{ij}^{\mathrm{CLVD}}. \tag{7.4}$$

ISO component represents dilatation, and DC component corresponds to shear fail-

ure. The CLVD component describes the simultaneous change in the axial strain and shear modulus. Although it is often mentioned that DC component is dominant in microseismic events observed in hydraulic fracturing (Nolen-Hoeksema and Ruff, 2001; Yu et al., 2015), Šílený et al. (2009) pointed out the dominant DC component is the result of a single observation well and showed that non-DC components can be retrieved by using multiple observation wells. Vavryčuk (2007) showed the relationship between recoverable components in MT inversion and the number of observation wells. Pesicek et al. (2016) found microseismic events induced during hydraulic fracturing of the Montney Shale in Canada contain significant non-DC components by analyzing seismic data recorded by using surface arrays.

7.2.2 Seismic Wave Propagation from a Source to Receivers

The seismic moment tensor and the displacement are related by the Green's function of a medium (Aki and Richard, 2002):

$$u_i(\boldsymbol{x}, t) = M_{kl} * G_{ik,l}, \tag{7.5}$$

where $u_i(\boldsymbol{x}, t)$ is the displacement vector measured at a point $\boldsymbol{x}$ and time t, and $G_{ik,l}$ is the spatial derivative of the Green's function. The symbol $*$ denotes the time convolution.

Assuming a homogeneous isotropic medium, the Green's function can be analytically derived. If the receiver is located far from the source, the far-field displacements of the P- and S-waves, u_i^{FP} and u_i^{FS}, are given by (Aki and Richard, 2002; Chapman,

2004)

$$u_i^{FP}(\boldsymbol{x},t) = \frac{R_{ij}^P \gamma_k}{4\pi\rho v_P^3 r}\dot{M}_{jk}\left(t - \frac{r}{v_P}\right), \tag{7.6}$$

$$u_i^{FS}(\boldsymbol{x},t) = \frac{R_{ij}^S \gamma_k}{4\pi\rho v_S^3 r}\dot{M}_{jk}\left(t - \frac{r}{v_S}\right), \tag{7.7}$$

where ρ is the density, v_P and v_S are the P- and S-wave velocities, r is the distance between the source and the receiver, and γ_i is the directional cosine from the source to the receiver. R_{ij}^P and R_{ij}^S give the radiation pattern factors for P- and S-waves. They are given by

$$R_{ij}^P \coloneqq \gamma_i\gamma_j, \tag{7.8}$$

$$R_{ij}^S \coloneqq \delta_{ij} - \gamma_i\gamma_j. \tag{7.9}$$

Let us define a source model $\Omega(\boldsymbol{x},t)$ as (Aki and Richard, 2002)

$$\Omega(\boldsymbol{x},t) \coloneqq \iint_\Sigma \Delta\dot{u}\left(\boldsymbol{\xi}, t - \frac{r}{c}\right)\,\mathrm{d}\Sigma(\boldsymbol{\xi}), \tag{7.10}$$

where Δu is the magnitude of the slip, c is the wave velocity. The dot denotes the time derivative. The time derivative of the moment tensor can be expressed by using the source model as

$$\dot{M}_{ij}(\boldsymbol{x},t) = \hat{M}_{ij}\Omega(\boldsymbol{x},t), \tag{7.11}$$

where $\hat{M}_{ij} \coloneqq C_{ijkl}\nu_k n_l$, and ν_k is the slip direction. Then, Eq. 7.6 and Eq. 7.7 can

be rewritten as

$$u_i^{FP}(\boldsymbol{x},t) = \frac{R_{ij}^P \gamma_k}{4\pi\rho v_P^3 r} \hat{M}_{jk} \Omega\left(t - \frac{r}{v_P}\right), \tag{7.12}$$

$$u_i^{FS}(\boldsymbol{x},t) = \frac{R_{ij}^S \gamma_k}{4\pi\rho v_S^3 r} \hat{M}_{jk} \Omega\left(t - \frac{r}{v_S}\right). \tag{7.13}$$

Let us denote the Fourier transform of $\Omega(\boldsymbol{x},t)$ with respect to t as $\Omega(\boldsymbol{x},\omega)$. The low frequency limit of $\Omega(\boldsymbol{x},\omega)$ approaches a constant value given by (Aki and Richard, 2002):

$$\Omega(\boldsymbol{x},\omega \to 0) = \iint_\Sigma \Delta u(\xi, t \to \infty)\, \mathrm{d}\Sigma = dA, \tag{7.14}$$

where d is the final slip over the fault, and A is the area of the fault. Taking the Fourier transform of Eq. 7.12 and Eq. 7.13 and substituting the above equation, we have

$$\Omega_0^{FP} = |u_i^{FP}(\boldsymbol{x},\omega \to 0)| = \frac{dA}{4\pi\rho v_P^3 r} \left| R_{ij}^P \gamma_k \hat{M}_{jk} \right|, \tag{7.15}$$

$$\Omega_0^{FS} = |u_i^{FS}(\boldsymbol{x},\omega \to 0)| = \frac{dA}{4\pi\rho v_S^3 r} \left| R_{ij}^S \gamma_k \hat{M}_{jk} \right|. \tag{7.16}$$

Substituting Eq. 7.1 into Eq. 7.15 and 7.16, we obtain

$$\Omega_0^{FP} = \frac{M_0 F_P}{4\pi\rho v_P^3 r}, \tag{7.17}$$

$$\Omega_0^{FS} = \frac{M_0 F_S}{4\pi\rho v_S^3 r}, \tag{7.18}$$

where F_P and F_S are the radiation pattern correction factors for P- and S-waves,

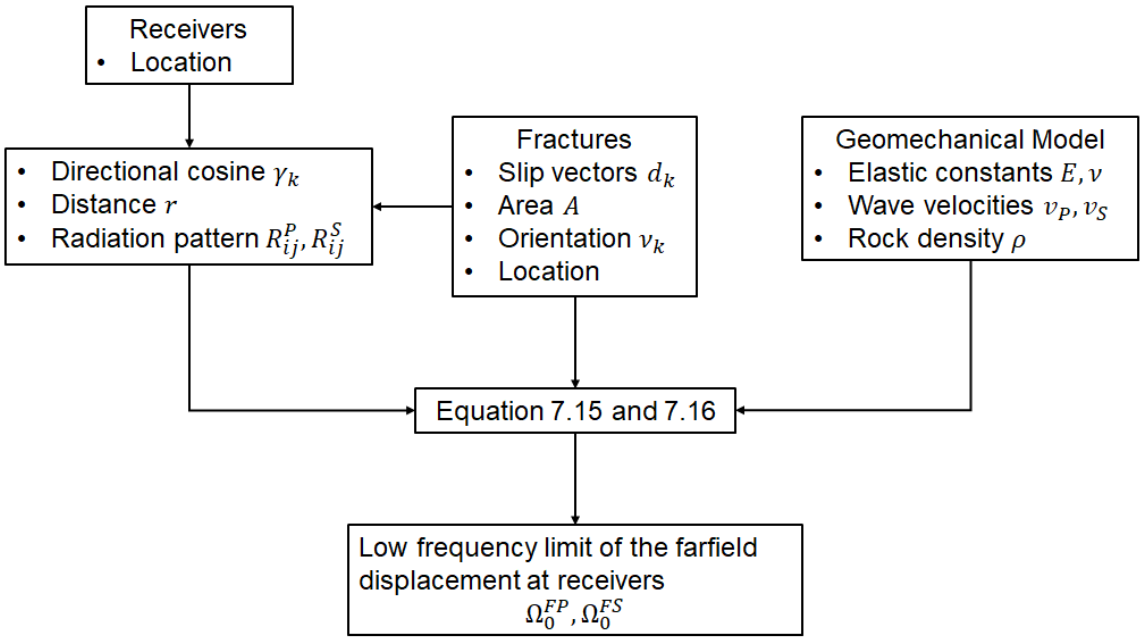

Figure 7.2: A flowchart of the forward modeling of microseismic events.

respectively. They are defined by

$$F_P := \frac{\left| R_{ij}^P \gamma_k \hat{M}_{jk} \right|}{G}, \tag{7.19}$$

$$F_S := \frac{\left| R_{ij}^S \gamma_k \hat{M}_{jk} \right|}{G}, \tag{7.20}$$

Since hydraulic fracturing simulations assume quasi-static condition, slip vectors computed from the simulations can be interpreted as the final slip in Eq. 7.14. Hence, the low frequency limit of the far-field displacements Ω_0^{FP} and Ω_0^{FS} correspond to the displacements at receivers computed from the simulations. Fig. 7.2 shows a flowchart of the forward modeling of microseismic events.

7.3 Inversion Analysis of Microseismic Data

7.3.1 Microseismic Event Location

The location of microseismic events is commonly estimated based on the arrival time analysis of P- and S-waves and the hodogram analysis of P-wave. While the former analysis yields the distance between a microseismic source and receivers, the latter analysis provides the direction from which wave propagated at receivers. Combining both results, the location of microseismic events can be obtained. The magnitude of microseismic events can be estimated from the polarity of P-wave and the low frequency limit of displacements. A schematic figure of the inversion analysis of microseismic data is shown in Fig. 7.3.

Let us assume a microseismic event occurs at time t_0. A receiver at an observation well detects the microseismic event at arrival times of P- and S- waves, t_P and t_S:

$$t_P = t_0 + \Delta t_P, \tag{7.21}$$

$$t_S = t_0 + \Delta t_S, \tag{7.22}$$

where $\Delta t_P = r/v_P$ and $\Delta t_S = r/v_S$ are travel times of P- and S-waves, respectively. Then, the distance from the receiver to the microseismic source can be computed from a differential arrival time of P- and S-waves (Eisner, et al., 2009):

$$r = \frac{v_P v_S}{v_P - v_S} \Delta t, \tag{7.23}$$

where $\Delta t = t_S - t_P = \Delta t_S - \Delta t_P$ is the differential arrival time between P- and S-waves.

The wave propagation direction of microseismic events is frequently estimated by

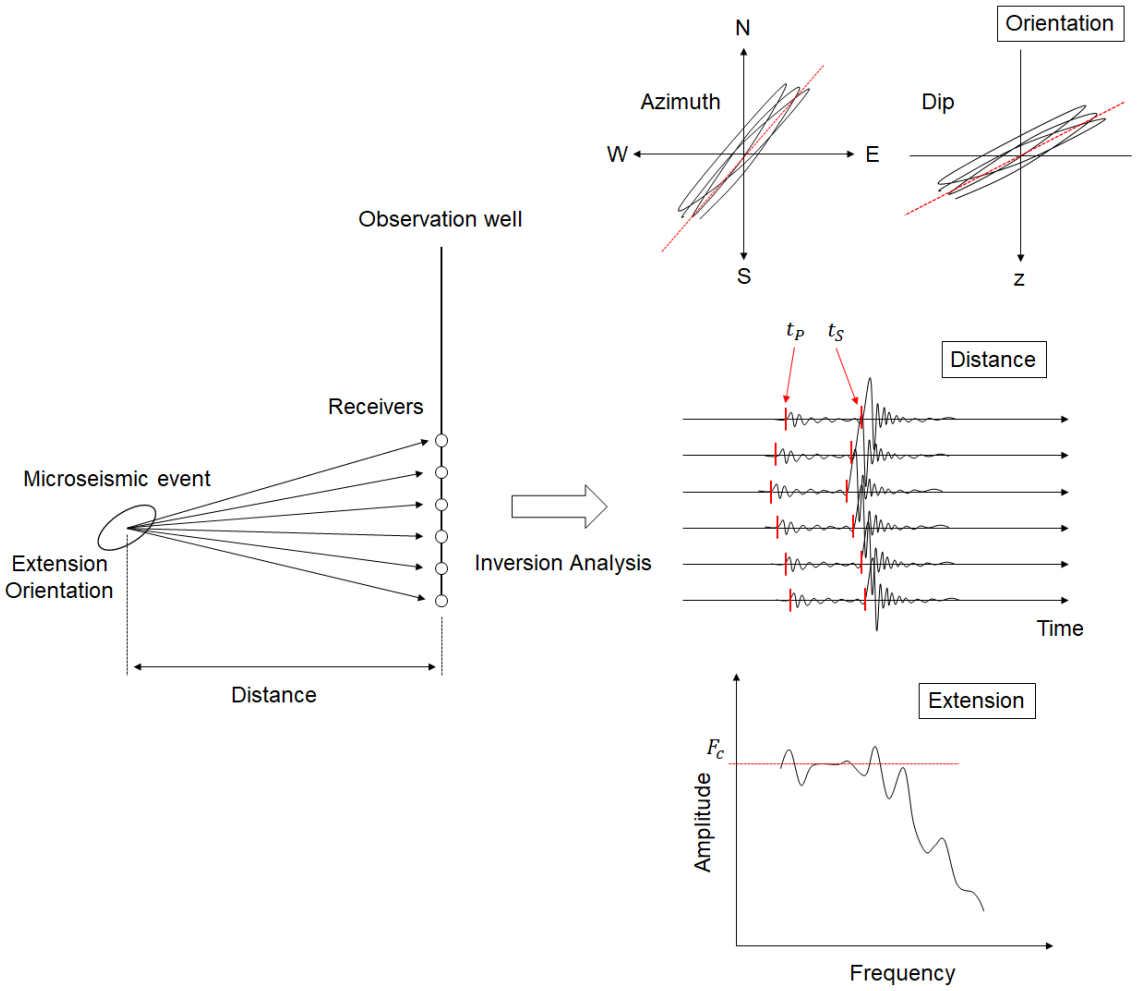

Figure 7.3: A schematic figure of the inversion analysis of microseismic data.

using hodogram analysis, which requires the full P waveform. The hodogram analysis is based on the fact that the polarization (the geometrical orientation of oscillation) and the propagation direction of P-wave are the same in homogeneous isotropic media. The hodogram analysis cannot be performed since the full waveform is not available in this dissertation. Instead, the wave propagation direction is given as the directional cosine γ_i in the forward modeling. The location of microseismic events are computed by

$$x_{si} = x_{ri} - r\gamma_i, \tag{7.24}$$

where x_{ri} and x_{ri} represents the location of source and receiver, respectively.

Ideally, the location of microseismic events can be exactly computed from Eq. 7.24 with only one receiver. In reality, however, multiple receivers installed in multiple observation wells are necessary to obtain an accurate location of microseismic events due to, for example, noise in observed data and errors associated with the location of receivers and arrival time picking. If the polarization measured at receivers contains an error, the different location of the microseismic event can be estimated for each receiver. In that cases, we simply average the estimated locations to obtain the location of the microseismic source:

$$x_{si} = \frac{1}{N_r}\sum_{j=1}^{N_r} x_{si} = \frac{1}{N_r}\sum_{j=1}^{N_r}\left(x_{ri}^j - r^j\gamma_i^j\right), \tag{7.25}$$

where N_r is the number of receivers, and the superscript j denotes the value at receiver j. A flowchart of the inversion analysis for the source location is presented in Fig. 7.4.

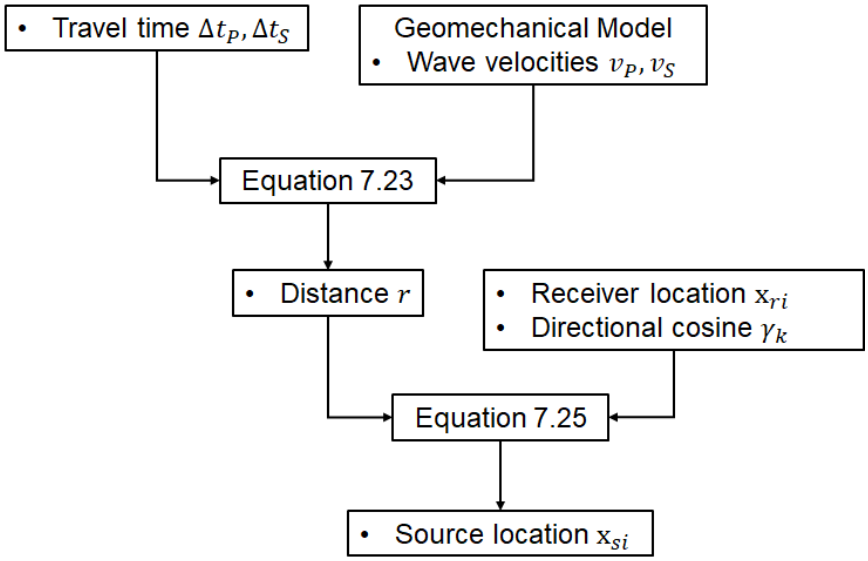

Figure 7.4: A flowchart of the inversion analysis for the location of microseismic events.

7.3.2 Seismic Moment

To estimate the seismic moment of microseismic events from seismic waves observed at observation wells, Eq. 7.1 cannot be used because A and d are unknown. Instead, Brune's equation is commonly used to evaluate seismic moment from measurements made at a receiver array (Brune, 1970; Gibowicz and Kijko, 1994; Warpinski et al., 2012):

$$M_0 = \frac{4\pi\rho c^3 r \Omega_0}{F_c}, \tag{7.26}$$

where ρ is rock density, c is the P- or S-wave velocity, Ω_0 is the low frequency amplitude of the displacement spectrum at a receiver, r is the distance from a receiver to an event, F_c is a correction factor for a radiation pattern. The root-mean-square (RMS) averages of radiation factor over the whole focal sphere $F_P = 0.52$ for the P-wave and $F_S = 0.63$ for the S-wave are generally used. Ω_0 is obtained by using the Fourier transform of the received signal. A flowchart of the inversion analysis of

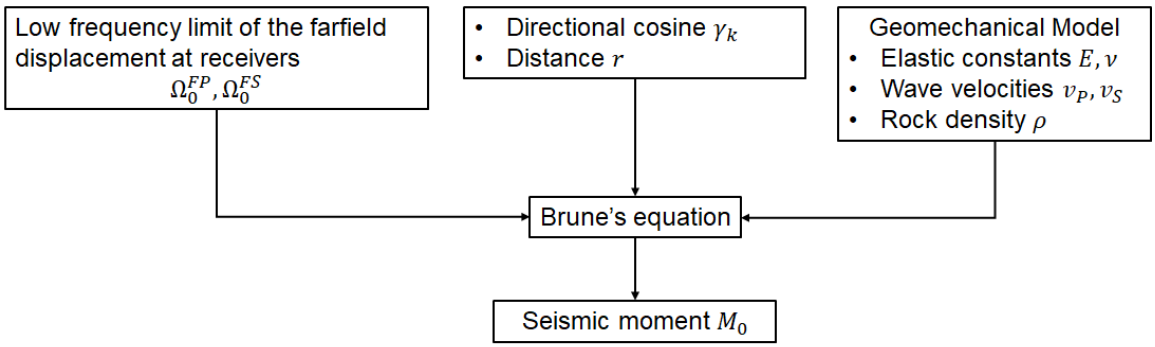

Figure 7.5: A flowchart of the inversion analysis for seismic moment.

seismic moment is shown in Fig. 7.5.

It should be mentioned that Eq. 7.26 and 7.17-7.18 are essentially equivalent. The difference is that the RMS of the radiation pattern correction factor is used in Eq. 7.26 since the direction of slip ν_k and the normal of fractures n_k in the moment tensor are not readily available. Obtaining ν_k and n_k, or equivalently M_ij, from observed waveforms is referred to as moment tensor inversion (MTI).

7.4 Application

7.4.1 Procedures

The forward modeling of microseismic events by using the result of hydraulic fracturing simulations in Chapter 6 and the inversion analysis of the synthetic microseismic events are performed in this section. First, synthetic receivers are placed along observation wells. Next, polarization, travel times, and the low frequency limit of far-field displacements at the receivers are generated for each microseismic event through the forward modeling. Finally, the location and seismic moment of the synthetic events are estimated through the inversion analysis.

The elastic moduli used in this chapter are not static moduli but dynamic ones. They are different from the static elastic moduli used in Chapter 6. The dynamic

Table 7.1: The P- and S-wave velocities, rock density, and dynamic elastic moduli. The wave velocities are estimated from Figure B-1 in Stegent and Candler (2018).

P-wave velocity	4000 m/s
S-wave velocity	2350 m/s
Rock density	3000 kg/m^3
Young's modulus	40.97 GPa
Poisson's ratio	0.2365
Shear modulus	16.57 GPa

elastic moduli can be computed from the P- and S-wave velocities:

$$E = \frac{\rho v_S^2(3v_P^2 - 4v_S^2)}{v_P^2 - v_S^2}, \tag{7.27}$$

$$\nu = \frac{v_P^2 - 2v_S^2}{2(v_P^2 - v_S^2)}, \tag{7.28}$$

where ρ is rock density, E is Young's modulus, and ν is Poisson ratio. The P- and S-wave velocities are estimated from Figure B-1 in Stegent and Candler (2018). These properties are summarized in Table 7.1.

Only the failure containing shear components are used in the forward modeling because the field observations show that shear failures are dominant in microseismic events in hydraulic fracturing (Nolen-Hoeksema and Ruff, 2001). The following criterion is used to filter shear failures:

$$\frac{\Delta_t}{\Delta_n} \geq 2, \tag{7.29}$$

where Δu_t and Δu_n are the magnitude of the tangential and normal components of displacement discontinuity, respectively.

7.4.2 The Locations and Moment Magnitudes of Microseismic Events

Case 1: One Observation Well without Noise

In Case 1, the simulation result of Fig. 6.10a is used for the forward modeling and the inversion analysis. A synthetic observation well (Well No. 1) is placed at $(x, y) = (50, 50)$, and receivers are installed at every 5 m from $z = -20$ to 20 along the wellbore. Noise is not introduced in the forward modeling step in this case.

Fig. 7.6 shows the moment magnitude and the location of synthetic microseismic events generated from the simulation result of Fig. 6.10a. Most of the moment magnitudes lie between -3 to -1, which agrees with the moment magnitudes observed in field experiments (Warpinski et al., 2012). It is found that all of the event locations lie exactly on the paths of hydraulic fractures. This is because noise is not added to the observed data, and thus we can recover the exact locations. We found that all of the event locations shown in Fig. 7.6 occur along natural fractures which are hydraulically connected and become a part of hydraulic fractures. The orientation of natural fractures can be estimated from some consecutive event locations.

Fig. 7.7 shows the moment magnitudes estimated using Brune's equation against those computed by using Eq. 7.1 for P- and S-waves. The moment magnitude produced from Eq. 7.1, which is the definition of the seismic moment, are correct. It is found that the correct moment magnitudes cannot be recovered even in this idealized case without noise and attenuation. This is because the average of the radiation pattern correction factor is used in Brune's equation.

To verify that using the average of the radiation pattern correction factor causes the deviation, the moment magnitudes are estimate by using Brune's equation with the correct radiation pattern correction factor computed by using Eq. 7.19 and 7.20. The result is shown in Fig. 7.8. The fact that the estimated and correct moment

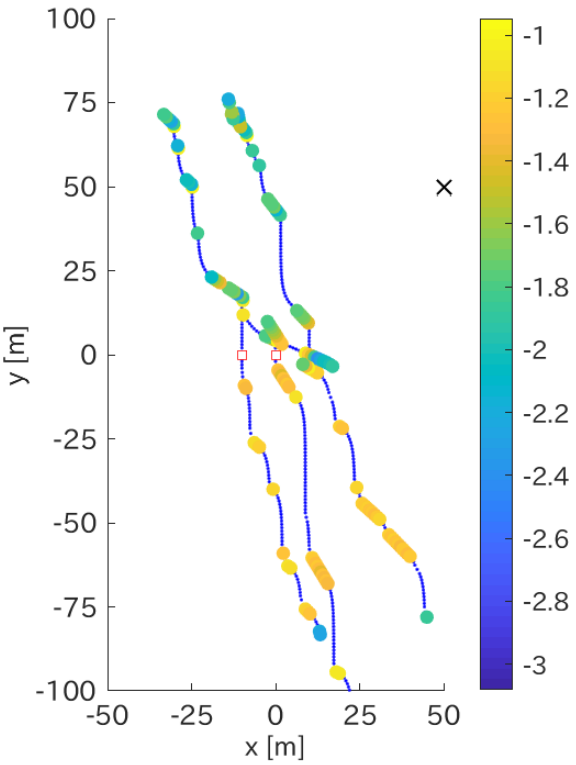

Figure 7.6: The moment magnitude and the location of the synthetic microseismic events estimated from the simulation result of Fig. 6.10a. The observation well is shown as a black cross. The color map represents the moment magnitude.

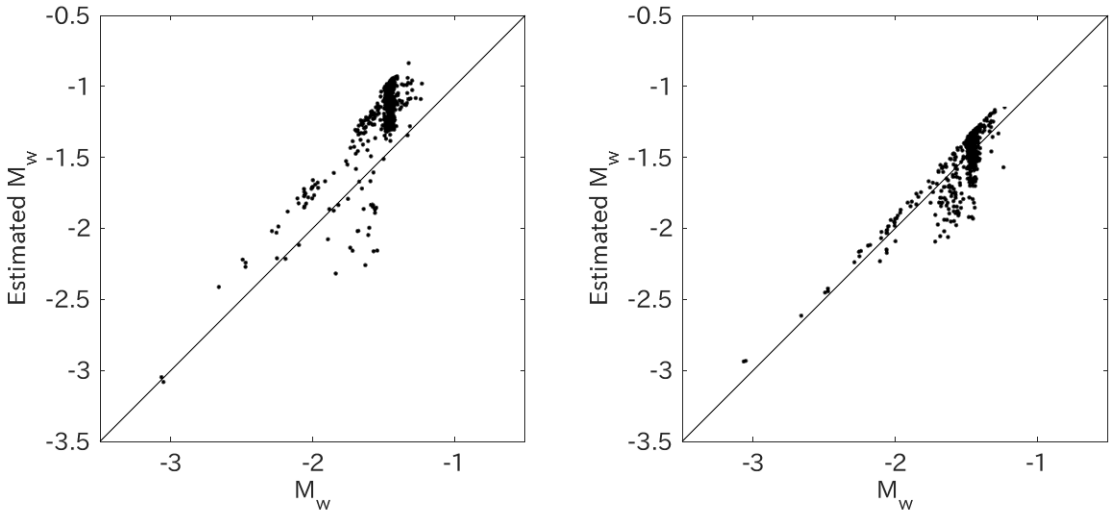

(a) P-wave (b) S-wave

Figure 7.7: The moment magnitudes estimated by using the Brune's equation against the moment magnitudes computed by using Eq. 7.1.

magnitudes matches exactly in Fig. 7.8 clearly indicates that the error in the estimated moment magnitudes using Brune's equation in Fig. 7.7 is caused by the usage of the average radiation pattern correction factor. We must cover the focal sphere of seismic sources as much as possible to estimate the radiation pattern correction factor, which is equivalent to placing many observation wells at different angles relative to the sources.

Case 2: One Observation Well with Noise

In Case 2, noise is added to the directional cosine γ_i and the differential travel time Δt generated in Case 1. The inversion analysis is then performed against the noisy data. The noise to the directional cosine is created as a normal distribution of rotation angles around the z-axis. The directional cosine is horizontally rotated by using the angle. The standard deviations of the normal distributions for noise are

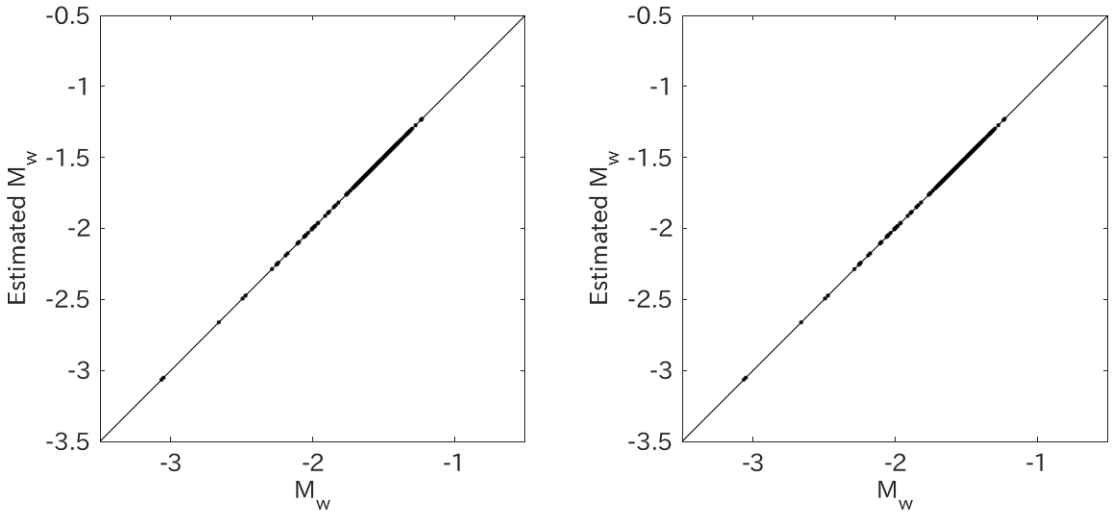

(a) P-wave (b) S-wave

Figure 7.8: The moment magnitudes estimated by using the Brune's equation with the correct radiation pattern correction factor against the moment magnitudes computed by using Eq. 7.1.

Table 7.2: The standard deviation of the normal distributions for noise.

Case name	Small noise	Large noise
Horizontal rotation angle for γ_i	45°	10°
Travel Time	2 ms	5 ms

shown in Table 7.2.

Fig. 7.9 shows the moment magnitude and the location of microseismic events estimated from the synthetic data containing noise. In contrast to Fig. 7.7, which does not contain noise, it is difficult to estimate the orientation of natural fractures from Fig. 7.9. The microseismic events are distributed around natural fractures, creating microseismic clouds. As the noise level becomes larger, the location of microseismic event becomes more dispersed. While it can be analyzed based on the event locations that two hydraulic fractures are growing in Fig. 7.9a, no clear fracture path

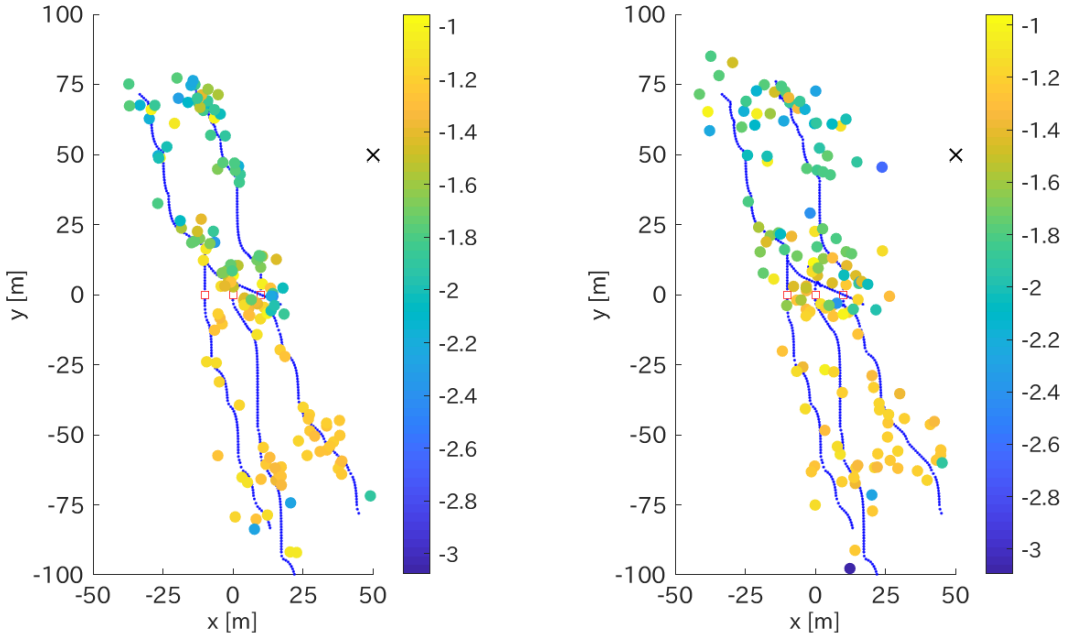

(a) Small noise

(b) Large noise

Figure 7.9: The moment magnitude and the location of the synthetic microseismic events estimated from the simulation result of Fig. 6.10a. The observation well is shown as a black cross. The color map represents the moment magnitude.

can be found in Fig. 7.9b. We can only state that hydraulic fractures are growing in the direction NNW-SSE. Therefore, it is critical to use microseismic data containing less noise to analyze the location and orientation of natural fractures and hydraulic fracture paths accurately.

Two Observation Wells with Noise

In Case 3, an additional synthetic observation well (Well No. 2) is placed at $(x, y) = (50, -50)$ with the same configuration of receivers with Well No. 1 to evaluate the effect of the focal coverage. The simulations of Case 1 and 2 are used to generate synthetic microseismic events. The small and large noise cases are analyzed as well

as Case 2.

Fig. 7.10 shows the moment magnitude and the location of microseismic events estimated from the synthetic data with noise measured at two observation wells. Comparing Fig. 7.10 with Fig. **??**, the microseismic events are mapped more closely to hydraulic fracture paths in Fig. 7.10. Let us define the error of microseismic event locations:

$$\epsilon := \sqrt{\frac{1}{N_s}\sum_{j=1}^{N_s} \|\boldsymbol{x}_{si} - \boldsymbol{x}_{si}^*\|^2}, \tag{7.30}$$

where N_s is the number of event locations, and the superscript $*$ denotes the correct value.

Fig. 7.11 shows the error of the event locations for different noise levels and the number of observation wells. It clearly shows that the error is reduced by using two observation wells compared to by using single observation well. Since the microseismic waves measured at observation wells always contain some noise, multiple observation wells are preferable to reduce the effect of noise and increase the accuracy of microseismic event locations.

7.4.3 The Slip, Orientation and Area of Fractures

In Case 1, we found that an accurate radiation pattern correction factor is required to obtain accurate seismic moments. In this section, we analyze whether the radiation pattern correction factor can be recovered through inversion analysis. Since the radiation pattern correction factor is composed of the direction of slip, the orientation of the fracture surface, and the wave propagation direction, it is equivalent with the inversion analysis of the slip and orientation of fractures from microseismic

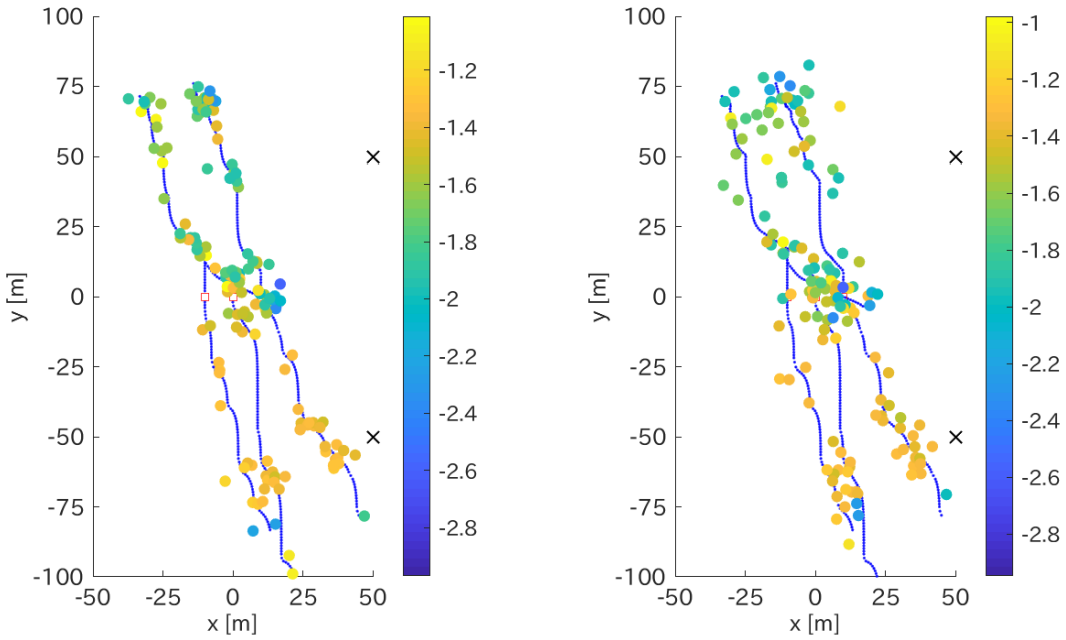

(a) Small noise

(b) Large noise

Figure 7.10: The moment magnitude and the location of the synthetic microseismic events estimated from the simulation result of Fig.6.10a. The observation wells are shown as black crosses. The color map represents the moment magnitude.

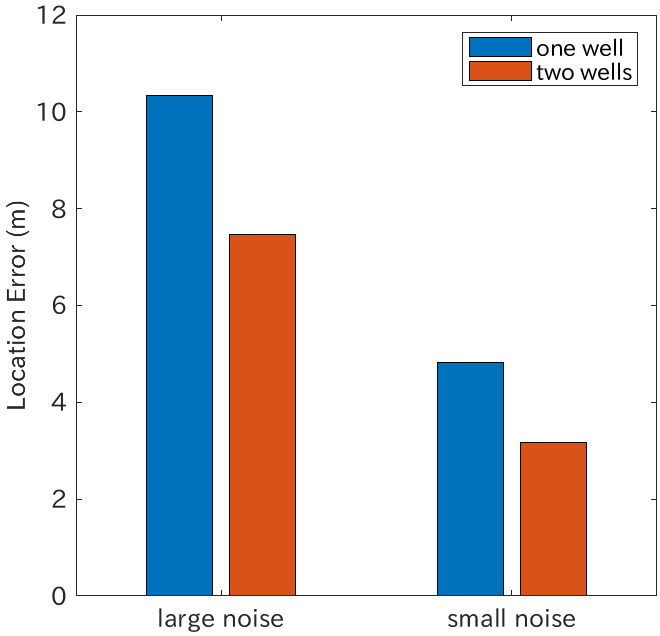

Figure 7.11: The error in the microseismic event locations.

data. The objective function to perform the inversion analysis is defined by

$$f := \sum_{i=1}^{N_r} \left[\left(\Omega_{0i}^{FP} - \Omega_{0i}^{FP*} \right)^2 + \left(\Omega_{0i}^{FS} - \Omega_{0i}^{FS*} \right)^2 \right] \tag{7.31}$$

where the subscript i denotes the receiver ID, and the superscript $*$ denotes the measured values. The low frequency limit of displacements in Eq. 7.31 is computed by using Equation Eq. 7.17 and 7.18. The matching parameters of the objective function are:

1. Fracture orientation, θ_f and ϕ_f in spherical coordinates.
2. Slip direction, θ_s and ϕ_s in spherical coordinates.
3. The magnitude of slips, d
4. The area of fractures, A.

The objective function is the function of the above parameters, $f = f(\theta_f, \phi_f, \theta_s, \phi_s, d, A)$. The normal vector of fractures n_i and the slip direction ν_i which appear in the radiation pattern correction factor are computed from the spherical coordinates:

$$n_i = \begin{bmatrix} \sin\theta_f \cos\phi_f & \sin\theta_f \sin\phi_f & \cos\theta_f \end{bmatrix}^T, \tag{7.32}$$

$$\nu_i = \begin{bmatrix} \sin\theta_s \cos\phi_s & \sin\theta_s \sin\phi_s & \cos\theta_s \end{bmatrix}^T. \tag{7.33}$$

To simplify the problem, we use a synthetic seismic source placed at the origin. The source is a vertical fracture whose normal vector is $(-1/\sqrt{2}, 1/\sqrt{2}, 0)$ and a pure shear failure whose slip direction is $(1/\sqrt{2}, 1/\sqrt{2}, 0)$. The magnitude of the slip is 1 mm, and the fracture area is $4\,\mathrm{m}^2$.

Two cases of observation well configurations are tested. Case 1 places receivers in a single vertical observation well at $(x, y) = (50, 0)$ from $z = -20$ to 20 m for every 5 m. Case 2 places receivers in two vertical observation wells at $(x, y) = (50, 0)$ and $(50, -20)$ at the same depths. Fig. 7.12 shows the location of the receivers and the fracture orientation and slip directions.

Since Eq. 7.31 is a nonlinear equation, a nonlinear optimization technique is required to perform the inversion analysis. After testing several methods provided by Matlab, he particle swarm function is selected as the optimization method used in the inversion analysis.

Case 1: One Observation Well

First, we start with Case 1. Table 7.3 shows the estimated parameters through the inversion analysis. Fig. 7.13 shows the correct and estimated low frequency amplitude for the P- and S-waves, and Fig. 7.14 shows the correct and estimated radiation

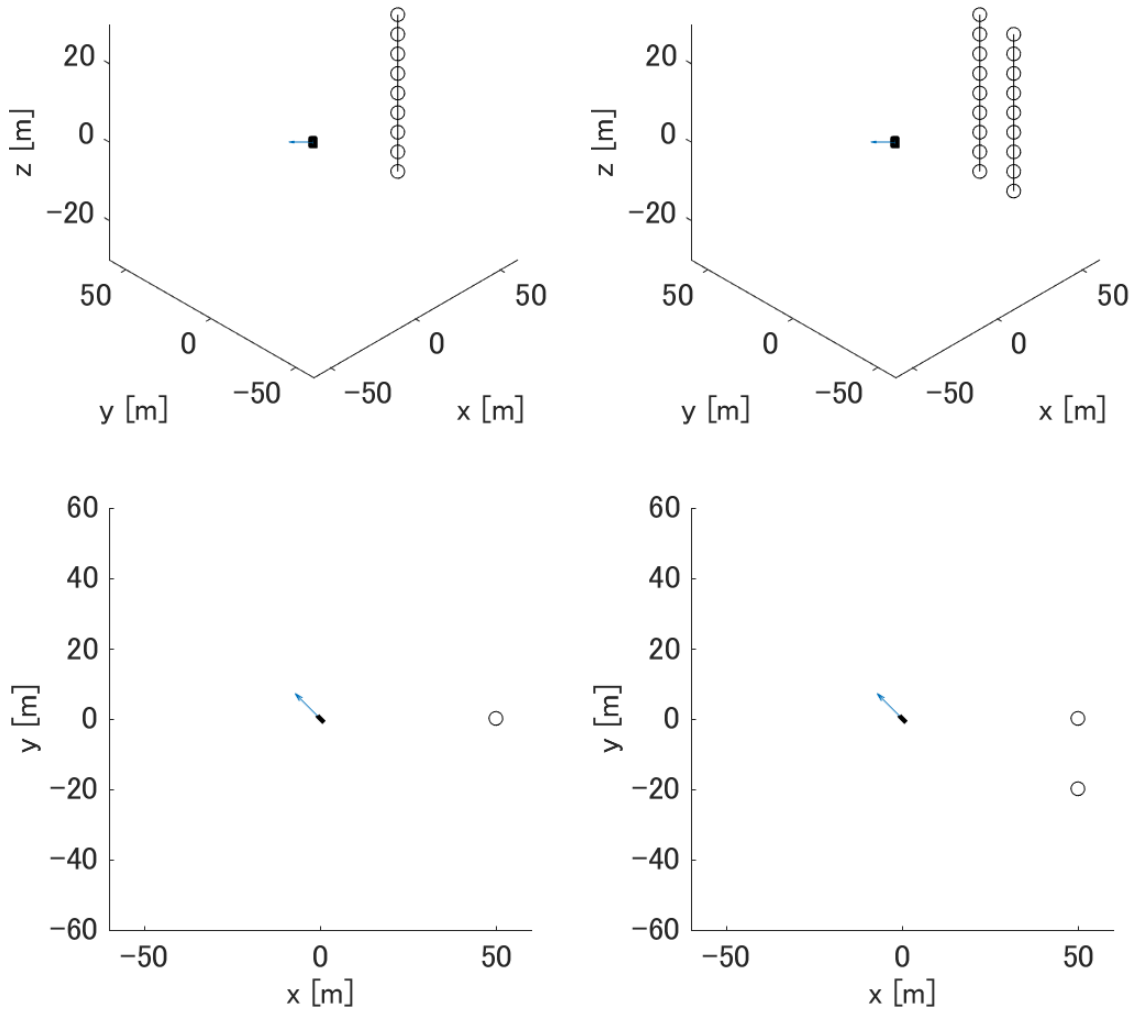

(a) Case 1

(b) Case 2

Figure 7.12: The location and orientation of a synthetic seismic source and receiver arrays. The arrow represents the slip direction. Lines represents observation wells, and circles represent receivers. Upper figures are a 3D view, and the lower figures are a plan view.

Table 7.3: The estimated parameters through the inversion analysis of Case 1.

θ_f	80.1548°
ϕ_f	138.5321°
θ_s	80.1549°
ϕ_s	41.4678°
d	0.0018 m
A	1.9276 m^2

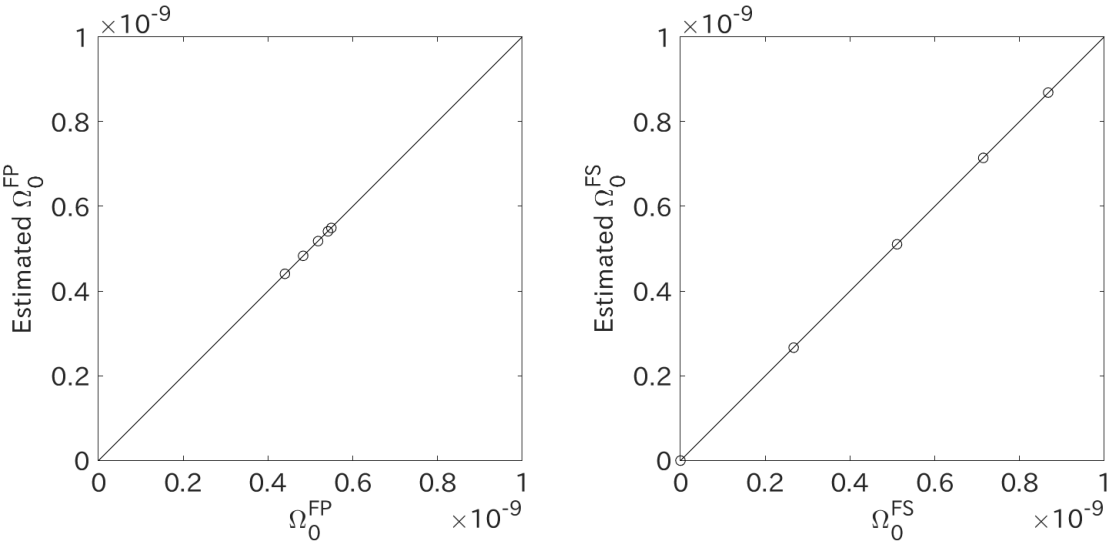

Figure 7.13: The measured and estimated low frequency amplitude at each receiver for Case 1.

pattern correction factor. As shown in Fig. 7.13, the low frequency amplitude estimated from the matching parameters by using Eq. 7.17 and 7.17 exactly matched the measured values. However, we could not match the radiation pattern correction factor as shown in Fig. 7.14. This is due to the multiple local minima existing in Eq. 7.31. Moreover, we could not obtain the correct slip magnitude and fracture area.

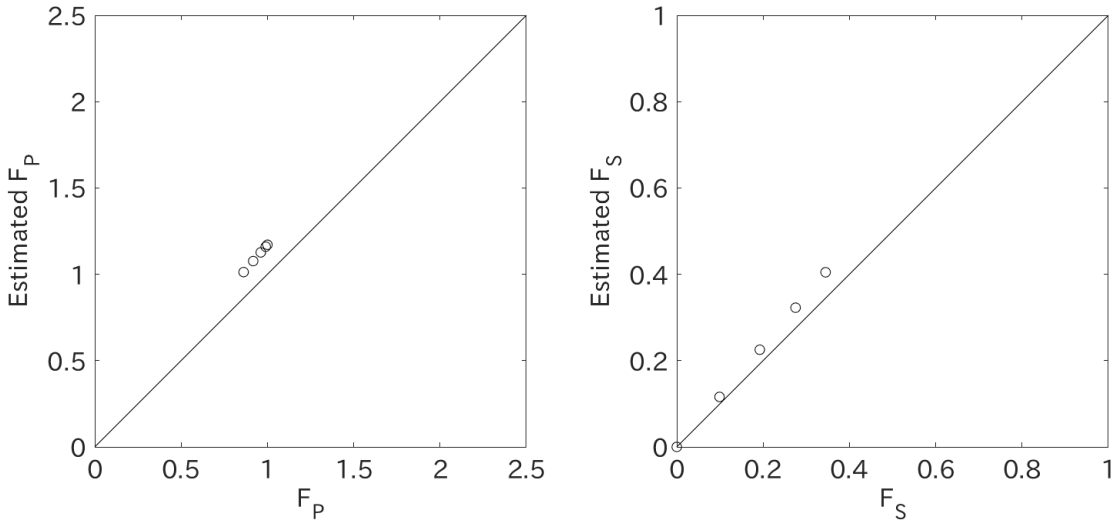

Figure 7.14: The computed and estimated radiation pattern correction factor at each receiver for Case 1.

Case 2: Two Observation Wells

Next, the same inversion analysis was performed for Case 2 to analyze the effect of the number of observation wells. Table 7.4 shows the estimated parameters through the inversion analysis. Fig. 7.15 shows the measured and estimated low frequency amplitude for the P- and S-waves, and Fig. 7.16 shows the measured and estimated radiation pattern correction factor for the P- and S-waves. In this case, we could recover both the low frequency amplitude and the radiation pattern correction factor for the P- and S-waves. Moreover, the slip magnitude and the fracture area are more accurately estimated compared to Case 1.

This result indicates the importance of using multiple observation wells. Measuring microseismic events at multiple observation wells is equivalent with covering the focal sphere of the seismic sources to understand the radiation pattern. Then, we can estimate the normal and slip directions of fractures more accurately since the radiation pattern originates from the normal and slip directions of fractures as described

Table 7.4: The estimated parameters through the inversion analysis of Case 2.

θ_f	90.0000°
ϕ_f	135.0000°
θ_s	90.0000°
ϕ_s	45.0000°
d	0.0013 m
A	3.1536 m^2

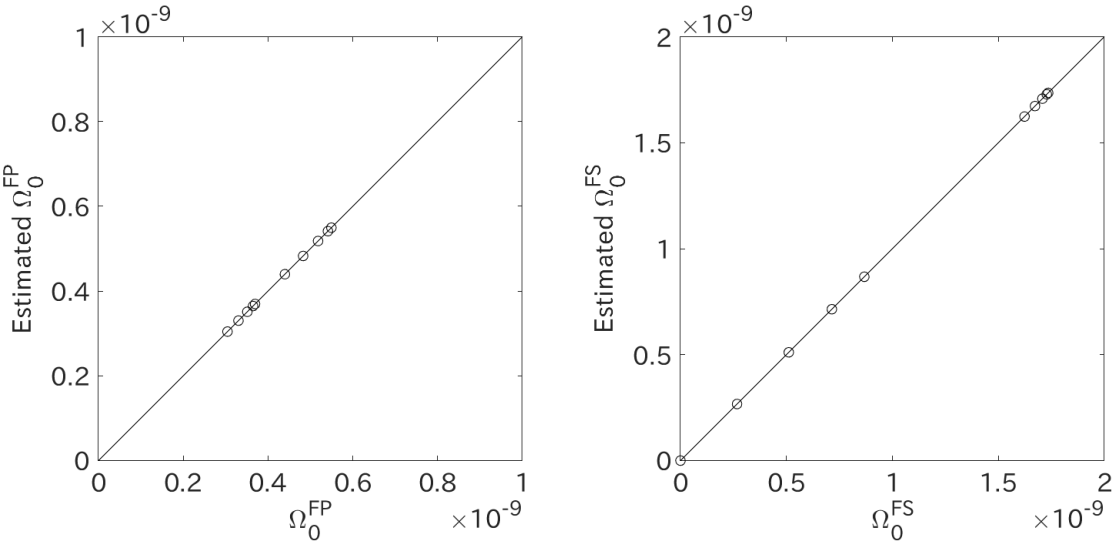

Figure 7.15: The measured and estimated low frequency amplitude at each receiver for Case 2.

in Eq. 7.19 and 7.20.

Case 3: Two Observation Wells with Noise

Finally, the effect of noise to the inversion analysis is analyzed. The noise generated from normal distributions is added to the low frequency amplitude measured at receivers. Two noise levels are considered: small and large noise. The standard deviations of the normal distribution for noise are listed i Table 7.5. The same seismic source and well configuration with Case 2 are used for Case 3.

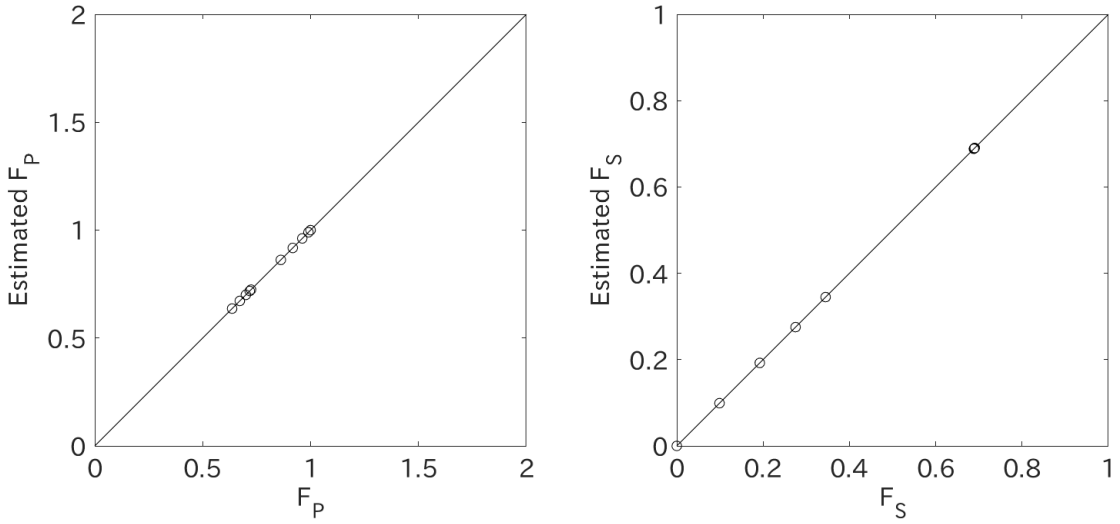

Figure 7.16: The computed and estimated radiation pattern correction factor at each receiver for Case 2.

Table 7.5: The standard deviation of the normal distributions for noise.

Case	Standard deviation
Small noise	5% of the maximum Ω_0^{FP} and Ω_0^{FS}
Large noise	20% of the maximum Ω_0^{FP} and Ω_0^{FS}

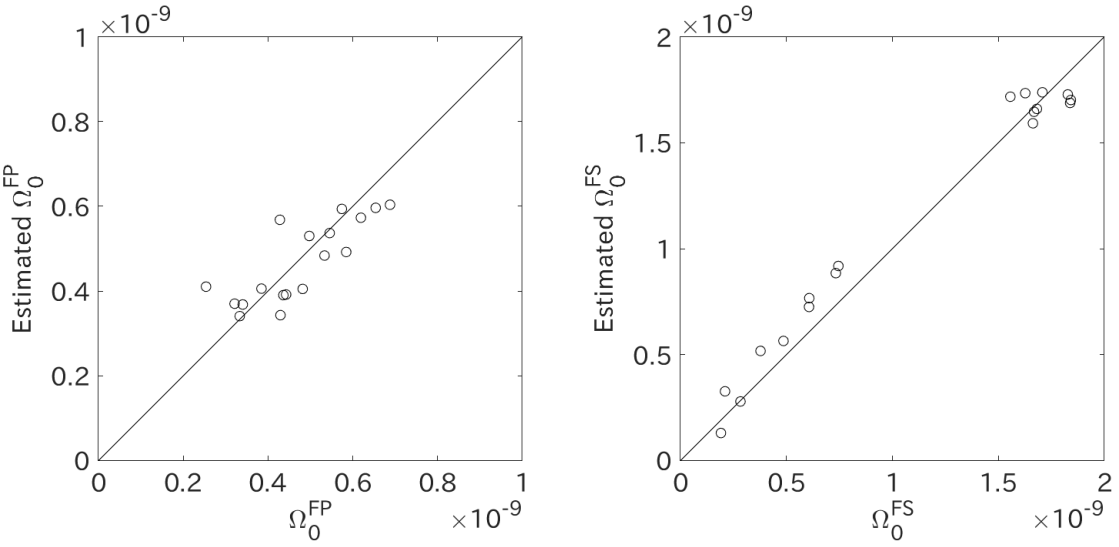

Figure 7.17: The measured and estimated low frequency amplitude at each receiver for Case 3 with small noise.

Fig. 7.17 and 7.18 shows the radiation pattern correction factor and the low frequency amplitude for P- and S-waves in the case of small noise. Fig. 7.19 and Eq. 7.20 shows the radiation pattern correction factor and the low frequency amplitude for P- and S-waves in the case of large noise. It is found the deviation between the estimated and measured low frequency amplitude is much smaller in the case of small noise compared to in the case of large noise. In contrast, the radiation pattern correction factors are estimated in a reasonable accuracy in both cases. This can be explained by the fact that the radiation pattern depends on the direction from the sources while the amplitude is primarily a function of the distance from the sources. Since two wells placed at different angles at similar distances from the source to cover the focal sphere of the synthetic seismic source, the radiation pattern correction factor is easier to fit through the inversion analysis.

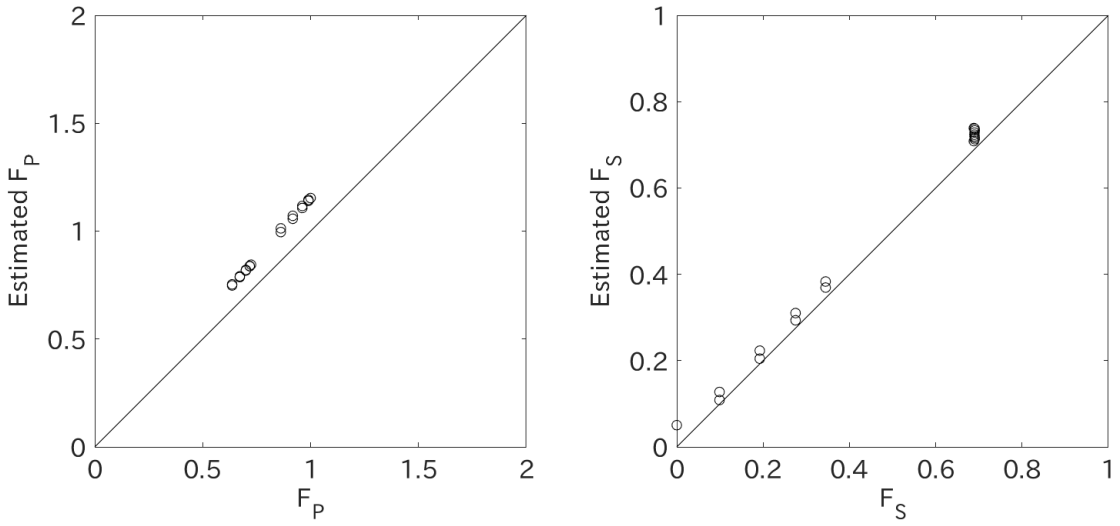

Figure 7.18: The computed and estimated radiation pattern correction factor at each receiver for Case 3 with small noise.

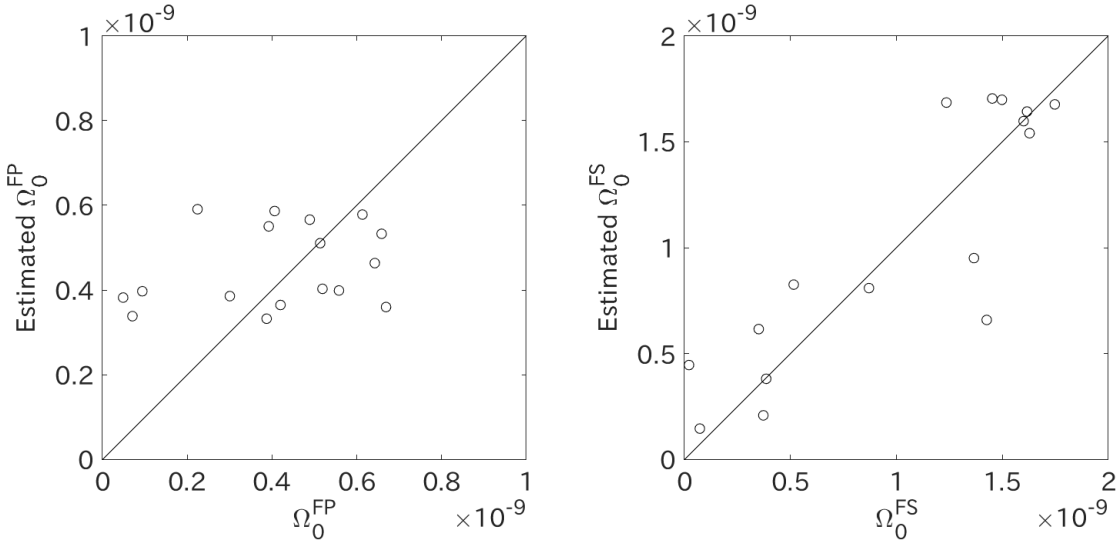

Figure 7.19: The measured and estimated low frequency amplitude at each receiver for Case 3 with large noise.

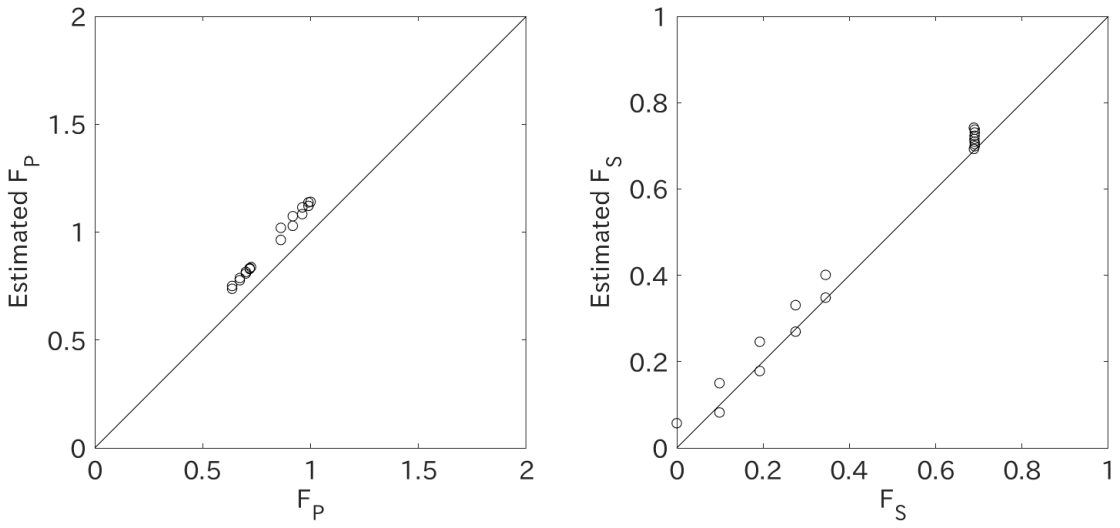

Figure 7.20: The computed and estimated radiation pattern correction factor at each receiver for Case 3 with large noise.

7.5 Conclusion

Synthetic microseismic events were generated from hydraulic fracturing simulations by assuming a homogeneous isotropic medium. The forward modeling of microseismic events by using the result of hydraulic fracturing simulations is proposed based on the seismology. The inversion analysis of synthetic microseismic data is formulated in a simple way by using Brune's equation and the differential arrival time analysis.

The moment magnitude of the microseismic events were mapped on hydraulic fracture paths. We found that the moment magnitudes of the microseismic sources estimated by using Brune's equation contain an error even without noise. The error originated from using the average radiation pattern correction factor. When noise is added to the measured synthetic data, the location of the microseismic events became dispersed, and microseismic clouds are generated similar to the microseismic monitoring in real fields. As noise became larger, the extension of the microseismic clouds became larger. We demonstrated the effect of the error can be mitigated by using multiple observation wells.

We also performed the inversion analysis of synthetic microseismic data to estimate the source parameters of microseismic events, i.e. the orientation and area of fractures, and the magnitude direction of slip. It is found that one observation well is not enough for the accurate estimation of the source parameters even in the case of noise-free. Using two observation wells, the source parameters are estimated more accurately. In addition, it became more resilient against noise.

Chapter 8: Conclusion and Future Work

The displacement discontinuity method (DDM) was extended and applied to hydraulic fracture modeling in heterogeneous rocks which contain layers and natural fractures. In this chapter, we summarize the conclusions and the future work.

8.1 Conclusion

8.1.1 Displacement Discontinuity Method for Layered Media

A new displacement discontinuity method (DDM) for layered media was developed based on the method of images. The influence coefficients of the new DDM were computed by numerically integrating the image solutions of kernel functions. Application to three-layered media in a plain strain condition showed the following conclusions:

1. Higher-order elements are more accurate than constant elements.
2. The number of Gauss points for numerical integration does not have a large impact on the accuracy of fracture width in the three-layered media.
3. The effect of the number of image solutions depends on the orientation of the fractures in the three-layered media. For vertical cracks, one image solution is enough to compute fracture width in reasonable accuracy.
4. Larger contrast of shear modulus between layers requires more image solutions. For vertical cracks, one image solution is enough to compute fracture width in reasonable accuracy up to the shear modulus contrast of 5.

8.1.2 DDM-Based Hydraulic Fracturing Model

A DDM-based hydraulic fracturing model was developed. The elastic response of fractures was described by using DDM, and the fluid flow inside fractures was modeled by using the finite volume method. A coupled system of the DDM and flow equations were solved with segregated and fully coupled methods. A new splitting scheme, fracture compliance splitting scheme, was proposed to improve the convergence speed of segregated methods. The hydraulic fracturing model was validated with the analytical solutions for radially growing fractures.

1. Fixed-width splitting scheme requires a large number of iterations due to its small relaxation factor. This large number of iterations negates the advantages of segregated methods: less memory requirement and easy implementation.
2. Fracture compliance splitting scheme enables us to use relaxation factors much larger than the fixed-width splitting scheme. This improves the convergence speed of segregated methods.
3. The importance of scaling and preconditioning procedures in the fully coupled method was shown.
4. The comparison of the fully-coupled and segregated methods revealed that the fully coupled method is effective to improve convergence speed. We found the fully coupled method did not require any relaxation.
5. The fully coupled method was faster than segregated methods for a fracture propagation problem of a 2D single planar fracture. Therefore, the fully coupled method should be used for small problems. For large problems, the segregated methods can be suitable since the fully coupled method can become computationally more expensive.

8.1.3 Interaction Between Hydraulic and Natural Fractures

The interaction between hydraulic and natural fractures were modeled. Crossing criteria for hydraulic and natural fractures were reviewed. The crossing criteria based on the Mohr-Coulomb criterion, energy release rate, and stress intensity factors (SIFs) were explained in detail. Comparison with experimental results led to the following conclusions:

1. Crossing criteria based on energy release rates and SIFs do not change the crossing behavior of hydraulic fractures. Natural fractures break after a hydraulic fracture is deflected more easily in the case of the energy-based criterion than the SIF-based criterion due to the contribution of the mode II SIF.
2. The crossing behavior of hydraulic fractures depends on horizontal stress contrasts if the Mohr-Coulomb-based criterion is used.

The remote failure of natural fractures which are not connected to hydraulic fractures was modeled by using the Mohr-Coulomb criterion. The increase of pore pressure due to poroelastic effects was taken into account by assuming an undrained condition in DDM. From sensitivity analysis, the following conclusions were derived:

1. The pore pressure increase due to poroelastic effect under the undrained condition has little effect on the remote failure of natural fractures.
2. Elastic stress change caused by hydraulic fracture propagation can trigger shear failure of natural fractures not connected to hydraulic fractures only in the vicinity of hydraulic fractures.

8.1.4 Hydraulic Fracturing Simulations in Naturally Fractured Rocks

Hydraulic fracturing simulations in synthetic natural fracture networks were performed. Natural fractures were statistically distributed by using the power-law dis-

tribution for fracture length and the von Mises distribution for fracture azimuth. We ignored the end-to-end connections of elements for simplification and corrected the influence coefficients of DDM to avoid singularity problems.

1. Hydraulic fractures intersect natural fractures more in the case of a=2 for the power-law distribution than a=3.
2. Remote failure of natural fractures creates more branches. Thus it creates more complex fracture networks.
3. Large horizontal stress contrasts force hydraulic fractures to propagate in the maximum horizontal stress direction. We observed hydraulic fractures which are deflected in natural fractures immediately turn in the maximum horizontal stress direction after they reach at an edge of natural fractures in the case of large stress contrasts.
4. Comparing two natural fractures with different areal densities, hydraulic fractures intersected natural fractures more frequently in denser natural fracture networks, and consequently more branches and merges were observed.
5. Bimodal distributions for fracture orientation generated more branches and merges compared to unimodal distributions. Field observation indicates multimodal distribution for natural fracture orientation. Thus, it is essential to incorporate multiple mode in fracture orientations.

8.1.5 Modeling of Microseismic Events

Synthetic microseismic events were generated from the hydraulic fracturing simulation results in Chapter 6. The areal map of moment magnitudes of the microseismic events was presented. In addition, inversion analysis of microseismic events was performed in terms of the low frequency amplitudes of synthetic seismic events and the radiation pattern correction factor. These analyses led to the following conclusions:

1. The moment magnitudes estimated by using Brune's equation contain the error which originates from the average radiation pattern correction factor.
2. The noise in the measured microseismic data made the location of the microseismic events less accurate, and microseismic clouds were generated. It is important to reduce the noise to analyze the growth of hydraulic fractures from microseismic monitoring.
3. One observation well is not enough for the inversion analysis of microseismic data to estimate the source parameters due to the inadequate coverage of focal sphere of microseismic sources.
4. Multiple observation wells are essential not only to estimate the source parameters but also to be resilient against noise in the microseismic data.

8.2 Future Work

The hydraulic fracturing model developed in this dissertation utilized rectangular elements for 3D DDM and a slightly compressible fluid without proppant transport for fluid flow inside fractures to simplify its formulation. Thus, the following extensions can be made to our model:

1. The geometry of fractures can be approximated better with triangular elements proposed by Kuriyama and Mizuta (1993) than with rectangular elements. Although their analytical solution becomes singular along the extension of any edge of triangular elements, this singularity problem can be avoided by using the BEM solution developed by Davey and Hinduja (1989).
2. Proppant transport equations can be added to the coupled system of equations in our model. The proppant distribution in hydraulic fractures is important to evaluate fracture conductivity in production period. One way is to iteratively couple the DDM-flow equations and proppant transport equation as described

in Shrivastava and Sharma (2018a).

3. Our model can be extended to non Newtonian fluids such as power-law fluids. Since non Newtonian fluids increase the nonlinearity of the flow equation, a nonlinear solver might be required instead of the current linear solver.

4. Current bottleneck of the performance of our fracturing model lies in solving the dense linear system of equations. The computation speed of this part can be much improved by using fast solvers such as the adaptive cross approximation method, adaptive integral method, and fast multipole method. These fast solvers have been developed for solving dense linear system of equations which arises in the boundary element method (BEM). Since we demonstrated the equivalence of BEM and DDM, the fast solvers can be directly applicable to our model.

5. The poroelastic effect was incorporated into our model by assuming an undrained condition. This assumptions is valid only for reservoirs with very low permeability and during fracturing operations. The undrained condition can be violated for reservoirs with non-negligible permeability or during production period. In these cases, we have two options: (1) use DDM for poroelastic media, (2) couple our model with reservoir simulator. DDM for poroelastic media is computationally more expensive than the conventional DDM because of its complicated Green's function and time integration. On the other hand, coupling our model with reservoir simulators requires some theoretical work to incorporate depletion of formations into our model.

6. In this dissertation, microseismic events were modeled without considering a source model, which is stress and the velocity of slip as a function of time. Combining a source model with our model is the next step to analyze dynamic behavior of natural fracture failure.

Appendices

Appendix A: Kernel Functions

A.1 Kernel Functions of BEM

The explicit form of the kernel functions is available for homogeneous isotropic linear elastic media. For 2D problems, it is given by (Gao and Davies, 2002; Liu, 2009)

$$U_{ij}(y;x) = -\frac{1}{8\pi G(1-\nu)}\left\{(3-4\nu)\delta_{ij}\ln r - r_{,i}r_{,j}\right\}, \tag{1}$$

$$\begin{aligned} T_{ij}(y;x) = &-\frac{1}{4\pi G(1-\nu)r^2}\left\{(1-2\nu)(n_i r_{,j} - n_j r_{,i})\right. \\ &\left. + (2\,r_{,i}r_{,j} + (1-2\nu)\delta_{ij})\,n_k r_{,k}\right\}, \end{aligned} \tag{2}$$

$$K_{ij}(y;x) = \frac{1}{4\pi(1-\nu)r}\left\{(1-2\nu)(r_{,k}n'_k\delta_{ij} + r_{,i}n'_j - n'_i r_{,j}) + 2\,r_{,k}n'_k r_{,i}r_{,j}\right\}, \tag{3}$$

$$\begin{aligned} H_{ij}(y;x) = &\frac{G}{2\pi(1-\nu)r^2}\left\{2\,r_{,k}n_k\left[(1-2\nu)n'_i r_{,j} + \nu(r_{,k}n'_k\delta_{ij} + r_{,i}n'_j) - 4\,r_{,k}n'_k r_{,i}r_{,j}\right]\right. \\ &+ 2\nu(r_{,k}n'_k n_i r_{,j} + n_k n'_k r_{,i}r_{,j}) - (1-4\nu)n'_i n_j \\ &\left. +(1-2\nu)(2\,r_{,k}n'_k r_{,i}n_j + n_k n'_k\delta_{ij} + n_i n'_j)\right\}, \end{aligned} \tag{4}$$

where $r_i \coloneqq y_i - x_i$, $r \coloneqq \|y-x\|$, and n'_i and n_i denote the normal vectors at x and y, respectively.

For 3D problems, it reads

$$U_{ij}(y;x) = \frac{1}{16\pi G(1-\nu)r}\left[(3-4\nu)\delta_{ij} + r_{,i}r_{,j}\right], \tag{5}$$

$$\begin{aligned} T_{ij}(y;x) = &-\frac{1}{8\pi G(1-\nu)r^2}\left\{n_k r_{,k}\left[(1-2\nu)\delta_{ij} + 3r_{,i}r_{,j}\right]\right. \\ &\left.-(1-2\nu)(r_{,i}n_j - n_i r_{,j})\right\}, \end{aligned} \tag{6}$$

$$K_{ij}(y;x) = \frac{1}{8\pi(1-\nu)r^2}\left[(1-2\nu)(\delta_{ij}r_{,k} + \delta_{jk}r_{,i} - \delta_{ik}r_{,j}) + 3r_{,i}r_{,j}r_{,k}\right] n'_k, \tag{7}$$

$$\begin{aligned} H_{ij}(y;x) = &\frac{G}{4\pi(1-\nu)r^3}\left\{2r_{,p}n_p\left[(1-2\nu)\delta_{ik}r_{,j} + \nu(\delta_{ij}r_{,k} + \delta_{jk}r_{,i}) - 5r_{,i}r_{,j}r_{,k}\right]\right. \\ &+ 3\nu(n_i r_{,j}r_{,k} + n_k r_{,i}r_{,j}) - (1-4\nu)\delta_{ik}n_j \\ &\left.+(1-2\nu)(3n_j r_{,i}r_{,k} + \delta_{ij}n_k + \delta_{jk}n_i)\right\} n'_k. \end{aligned} \tag{8}$$

A.2 Kernel Functions of DDM

The kernel functions of DDM take the form of Eq. 2.51 or Eq. 2.53. The analytical expressions of the kernel functions for line and rectangular elements with constant strength are described here. It should be mentioned that the sign of the function $g(x_i)$ is flipped from original papers (Crouch, 1976; Shou et al., 1997) because of the difference of the definition of displacement discontinuity.

The kernel function of DDM for line elements with constant strength takes the following form in the intrinsic coordinate system:

$$f_i(x_1, x_2) = \Delta u_i g(x_1, x_2), \tag{9}$$

$$g(x_1, x_2) = \frac{1}{4\pi(1-\nu)}\int_{-a}^{a} \ln r \, \mathrm{d}\xi_1, \tag{10}$$

where a is the half-length of an element, $r = \sqrt{\bar{x}_1^2 + x_2^2}$, and $\bar{x}_i \coloneqq x_i - \xi_i$. β in Eq. 2.53 is omitted for brevity. The analytical integration of $g(x_1, x_2)$ is given by (Crouch,

1976)

$$g(x_1, x_2) = \frac{1}{4\pi(1-\nu)} \left[I(x_1, x_2, a) - I(x_1, x_2, -a) \right], \tag{11}$$

$$I(x_1, x_2, \xi_1) \coloneqq -x_2 \tan^{-1} \frac{\bar{x}_1}{x_2} - \bar{x}_1 \ln r. \tag{12}$$

The partial derivatives of $I(x_1, x_2, \xi_1)$ in terms of x_i are given by

$$I_{,1} = -\ln r, \tag{13}$$

$$I_{,2} = -\tan^{-1} \frac{\bar{x}}{y}, \tag{14}$$

$$I_{,11} = -\frac{\bar{x}_1}{r^2}, \tag{15}$$

$$I_{,12} = -\frac{x_2}{r^2}, \tag{16}$$

$$I_{,22} = -I_{,11}, \tag{17}$$

$$I_{,122} = -\frac{\bar{x}_1^2 - x_2^2}{r^2}, \tag{18}$$

$$I_{,222} = -\frac{2\bar{x}_1 x_2}{r^2}. \tag{19}$$

The kernel function of DDM for rectangular elements with constant strength is given by

$$f_i(x_1, x_2, x_3) = \Delta u_i g(x_1, x_2, x_3), \tag{20}$$

$$g(x_1, x_2, x_3) = -\frac{1}{8\pi(1-\nu)} \int_{-a}^{a} \int_{-b}^{b} \frac{1}{r} \, \mathrm{d}\xi_2 \, \mathrm{d}\xi_1, \tag{21}$$

where a and b are respectively the half-length of an element in the local x_1 and x_2 directions, and $r = \sqrt{\bar{x}_1^2 + \bar{x}_2^2 + x_3^2}$. The analytical integration of $g(x_1, x_2, x_3)$ is given

by (Shou et al., 1997; Wu and Olson, 2015a)

$$g(x_1,x_2,x_3) = -\frac{1}{8\pi(1-\nu)}\left[I(x_1,x_2,x_3,a,b) - I(x_1,x_2,x_3,-a,b)\right.$$
$$\left. -I(x_1,x_2,x_3,a,-b) + I(x_1,x_2,x_3,-a,-b)\right], \tag{22}$$

$$I(x_1,x_2,x_3,\xi_1,\xi_2) \coloneqq \bar{x}_1 \ln(r+\bar{x}_2) + \bar{x}_2 \ln(r+\bar{x}_1) - x_3 \tan^{-1}\frac{\bar{x}_1\bar{x}_2}{rx_3}. \tag{23}$$

The partial derivatives of $I(x_1,x_2,x_3,\xi_1,\xi_2)$ in terms of x_i are given by

$$I_{,1} = \ln(r+\bar{x}_2), \tag{24}$$

$$I_{,2} = \ln(r+\bar{x}_1), \tag{25}$$

$$I_{,3} = -\tan^{-1}\frac{\bar{x}_1\bar{x}_2}{rx_3}, \tag{26}$$

$$I_{,11} = \frac{\bar{x}_1}{r(r+\bar{x}_2)}, \tag{27}$$

$$I_{,22} = \frac{\bar{x}_2}{r(r+\bar{x}_1)}, \tag{28}$$

$$I_{,33} = \frac{\bar{x}_1\bar{x}_2(x_3^2+r^2)}{r(x_3^2+\bar{x}_1^2)(x_3^2+\bar{x}_2^2)}, \tag{29}$$

$$I_{,12} = \frac{1}{r}, \tag{30}$$

$$I_{,13} = \frac{x_3}{r(r+\bar{x}_2)}, \tag{31}$$

$$I_{,23} = \frac{x_3}{r(r+\bar{x}_1)}, \tag{32}$$

$$I_{,111} = -\frac{(r+\bar{x}_2)(\bar{x}_1^2-r^2)+\bar{x}_1^2 r}{r^3(r+\bar{x}_2)^2}, \tag{33}$$

$$I_{,112} = -\frac{\bar{x}_1}{r^3}, \tag{34}$$

$$I_{,113} = -\frac{\bar{x}_1 x_3(2r+\bar{x}_2)}{r^3(r+\bar{x}_2)^2}, \tag{35}$$

$$I_{,122} = -\frac{\bar{x}_2}{r^3}, \tag{36}$$

$$I_{,123} = -\frac{x_3}{r^3}, \tag{37}$$

$$I_{,133} = -\frac{(r+\bar{x}_2)(x_3^2 - r^2) + x_3^2 r}{r^3(r+\bar{x}_2)^2}, \tag{38}$$

$$I_{,222} = -\frac{(r+\bar{x}_1)(\bar{x}_2^2 - r^2) + \bar{x}_2^2 r}{r^3(r+\bar{x}_1)^2}, \tag{39}$$

$$I_{,223} = -\frac{\bar{x}_2 x_3(2r+\bar{x}_1)}{r^3(r+\bar{x}_2)^2}, \tag{40}$$

$$I_{,233} = -\frac{(r+\bar{x}_1)(x_3^2 - r^2) + x_3^2 r}{r^3(r+\bar{x}_1)^2}, \tag{41}$$

$$I_{,333} = -x_3\bar{x}_1\bar{x}_2\frac{(\bar{x}_1^2 + x_3^2)^2(\bar{x}_2^2 + x_3^2 + 2r^2) + (\bar{x}_2^2 + x_3^2)^2(\bar{x}_1^2 + x_3^2 + 2r^2)}{r^3(x_3^2 + \bar{x}_2^2)^2(x_3^2 + \bar{x}_1^2)^2}. \tag{42}$$

Appendix B: Shape Functions

We assume the intrinsic coordinate ξ varies from -1 to 1. For 2D problems, the shape function for constant displacement discontinuity (DD) elements is given by

$$N_1(\xi) = 1, \tag{43}$$

and the corresponding nodal point is $\xi_1 = 0$, which is the element center. For linear DD elements, the shape function becomes

$$N_1(\xi) = \frac{1}{2} - \frac{1}{\sqrt{2}}\xi, \tag{44}$$

$$N_2(\xi) = \frac{1}{2} + \frac{1}{\sqrt{2}}\xi, \tag{45}$$

and the corresponding nodal points are $\xi_1 = -1/\sqrt{2}$ and $\xi_2 = -1/\sqrt{2}$. For quadratic DD elements

$$N_1(\xi) = -\frac{1}{\sqrt{3}}\xi + \frac{2}{3}\xi^2, \tag{46}$$

$$N_2(\xi) = 1 - \frac{4}{3}\xi^2, \tag{47}$$

$$N_3(\xi) = \frac{1}{\sqrt{3}}\xi + \frac{2}{3}\xi^2, \tag{48}$$

and the corresponding nodal points are given by $\xi_1 = -\sqrt{3}/2$, $\xi_2 = 0$, and $\xi_3 = \sqrt{3}/2$.

For 3D problems, shape functions can be defined as described in Shou et al. (1997). Higher-order DD elements are, however, seldom used for 3D problems since (1) constant DD elements can produce sufficient accuracy, and (2) the function become too complicated.

References

Adachi, J. I. and Detournay, E. Self-similar solution of a plane-strain fracture driven by a power-law fluid. *Int. J. Numer. Anal. Methods Geomech.*, 26(6):579–604, 2002. doi: 10.1002/nag.213.

Advani, S. H., Lee, T. S., and Lee, J. K. Three-dimensional modeling of hydraulic fractures in layered media: part I – finite element formulations. *J. Energy Resour. Technol.*, 112(1):1–9, 1990. doi: 10.1115/1.2905706.

Aki, K. and Richard, P. *Quantitative Seismology*. University Science Books, Sausalito, 2nd edition, 2002.

Alghalandis, Y. F., Dowd, P. A., and Xu, X. Connectivity field: A measure for characterising fracture networks. *Math. Geosci.*, 47:63–83, 2015. doi: 10.1007/s11004-014-9520-7.

Aliabadi, M. H. *The Boundary Element Method, Volume 2, Applications in Solids and Structures*. John Wiley & Sons, West Sussex, 2002.

Ben-menahem, A. and Singh, S. J. Eigenvector expansions of Green's dyads with applications to geophysical theory. *Geophys. J. R. Astron. Soc.*, 16(4):417–452, 1968. doi: 10.1111/j.1365-246X.1968.tb00234.x.

Best, D. J. and Fisher, N. I. Efficient simulation of the von Mises distribution. *J. R. Stat. Soc. Ser. C*, 28(2):152–157, 1979. doi: 10.2307/2346732.

Blanton, T. L. An experimental study of interaction between hydraulically induced

and pre-existing fractures. In *SPE Unconv. Gas Recover. Symp.*, Pittsburgh, 1982. doi: 10.2118/10847-MS.

Blanton, T. L. Propagation of hydraulically and dynamically induced fractures in naturally fractured reservoirs. In *Unconv. Gas Technol. Symp.*, Louisville, 1986. doi: 10.2118/15261-MS.

Boroumand, N. and Eaton, D. W. Energy-based hydraulic fracture numerical simulation: Parameter selection and model validation using microseismicity. *Geophysics*, 80(5):W33–W44, 2015. doi: 10.1190/geo2014-0091.1.

Brune, J. Tectonic stress and the spectra of seismic shear waves from earthquakes. *J. Geophys. Res.*, 75(26):4997–5009, 1970. doi: 10.1029/JB075i026p04997.

Bufler, H. Theory of elasticity of a multilayered medium. *J. Elast.*, 1(2):125–143, 1971. doi: 10.1007/BF00046464.

Bunger, A. P., Detournay, E., and Garagash, D. I. Toughness-dominated hydraulic fracture with leak-off. *Int. J. Fract.*, 134(2):175–190, 2005. doi: 10.1007/s10704-005-0154-0.

Carrier, B. and Granet, S. Numerical modeling of hydraulic fracture problem in permeable medium using cohesive zone model. *Eng. Fract. Mech.*, 79:312–328, 2012. doi: 10.1016/j.engfracmech.2011.11.012.

Carvalho, J. L. and Curran, J. H. Two-dimensional Green's functions for elastic bi-materials. *J. Appl. Mech.*, 59(2):321–327, 1992. doi: 10.1115/1.2899523.

Carvalho, J. L. and Curran, J. H. Three-dimensional displacement discontinuity solutions for fluid-saturated porous media. *Int. J. Solids Struct.*, 35:4887–4893, 1998. doi: 10.1016/S0020-7683(98)00099-7.

Castelletto, N., White, J. A., and Tchelepi, H. A. Accuracy and convergence properties of the fixed-stress iterative solution of two-way coupled poromechanics. *Int. J. Numer. Anal. Methods Geomech.*, 39:1593–1618, 2015. doi: 10.1002/nag.2400.

Chang, X., Guo, Y., Zhou, J., Song, X., and Yang, C. Numerical and experimental investigations of the interactions between hydraulic and natural fractures in shale formations. *Energies*, 11(10):2541, 2018. doi: 10.3390/en11102541.

Chapman, C. H. *Fundamentals of Seismic Wave Propagation*. Cambridge University Press, Cambridge, 2004.

Chen, M. and Tang, R. An explicit tensor expression for the fundamental solutions of a bimaterial space problem. *Appl. Math. Mech.*, 18(4):331–340, 1997. doi: 10.1007/BF02457547.

Cheng, W., Jin, Y., Li, H., and Chen, M. A novel linear triangular element of a three-dimensional displacement discontinuity method. *Eng. Anal. Bound. Elem.*, 59:89–96, 2015a. doi: 10.1016/j.enganabound.2015.04.020.

Cheng, W., Jin, Y., Lin, Q., Chen, M., Zhang, Y., Diao, C., and Hou, B. Experimental investigation about influence of pre-existing fracture on hydraulic fracture propagation under tri-axial stresses. *Geotech. Geol. Eng.*, 33(3):467–473, 2015b. doi: 10.1007/s10706-014-9832-x.

Ciezobka, J., Courtier, J., and Wicker, J. Hydraulic Fracturing Test Site (HFTS) – Project Overview and Summary of Results. In *Unconv. Resour. Technol. Conf.*, Houston, 2018. doi: 10.15530/urtec-2018-2937168.

Cipolla, C., Maxwell, S., Mack, M., and Downie, R. A practical guide to interpret-

ing microseismic measurements. In *SPE North Am. Unconv. Gas Conf. Exhib.*, Woodlands, 2011. doi: 10.2118/144067-MS.

Cleary, M., Keck, R., and Mear, M. Microcomputer Models for the Design of Hydraulic Fractures. In *SPE/DOE Symp. Low Perm. Gas Res. Symp.*, Denver, 1983. doi: 10.2118/11628-MS.

Courtier, J., Ciezobka, J., Chandler, K., Martin, S., and Thomas, R. Best practices in designing and executing a comprehensive Hydraulic fracturing Test Site in the Permian Basin. In *Unconv. Resour. Technol. Conf.*, Austin, 2017. doi: 10.15530/urtec-2017-2697483.

Crawford, A. M. and Curran, J. H. Higher-order functional variation displacement discontinuity elements. *Int. J. Rock Mech. Min. Sci. Geomech.*, 19(3):143–148, 1982. doi: 10.1016/0148-9062(82)91154-8.

Crouch, S. L. Solution of plane elasticity problems by the displacement discontinuity method. *Int. J. Numer. Methods Eng.*, 10(2):301–343, 1976. doi: 10.1002/nme.1620100206.

Crouch, S. L. and Starfield, A. M. *Boundary Blement Methods in Solid Mechanics*. George Allen & Unwin, London, 1983.

Cruse, T. A. Numerical evaluation of elastic stress intensity factors by the boundary-integral equation method. In Swedlow, J. L., editor, *The surface crack: Physical problems and computational solutions*, pages 153–170. 1972.

Cruse, T. A. Two-dimensional BIE fracture mechanics analysis. *Appl. Math. Model.*, 2(4):287–293, 1978. doi: 10.1016/0307-904X(78)90023-9.

Cruse, T. A. *Boundary Element Analysis in Computational Fracture.* Kluwer Academic Publishers, Dordrecht, 1988.

Dahi Taleghani, A. *Analysis of hydraulic fracture propagation in fractured reservoirs: an improved model for the interaction between induced and natural fractures.* Ph.D. dissertation, The University of Texas at Austin, 2009.

Dahi-Taleghani, A. and Olson, J. E. Numerical modeling of multistranded-hydraulic-fracture propagation: accounting for the interaction between induced and natural fractures. *SPE J.*, 16(03):575–581, 2011. doi: 10.2118/124884-PA.

Dahi Taleghani, A. and Olson, J. E. How natural fractures could affect hydraulic-fracture geometry. *SPE J.*, 19(01):161–171, 2013. doi: 10.2118/167608-PA.

Davey, K. and Hinduja, S. Analytical integration of linear three-dimensional triangular elements in BEM. *Appl. Math. Model.*, 13(8):450–461, 1989. doi: 10.1016/0307-904X(89)90093-0.

Davy, P. On the frequency-length distribution of the San Andreas fault system. *J. Geophys. Res.*, 98(B7):12141–12151, 1993. doi: 10.1029/93JB00372.

Davy, P., Darcel, C., Goc, R. L., and Ivars, D. M. Elastic properties of fractured rock masses with frictional properties and power law fracture size distributions. *J. Geophys. Res. Solid Earth*, 123(8):6521–6539, 2018. doi: 10.1029/2017JB015329.

Detournay, E. Propagation Regimes of fluid-driven fractures in impermeable rocks. *Int. J. Geomech.*, 4(1):35–45, 2004. doi: 10.1061/(ASCE)1532-3641(2004)4:1(35).

Detournay, E. Mechanics of hydraulic fractures. *Annu. Rev. Fluid Mech.*, 48(1): 311–339, 2016. doi: 10.1146/annurev-fluid-010814-014736.

Dohmen, T., Zhang, J., Barker, L., and Blangy, J. P. Microseismic magnitudes and b-Values for delineating hydraulic fracturing and depletion. *SPE J.*, pages 1624–1634, 2017. doi: 10.2118/186096-PA.

Dong, C. Y. and De Pater, C. J. Numerical implementation of displacement discontinuity method and its application in hydraulic fracturing. *Comput. Methods Appl. Mech. Eng.*, 191(8-10):745–760, 2001. doi: 10.1016/S0045-7825(01)00273-0.

Dontsov, E. V. An approximate solution for a penny-shaped hydraulic fracture that accounts for fracture toughness, fluid viscosity and leak-off. *R. Soc. Open Sci.*, 3 (160737), 2016. doi: 10.1098/rsos.160737.

Du, Y., Segall, P., and Gao, H. Dislocations in inhomogeneous media via a moduli perturbation approach: General formulation and two dimensional solutions. *J. Geophys. Res.*, 99(B7):13767–13779, 1994. doi: 10.1029/94JB00339.

Du, Y., Segall, P., and Gao, H. Quasi-static dislocations in three dimensional inhomogeneous media. *Geophys. Res. Lett.*, 24(18):2347–2350, 1997. doi: 10.1029/97GL02341.

Du, Y., Segall, P., and Gao, H. *Geophysical inversion of far-field deformation for hydraulic fracture & reservoir information.* Ph.D. dissertation, The University of Texas at Austin, 2000.

Duarte, C. A., Hamzeh, O. N., Liszka, T. J., and Tworzydlo, W. W. A generalized finite element method for the simulation of three-dimensional dynamic crack propagation. *Comput. Methods Appl. Mech. Eng.*, 190:2227–2262, 2001. doi: 10.1016/S0045-7825(00)00233-4.

Dundurs, J. and Hetényi, M. Transmission of force between two semi-infinite solids. *J. Appl. Mech.*, 32(3):671–674, 1965. doi: 10.1115/1.3627277.

Erdogan, F. and Sih, G. C. On the crack extension in plates under plane loading and transverse shear. *J. Basic Eng.*, 85(4):519–525, 1963. doi: 10.1115/1.3656897.

Fares, N. and Li, V. C. General image method in a plane-layered elastostatic medium. *J. Appl. Mech.*, 55(4):781–785, 1988. doi: 10.1115/1.3173722.

Fares, N. F. *Green's functions for plane-layered elastostatic and viscoelastic regions with application to 3-D crack analysis.* Ph.D. dissertation, Massachusetts Institute of Technology, 1987.

Farmahini-Farahani, M. and Ghassemi, A. Simulation of micro-seismicity in response to injection/production in large-scale fracture networks using the fast multipole displacement discontinuity method (FMDDM). *Eng. Anal. Bound. Elem.*, 71:179–189, 2016. doi: 10.1016/j.enganabound.2016.07.004.

Fatahi, H., Hossain, M. M., and Sarmadivaleh, M. Numerical and experimental investigation of the interaction of natural and propagated hydraulic fracture. *J. Nat. Gas Sci. Eng.*, 37:409–424, 2017. doi: 10.1016/j.jngse.2016.11.054.

Feng, F., Wang, X., Guo, B., and Ai, C. Mathematical model of fracture complexity indicator in multistage hydraulic fracturing. *J. Nat. Gas Sci. Eng.*, 38:39–49, 2017. doi: 10.1016/j.jngse.2016.12.012.

Fisher, N. I. *Statistical Analysis of Circular Data.* Cambridge University Press, Cambridge, 1993.

Fry, M. F., Patel, H., Gil, I. R., Hazzard, J., and Damjanac, B. Discrete element modelling of microseismic energy associated with hydraulic fracturing in natural

fractures reservoirs. In *49th US Rock Mech. / Geomech. Symp.*, San Francisco, 2015.

Fung, Y. C. *Foundations of Solid Mechanics*. Prentice-Hall, Englewood Cliffs, New Jersey, 1965.

Gale, J. F. W., Reed, R. M., and Holder, J. Natural fractures in the Barnett Shale and their importance for hydraulic fracture treatments. *AAPG Bull.*, 91(4):603–622, 2007. doi: 10.1306/11010606061.

Gale, J. F. W., Laubach, S. E., Olson, J. E., Eichhubl, P., and Fall, A. Natural fractures in shale: A review and new observations. *AAPG Bull.*, 98(11):2165–2216, 2014. doi: 10.1306/08121413151.

Gao, X.-W. and Davies, T. G. *Boundary Element Programming in Mechanics*. Cambridge University Press, New York, 2002.

Garagash, D. I. Transient solution for a plane-strain fracture driven by a shear-thinning, power-law fluid. *Int. J. Numer. Anal. Methods Geomech.*, 30:1439–1475, 2006. doi: 10.1002/nag.535.

Garagash, D. I. and Detournay, E. Plane-strain propagation of a fluid-driven fracture: Small toughness solution. *J. Appl. Mech.*, 72(6):916, 2005. doi: 10.1115/1.2047596.

Garagash, D. I., Detournay, E., and Adachi, J. I. Multiscale tip asymptotics in hydraulic fracture with leak-off. *J. Fluid Mech.*, 669:260–297, 2011. doi: 10.1017/S002211201000501X.

Geertsma, J. and de Klerk, F. A rapid method of predicting width and extent of hydraulically induced fractures. *J. Pet. Tech.*, 21(12):1571–1581, 1969. doi: 10.2118/2458-PA.

Ghassemi, A. and Roegiers, J.-C. A three-dimensional poroelastic hydraulic fracture simulator using the displacement discontinuity method. In Aubertin, M., Hassani, F., and Mitri, H., editors, *Proc. 2nd North Am. Rock Mech. Symp. Rock Mech. Tools Tech. Vol. 1*, pages 981–987, Rotterdam, 1996. Balkema.

Gibowicz, S. and Kijko, A. *An Introduction to Mining Seismology.* Academic Press, San Diego, 1994.

Girault, V., Kumar, K., and Wheeler, M. F. Convergence of iterative coupling of geomechanics with flow in a fractured poroelastic medium. *Comput. Geosci.*, 20 (5):997–1011, 2016. doi: 10.1007/s10596-016-9573-4.

Grechka, V. and Yaskevich, S. Azimuthal anisotropy in microseismic monitoring: A Bakken case study. *Geophysics*, 79(1):KS1–KS12, 2014. doi: 10.1190/geo2013-0211.1.

Gu, H. and Siebrits, E. Effect of formation modulus contrast on hydraulic fracture height containment. *SPE Prod. Oper.*, pages 170–176, 2008. doi: 10.2118/103822-PA.

Gu, H. and Weng, X. Criterion for fractures crossing frictional interfaces at non-orthogonal angles. In *44th US Rock Mech. Symp. 5th U.S.-Canada Rock Mech. Symp.*, pages 1–6, Salt Lake City, 2010. ARMA-10-198.

Gu, H., Weng, X., Lund, J. B., Mack, M. G., Ganguly, U., and Suarez-Rivera, R. Hydraulic fracture crossing natural fracture at nonorthogonal angles: A criterion and its validation. *SPE Prod. Oper.*, 27(01):20–26, 2012. doi: 10.2118/139984-PA.

Guo, T., Zhang, S., Qu, Z., Zhou, T., Xiao, Y., and Gao, J. Experimental study of

hydraulic fracturing for shale by stimulated reservoir volume. *Fuel*, 128:373–380, 2014. doi: 10.1016/j.fuel.2014.03.029.

Gupta, P. and Duarte, C. Simulation of non-planar three-dimensional hydraulic fracture propagation. *Int. J. Numer. Anal. Methods Geomech.*, 38(13):1397–1430, 2014. doi: 10.1002/nag.2305.

Gutenberg, B. and Richter, C. F. Frequency of earthquakes in California. *Bull. Seismol. Soc. Am.*, 34(4):185–188, 1944.

Hansen, W. W. A new type of expansion in radiation problems. *Phys. Rev.*, 47(2): 139–143, 1935. doi: 10.1103/PhysRev.47.139.

Hirose, S. and Sharma, M. M. Numerical modelling of fractures in multilayered rock formations using a displacement discontinuity method. In *52nd U.S. Rock Mechanics/Geomechanics Symposium*, Seattle, 2018. ARMA-2018-495.

Hooker, J. N., Laubach, e. E., and Marrett, R. Fracture-aperture size-frequency, spatial distribution, and growth processes in strata-bounded and non-strata-bounded fractures, Cambrian Mesón Group, NW Argentina. *J. Struct. Geo.*, 54:54–71, 2013. doi: 10.1016/j.jsg.2013.06.011.

Howard, G. C. and Fast, C. R. Optimum fluid characteristics for fracture extension. In *Drill. Prod. Pract.*, pages 261–269, New York, 1957.

Hu, J. and Garagash, D. I. Plane-strain propagation of a fluid-driven crack in a permeable rock with fracture toughness. *J. Eng. Mech.*, 136(9):1152–1166, 2010. doi: 10.1061/(asce)em.1943-7889.0000169.

Huang, K.-F. and Wang, M.-Z. Fundamental solution of bi-material elastic space. *Sci. China A*, 34(3):309–315, 1991. doi: 10.1360/ya1991-34-3-309.

Ishimoto, M. and Iida, K. Observations sur les Seismes enregistres par le Microsismographe construit dernierement.(1) (in Japanese). *Bull. Earthq. Res. Inst.*, 17(2): 443–478, 1939.

Jaeger, J. C., Cook, N. G. W., and Zimmerman, R. W. *Fundamentals of Rock Mechanics*. Blackwell Publishing, Malden, fourth edition, 2007.

Jiao, W., Davidson, M., Sena, A., Bankhead, B. L., Xia, Y., Sil, S., and Zhou, C. The matter of size: On the moment magnitude of microseismic events. *Geophysics*, 79(3), 2014. doi: 10.1190/GEO2013-0194.1.

Kanamori, H. The energy release in great earthquakes. *J. Geophys. Res.*, 82(20): 2981–2987, 1977. doi: 10.1029/JB082i020p02981.

Khristianovic, S. A. and Zheltov, Y. P. Formation of vertical fractures by means of highly viscous liquid. *World Pet. Congr.*, 5:579–586, 1955.

Kim, J., Tchelepi, H. A., and Juanes, R. Stability, accuracy, and efficiency of sequential methods for coupled flow and geomechanics. *SPE J.*, 16(02):249–262, 2011a. doi: 10.2118/119084-PA.

Kim, J., Tchelepi, H. A., and Juanes, R. Stability and convergence of sequential methods for coupled flow and geomechanics: Fixed-stress and fixed-strain splits. *Comput. Methods Appl. Mech. Eng.*, 200(13-16):1591–1606, 2011b. doi: 10.1016/j.cma.2010.12.022.

Kim, J., Tchelepi, H. A., and Juanes, R. Stability and convergence of sequential methods for coupled flow and geomechanics: Drained and undrained splits. *Comput. Methods Appl. Mech. Eng.*, 200(23-24):2094–2116, 2011c. doi: 10.1016/j.cma.2011.02.011.

Knopoff, L. and Randall, M. J. The compensated linear-vector dipole: A possible mechanism for deep earthquakes. *J. Geophys. Res.*, 75(26):4957–4963, 1970. doi: 10.1029/JB075i026p04957.

Krishnasamy, G., Rizzo, F. J., and Liu, Y. Boundary integral equations for thin bodies. *Int. J. Numer. Methods Eng.*, 37(1):107–121, 1994. doi: 10.1002/nme.1620370108.

Kumar, A., Chao, K., Hammack, R. W., and Harbert, W. Surface Seismic monitoring of Hydraulic Fracturing Test Site (HFTS) in the Midland Basin, Texas. In *Unconv. Resour. Technol. Conf.*, Houston, 2018. doi: 10.15530/urtec-2018-2902789.

Kuriyama, K. and Mizuta, Y. Three-dimensional elastic analysis by the displacement discontinuity method with boundary division into triangular leaf elements. *Int. J. Rock Mech. Min. Sci. Geomech. Abstr.*, 30(2):111–123, 1993. doi: 10.1016/0148-9062(93)90704-H.

Lee, H. P., Olson, J. E., Holder, J., Gale, J. F. W., and Myers, R. D. The interatction of propagating opening mode fractures with preexisting discontinuities in shale. *J. Geophys. Res. B Solid Earth*, pages 169–181, 2014. doi: 10.1002/2014JB011358. Received.

Lee, T. S., Advani, S. H., and Lee, J. K. Three-dimensional modeling of hydraulic fractures in layered media: part II—calibrations, parametric sensitivity and field simulations. *J. Energy Resour. Technol.*, 112(1):10–19, 1990. doi: 10.1115/1.2905705.

Li, B. Natural fractures in unconventional shale reservoirs in US and their roles in well completion design and improving hydraulic fracturing. In *SPE Ann. Tech. Conf. Exhib.*, pages 1–19, Amsterdam, 2014. doi: 10.2118/170934-MS.

Li, T., Razavi, O., and Olson, J. E. Modeling fracture in layered formations using a simplified 3D displacement discontinuity method. In *52nd US Rock Mechanics/Geomechanics Symposium*, Seattle, 2018. ARMA-2018-1079.

Lin, W. and Keer, L. M. Analysis of a vertical crack in a multilayered medium. *J. Appl. Mech.*, 56(1):63–69, 1989. doi: 10.1115/1.3176067.

Liu, Y. Analysis of shell-like structures by the boundary element method based on 3-D elasticity: formulation and verification. *Int. J. Numer. Meth. Eng.*, 41(3):541–558, 1998. doi: 10.1002/(SICI)1097-0207(19980215)41:3<541::AID-NME298>3.0.CO;2-K.

Liu, Y. On the displacement discontinuity method and the boundary element method for solving 3-D crack problems. *Eng. Fract. Mech.*, 164:35–45, 2016. doi: 10.1016/j.engfracmech.2016.07.009.

Liu, Y. J. *Fast Multipole Boundary Element Method.* Cambridge University Press, New York, 2009. ISBN 978-0-521-11659-6.

Liu, Y. J. and Li, Y. X. Revisit of the equivalence of the displacement discontinuity method and boundary element method for solving crack problems. *Eng. Anal. Bound. Elem.*, 47(1):64–67, 2014. doi: 10.1016/j.enganabound.2014.06.006.

Ma, C.-C. and Lin, R.-L. Image singularities of Green's functions for isotropic elastic bimaterials subjected to concentrated forces and dislocations. *Int. J. Solids Struct.*, 39(20):5253–5277, 2002. doi: 10.1016/S0020-7683(02)00419-5.

Maity, D. and Ciezobka, J. An interpretation of proppant transport within the stimulated rock volume at the Hydraulic-Fracturing Test Site in the Permian Basin. *SPE Reserv. Eval. Eng.*, 22(2):1–15, 2019. doi: 10.2118/194496-PA.

Manchanda, R. *A general poro-elastic model for pad-Scale fracturing of horizontal wells*. Ph.D. dissertation, The University of Texas at Austin, 2015.

Manchanda, R., Bryant, E. C., Bhardwaj, P., Cardiff, P., and Sharma, M. M. Strategies for effective stimulation of multiple perforation clusters in horizontal wells. *SPE Prod. Oper.*, 33(3):539–556, 2017. doi: 10.2118/179126-PA.

Maxwell, S., Shemeta, J., Campbell, E., and Quirk, D. Microseismic deformation rate monitoring. In *SPE Annu. Tech. Conf. Exhib.*, Denver, 2008. doi: 10.2118/116596-MS.

Maxwell, S. C., Jones, M., Parker, R., Miong, S., Leaney, S., Dorval, D., D'Amico, D., Logel, J., Anderson, E., and Hammermaster, K. Fault activation during hydraulic fracturing. In *SEG Annu. Meet.*, pages 1552–1556, Houston, 2009. doi: 10.1190/1.3255145.

Maxwell, S. C., Rutledge, J., Jones, R., and Fehler, M. Petroleum reservoir characterization using downhole microseismic monitoring. *Geophysics*, 75(5):75A129–75A137, 2010. doi: 10.1190/1.3477966.

Maxwell, S. C., Mack, M., Zhang, F., Chorney, D., Goodfellow, S. D., and Grob, M. Differentiating wet and dry microseismic events induced during hydraulic fracturing. In *Unconv. Resour. Technol. Conf.*, San Antonio, 2015. doi: 10.15530/URTEC-2015-2154344.

Melan, E. Der Spannungszustand der durch eine Einzelkraft im Innern beanspruchten Halbscheibe. *Zeitschrift für Angew. Math. und Mech.*, 12:343–346, 1932.

Mikelić, A., Wheeler, M. F., and Wick, T. A quasi-static phase-field approach to pres-

surized fractures. *Nonlinearity*, 28(5):1371–1399, 2015a. doi: 10.1088/0951-7715/28/5/1371.

Mikelić, A., Wheeler, M. F., and Wick, T. Phase-field modeling of a fluid-driven fracture in a poroelastic medium. *Comput. Geosci.*, 19(6):1171–1195, 2015b. doi: 10.1007/s10596-015-9532-5.

Mikelić, A., Wheeler, M. F., and Wick, T. A phase-field method for propagating fluid-filled fractures coupled to a surrounding porous medium. *Multiscale Model. Simul.*, 13(1):367–398, 2015c. doi: 10.1137/140967118.

Morse, P. M. and Feshbach, H. Vector fields. In *Methods of theoretical physics*, chapter 13, pages 1759–1902. McGraw-Hill, New York, 1953.

Naceur, K. B., Thiercelin, M., and Touboul, E. Simulation of fluid flow in hydraulic fracturing: implications for 3D propagation. *SPE Prod. Eng.*, 5(02):133–141, 1990. doi: 10.2118/16032-PA.

Nagel, N. B. and Sanchez-nagel, M. Stress shadowing and microseismic events: a numerical evaluation. In *SPE Annu. Tech. Conf. Exhib.*, Denver, 2011. doi: 10.2118/147363-MS.

Nolen-Hoeksema, R. C. and Ruff, L. J. Moment tensor inversion of microseisms from the B-sand propped hydrofracture, M-site, Colorado. *Tectonophysics*, 336(1-4):163–181, 2001. doi: 10.1016/S0040-1951(01)00100-7.

Nordgren, R. P. Propagation of a vertical hydraulic fracture. *Soc. Pet. Eng. J.*, 12 (4):306–314, 1972. doi: 10.2118/3009-PA.

Nuismer, R. J. An energy release rate criterion for mixed mode fracture. *Int. J. Fract.*, 11(2):245–250, 1975. doi: 10.1007/BF00038891.

Olson. *Fracture mechanics analysis of joints and veins.* Ph.D. dissertation, Stanford University, 1991.

Olson, J. Multi-fracture propagation modeling: Applications to hydraulic fracturing in shales and tight gas sands. In *42nd US Rock Mech. Symp.*, San Francisco, 2008. ARMA-08-327.

Olson, J. E. and Wu, K. Sequential vs. simultaneous multizone fracturing in horizontal wells: Insights from a non-planar, multifrac numerical model. In *SPE Hydraul. Fract. Technol. Conf.*, Woodlands, 2012. doi: 10.2118/152602-MS.

Ouchi, H., Katiyar, A., York, J., Foster, J. T., and Sharma, M. M. A fully coupled porous flow and geomechanics model for fluid driven cracks: a peridynamics approach. *Comput. Mech.*, 55(3):561–576, 2015. doi: 10.1007/s00466-015-1123-8.

Ouchi, H., Katiyar, A., Foster, J. T., and Sharma, M. M. A peridynamics model for the propagation of hydraulic fractures in naturally fractured Reservoirs. *SPE J.*, 22(04):1082–1102, 2017. doi: 10.2118/173361-PA.

Perkins, T. and Kern, L. Widths of hydraulic fractures. *J. Pet. Technol.*, 13(9): 937–949, 1961. doi: 10.2118/89-PA.

Pesicek, J. D., Cieślik, K., Lambert, M.-a., Carrillo, P., and Birkelo, B. Dense surface seismic data confirm non-double-couple source mechanisms induced by hydraulic fracturing. *Geophysics*, 81(6):KS207–KS217, 2016. doi: 10.1190/geo2016-0192.1.

Phan-Thien, N. On the image system for the Kelvin-state. *J. Elast.*, 13(2):231–235, 1983. doi: 10.1007/BF00041239.

Renshaw, C. E. and Pollard, D. D. An experimentally verified criterion for propaga-

tion across unbounded frictional interfaces in brittle, linear elastic materials. *Int. J. Rock Mech. Min. Sci.*, 32(3):237–249, 1995. doi: 10.1016/0148-9062(94)00037-4.

Rentsch, S., Buske, S., Lüth, S., and Shapiro, S. Fast location of seismicity: A migration-type approach with application to hydraulic-fracturing data. *Geophysics*, 72(1):S33–S40, 2007. doi: 10.1190/1.2401139.

Rice, J. R. Mathematical analysis in the mechanics of fracture. In Liebowitz, H., editor, *Fract. An Adv. Treatise, Vol.2*, chapter 3, pages 191–311. Academic Press, New York, 1968.

Rongved, L. Force interior to one of two joined semi-infinite solids. In *Proc. Second Midwest. Conf. Solid Mech.*, pages 1–13, West Lafayette, 1955.

Rongved, L. and Hill, N. J. M. Dislocation over a bounded plane area in an infinite solid. *J. Appl. Mech.*, 24:252–254, 1957.

Rungamornrat, J. Analysis of 3D cracks in anisotropic multi-material domain with weakly singular SGBEM. *Eng. Anal. Bound. Elem.*, 30(10):834–846, 2006. doi: 10.1016/j.enganabound.2006.05.005.

Rungamornrat, J., Wheeler, M., and Mear, M. A numerical technique for simulating non-planar evolution of hydraulic fractures. In *Proc. SPE Annu. Tech. Conf. Exhib.*, Dallas, 2005. doi: 10.2523/96968-MS.

Rutledge, J. T. and Phillips, W. S. Hydraulic stimulation of natural fractures as revealed by induced microearthquakes, Carthage Cotton Valley gas field, east Texas. *Geophysics*, 68(2):441–452, 2003. doi: 10.1190/1.1567212.

Salamon, M. Elastic analysis of displacements and stresses induced by the mining of

seam or reef deposits: part IV: inclined reef. *J. South African Inst. Min. Metall.*, 65(5):319–338, 1964.

Savin, G. N. *Stress Concentration Around Holes*. Pergamon Press, New York, 1961.

Savitski, A. A. and Detournay, E. Propagation of a penny-shaped fluid-driven fracture in an impermeable rock: Asymptotic solutions. *Int. J. Solids Struct.*, 39(26):6311–6337, 2002. doi: 10.1016/S0020-7683(02)00492-4.

Schultz, R. A. Stress intensity factors for curved cracks obtained with the displacement discontinuity method. *Int. J. Fract.*, 37(2):31–34, 1988. doi: 10.1007/BF00041718.

Selcuk, S. and Crouch, S. L. A direct boundary integral method for multilayered rock with fractures. In *33rd US Symp. Rock Mech.*, pages 629–638, Santa Fe, 1992. ARMA-92-0629.

Settari, A. and Cleary, M. P. Development and testing of a pseudo-three-dimensional model of hydraulic fracture geometry. *SPE Prod. Eng.*, 1(06):449–466, 1986. doi: 10.2118/10505-PA.

Settgast, R. R., Fu, P., Walsh, S. D., White, J. A., Annavarapu, C., and Ryerson, F. J. A fully coupled method for massively parallel simulation of hydraulically driven fractures in 3-dimensions. *Int. J. Numer. Anal. Methods Geomech.*, 41(5):627–653, 2017. doi: 10.1002/nag.2557.

Sheibani, F. *Solving three dimensional problems in natural and hydraulic fracture development: insight from displacement discontinuity modeling*. Ph.D. dissertation, The University of Texas at Austin, 2013.

Sheibani, F. and Olson, J. Stress intensity factor determination for three-dimensional crack using the displacement discontinuity method with applications to hydraulic fracture height growth and non-planar propagation paths. *Eff. Sustain. Hydraul. Fract.*, 2013. doi: 10.5772/56308.

Shou, K.-J. *A higher order three-dimensional displacement discontinuity method with application to bonded half-space problems.* Ph.D. dissertation, The University of Minnesota, 1993.

Shou, K.-j. A two-dimensional displacement discontinuity method for multilayered elastic media. *Int. J. Rock Mech. Min. Sci.*, 34(3-4):288.e1–288.e14, 1997. doi: 10.1016/S1365-1609(97)00178-0.

Shou, K. J. and Napier, J. A. L. A two-dimensional linear variation displacement discontinuity method for three-layered elastic media. *Int. J. Rock Mech. Min. Sci.*, 36(6):719–729, 1999. doi: 10.1016/S0148-9062(99)00042-X.

Shou, K.-J., Siebrits, E., and Crouch, S. L. A higher order displacement discontinuity method for three-dimensional elastostatic problems. *Int. J. Rock Mech. Min. Sci.*, 34(2):317–322, 1997.

Shou, S. J. and Crouch, S. A higher order displacement discontinuity method for analysis of crack problems. *Int. J. Rock Mech. Min. Sci.*, 32(1):49–55, 1995. doi: 10.1016/0148-9062(94)00016-V.

Shrivastava, K. and Sharma, M. M. Proppant transport in complex fracture networks. In *SPE Hydraul. Fract. Technol. Conf. Exhib.*, Woodlands, 2018a. doi: 10.2118/189895-MS.

Shrivastava, K. and Sharma, M. M. Mechanisms for the formation of complex fracture networks in naturally fractured rocks. In *SPE Hydraul. Fract. Technol. Conf. Exhib.*, Woodlands, 2018b. doi: 10.2118/189864-MS.

Shrivastava, K., Blyton, C. A. J., and Sharma, M. M. Local linearization method for efficient solution of coupled fluid flow and geomechanics problem. In *51st US Rock Mech. / Geomech. Symp.*, San Francisco, 2017.

Shrivastava, K., Hwang, J., and Sharma, M. Formation of complex fracture networks in the Wolfcamp Shale: calibrating model predictions with core measurements from the Hydraulic Fracturing Test Site. In *SPE Annu. Tech. Conf. Exhib.*, Dallas, 2018. doi: 10.2118/191630-MS.

Siebrits, E. and Crouch, S. L. On the paper "A two-dimensional linear variation displacement discontinuity method for three-layered elastic media" by Keh-Jian Shou and J . A . L . Napier , International Journal of Rock Mechanics and Mining Sciences, Vol.36(6), 719-729, 1999. *Int. J. Rock Mech. Min. Sci.*, 37(5):873–875, 2000. doi: 10.1016/S1365-1609(00)00018-6.

Sih, G. C. and Liebowitz, H. Mathematical theories of brittle fracture. In Liebowitz, H., editor, *Fract. An Adv. Treatise, Vol.2*, chapter 2, pages 67–190. Academic Press, New York, 1968.

Šílený, J., Hill, D. P., Eisner, L., and Cornet, F. H. Non-double-couple mechanisms of microearthquakes induced by hydraulic fracturing. *J. Geophys. Res. Solid Earth*, 114(8):1–15, 2009. doi: 10.1029/2008JB005987.

Singh, S. J. Static deformation of a multilayered half-space by internal sources. *J. Geophys. Res.*, 75(17):3257–3263, 1970. doi: 10.1029/JB075i017p03257.

Slaughter, W. S. *The Linearized Theory of Elasticity*. Birkhäuser, Boston, 2002.

Sneddon, I. N. The distribution of stress in the neighbourhood of a crack in an elastic solid. *Proc. R. Soc. Lond. A. Math. Phys. Sci.*, 187(1009):229–260, 1946.

Stagni, L. and Lizzio, R. The elastic field within an internally stressed infinite strip. *Int. J. Eng. Sci.*, 24(4):471–477, 1986. doi: 10.1016/0020-7225(86)90039-X.

Stagni, L. and Lizzio, R. Interaction of an edge dislocation with a lamellar inhomogeneity. *Mech. Mater.*, 6(1):17–25, 1987. doi: 10.1016/0167-6636(87)90019-6.

Stegent, N. and Candler, C. Downhole microseismic mapping of more than 400 fracturing stages on a multiwell pad at the Hydraulic Fracturing Test Site (HFTS): discussion of operational challenges and analytic results. In *Unconv. Res. Tech. Conf.*, Houston, 2018. doi: 10.15530/urtec-2018-2902311.

Sui, L., Yu, J., Cang, D., Miao, W., Wang, H., Zhang, J., Yin, S., and Chang, K. The fractal description model of rock fracture networks characterization. *Caos, Solitons and Fractals*, 129:71–76, 2019. doi: 10.1016/j.chaos.2019.07.055.

Telles, J. C. and Brebbia, C. A. Boundary element solution for half-plane problems. *Int. J. Solids Struct.*, 17(12):1149–1158, 1981. doi: 10.1016/0020-7683(81)90094-9.

Usher, P. J., Angus, D. A., and Verdon, J. P. Influence of a velocity model and source frequency on microseismic waveforms: some implications for microseismic locations. *Geophys. Prospect.*, 61(SUPPL.1):334–345, 2013. doi: 10.1111/j.1365-2478.2012.01120.x.

Vavryčuk, V. Inversion for parameters of tensile earthquakes. *J. Geophys. Res. B Solid Earth*, 106(B8):16339–16355, 2001.

Vavryčuk, V. On the retrieval of moment tensors from borehole data. *Geophys. Prospect.*, 55(3):381–391, 2007. doi: 10.1111/j.1365-2478.2007.00624.x.

Vijayakumar, S. and Cormack, D. Green's functions for the biharmonic equation: bonded elastic media. *SIAM J. Appl. Math.*, 47(5):982–997, 1987. doi: 10.1137/0147065.

Wang, H. F. *Theory of Linear Poroelasticity with Applications to Geomechanics and Hydrogeology*. Princeton University Press, Princeton, 2000.

Wang, J.-J. and Clifton, R. J. Numerical modeling of hydraulic fracturing in layered formations with multiple elastic moduli. In *Rock Mech. Contrib. Challenges: Proc. 31st U.S. Symp.*, pages 303–310, Golden, 1990.

Warpinski, N. and Teufel, L. Influence of geologic discontinuities on hydraulic fracture propagation. *J. Pet. Technol.*, 39(02):209–220, 1987. doi: 10.2118/13224-PA.

Warpinski, N. R. and Wolhart, S. A validation assessment of microseismic monitoring. In *SPE Hydraul. Fract. Technol. Conf.*, Woodlands, 2016. doi: 10.2118/179150-MS.

Warpinski, N. R., Kramm, R. C., Heinze, J. K., and Waltman, C. K. Comparison of single and dual array microseismic mapping techniques in the Barnett Shale. In *SPE Annu. Tech. Conf. Exhib.*, Dallas, 2005. doi: 10.2118/95568-MS.

Warpinski, N. R., Du, J., and Zimmer, U. Measurements of hydraulic-fracture-induced seismicity in gas shales. *SPE Prod. Oper.*, pages 240–252, 2012. doi: 10.2118/151597-PA.

Warpinski, N. R., Mayerhofer, M. J., and Agarwal, K. Hydraulic fracture geomechanics and microseismic source mechanisms. *SPE J.*, 18(4):766–780, 2013. doi: 10.2118/158935-PA.

Weng, X., Kresse, O., Chuprakov, D., Cohen, C. E., Prioul, R., and Ganguly, U. Applying complex fracture model and integrated workflow in unconventional reservoirs. *J. Pet. Sci. Eng.*, 124:468–483, 2014. doi: 10.1016/j.petrol.2014.09.021.

Witherspoon, P. A., Wang, J. S., Iwai, K., and Gale, J. E. Validity of cubic law for fluid flow in a deformable rock fracture. *Water Resour. Res.*, 16(6):1016–1024, 1980. doi: 10.1029/WR016i006p01016.

Wong, S.-W., Geilikman, M., and Xu, G. The geomechanical interaction of multiple hydraulic fractures in horizontal wells. In *Int. Conf. Eff. Sustain. Hydraul. Fract.*, pages 661–677, Brisbane, 2013. doi: 10.2118/163982-MS.

Wu, K. *Numerical modeling of complex hydraulic fracture development in unconventional reservoirs*. Ph.D. dissertation, The University of Texas at Austin, 2014.

Wu, K. and Olson, J. Investigation of the impact of fracture spacing and fluid properties for interfering simultaneously or sequentially generated hydraulic fractures. *SPE Prod. Oper.*, pages 427–436, 2013. doi: 10.2118/163821-PA.

Wu, K. and Olson, J. E. A simplified three-dimensional displacement discontinuity method for multiple fracture simulations. *Int. J. Fract.*, 193(2):191–204, 2015a. doi: 10.1007/s10704-015-0023-4.

Wu, K. and Olson, J. E. Mechanisms of Simultaneous Hydraulic-Fracture Propagation From Multiple Perforation Clusters in Horizontal Wells. *SPE J.*, 21(3):1000–1008, 2015b. doi: 10.2118/178925-PA.

Wu, K., Olson, J., Balhoff, M. T., and Yu, W. Numerical analysis for promoting uniform development of simultaneous multiple-fracture propagation in horizontal wells. *SPE Prod. Oper.*, 32:41–50, 2016. doi: 10.2118/174869-PA.

Xiao, H. T. and Yue, Z. Q. A three-dimensional displacement discontinuity method for crack problems in layered rocks. *Int. J. Rock Mech. Min. Sci.*, 48(3):412–420, 2011. doi: 10.1016/j.ijrmms.2011.02.005.

Xiao, H. T., Yue, Z. Q., and Zhao, X. M. A generalized Kelvin solution based method for analyzing elastic fields in heterogeneous rocks due to reservoir water impoundment. *Comput. Geosci.*, 43:126–136, 2012. doi: 10.1016/j.cageo.2011.09.014.

Xie, L., Min, K. B., and Shen, B. Simulation of hydraulic fracturing and its interactions with a pre-existing fracture using displacement discontinuity method. *J. Nat. Gas Sci. Eng.*, 36:1284–1294, 2016. doi: 10.1016/j.jngse.2016.03.050.

Xu, G. and Wong, S.-w. Interaction of multiple non-planar hydraulic fractures in horizontal wells. In *Int. Pet. Technol. Conf.*, 2013.

Yamamoto, K., Shimamoto, T., and Sukemura, S. Multiple fracture propagation model for a three-dimensional hydraulic fracturing simulator. *Int. J. Geomech.*, 4 (1):46–57, 2004. doi: 10.1061/(ASCE)1532-3641(2004)4:1(46).

Yan, C., Zheng, H., Sun, G., and Ge, X. Combined finite-discrete element method for simulation of hydraulic fracturing. *Rock Mech. Rock Eng.*, 49(4):1389–1410, 2016. doi: 10.1007/s00603-015-0816-9.

Yi, S. S. and Sharma, M. M. A new method to calculate slurry distribution among multiple fractures during fracturing and refracturing. *J. Petr. Sci. Eng.*, 170:304–314, 2018. doi: 10.1016/j.petrol.2018.06.048.

Yi, S. S., Wu, C.-H., and Sharma, M. M. Proppant distribution among multiple

perforation clusters in a horizontal wellbore. *SPE Prod. Oper.*, 170:654–665, 2017. doi: 10.2118/184861-MS.

Yousefzadeh, A., Li, Q., Virues, C., and Aguilera, R. An interpretation of microseismic spatial anomalies, b-values, and magnitude analyses to identify activated fracture networks in Horn River Basin. *SPE Prod. Oper.*, pages 679–696, 2018. doi: 10.2118/179153-PA.

Yu, X., Rutledge, J., Leaney, S., Sun, J., Pankaj, P., Weng, X., Onda, H., Donovan, M., Nielsen, J., and Duhault, J. Integration of microseismic data and an unconventional fracture modeling tool to generate the hydraulically induced fracture network: A case study from the Cardium Formation, West Central Alberta, Canada. In *Proc. 3rd Unconv. Resour. Technol. Conf.*, pages 2430–2444, San Antonio, 2015. doi: 10.15530/urtec-2015-2154594.

Yue, Z. Q. On generalized Kelvin solutions in a multilayered elastic medium. *J. Elast.*, 40(1):1–43, 1995. doi: 10.1007/BF00042082.

Yue, Z. Q. On elastostatics of multilayered solids subjected to general surface traction. *Q. J. Mech. Appl. Mech.*, 49(3):471–499, 1996. doi: 10.1093/qjmam/49.3.471.

Yue, Z. Q. and Xiao, H. T. Generalized Kelvin solution based boundary element method for crack problems in multilayered solids. *Eng. Anal. Bound. Elem.*, 26(8): 691–705, 2002. doi: 10.1016/S0955-7997(02)00038-3.

Yue, Z. Q., Xiao, H. T., and Tham, L. G. Boundary element analysis of crack problems in functionally graded materials. *Int. J. Solids Struct.*, 40:3273–3291, 2003. doi: 10.1016/S0020-7683(03)00094-5.

Zehnder, A. T. *Fracture Mechanics*. Springer, New York, 2012. doi: 10.1007/978-94-007-2595-9.

Zhang, X. and Jeffrey, R. G. Numerical studies on crack problems in three-layered elastic media using an image method. *Int. J. Fract.*, 139(3-4):477–493, 2006. doi: 10.1007/s10704-006-0054-y.

Zhang, Z., Li, X., He, J., Wu, Y., and Li, G. Numerical study on the propagation of tensile and shear fracture network in naturally fractured shale reservoirs. *J. Nat. Gas Sci. Eng.*, 37:1–14, 2017. doi: 10.1016/j.jngse.2016.11.031.

Zhou, J., Chen, M., Jin, Y., and Zhang, G.-q. Analysis of fracture propagation behavior and fracture geometry using a tri-axial fracturing system in naturally fractured reservoirs. *Int. J. Rock Mech. Min. Sci.*, 45(7):1143–1152, 2008. doi: 10.1016/j.ijrmms.2008.01.001.

Zhou, X. and Ghassemi, A. Three-dimensional poroelastic analysis of a pressurized natural fracture. *Int. J. Rock Mech. Min. Sci.*, 48(4):527–534, 2011. doi: 10.1016/j.ijrmms.2011.02.002.

Zhou, X. X. and Ghassemi, A. Three-dimensional poroelastic simulation of hydraulic and natural fractures using the displacement discontinuity method. In *34th Work. Geotherm. Reserv. Eng.*, Stanford, 2009. SGP-TR-187.

Zimmerman, R. W. and Yeo, I. W. Fluid flow in rock fractures: from the Navier-Stokes equations to the cubic law. In Faybishenko, B., Witherspoon, P. A., and Benson, S. M., editors, *Dyn. Fluids Fract. Rock Geophys. Monogr. Ser.*, volume 122, pages 213–224. American Geophysical Union, Washington, DC, 2000. doi: 10.1029/GM122p0213.

Zoback, M. D. *Reservoir Geomechanics*. Cambridge University Press, Cambridge, 2007. doi: 10.1017/CBO9780511586477.